ISBN 978-82-326-3086-8 (printed version)
ISBN 978-82-326-3087-5 (electronic version)
ISSN 1503-8181

Doctoral Thesis

Jan Hendrik Cloete

NTNU
Norwegian University of
Science and Technology

Doctoral theses at NTNU, 2018:148

Jan Hendrik Cloete

Development of Anisotropic Filtered Two Fluid Model Closures

Jan Hendrik Cloete

Doctoral Thesis

NTNU
Norwegian University of
Science and Technology
Faculty of Engineering
Department of Energy and Process Engineering

NTNU
Norwegian University of
Science and Technology

Doctoral theses at NTNU, 2018:148

NTNU

Jan Hendrik Cloete

Development of Anisotropic Filtered Two Fluid Model Closures

Thesis for the degree of Philosophiae Doctor

Trondheim, May 2018

Norwegian University of Science and Technology
Faculty of Engineering
Department of Energy and Process Engineering

NTNU
Norwegian University of
Science and Technology

NTNU
Norwegian University of Science and Technology

Thesis for the degree of Philosophiae Doctor

Faculty of Engineering
Department of Energy and Process Engineering

ISBN 978-82-326-3086-8 (printed version)
ISBN 978-82-326-3087-5 (electronic version)
ISSN 1503-8181

Doctoral theses at NTNU, 2018:148

Printed by Skipnes Kommunikasjon as

Abstract

Filtered modelling of dynamic gas-particle flows has been actively studied by various groups around the world for more than a decade. Even so, the great complexity of this field of study means that several important knowledge gaps still exist. This thesis represents a significant step forward by closing several of the most important knowledge gaps through the development and rigorous assessment of new closures via detailed *a priori* and *a posteriori* analyses. The resulting set of filtered closures clearly outperforms the current state of the art, resulting in several valuable conclusions and recommendations.

The primary conclusion from the present work is related to the critical importance of accounting for anisotropy in the filtered closures for drag and solids mesoscale stresses. For the filtered drag force, it was found that conventional isotropic closures strongly underpredict the drag correction in the directions perpendicular to gravity. A new formulation based on the drift velocity concept was found to account for this anisotropic effect in an efficient and natural manner. For the solids mesoscale stresses, the present work confirmed that the conventional approach based on the Boussinesq approximation results in large errors. In fact, studies showed that coarse grid simulations completely neglecting the solids mesoscale stresses perform better than those relying on the Boussinesq-based approach. Based on this knowledge, a new closure formulation was devised, conveniently allowing the prediction of the anisotropic solids mesoscale stresses via a single expression.

Findings from the present study also challenged other conventions in the field. Firstly, the use of the filtered slip velocity as a second marker in the filtered drag force closure was found to lead to poor model performance. Secondly, a filter size to grid size ratio of unity appears to be the fundamentally correct ratio instead of the commonly employed ratio of 2. And thirdly, the 2D models derived in this work outperformed a 3D model from the literature in a validation study, suggesting that domain size independence of resolved simulations is more important than performing simulations in 3D.

For reactive flows, the present work showed that a relatively simple closure can accurately predict the filtered reaction rate. In addition, the closure for the mesoscale species dispersion rate used in the filtered species transport equation was shown to have only a minor effect on reactor performance predictions. However, coarse grid reactive simulations were sensitive to the accuracy of the hydrodynamic filtered closures employed. Good hydrodynamic modelling is therefore the most important prerequisite for accurate large scale reactor performance predictions.

Despite the progress made in this thesis, some important knowledge gaps persist. Firstly, this study did not attempt to quantify the generality of the proposed closures to flow situations with different particle and fluid properties. Such studies are required before the newly proposed closures can be recommended for use in reactors with particle and fluid properties that are very different from the FCC-type system considered in the present work. Secondly, an important effect related to the ratio of the domain width to the length of macro-clusters resolved in coarse grid simulations was identified. This effect required the use of a larger filter size to grid size ratio in narrow domains and further studies are required to find a general solution to this challenge.

However, informed application of the anisotropic closures proposed in this thesis to real fluidized bed reactor problems can already be recommended. Experience from such studies can further accelerate the development of closures for filtered models towards the goal of their ubiquitous deployment for design, optimization and scale-up of fluidized bed reactors in industry.

Acknowledgements

Firstly, I would like to thank the European Commission for funding NanoSim, the project that included this PhD study. NanoSim allowed our research group to enter the field of filtered Two Fluid Model (fTFM) development. Subsequently, much has been learned regarding the development and application of these models, as detailed in this thesis. These findings will serve as an excellent platform for our future efforts to develop reliable fTFMs for large scale fluidized bed reactor simulations. I'm also thankful for the opportunity to engage and collaborate with top scientists from around Europe and from diverse modelling fields, made possible by being part of NanoSim.

I am very grateful for the computational resources provided at NTNU by UNINETT Sigma2 AS, https://www.sigma2.no, as part of the national infrastructure for computational science in Norway. Considering the great computational expense of performing resolved TFM simulations, this study would not have been feasible without these resources.

My sincerest thanks go to my supervisors, two of the busiest and most hard-working individuals that I know. It was due to the initial interest of Dr. Shahriar Amini in fTFMs, as well as his subsequent creation of the NanoSim project, that paved the way for the work performed in this study. I am also very appreciative of his continued efforts to ensure that the progress of the present study is continued in future projects. On the other hand, it was CPPPO, the initiative of Dr. Stefan Radl, that allowed us to investigate the resolved simulation data in enough detail to lead to the important conclusions presented in this thesis. I was also incredibly lucky to be able to draw on his fundamental understanding of particulate flows and his knowledge of the fTFM literature for three years.

A special thank you goes to Dr. Schalk Cloete, who fulfilled the roles of co-worker, brother and friend over the last couple of years. Few people can match his incredible commitment to scientific research and the outcomes of this study would not have been the same without his insights and collaborative work. But on the other hand, always having someone available for long ski sessions in the mountains is probably one of the most important factors that kept me productive throughout this PhD study.

Thanks is also due to Dr. Federico Municchi for his efforts to implement the new features that I required in CPPPO, as well as for always being available to fix any bugs that I might uncover. I would also like to extend my thanks to Dr. Simon Schneiderbauer for his assistance in providing input on his particle-wall friction model early in the project, as well as for subsequent discussions regarding fTFMs.

Lastly, I would not have reached where I am today without the help of my family. My mother and father, Alta and Schalk, have always been there to support and nurture my dreams. Also, while growing up their respective professions as fictional writer and agricultural researcher provided an ideal environment for me to develop the skills required to be a competent researcher. Finally, a very special thank you goes to my incredible wife, Janet. Completing my PhD in Norway required the two of us to face many challenges over three extremely busy years. Yet, I could not have asked for a better partner in this endeavour, always striking a perfect balance between motivating me to work harder and allowing me time to relax by accompanying me on camping and photography trips. I will forever be grateful for the support and understanding during my studies.

Table of contents

Chapter 1: Introduction 1

1.1 The importance of filtered Two Fluid Models to industry 1

1.2 Filtered TFM literature 2

1.3 Filtered TFMs as part of a multi-scale modelling approach 3

1.4 Objectives 4

Chapter 2: Summary of governing equations 6

2.1 Governing equations of the resolved TFM 6

2.2 Governing equations of the filtered TFM 7

2.3 Summary of fTFM closures 10

Chapter 3: Development and a priori analysis of new fTFM closures 16

3.1 Resolved simulations 16

3.2 Data analysis 18

3.3 Considerations when developing closures for fTFMs 19

3.4 Filtered drag force closures 21

3.5 Mesoscale interphase force closures 49

3.6 Solids mesoscale stress closures 54

3.7 Frictional stress closures 69

3.8 Species transport closures 72

Chapter 4: Verification of fTFM closures in a partially-periodic domain 76

Chapter 5: Further verification and validation of fTFM closures 91

5.1 Verification in a fully-periodic domain 91

5.2 Verification in wall-bounded domains 108

5.3 Validation of fTFM closures 136

Chapter 6: Conclusions 148

Nomenclature 151

References 155

Appendix 160

A. Publication list 160

B. The sensitivity of fTFM closures to the resolved TFM configuration 161

C. Evaluation of wall boundary conditions for riser flow 175

D. Supplementary results and discussion 195

E. Additional equations 198

F. Supplementary fTFM closures 201
G. Filtered TFM closures used in the validation study 207

Chapter 1: Introduction

1.1 The importance of filtered Two Fluid Models to industry

Fluidized beds are widely used in fluid catalytic cracking, coal gasification and polymerization processes, as well as for drying, cooling and coating of solids. Due to the excellent mass and heat transfer that they enable in a wide range of applications, fluidized beds form an essential part of many processing industries. In the last decade two decades, computational fluid dynamics (CFD) has become a useful tool for investigating the behaviour of fluidized beds. This is mainly due to the rapidly advancing computational resources, progress in theoretical models and new numerical methods. The primary use of CFD simulations is that they allow a better understanding to be developed. This is especially relevant for the complex multiphase flow in fluidized beds, since it can be challenging and costly to measure or visualise these flows by means of experiments. Also, as the modelling methods mature, such simulations can be used to aid the design process, decreasing the cost and time required for the optimization and scale-up of new technologies based on fluidized beds.

Several simulation methods exist for the modelling of fluidized beds, but all face a common challenge: the extremely large number of particles in fluidized beds, which can be in the order of 10^{12} in industrial systems. Particle-Resolved Direct Numerical Simulation (PR-DNS), where the flow is resolved around individual particles, is only feasible for very small systems (i.e., typically involving less than $O(10^5)$ particles). PR-DNS is mainly used for the development of models, for example for the drag between the fluid and the particles [1]. Particle-Unresolved Euler-Lagrange models (PU-EL; the most prominent example being CFD-DEM-based models) allow a substantial reduction in the computational requirements by not resolving the flow around the particles. Yet, PU-EL is limited by the number of particles that need to be tracked individually (typically, these simulations involve less than $O(10^7)$ particles). The computational cost of CFD-DEM can be further reduced by tracking “parcels”, containing multiple particles each [2, 3]. However, models for correcting for the effects of this assumption are still in early development.

The computational cost of fluidized bed simulations can further be decreased by not considering particles as discrete entities, but by assuming the solids phase to behave as a continuum. The Two Fluid Model (TFM) closed by the Kinetic Theory of Granular Flow (KTGF) follows such an argument, and accounts for the collisions and translation of individual particles by making using of closure models. Particle rotation is typically neglected, or simply lumped into closure models. The TFM is widely used and has been proven to be a useful tool for investigating the behaviour inside laboratory scale fluidized beds [4-10]. However, the primary limitation of this approach is that it requires the transient multiphase structures, which occur in fluidized beds in the form of gas bubbles and particle clusters, to be resolved [11]. These structures are similar to turbulent motion in turbulent flow, with the additional complexity that they form spontaneously and involve two or more phases. Multiphase flow structures exist over a large range of length scales, referred to as the mesoscale, and even the small structures can have an important effect on the overall bed behaviour. The TFM approach therefore requires very small grid cells and time steps to resolve all relevant structures, resulting in unfeasibly large computational times for industrial scale reactors - even on state-of-the art computing clusters.

The filtered TFM (fTFM) offers a solution to allow accurate solutions on coarse grids, where the mesoscale multiphase structures are not accurately resolved. fTFMs are based on the principle of performing a spatial averaging operation on the governing equations, which results in additional terms for the unresolved effects that have to be closed. The size of the grid in the coarse grid simulations will determine the range of scales that are unresolved, and therefore also the magnitude of the sub-grid corrections. The fTFM closures are generally obtained by performing resolved simulations, followed by a statistical analysis of spatially-averaged data to derive the required closure models [12-19]. Theoretical considerations can help to accelerate this closure development process, and can ensure that the developed closure is applicable to a wide range of flow situations [20].

1.2 Filtered TFM literature

The research community has long know about the presence of mesoscale structures in fluidized beds and its effect on simulations behaviour has frequently been studied [12, 21-23]. However, it has been less than a decade since the first complete fTFM has been proposed [16]. Since then, predominantly three groups have been developing TFM closures: The group of Prof. Sundaresan at Princeton University, the group of Prof. Simonin at INP Toulouse, and the group of Dr. Schneiderbauer at JKU Linz. This section will briefly discuss the various contributions from these different groups.

In the work from the Sundaresan group it was found that primarily two hydrodynamic contributions from the mesoscale structures have to be accounted for to compensate for their effects in coarse grid simulations. The most important effect is that the effective drag coefficient is reduced compared to what is predicted by microscopic drag closure models that requires the mesoscale structures to be resolved. In the work from the Sundaresan group this effect is accounted for by using a drag correction factor. This factor simply scales the drag force (relative to the microscopic drag law predictions) as a function of the filter size, i.e., the size of the averaging region, and additional independent variables. The latter are referred to as “markers”, and the filtered solids volume fraction is the most prominent example thereof. The second contribution comes from the sub-grid solids velocity fluctuations, which results in additional stresses. The Sundaresan group has closed this contribution using the Boussinesq approximation, modelling the mean normal stress as an added filtered solids pressure, and the deviatoric stresses through a filtered solids viscosity.

The original fTFM [12, 16, 19, 24], was developed from 2D simulations. Specifically, closures for the drag correction factor, the filtered solids pressure and the filtered solids viscosity were proposed, all based on one marker, namely the filtered solids volume fraction. However, these closures require additional corrections near walls to give accurate results [25], complicating the implementation in complex geometries. Subsequently, also in 2D, the closure models were extended to 2-marker closures [14], adding the filtered slip velocity magnitude as a marker for the drag correction factor and the filtered deviatoric shear rate magnitude as a marker for the filtered solids pressure and the filtered solids viscosity. Recently, 2-marker closure models have also been derived from 3D simulations [13]. The 2-marker closure models from the Sundaresan group have been shown to give reasonable predictions in validation studies without the use of wall-corrections [13, 26]. This group is also the only to have proposed closures for the effect of mesoscale structures on heat transfer [27], scalar transport [27] and on the rate of heterogeneous chemical reactions [28].

The group of Prof. Simonin introduced the concept of a sub-grid drift velocity [17] to close the reduction in the drag due to mesoscale structures. The closure for the drift velocity was formulated as

a function of the filter size and the filtered solids volume fraction. A dynamic parameter adjustment concept was also introduced. Later work from this group [18] extended the drift velocity closure and also proposed closures for the solids mesoscale stresses based on the Boussinesq approximation. The studies of this group also introduced the concept of an *a priori* analysis to the fTFM field by comparing model predictions to observed values in the resolved simulation data.

The work by the Schneiderbauer group [15] initially followed an approach similar to the 2-marker closure models from the Sundaresan group [13, 14]. However, recently, Schneiderbauer has proposed a Spatially-Averaged TFM (SA-TFM) based on a theoretical development with well-reasoned assumptions [20]. In this approach, algebraic expressions were derived for the solids and gas phase turbulent kinetic energy (which are related to the mesoscale stresses), and the solids volume fraction variance. A drag correction closure, using these three quantities as independent variables, was then derived from theoretical principles based on certain assumptions. The filtered solids pressure and the filtered solids viscosity were calculated from the solids turbulent kinetic energy based on the Boussinesq approximation. Despite several simplifying assumptions that were adopted – some of which that requires a more detailed analysis, as will be discussed in the present study - the SA-TFM has been shown to give good predictions over a range of flow conditions [29].

It can be noted that all of the studies above focussed on sub-grid corrections for monodisperse flows. If more than one particle diameter is considered for the solids phase, there exist additional drag forces between the different particle classes, which also required a closure model for the effect of mesoscale structures. At present, the only rigorous set of fTFM closures for bidisperse flows comes from the Sundaresan group [30]. However, bidisperse or polydisperse flows will not be discussed as part of the scope of the present study.

Lastly, it can be noted that filtered closures have also been developed based on CFD-DEM simulations [2, 31, 32]. However, here different physics are at play compared to the TFM-based closure models, and much smaller filter sizes are generally considered. However, it has been shown that there is some similarity between the closures derived from TFM and CFD-DEM simulations [31].

1.3 Filtered TFMs as part of a multi-scale modelling approach

The present study was performed as part of NanoSim, a project that investigated a multi-scale simulation-based approach to design cost-effective technologies for Chemical Looping Reforming (CLR). This entailed modelling at the atomistic-, particle-, reactor- and plant scales, with information exchanged between the different scales. Filtered Two Fluid Modelling fits perfectly into such a multi-scale modelling environment due to several reasons:

Firstly, the development of fTFMs, by itself, requires a multiscale modelling approach. This is because resolved simulations that accurately simulate the mesoscale in fluidized beds are required to generate data that is used for deriving fTFM closures. The closures can then be used to perform simulations on the macro (i.e., reactor) scale, without having to resolve the mesoscale structures.

Secondly, more accurate fTFM closures can be developed based on improved closures developed on the micro (i.e., particle) scale. This is because an fTFM closure can only be as accurate as the resolved TFM simulations on which it is based. Since the TFM assumes the solids to be a continuum, closures are necessary to account for the behaviour of individual particles. Such closures, for example for the

interphase momentum exchange or mass- and heat transfer, can be improved by making use of modelling techniques where individual particles are tracked, for example PR-DNS or PU-EL.

Lastly, since fTFMs allow several orders of magnitude speedup in reactor scale simulations, coarse grid filtered simulations may become an extremely useful tool for data generation: For example, a large number of reactor simulations can be performed to map out the reactor performance for a range of operating conditions, or design parameters. Subsequently, this data can be fed into system-scale simulations that can be used to predict the performance of a set of devices, or even a whole plant. Going even a step further, techno-economic assessments can be made that ultimately may lead to optimal design and optimal operating conditions for fluidized bed reactors, or the systems they are embedded in.

1.4 Objectives

1.4.1 Original objectives

In a work before the start of the present study [25], it was found that early 1-marker fTFMs [16, 19] failed completely in wall-bounded domains (when using coarse computational meshes typical for industrial applications) in case dedicated wall corrections are not employed. Dedicated wall corrections complicate the functional form of the closure, and are difficult to implement in a generic manner, especially in complex geometries. It is therefore highly desirable to derive closures that can correctly account for regions with large flow gradients (i.e., regions close to walls). This could potentially be accomplished through more sophisticated closure models based on multiple markers. The primary objective of the present study was therefore to develop fTFM closures that accurately predict the flow behaviour near walls without wall corrections.

1.4.2 Revised objectives and scope

Shortly before and during the present study, the more advanced 2-marker closure models from the Sundaresan group [13, 14] were published. Validation studies performed with these closure models showed that they perform reasonably well in wall-bounded domains, and did not require dedicated wall corrections [13, 26]. However, early in the present study, the performance of the closure models was evaluated in domains that were set up to minimise the complicating effect of walls. As will be discussed in Chapter 4.1.2, it was found that these fTFMs failed completely for the verification case considered. This raised questions regarding the reliability of these 2-marker closure models for reasons that did not concern wall effects.

As a result, the primary objective of this study was revised to focus on developing a better understanding of fTFM closures and how their accuracy and generality can be improved. Clearly, filtered data from resolved simulations must be analysed in greater detail than the current state of the art. Such a detailed analysis would lead to new functional forms based on new markers, ultimately resulting in closures that perform much more reliably in dedicated verification studies.

This change in focus also necessitated a change in scope. An improved understanding of how fTFM closures behave and how improvements in the closures influence the predictions on coarse grids would require detailed verification against resolved simulations over a range of different conditions. However, performing several resolved simulations on relevantly large domain sizes is simply not feasible in 3D. For this reason, all closure development and verification in this study was limited to 2D

simulations. This was justified based on the finding that fTFM closures derived from 2D and 3D simulations are qualitatively similar [12]. This implies that any improvements made to fTFM closures based on 2D simulations can be similarly applied to data generated in 3D simulations in future work. Therefore, by first developing and verifying fTFM closures in 2D, and then applying the same improved principles to 3D data, the overall rate of fTFM closure development may be increased. It can further be noted that the validation studies presented in Chapter 5.3 document that the newly developed fTFM closures of the present work, based on 2D simulation data, are useful: these closures outperformed a recent fTFM from literature [13] that was based on 3D simulation data. This finding again justifies the approach followed in the present study.

It is also known that there exists a substantial uncertainty regarding the scaling of fTFM closures to different particle and fluid properties than those they were derived for [33]. To limit the scope of the present study, it was also decided to focus on a single fluid/particle combination. Again, the argument is followed that if an accurate approach could be established for the specific case considered, future work can then aim to generalize the findings from the present study.

Also, as mentioned earlier, the initial focus of this study was to develop improved closures in the near-wall regions where large flow gradients occur, therefore resolved simulations in wall-bounded domains were planned to generate data for closure development. For this reason, early work evaluated a recent closure model for the particle-wall boundary condition [34] in riser flow and compared it to the most commonly used closure in literature [35]. The results of this study are given in Appendix C. The intention was to use the more recent closure in wall-bounded resolved simulations for closure development. However, due to the change of scope described in this section, resolved simulations for closure development were limited to fully-periodic domains. Future work will consider data from wall-bounded domains using realistic particle-wall boundary conditions.

To summarise, the present study therefore considers data from 2D resolved simulations performed in fully-periodic domains for a single fluid/particle configuration to develop improved fTFM closures. Additionally, the closure development process is continuously guided by detailed verification against 2D resolved simulations, allowing an improved understanding of the effect of different closure formulations and the evaluation of the performance of the developed closures.

Chapter 2: Summary of governing equations

This chapter will summarise the governing equations that are solved during simulations in this study. These equations are split in three sections: (i) The first section provides the transport equations and closures that are solved in the resolved KTGF-based TFM simulations. These equations are used for generating data for closure derivation, and for performing simulations against which to verify the fTFM closures developed in this study. (ii) The next section derives the filtered transport equations, which are solved during coarse grid simulations using fTFM closures, and highlights the different terms that require closure. (iii) Lastly, the third section summarises the closures proposed during the present study.

This chapter will focus on the equations needed to predict the hydrodynamics of mono-disperse gas-particle flows, as well as simple isothermal reactions. Filtered quantities present in generic scalar and energy transport equations were only considered as part of a study investigating the sensitivity of fTFM closures to the closure choices in the resolved simulations, the complete results of which are presented in Appendix B. The equations relevant to scalar and energy transport are therefore given in Appendix E.1 and Appendix E.2.

2.1 Governing equations of the resolved TFM

This section briefly presents the equations solved in the resolved TFM-based simulations, as well as the closures used. A more detailed description of the equations used can be found in an earlier work [11].

2.1.1 Continuity equations

Continuity equations are solved for the gas and solids phases, which read as follows:

$$\frac{\partial}{\partial t}(\alpha_g \rho_g) + \nabla \cdot (\alpha_g \rho_g \vec{v}_g) = 0 \qquad \text{Equation 1}$$

$$\frac{\partial}{\partial t}(\alpha_s \rho_s) + \nabla \cdot (\alpha_s \rho_s \vec{v}_s) = 0 \qquad \text{Equation 2}$$

Additionally, the sum of the volume fractions for the different phases should be equal to unity.

2.1.2 Momentum transport equations

The following momentum conservation equation is solved for the gas

$$\frac{\partial}{\partial t}(\alpha_g \rho_g \vec{v}_g) + \nabla \cdot (\alpha_g \rho_g \vec{v}_g \vec{v}_g) = -\alpha_g \nabla p + \nabla \cdot \bar{\bar{\tau}}_g + \alpha_g \rho_g \vec{g} + K_{sq}(\vec{v}_s - \vec{v}_g) \qquad \text{Equation 3}$$

,while that for the solids phase reads:

$$\frac{\partial}{\partial t}(\alpha_s \rho_s \vec{v}_s) + \nabla \cdot (\alpha_s \rho_s \vec{v}_s \vec{v}_s) = -\alpha_s \nabla p - \nabla p_s + \nabla \cdot \bar{\bar{\tau}}_s + \alpha_s \rho_s \vec{g} + K_{gs}(\vec{v}_g - \vec{v}_s) \qquad \text{Equation 4}$$

, where the solids stress tensor is defined as follows:

$$\bar{\bar{\tau}}_s = \alpha_s \mu_s (\nabla \vec{v}_s + \nabla \vec{v}_s^T) + \alpha_s (\lambda_s - \frac{2}{3}\mu_s) \nabla \cdot \vec{v}_s \bar{\bar{I}} \quad \text{Equation 5}$$

In both momentum equations, the last term on the right-hand side describes the volumetric interphase momentum exchange rate, modelled by the Huilin-Gidaspow model [36] in the present study. This model employs the Ergun equation [37] for solids volume fractions greater than 0.2 and the Wen-Yu drag model [38] for more dilute flows. A blending function is used to smooth out the discontinuity between these equations. Furthermore, closures are required in the solids momentum equation (Equation 4) for the solids pressure [39], p_s in the second term on the right, and the shear [40] and bulk [39] viscosities in Equation 5. The radial distribution function, which is used in the three previous closures, is calculated according to Ogawa [41]. In the case of prolonged, frictional contacts between particles in very dense flows, an additional frictional component is added to the solids pressure and solids viscosity. In this study the model by Johnson & Jackson [35] is used for the frictional pressure and the model by Schaeffer [42] for the frictional viscosity.

2.1.3 Granular temperature transport equation

The closures for the solids pressure and viscosities require information on the fluctuation velocity of the particles. The following transport equation for the granular temperature is used to supply relevant local information on this fluctuation velocity:

$$\frac{3}{2}[\frac{\partial}{\partial t}(\alpha_s \rho_s \Theta_s) + \nabla \cdot (\alpha_s \rho_s \vec{v}_s \Theta_s)] = (-p_s \bar{\bar{I}} + \bar{\bar{\tau}}_s) : \nabla \vec{v}_s + \nabla \cdot (k_{\Theta_s} \nabla \Theta_s) - \gamma_{\Theta_s} + \phi_{gs} \quad \text{Equation 6}$$

The first term on the right-hand side represents the generation of granular temperature due to solids stresses. The other terms on the right-hand side are the granular conductivity [40] ($k_{\Theta_s} \nabla \Theta_s$), the collisional dissipation of kinetic energy [39] (γ_{Θ_s}) and the dissipation of granular temperature due to momentum exchange between the phases [40] (ϕ_{gs}). The interested reader is referred to a previous study for detailed information on how to close these terms [11].

2.1.4 Species transport equation

In the present study, a hypothetical first-order, solids-catalysed reaction is considered, converting species A into species B. The following species conservation equation is solved for the reactant:

$$\frac{\partial}{\partial t}(\alpha_g \rho_g X_A) + \nabla \cdot (\alpha_g \rho_g X_A \vec{v}_g) = \nabla \cdot (D \alpha_g \nabla X_A) - k_A \rho_g \alpha_s X_A \quad \text{Equation 7}$$

2.2 Governing equations of the filtered TFM

2.2.1 Definition of filtered quantities

The filtered conservation equations are obtained by performing a spatial averaging procedure on the microscopic conservation equations presented in Chapter 2.1. In the resulting filtered equations, details of the flow structure smaller than the filter size are smoothed out. Consequently, the effects of the sub-filter scale structures need to be modelled to close new terms appearing in the filtered transport equations. The filtered equations are then, in principle, capable of predicting the same

macroscopic flow behaviour (i.e., in the sense of spatial averages) as the resolved simulations, but without having to resolve the small scale multiphase structures using costly, fine grids.

The filtered phase volume fraction is defined as

$$\overline{\alpha_k}(\vec{x},t) = \int_{A_\infty} G(\vec{x},\vec{y})\alpha_k(\vec{y},t)d\vec{y} \qquad \text{Equation 8}$$

Where A_∞ is the area of the simulation domain, $\vec{x}$ represents the position of the centre of the filter being evaluated and $\vec{y}$ represents the position of the computational cell being evaluated. G, the weight function, is a function of $\vec{x}-\vec{y}$ and is constrained by $\int_{A_\infty} G(\vec{x},\vec{y})d\vec{y} = 1$. A simple box filter is used in this study, therefore averaging is performed over a cubical region (or a square in 2D). The side of lengths of the filter cube is given by the filter size Δ_f. The filter size is non-dimensionalized based on the particles' relaxation length:

$$\hat{\Delta}_f = \frac{\Delta_f}{v_t^2/g} \qquad \text{Equation 9}$$

The local phase volume fraction is divided into a filtered and a fluctuating part:

$$\alpha_k{}'(\vec{y},t) = \alpha_k(\vec{y},t) - \overline{\alpha_k}(\vec{y},t) \qquad \text{Equation 10}$$

The following generic equations can also be defined for $\theta_k'(\vec{y},t)$ and $\tilde{\theta}_k(\vec{y},t)$, representing any of the conserved variables considered in this study for a specific phase, k.

$$\overline{\alpha_k}(\vec{x},t)\tilde{\theta}_k(\vec{x},t) = \int_{A_\infty} G(\vec{x},\vec{y})\alpha_k(\vec{y},t)\theta_k(\vec{y},t)d\vec{y} \qquad \text{Equation 11}$$

$$\theta_k''(\vec{y},t) = \theta_k(\vec{y},t) - \tilde{\theta}_k(\vec{y},t) \qquad \text{Equation 12}$$

It should be noted that a single prime is used to denote the fluctuating part based on algebraic averages, whereas a double prime denotes the fluctuating part based on a phase-weighted variable. The latter is defined as: $\widetilde{\theta_k} = \overline{\alpha_k\theta_k}/\overline{\alpha_k}$.

2.2.2 Filtered equations

2.2.2.1 Filtered continuity equations

Applying a spatial average to Equation 1 and Equation 2, as well as rearranging, the filtered continuity equations can be derived. From Equation 13 and Equation 14, it is evident that no additional terms appear that require closure.

$$\frac{\partial}{\partial t}(\overline{\alpha_g}\rho_g) + \nabla\cdot(\overline{\alpha_g}\rho_g\widetilde{\vec{v}_g}) = 0 \qquad \text{Equation 13}$$

$$\frac{\partial}{\partial t}(\overline{\alpha_s}\rho_s) + \nabla\cdot(\overline{\alpha_s}\rho_s\widetilde{\vec{v}_s}) = 0 \qquad \text{Equation 14}$$

2.2.2.2 Filtered momentum transport equations

The filtered solids momentum equation can be derived as:

$$\frac{\partial}{\partial t}(\rho_s\overline{\alpha_s}\widetilde{\vec{v}_s}) + \nabla\cdot(\rho_s\overline{\alpha_s}\widetilde{\vec{v}_s}\widetilde{\vec{v}_s}) = -\overline{\alpha_s}\nabla\bar{p} - \nabla\overline{p_s} - \nabla\cdot(\rho_s\overline{\alpha_s\vec{v}_s''\vec{v}_s''}) + \nabla\cdot\bar{\bar{\tau}}_s + \overline{\alpha_s}\rho_s\vec{g} + \overline{K_{gs}(\vec{v}_g - \vec{v}_s)} - \overline{\alpha_s'\nabla p'} \quad \text{Equation 15}$$

Considering individual spatial components of the solids momentum equation in two dimensions, one obtains the following equations for the *x*- and *y*-direction, respectively:

$$\begin{aligned}\frac{\partial(\rho_s\overline{\alpha_s}\widetilde{u_s})}{\partial t} &+ \frac{\partial(\rho_s\overline{\alpha_s}\widetilde{u_s}\widetilde{u_s})}{\partial x} + \frac{\partial(\rho_s\overline{\alpha_s}\widetilde{u_s}\widetilde{v_s})}{\partial y} \\ &= -\overline{\alpha_s}\frac{\partial\bar{p}}{\partial x} - \frac{\partial\overline{p_s}}{\partial x} + \frac{\partial\left(\overline{\alpha_s\mu_s\left(\frac{4}{3}\frac{\partial u}{\partial x} - \frac{2}{3}\frac{\partial v}{\partial y}\right)}\right)}{\partial x} \\ &+ \frac{\partial\left(\overline{\alpha_s\mu_s\left(\frac{\partial u}{\partial y} + \frac{\partial v}{\partial x}\right)}\right)}{\partial y} + \frac{\partial\left(\overline{\alpha_s\lambda_s\left(\frac{\partial u}{\partial x} + \frac{\partial v}{\partial y}\right)}\right)}{\partial x} - \frac{\partial(\rho_s\overline{\alpha_s u_s'' u_s''})}{\partial x} \\ &- \frac{\partial(\rho_s\overline{\alpha_s u_s'' v_s''})}{\partial y} + \overline{K_{gs}(u_g - u_s)} - \overline{\alpha_s'\frac{\partial p'}{\partial x}}\end{aligned} \quad \text{Equation 16}$$

$$\begin{aligned}\frac{\partial(\rho_s\overline{\alpha_s}\widetilde{v_s})}{\partial t} &+ \frac{\partial(\rho_s\overline{\alpha_s}\widetilde{v_s}\widetilde{v_s})}{\partial y} + \frac{\partial(\rho_s\overline{\alpha_s}\widetilde{v_s}\widetilde{u_s})}{\partial x} \\ &= -\overline{\alpha_s}\frac{\partial\bar{p}}{\partial y} - \frac{\partial\overline{p_s}}{\partial y} + \frac{\partial\left(\overline{\alpha_s\mu_s\left(\frac{4}{3}\frac{\partial v}{\partial y} - \frac{2}{3}\frac{\partial u}{\partial x}\right)}\right)}{\partial y} \\ &+ \frac{\partial\left(\overline{\alpha_s\mu_s\left(\frac{\partial u}{\partial y} + \frac{\partial v}{\partial x}\right)}\right)}{\partial x} + \frac{\partial\left(\overline{\alpha_s\lambda_s\left(\frac{\partial u}{\partial x} + \frac{\partial v}{\partial y}\right)}\right)}{\partial y} - \frac{\partial(\rho_s\overline{\alpha_s v_s'' v_s''})}{\partial y} \\ &- \frac{\partial(\rho_s\overline{\alpha_s u_s'' v_s''})}{\partial x} + \overline{K_{gs}(v_g - v_s)} - \overline{\alpha_s'\frac{\partial p'}{\partial y}} + \overline{\alpha_s}\rho_s g\end{aligned} \quad \text{Equation 17}$$

The three terms on the left-hand side, as well as the first term on the right-hand side in both equations can be calculated directly in an fTFM simulation. The same is true for the gravity term in the *y*-direction equation (i.e., the last term on the right-hand side of Equation 17). All other terms require closure. For both directions, the second term on the right represents the filtered microscopic solids pressure (consisting of a kinetic theory-based and a frictional part), the third and fourth terms represent the microscopic solids viscosity (also consisting of a kinetic theory-based and a frictional part), the fifth term represents the filtered microscopic bulk viscosity, the sixth and seventh terms the mesoscale solids normal and shear stresses, the eighth term the filtered interphase drag and the ninth term the interphase force due to fluctuations in the pressure gradient. The pressure gradient fluctuation term is referred to as the mesoscale interphase force in the present study, as will be discussed in Chapter 3.5.

The filtered kinetic theory-based terms (present in terms two to five on the right-hand side) are generally considered small relative to the mesoscale stresses (i.e., terms 6 and 7 on the right-hand side). This is true at least for filter sizes used in industrially relevant simulations. Therefore, they are either (i) neglected [20], (ii) modelled as a function of the filter size and several markers (not including the granular temperature) [13], or (iii) calculated directly from the kinetic theory without applying filtering to the kinetic theory-based closures or the granular temperature transport equation [15, 16].

In this study, the latter approach is followed, therefore closures for the filtered kinetic theory stresses or the filtered granular temperature equation will not be considered. Closures will, however, be discussed for the filtered frictional stresses in Chapter 3.7.

In the filtered gas-phase momentum equation shown in Equation 18, the filtered gas phase stress tensor is usually evaluated from its filtered values, and therefore does not require closure [20, 43]. This is justified for typical particle concentrations (ranging from ~ 1% to the close packing limit), and by considering that the gas density is typically much lower than the particle density. The same closures for the filtered interphase forces (i.e., terms five and six on the right in Equation 18) can be used for both the gas and solid phase momentum equations. Therefore, only the mesoscale gas stresses (i.e., term two on the right) require closure in addition. The gas-phase mesoscale stresses are generally considered to be small compared to that of the solids phase [14] and have therefore often been neglected [16, 18]. An evaluation in this study has confirmed that forces due to mesoscale stresses in the gas phase are insignificant compared to those resulting from the solids mesoscale stresses. Consequently, this study will not attempt to close the gas phase mesoscale stresses. However, it should be noted that closures for the gas phase mesoscale stresses have been proposed in some recent studies [13, 14]. However, the impact of these closures on predictions made by coarse grid simulations has not been evaluated so far.

$$\frac{\partial}{\partial t}(\rho_g \overline{\alpha_g}\widetilde{\vec{v}_g}) + \nabla \cdot (\rho_g \overline{\alpha_g}\widetilde{\vec{v}_g}\widetilde{\vec{v}_g}) = -\overline{\alpha_g}\nabla\bar{p} - \nabla \cdot (\rho_g \overline{\alpha_g \vec{v}_g{}'' \vec{v}_g{}''}) + \nabla \cdot \overline{\bar{\bar{\tau}}_g} + \overline{\alpha_g}\rho_g\vec{g} + \overline{K_{sg}(\vec{v}_s - \vec{v}_g)} - \overline{\alpha_g{}'\nabla p'} \quad \text{Equation 18}$$

In summary for the hydrodynamics, closures are required for the filtered drag force, the mesoscale interphase force, the solids mesoscale stresses and the filtered frictional stresses based on the arguments given. Closures for these quantities will be detailed in Chapter 3.

2.2.2.3 Filtered species equation

The filtered species transport equation for a reactant A can be written as follows, considering a first order, solids catalysed reaction:

$$\frac{\partial}{\partial t}(\rho_g \overline{\alpha_g}\widetilde{X_A}) + \nabla \cdot (\rho_g \overline{\alpha_g}\widetilde{X_A}\widetilde{\vec{v}_g}) = \nabla \cdot (D\overline{\alpha_g \nabla X_A}) - \nabla \cdot (\rho_g \overline{\alpha_g X_A{}'' \vec{v}_g{}''}) - k_A \rho_g \overline{\alpha_s X_A} \quad \text{Equation 19}$$

The species dispersion due to the filtered microscopic diffusion (i.e., the first term on the right-hand side) is expected to be small relative to mesoscale dispersion, as well as convective transport. Therefore, in line with previous work regarding scalar dispersion in fTFMs [27], it will not be closed in the present study. Closures for the mesoscale species dispersion rate (i.e., the second term on the right-hand side), as well as the filtered reaction rate (third term on the right) will be discussed in Chapter 3.8.

2.3 Summary of fTFM closures

In this section, the most important closure models developed in the present study will be summarised. Although the closure models are repeated in Chapter 3 where they are derived, this summary gives a

useful overview of the closure development work performed in the present study. It also illustrates the increase in complexity of the closures as more physical effects are incorporated. It can be noted that scaled velocities, denoted with an asterisk, are scaled by the steady state sedimentation velocity, as discussed in Chapter 3.4.1.2.

2.3.1 Filtered interphase forces

2.3.1.1 Isotropic model

Here, the combined filtered drag and mesoscale interphase forces, used in the filtered momentum transport equations (Equation 15 and Equation 18), are closed as follows:

$$\overline{K_{gs}(\vec{v}_g - \vec{v}_s)} - \overline{\alpha_s{}'\nabla p'} = CK_{gs,hom}(\widetilde{\vec{v}_g} - \widetilde{\vec{v}_s}) \qquad \text{Equation 20}$$

$$\begin{aligned} -\log(C) = \operatorname{atan}(x_1\Delta_f^*\bar{\alpha}_s)\operatorname{atan}\left(x_2\Delta_f^* max(\bar{\alpha}_{\max} - \bar{\alpha}_s, 0)\right)\operatorname{atan}(x_3\Delta_f^*)\left(\frac{2}{\pi}\right)^3 \\ \times\left(x_4\log\|\widetilde{v_{slip}}^*\| + x_5{\Delta_f^*}^{x_6}\right. \\ \left. + x_7\left(\log\|\widetilde{v_{slip}}^*\|\right)^2\left(1 - \frac{\operatorname{atan}(x_8\Delta_f^*)}{\pi/2}\right)\right) \end{aligned} \qquad \text{Equation 21}$$

$$\text{if} -\log(C) < 0 \qquad C = 1$$

$x_1 = 36.6,\ x_2 = 22.6,\ x_3 = 1.68,\ x_4 = 0.835,\ x_5 = 0.140,\ x_6 = 0.188,\ x_7 = 1.33,\ x_8 = 3.28$ and $\bar{\alpha}_{max} = 0.551$.

2.3.1.2 Anisotropic models

For these models, the filtered drag force is closed separately:

$$\overline{K_{gs}(v_{g,i} - v_{s,i})} = C_{NL}K_{gs,hom}(\tilde{v}_{g,i} - \tilde{v}_{s,i} - v_{d,i}) \qquad \text{Equation 22}$$

Where the non-linearity correction factor, C_{NL}, can be closed as:

$$\begin{aligned} C_{NL} = 1 + \left\{\left[\operatorname{atan}(x_1\overline{\alpha_s}) - x_2\operatorname{atan}\left(x_3\max(\overline{\alpha_s} - x_4, 0)\right)\right]x_5\right. \\ + \left[\operatorname{atan}\left(x_6\|\widetilde{v_{slip}}^*\|^{x_7}\overline{\alpha_s}\right)\right. \\ \left.\left. - \operatorname{atan}\left(x_8\|\widetilde{v_{slip}}^*\|^{x_7}\max(\overline{\alpha_s} - x_4, 0)\right)\right]x_9\|\widetilde{v_{slip}}^*\|^{x_{10}}\right\} \\ \times\left(\frac{2}{\pi}\right)^2\operatorname{atan}\left(x_{11}\max(\overline{\alpha_s} - x_{12}, 0)\right) \end{aligned} \qquad \text{Equation 23}$$

$x_1 = 23.5, x_2 = 1.29, x_3 = 7.73 - 2.17\left(\frac{2}{\pi}\right)\text{atan}(0.194\Delta_{fil}^*), x_4 = 0.154,$
$x_5 = 2.04\left(\frac{2}{\pi}\right)\text{atan}(0.710\Delta_{fil}^*), x_6 = 135, x_7 = -0.451, x_8 = 43.6,$
$x_9 = -0.547\left(\frac{2}{\pi}\right)\text{atan}(0.825\Delta_{fil}^*), x_{10} = 0.390, x_{11} = 13.0$ and $x_{12} = 0.570.$

The adjusted slip velocity, $\tilde{v}_{g,i} - \tilde{v}_{s,i} - v_{d,i}$, is closed via the drift velocity, $v_{d,i}$, using 1-marker, 2-marker and 3-marker closures, as follows:

$$v_{adj,i}^* = \tilde{v}_{slip,i}^* - v_{d,i}^* \quad \text{Equation 24}$$

$$v_{d,i}^* = k_1 + \tilde{v}_{slip,i}^*\left(1 - 10^{-k_2}\right) + k_3 \quad \text{Equation 25}$$

$$k_1 = x_1\left(\frac{2}{\pi}\right)\left(\overline{\alpha_s}^{x_2}\right)\text{atan}\left(x_3\max(x_4 - \overline{\alpha_s}, 0)\right) \quad \text{Equation 26}$$

$k_1 = 0$ if i is in the direction perpendicular to gravity

$$k_2 = \left(\frac{2}{\pi}\right)^2 \text{atan}(x_5\overline{\alpha_s})\,\text{atan}\left(x_3\max(x_4 - \overline{\alpha_s}, 0)\right)\left(x_6\overline{\alpha_s}^{x_7} + x_8\left(\frac{2}{\pi}\right)\text{atan}\left(x_9\overline{\alpha_s}^{x_{10}}\left|\tilde{v}_{slip,i}^*\right|\right) log\left|\tilde{v}_{slip,i}^*\right|\right) \quad \text{Equation 27}$$

$$k_3 = \left(\frac{2}{\pi}\right)^3 \text{atan}(x_{11}\overline{\alpha_s})\,\text{atan}\left(x_{12}\max(x_4 - \overline{\alpha_s}, 0)\right) atan\left(x_{13}\widehat{\text{M}}_{drift,i}\right)\left\{x_{14} + \left|\tilde{v}_{slip,i}^*\right|^{x_{15}}\left[\left(x_{16}\left|\overline{\alpha_s} - \frac{x_4}{2}\right|^{x_{17}} + x_{18}\right) + \min\left(sign\left(\tilde{v}_{slip,i}^*\widehat{\text{M}}_{drift,i}\right), 0\right)x_{19}\left|\overline{\alpha_s} - \frac{x_4}{2}\right|^{x_{17}}\right]\right\} \quad \text{Equation 28}$$

The non-dimensional drift GPM, $\widehat{\text{M}}_{drift,i}$, is defined as:

$$\widehat{\text{M}}_{drift,i} = \frac{\left(\frac{d\overline{\alpha_g}}{dx}\frac{d\bar{v}_{g,i}}{dx} + \frac{d\overline{\alpha_g}}{dy}\frac{d\bar{v}_{g,i}}{dy}\right)}{\overline{\alpha_s}\,\overline{\alpha_g}\bar{v}_{ss\_slip}}\frac{v_t^4}{g^2} \quad \text{Equation 29}$$

$$\bar{v}_{g,i} = \tilde{v}_{g,i} - \bar{\alpha}_s v_{d,i} \quad \text{Equation 30}$$

The following coefficients (Table 1) are used for the three adjusted slip velocity closure models:

Table 1 – Summary of the coefficients used in the 1-marker, 2-marker and 3-marker adjusted slip velocity closures.

Coefficient	1-marker	2-marker	3-marker
x_1	-3.44	-1.40	$-1.74\left(\frac{2}{\pi}\right)atan(1.71\Delta_{fil}^*)$
x_2	2.09	1.38	1.54
x_3	$21.6\left(\frac{2}{\pi}\right)\text{atan}(0.216\Delta_{fil}^*)$	$48.5\left(\frac{2}{\pi}\right)\text{atan}(0.235\Delta_{fil}^*)$	$21.8\left(\frac{2}{\pi}\right)atan(0.708\Delta_{fil}^*)$
x_4	0.559	0.553	0.558
x_5	$99.7{\Delta_{fil}^*}^{3.31}$	$333{\Delta_{fil}^*}^{1.92}$	$45.6{\Delta_{fil}^*}^{2.10}$
x_6	2.19	$1.76\left(\frac{2}{\pi}\right)\text{atan}(1.29\Delta_{fil}^*)$	$2.09\left(\frac{2}{\pi}\right)atan(0.331\Delta_{fil}^*)$
x_7	$1/(2.08{\Delta_{fil}^*}^{0.246})$	$1/(2.40{\Delta_{fil}^*}^{0.234})$	0.248
x_8	0	$\frac{1}{\left(2.44\left(\frac{2}{\pi}\right)\text{atan}(1.92\Delta_{fil}^*)\right)}$	0.308
x_9	0	$25.6\Delta_{fil}^*$	$6.35\Delta_{fil}^*$
x_{10}	0	1.56	1.22
x_{11}	0	0	4030
x_{12}	0	0	194
x_{13}	0	0	$0.0742{\Delta_{fil}^*}^{1.89}$
x_{14}	0	0	$\frac{1}{3.53\left(\frac{2}{\pi}\right)atan(0.303\Delta_{fil}^*)}$
x_{15}	0	0	$\frac{1}{1+4.69\left(\frac{2}{\pi}\right)atan(0.0604\Delta_{fil}^*)}$
x_{16}	0	0	9.18
x_{17}	0	0	2.84
x_{18}	0	0	$\frac{1}{2.24\Delta_{fil}^*}$
x_{19}	0	0	$\frac{1}{0.0742\left(\frac{2}{\pi}\right)atan(0.419\Delta_{fil}^*)}$

Lastly, the mesoscale interphase force is also closed individually:

$$\hat{F}_{M,i} = \frac{-\overline{\alpha_s{}' \frac{\partial p'}{\partial \iota}}}{\rho_g g} = k_1 + k_2 \quad \text{Equation 31}$$

$$k_1 = x_1 \left(\frac{2}{\pi}\right) \overline{\alpha_s}^{x_2} \, atan\left(x_3 max(\overline{\alpha_s} - x_4, 0)^{x_5}\right) \quad \text{Equation 32}$$

$k_1 = 0$ if i is in a direction perpendicular to gravity

$$k_2 = x_6 \left(\frac{2}{\pi}\right)^3 atan(x_7 \overline{\alpha_s}) \, atan\left(x_8 \, max(x_4 - \overline{\alpha_s}, 0)\right) atan\left(x_9 \tilde{v}^*_{slip,i}\right) \quad \text{Equation 33}$$

$x_1 = 29000 \left(\frac{2}{\pi}\right) \text{atan}\left(0.690 \Delta^*_{fil}\right)$, $x_2 = 185$, $x_3 = 0.168$, $x_4 = 0.551$, $x_5 = 1.43$,
$x_6 = 92.4 - 65.4 \left(\frac{2}{\pi}\right) \text{atan}\left(0.167 \Delta^*_{fil}\right)$, $x_7 = 5.65$, $x_8 = 7.06$ and $x_9 = 0.475$.

2.3.2 Solids mesoscale stresses

The closures for the solids mesoscale stresses are used in the filtered solids momentum transport equations (Equation 15).

2.3.2.1 Isotropic model

Here, the solids mesoscale stresses are closed based on the Boussinesq approximation:

$$\rho_s \overline{\alpha_s v_{s,\iota}'' v_{s,J}''} \approx p_{s,fil} \delta_{ij} - \overline{\alpha_s} \mu_{s,fil} \left(\frac{\partial \widetilde{v_\iota}}{\partial x_j} + \frac{\partial \widetilde{v_j}}{\partial x_i} - \frac{2}{3} \frac{\partial \widetilde{v_k}}{\partial x_k} \delta_{ij} \right) \quad \text{Equation 34}$$

The following closures are derived for the filtered solids pressure, $p_{s,fil}$, and the filtered solids viscosity, $\mu_{s,fil}$:

$$\frac{p_{s,fil}}{\rho_s v_t^2} = \frac{2}{\pi} x_1 \overline{\alpha_s}^{x_2} \text{atan}\left(x_3 \Delta_f^{*x_4} \left\| \hat{S}_{s,fil} \right\|^{x_5} \max(x_6 - \overline{\alpha_s}, 0)\right) \Delta_f^{*x_7} \left\| \hat{S}_{s,fil} \right\|^{x_8 + x_9 \Delta_f^{*x_{10}}} + \frac{2}{\pi} x_{11} \overline{\alpha_s}^{x_{12}} \text{atan}(x_{13} \max(x_{14} - \overline{\alpha_s}, 0)) \Delta_f^{*x_{15}} \quad \text{Equation 35}$$

$x_1 = 0.774$, $x_2 = 1.72$, $x_3 = 0.403$, $x_4 = 0.610$, $x_5 = 1.19$, $x_6 = 0.684$, $x_7 = 1.57$, $x_8 = 1.00$, $x_9 = 0.331$, $x_{10} = -0.103$, $x_{11} = 0.123$, $x_{12} = 0.621$ $x_{13} = 2.89$, $x_{14} = 0.591$ and $x_{15} = 1.05$

$$\frac{\mu_{s,fil}}{\rho_s v_t^3 / g} = \left[\frac{2}{\pi} x_1 \overline{\alpha_s}^{x_2} \text{atan}\left(x_3 \Delta_f^{*x_4} \left\| \hat{S}_{s,fil} \right\|^{x_5} \max(x_6 - \overline{\alpha_s}, 0)\right) \Delta_f^{*x_7} \left\| \hat{S}_{s,fil} \right\|^{x_8 + x_9 \Delta_f^{*x_{10}}} + \frac{2}{\pi} x_{11} \overline{\alpha_s}^{x_{12}} \text{atan}(x_{13} \max(x_{14} - \overline{\alpha_s}, 0)) \Delta_f^{*x_{15}}\right] / \left\| \hat{S}_{s,fil} \right\| \quad \text{Equation 36}$$

$x_1 = 0.350$, $x_2 = 0.545$, $x_3 = 2.43$, $x_4 = 0.141$, $x_5 = 0.772$, $x_6 = 0.624$, $x_7 = 1.83$, $x_8 = 1.40$, $x_9 = 0.348$, $x_{10} = -0.0905$, $x_{11} = 0.130$, $x_{12} = -0.498$, $x_{13} = 3.58$, $x_{14} = 0.618$ and $x_{15} = 0.968$.

The dimensionless filtered deviatoric shear rate magnitude is defined as:

$$\left\|\hat{S}_{s,fil}\right\| = \frac{v_t}{g}\sqrt{2\bar{\bar{S}}_{s,fil}:\bar{\bar{S}}_{s,fil}} \quad \text{Equation 37}$$

$$\bar{\bar{S}}_{s,fil} = \frac{1}{2}\left(\nabla\tilde{\vec{v}}_s + \nabla\tilde{\vec{v}}_s{}^T\right) - \frac{1}{3}\nabla\cdot\tilde{\vec{v}}_s\bar{\bar{I}} \quad \text{Equation 38}$$

2.3.2.2 *Anisotropic model*

In this closure model, each component of the solids mesoscale stress tensor is closed individually as follows:

$$\begin{aligned}\frac{\rho_s\overline{\alpha_s v_{s,i}'' v_{s,j}''}}{\rho_s v_t^2} &= sign(\hat{M}_{ij})\left(\frac{2}{\pi}\right)^2 x_1\,\mathrm{atan}\left(x_2\Delta_f^{*x_3}\hat{M}_{ij}{}^{x_4}(\overline{\alpha_s}+x_5)\right)\\ &\times\mathrm{atan}\left(x_6\Delta_f^{*x_7}\hat{M}_{ij}{}^{x_8}\max(x_9-\overline{\alpha_s},0)\right)\Delta_f^{*x_{10}}\hat{M}_{ij}{}^{x_{11}+x_{12}\Delta_f^{*x_{13}}}\\ &+D\left(\frac{2}{\pi}\right)^2 x_{14}\,\mathrm{atan}(x_{15}\overline{\alpha_s})\,\mathrm{atan}(x_{16}\max(x_{17}-\overline{\alpha_s},0))\,\Delta_f^{*x_{18}}\end{aligned} \quad \text{Equation 39}$$

$x_1 = 0.542, x_2 = 2.53, x_3 = 0.102, x_4 = -0.460, x_5 = 0.0400, x_6 = 3.66, x_7 = 0.876, x_8 = 0.213, x_9 = 0.685, x_{10} = 1.75, x_{11} = 0.80, x_{12} = 0.593, x_{13} = -0.218, x_{14} = 56.0, x_{15} = 2.61, x_{16} = 0.00743, x_{17} = 0.601$ and $x_{18} = 1.03$. $D = 1$ if $i = j$. Otherwise, $D = 0$.

The dimensionless GPM, $\hat{M}_{ij}$, is defined as:

$$\hat{\mathrm{M}}_{ij} = \overline{\alpha_s}\left(\frac{d\tilde{v}_{s,i}}{dx}\frac{d\tilde{v}_{s,j}}{dx} + \frac{d\tilde{v}_{s,i}}{dy}\frac{d\tilde{v}_{s,j}}{dy}\right)\frac{v_t^2}{g^2} \quad \text{Equation 40}$$

2.3.3 Filtered frictional pressure

The filtered frictional pressure is used in the filtered solids momentum transport equation (Equation 15) and is closed as follows:

$$\frac{\bar{p}_{s,fric}}{\rho_s v_t^2} = \bar{\alpha}_s{}^{x_1}\Delta_f^{*x_2+x_3\Delta_f^{*x_4}}\left(x_5\left\|\hat{S}_{s,fil}\right\|^{x_6+x_7\Delta_f^{*x_8}}\Delta_f^{*x_9} + x_{10}\frac{e^{x_{11}\max(\bar{\alpha}_s-x_{12},0)}}{(\alpha_{s,\max}-\bar{\alpha}_s)^{x_{13}}}\right) \quad \text{Equation 41}$$

$x_1 = 2.78, x_2 = 1.00, x_3 = -0.0726, x_4 = 0.722, x_5 = 0.124, x_6 = 2.00, x_7 = -0.0689, x_8 = 0.684, x_9 = 0.807, x_{10} = 7.38\times10^{-6}, x_{11} = 36.0, x_{12} = 0.485, x_{13} = 3.64$ and $\alpha_{s,\max} = 0.63$.

2.3.4 Filtered reaction rate

The filtered reaction rate in the filtered species transport equation (Equation 19) is closed using a reaction rate correction factor:

$$k_A\rho_g\overline{\alpha_s X_A} = \mathrm{R}k_A\rho_g\overline{\alpha_s}\tilde{X}_A \quad \text{Equation 42}$$

$$\begin{aligned}-\log(R) = \left(\frac{2}{\pi}\right)^3 &\mathrm{atan}\left(x_1\Delta_f^{*x_2}\bar{\alpha}_s\right)\mathrm{atan}\left(x_3\Delta_f^{*x_4}\max(\mathrm{x}_5-\bar{\alpha}_s,0)\right)\\ &\times\left(x_6\,\mathrm{atan}\left(x_7\left\|\tilde{v_{slip}}^*\right\|\right)\log\left\|\tilde{v_{slip}}^*\right\| + x_8\mathrm{atan}(x_9\Delta_f^*)\right)\end{aligned} \quad \text{Equation 43}$$

$x_1 = 5.66, x_2 = 0.0118, x_3 = 25.0, x_4 = 0.232, x_5 = 0.559, x_6 = 0.341, x_7 = 0.380, x_8 = 1.09$ and $x_9 = 0.683$.

Chapter 3: Development and *a priori* analysis of new fTFM closures

3.1 Resolved simulations

3.1.1 Simulation geometry

A 2D geometry with a spatial extension of 0.64 m by 0.64 m is simulated to generate data for closure model development. It has been previously shown that this geometry yields domain size independent results [12]. The length of the domain therefore corresponds to 132 dimensionless units, when the particle relaxation length (v_t^2/g) is considered as the characteristic length scale. Recent work by Capecelatro et al. [44] also suggests that such a large domain, or even slightly larger, is necessary to yield domain size independent filtered statistics. The coordinates in the 2D domain are chosen such that gravity acts in the negative *y*-direction. Spatial discretization is performed on a uniform grid with a cell width of 0.625 mm (i.e., 8.33 particle diameters). This grid size was found to yield essentially grid size independent filtered statistics by Sarkar et al. [13].

3.1.2 Initial and boundary conditions

Simulations are performed at domain-averaged solids volume fractions of 0.02, 0.05, 0.1, 0.2, 0.3, 0.4 and 0.45 to collect relevant statistics by probing a wide range of flow features. Local volume fractions and velocities are initialized at a slightly perturbed state to allow a pseudo-steady state to be reached in a shorter time. These perturbations do not affect the data, since they are much smaller than the heterogeneity inherent to the systems under investigation. Figure 1 shows examples of the instantaneous volume fraction contour plots over the range of domain-averaged solids volume fractions considered. It is evident that a large range of flow conditions is included in the simulations, ranging from small clusters in dilute flow regions, to small bubbles in dense flows, with a region where bubbles and clusters are equally sized in between. It can also be noted that the filter sizes considered in this study range from 3 cells to 141 cells (about an eighth of the domain length) wide. Therefore, the mesoscale structure size can range from much smaller than the filter size to much larger than the filter size, depending on the domain-average solids volume fraction and the filter being considered.

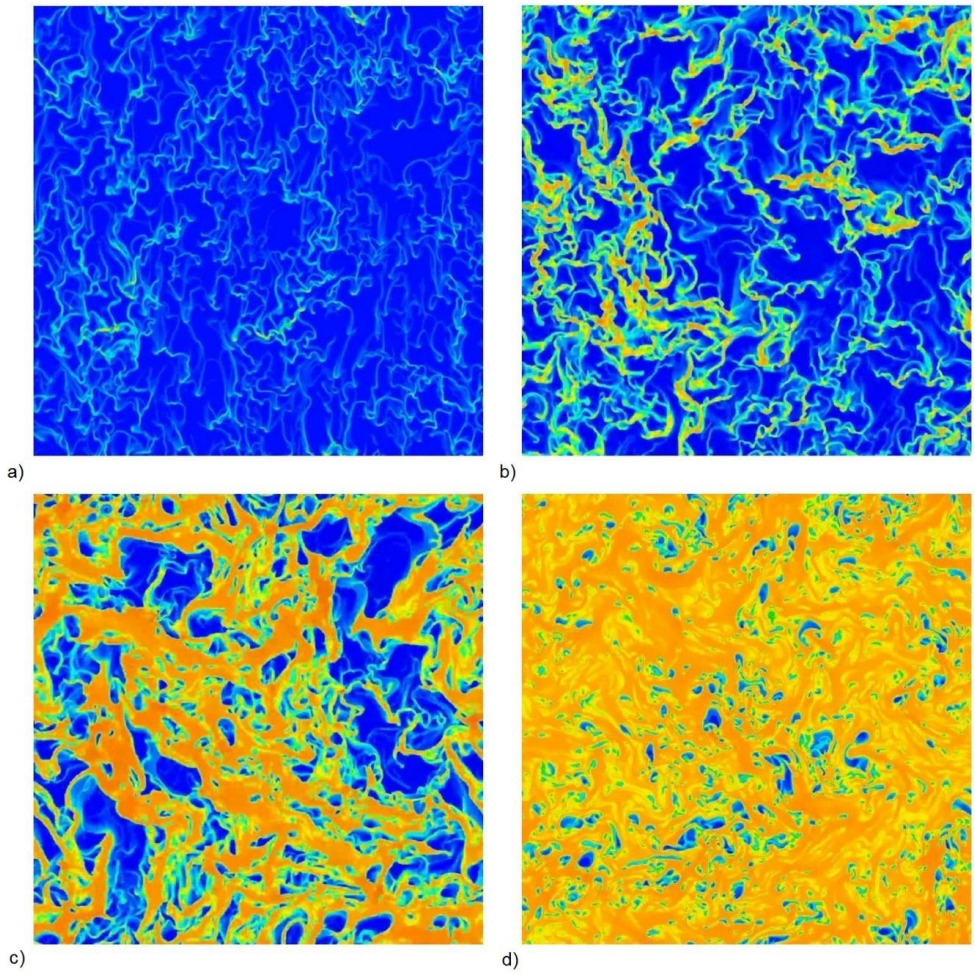

Figure 1 – Instantaneous contour plots of the solids volume fraction for simulations with domain-averaged solids volume fractions of a) 0.02, b) 0.1, c) 0.3 and d) 0.45. Blue indicates a zero solids volume fraction and red indicates the solids volume fraction at the maximum packing limit.

The simulated domain is fully periodic, with periodic boundary conditions in the vertical and horizontal directions. The simulations therefore represent a region within a fluidized bed that is independent of inlet, outlet and wall effects. The average (gas phase) pressure gradient in the vertical direction is controlled to maintain a constant gas superficial velocity, as previously used in the investigation of a periodic riser section [11]. A domain-averaged superficial velocity of 0.25 m/s was found to be a suitable value. It can also be noted that, for the periodic simulations considered in this study, the specified gas-phase superficial velocity should not impact the statistics that are collected. This is because, in the absence of walls, different average gas-phase superficial velocities will only change the speed the system moves as a whole, but not the relative velocities.

3.1.3 Material properties

The material properties used in this study are similar to that used in the fTFM papers from the Princeton group [12, 14, 16, 19]. These properties are summarised in Table 2.

Table 2 – The material properties used in this study.

d_p	Particle diameter	$75 \times 10^{-6}\ m$
ρ_s	Particle density	$1500\ kg/m^3$
ρ_g	Gas density	$1.3\ kg/m^3$
μ_g	Gas viscosity	$1.8 \times 10^{-5}\ kg/(m.s)$
D	Mass diffusivity	$1.385 \times 10^{-5}\ m^2/s$
v_t	Terminal settling velocity	$0.2184\ m/s$

3.1.4 TFM solver

Simulations are performed using ANSYS FLUENT 16.2.0. Pressure-velocity coupling is performed using the phase-coupled SIMPLE algorithm [45], and all other equations are discretised using the QUICK scheme [46]. Second-order implicit time stepping was used since it has previously been shown to be a requirement for time step independent prediction of fast, dilute flows [11].

3.2 Data analysis

Once the simulations reach a statistical steady state, data for relevant quantities is saved for each cell at an interval of four characteristic time units, $t_{char} = v_t/g$. The flow is considered to be fully developed when the domain-averaged solids mass flux clearly fluctuates around a constant mean value. For the statistical analysis of the data, CPPPO (https://github.com/CFDEMproject/C3PO-PUBLIC), a data analysis tool developed by Municchi et al. [47], is used. Firstly, the quantities that require closure are spatially averaged for several different filter sizes. Filter sizes of $x_f \times x_f$ grid cells are considered, where x_f is the nearest odd integer to $x_f = 3^{(i/2)}$, with i taking integer values of 2 to 9. Next, the filtered values are allocated to multi-dimensional bins according to a number of user defined marker values. Running means and variances are calculated in each bin. The values of the averaged quantities in each bin are then used to calculate information that is relevant for closure development, e.g., drag correction factors. This data is then exported to IBM SPSS Statistics 24, where the parameters in the chosen expression are fitted to best approximate the binned data.

Scripts in MATLAB R2016b are used to visualize the data, and to compare closure model predictions of the filtered quantity that must be closed with data collected in resolved TFM simulations. For each cell in the resolved simulation, the markers computed by CPPPO are used to calculate the model predictions for the filtered quantity, and the observed values for the filtered quantity (pre-computed by CPPPO) are collected as well. The sum of the squared difference of the model predictions from the observed values for the filtered quantity is then used to calculate the coefficient of determination as $R^2 = 1 - \sum_i (y_i - f_i)^2 / \sum_i (y_i - \bar{y})^2$. Here y_i is the observed value, $\bar{y}$ is the mean of all observed

values and f_i is the predicted value. This analysis is performed for four sets of data, each containing one time instance from each of the domain-averaged volume fractions considered. This allows 95% confidence intervals to be calculated whenever this is desired.

3.3 Considerations when developing closures for fTFMs

3.3.1 The sensitivity of fTFM closures to the resolved TFM configuration

As an early part of the present study, an investigation was made into the effect that the closures used in the resolved simulations have on the filtered statistics. This is an important topic, since the fTFM closure models can only be as accurate as the TFM simulations from which they were derived. The TFM approach involves several important closure laws, each with a range of alternative formulations published over the past three decades. In addition, system-dependent coefficients such as the particle-particle restitution can potentially influence TFM model results. It is therefore important to understand the effect of TFM closures on filtered quantities in order to assess the uncertainty involved when applying the fTFM approach. Only a summary of the most important conclusions from this study will be presented here, but the interested reader may find the complete study in Appendix B.

The primary conclusion from this study was that, generally, the average change in filtered quantities with different resolved TFM formulations is small, 1 to 12% for all factors excluding the drag. This provides reason for increased confidence in the fTFM approach, since it indicates that fTFMs are not very susceptible to uncertainties in the choice of TFM closures used in the resolved simulations from which the filtered models are derived.

A larger effect was observed for the drag model: approximately 20% average deviation from the base case. This is an important finding since there is not yet consensus in the literature regarding the best choice of drag model and therefore several different drag models are commonly used. Inclusion of a frictional pressure model also had a significant effect, with average differences from the base case in the range of 4% to 12%. However, these differences are mostly present in the very large solids volume fraction range where differences can increase up to 70% due to larger, more viscous solids clusters when frictional pressure is included. Based on these findings, it was decided to include a frictional pressure model in the resolved simulations used for fTFM closure derivation in the present study. This is in contrast to other fTFM studies in literature, which have all neglected frictional stresses. Additionally, the Huilin-Gidaspow model [36], which is expected to be accurate over a wider range of conditions, was used to model the drag, in contrast to the simpler Wen-Yu model [38], which has primarily been used in fTFM studies.

Finally, it was noted that the filtered quantities could be divided into two groups according to how they reacted to changes in the resolved TFM formulations. The filtered drag, heat transfer and reaction corrections were significantly influenced by the choice of drag law and the inclusion of frictional stresses. The quantities containing variances, the filtered solids stresses and filtered scalar co-variances, were significantly affected by changes in the drag law, inclusion of frictional pressure and changes in the particle-particle restitution coefficient. The similar behaviour within groups suggests that the transport processes within each group are controlled by the same mechanisms. This knowledge may be used when selecting markers and formulating closures for filtered quantities within these groups.

3.3.2 Layout of bins for collecting statistics

When the filtered resolved simulation data is binned based on different markers, it is desirable that a statistically significant number of data samples should be present in as many bins as possible and over as large a range of marker values as possible. This would lead to a more accurate and more widely applicable closure model. However, the number of samples tend to decay with increasing values of certain markers. For example, when the filtered solids volume fraction and the filtered slip velocity magnitude are used as markers, the number of data samples tend to decrease rapidly with increasing filtered slip velocity magnitude values, as seen in Figure 2.a. This behaviour can be counteracted by having the bin size with respect to the filtered slip velocity magnitude increase exponentially with increasing filtered slip velocity magnitudes. Figure 2.b shows that a simple scaling can substantially increase the number of samples in each bin at large filtered slip velocity magnitudes. This leads to improved data at large slip velocities for use in closure derivation. As a result of this finding, simple scalings of the bin sizes are applied in this study whenever it is desirable to do so.

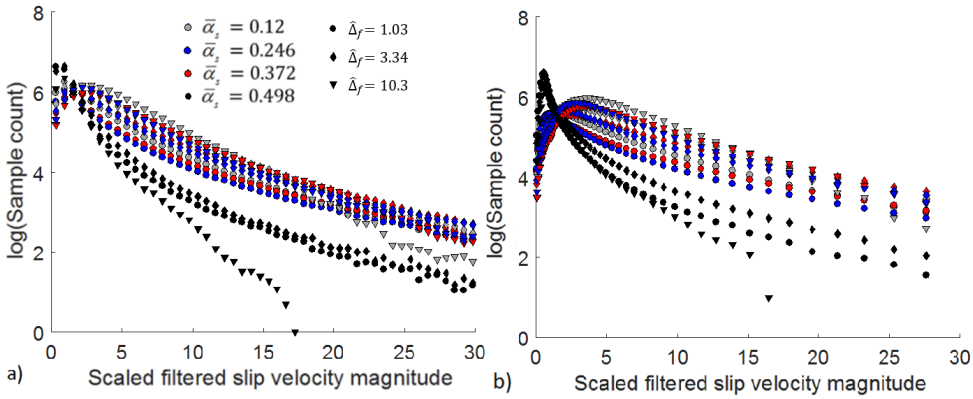

Figure 2 – The number of samples in each bin as a function of the scaled filtered slip velocity magnitude when a) using uniform bins and b) using bins that increases exponentially in size. The filtered slip velocity magnitude is scaled with the steady state sedimentation velocity, as discussed later in Chapter 3.4.1.2.

3.3.3 Respecting physical limits in functional forms

From physical arguments, the functional behaviour of the sub-grid quantities can be deduced at the limits of certain markers. This is especially the case for the filter size and the filtered solids volume fraction as markers: both markers are of key importance in previous studies, and are also used in all of the closure models derived in the present work. Respecting these limits ensure that the fTFM will predict realistic behaviour, even when used outside the parameter space where data is available from the resolved simulations used for parameter calibration. Such limits, however, have not always been respected in the literature, the most recent example being the drag closure suggested by Sarkar et al. [13], which does not respect the physical limit that no clustering can occur in very dense flows. As will be shown in Chapter 5.3.2.1, this causes the fTFM to fail completely in very dense flows. To prevent such a situation from occurring, the functional forms of the closure models developed in this study respect the following limits:

Firstly, for the filtered solids volume fraction, the model formulation should ensure that the sub-grid corrections tend to zero at zero filtered solids volume fractions and at very dense packings. This is

necessary since the suspension will be homogenous at these limits and therefore no sub-grid corrections due to mesoscale structures should exist.

Secondly, for the filter size, no sub-grid correction should be performed when the cell size of the fine grid simulations (or smaller) is used in simulations using the filtered drag closure. This is achieved by using a scaled filter size in the closures, defined as $\Delta_f^* = \min(\hat{\Delta}_f - \hat{\Delta}_{fine}, 0)$. Here, the minimum dimensionless filter size, $\hat{\Delta}_{fine} = 0.1285$, which corresponds to using the drag closure at the grid size at which the fine grid simulations for model derivation were performed. At very large filter sizes, the behaviour may differ depending on the quantity that is closed. For example, the drag correction tends to reach a maximum at very large filter sizes, whereas the solids mesoscale stresses tend to increase continuously.

3.3.4 Gradients of filtered variables as markers

It can be noted that several of the markers proposed in the present study requires the gradients of filtered variables to be calculated. It was found that the method used to calculate the gradient of the filtered value had a significant impact on the magnitude of the gradient. To the knowledge of the authors, this topic has not been previously discussed in the filtering literature. In the present work, gradients were calculated using the second order central differencing scheme, which was found to be sufficient to capture the gradients of the relatively smooth filtered fields. It was found that the best comparison with the resolved data could be obtained if the neighbouring values in the central differencing were taken at half the filter length from the cell under consideration. This method smoothens over rapid changes in the filtered values, leading to - on average - smaller gradients calculated in the analysis, if compared to another approach: calculating filtered gradients by considering the neighbouring cells (in the resolved simulations) as the neighbours in the central differencing. As a result, the method of calculating the filtered gradient leads to quantitative differences in the closure that is derived. It is important to realize that, when performing coarse grid simulations, the value inside the neighbouring coarse-grid cell has to be used to calculate gradients. Thus, an equivalent value to the neighbouring value in the resolved simulations is not available in coarse grid simulations. Therefore, the proposed method of evaluating the gradient over the filter width is more meaningful.

3.4 Filtered drag force closures

The closure for the filtered drag force (sixth term on the right of Equation 15) is generally accepted to be the most important closure in fTFMs. This section will discuss two methods for closing the filtered drag force: using an isotropic drag correction factor, or by modelling an anisotropic drift velocity from which an adjusted slip velocity is calculated. Additionally, for the anisotropic adjusted slip velocity model, 1-marker, 2-marker and 3-marker models are proposed to evaluate the benefit of increasing the complexity of the closure model by adding additional independent variables. Finally, the performance of the proposed models is evaluated in an *a priori* manner: this is done by comparing model predictions of the filtered drag force to observed values in the resolved simulation data used for model derivation as described in Chapter 3.2.

3.4.1 Isotropic drag closures

In the isotropic approach, the filtered drag force can be modelled together with the mesoscale interphase force (seventh term on the right of Equation 15), as is commonly done in the literature [13, 14]. This combined contribution is referred to as the filtered interphase force in the present study and can be closed as follows:

$$\overline{K_{gs}(\vec{v}_g - \vec{v}_s)} - \overline{\alpha_s{}'\nabla p'} = CK_{gs,hom}(\widetilde{\vec{v}_g} - \widetilde{\vec{v}_s}) \qquad \text{Equation 44}$$

Here, $K_{gs,hom}$ is the interphase momentum exchange coefficient evaluated at the filtered solids volume fraction and the filtered slip velocity magnitude. The drag correction factor, C, must be closed. Mesoscale structures mostly tend to reduce the filtered interphase force compared to the drag force predicted by the microscopic drag law, since gas will tend to slip around clusters, thereby reducing the overall drag. On the other hand, the mesoscale interphase force tends to add a force in the direction of the filtered slip velocity (as discussed in Chapter 3.5), thereby opposing the effect of the mesoscale structures on the filtered drag force. However, the reduction in the filtered drag compared to that predicted by the microscopic drag law tends to be substantially larger than the mesoscale interphase force. Therefore, the drag correction factor is generally smaller than unity, i.e., the combined filtered drag and mesoscale interphase forces are smaller than the force predicted by the microscopic drag law.

In this work, the drag correction factor is calculated based on the vertical direction data, as is common practice in the literature [13, 14, 16]. This is done assuming that the drag in the vertical direction is of much greater significance than the drag in the lateral directions. The implications of this assumption will be discussed further in Chapter 3.4.2.

3.4.1.1 Exploring markers for isotropic drag closures

The first fTFMs closed the drag correction factor using 1-marker closure models, using the filter size and the filtered solids volume fraction as independent variables [16]. Later studies [13, 14] expanded the drag closures to 2-marker models, using the filtered slip velocity magnitude as an additional independent variable. The filtered slip velocity is highly correlated with the reduction in the drag because, with increasing cluster formation, gas will tend to slip around dense clusters, increasing the slip velocity, but also decreasing the overall drag between the phases. It can further be noted that both (i) the filtered solids volume fraction and (ii) the filtered slip velocity are directly available on the coarse grid scale. Therefore, they can be grouped as 'grid-based' markers.

More recent studies have revealed three additional markers that may serve as good independent variables for filtered drag closures: these include (i) the solids volume fraction variance [20, 32], (ii) the drift velocity [17, 18, 32] and (iii) the solid-phase turbulent kinetic energy [20, 48, 49]. These three markers were evaluated as potential candidates for use in a 2-marker drag closure in combination with the filtered solids volume fraction. The results revealed that the scaled drift velocity, defined here as $v_{d,i}^{*} = \frac{\overline{\alpha_s v_{g,i}}/\overline{\alpha_s} - \widetilde{v}_{g,i}}{\widetilde{v}_{g,i} - \widetilde{v}_{s,i}}$, performed the best of the above-mentioned candidates. The results for the drift velocity are therefore further discussed here, whereas the results for the solids volume fraction variance and the solids turbulent kinetic energy are given in Appendix D.2.

Figure 3.a shows that there is a linear proportionality between the drag correction factor and the scaled drift velocity, which would be simple to model. Additionally, Figure 3.b shows that a simple scaling of the filtered drag correction factor with the drift velocity can substantially reduce the range of the filtered drag correction: $C/\left(1+v_{d,i}^{*}\right)$ varies only between unity and three (in contrast, C typically varies by more than an order of magnitude). It should be noted that the behaviour of the drag correction near a filtered solids volume fraction of 0.2 is linked to the use of the Huilin-Gidaspow drag closure [36] in the resolved simulations, since this closure blends the Wen-Yu and Gidaspow drag models around a solids volume fraction of 0.2. The nature of the filtered drag correction shown in Figure 3.b is hence, to some degree, also a function of the underlying microscopic drag law. This observation is in agreement with the work presented in Appendix B.

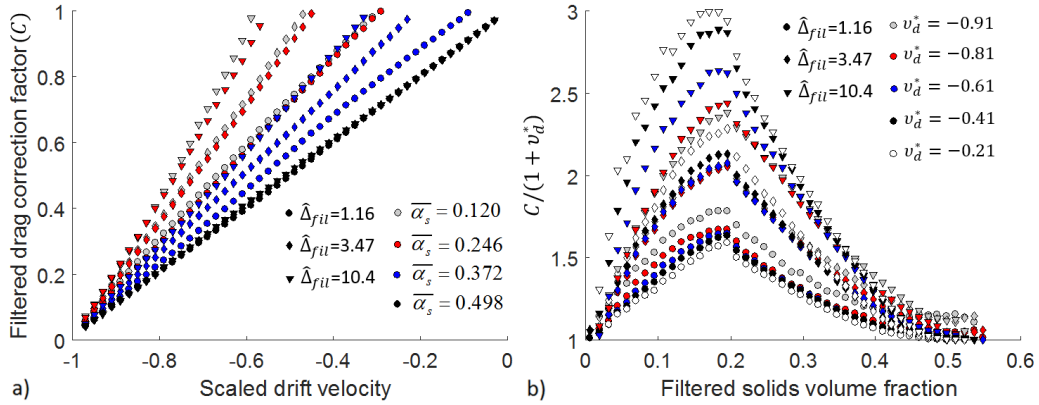

Figure 3 - a) The filtered drag correction factor as a function of the scaled drift velocity. b) The filtered drag correction factor scaled by the scaled drift velocity as a function of the filtered solids volume fraction. Different symbols denote different dimensionless filter sizes.

The disadvantage of using the drift velocity, as well as the other potential candidates mentioned earlier, is that these quantities require additional modelling. This is because they express sub-grid flow phenomena, are consequently not directly available in coarse grid simulations and hence are referred to as 'sub-grid-based' markers. The use of sub-grid-based markers necessitates a "model-in-model" approach which could potentially create complex interactions between inaccuracies on the two closure levels. This added complexity is only justifiable if the sub-grid-based marker offers clear advantages for collapsing the resolved data to a form that is easy to model. Further investigation revealed that similar advantages are offered by the slip velocity magnitude (a grid-based marker) when it is correctly scaled. The next section will detail the advantages of such a scaled slip velocity magnitude marker.

3.4.1.2 Improving filtered drag closures by using a scaled slip velocity magnitude marker

The filtered slip velocity magnitude used as marker in filtered drag closures is commonly non-dimensionalized using the single-particle terminal velocity [13-15]. However, it was found that it is beneficial to instead scale the filtered slip velocity magnitude with the steady state sedimentation velocity of a homogenous suspension. This is the velocity at which the interphase drag force and the gravitational force on the particles would balance if the particles were uniformly distributed within a

filtered region. Using such a scaled filtered slip velocity magnitude as the second marker results in two important benefits:

(i) The dependency of the second marker upon the filtered solids volume fraction (i.e., the first marker) is substantially reduced as shown in Figure 4: the filtered slip velocity magnitude non-dimensionalized with the particle terminal velocity, $\|\widetilde{v_{slip}}\|$, tends to strongly decrease with increasing filtered solids volume fraction (see Figure 4.a; the y-axis is scaled to illustrate the change of nearly two orders-of-magnitude). On the other hand, the scaled filtered slip velocity magnitude, $\|\widetilde{v_{slip}}^*\|$, remains relatively constant up to a filtered solids volume fraction of approximately 0.4 and changes at most by a factor of approximately six (see Figure 4.b). This scaling therefore leads to a more even distribution of data samples during the statistical analysis of TFM simulation output. Hence, more statistically meaningful data can be produced from a fixed resolved simulation campaign. In other words, the computational cost of resolved TFM-based simulations can be reduced to produce data with the same statistical significance. In addition, it is desirable that the independent variables used in the model fit are not highly correlated. Removal of much of the filtered volume fraction dependency by the proposed new scaling should therefore improve the model.

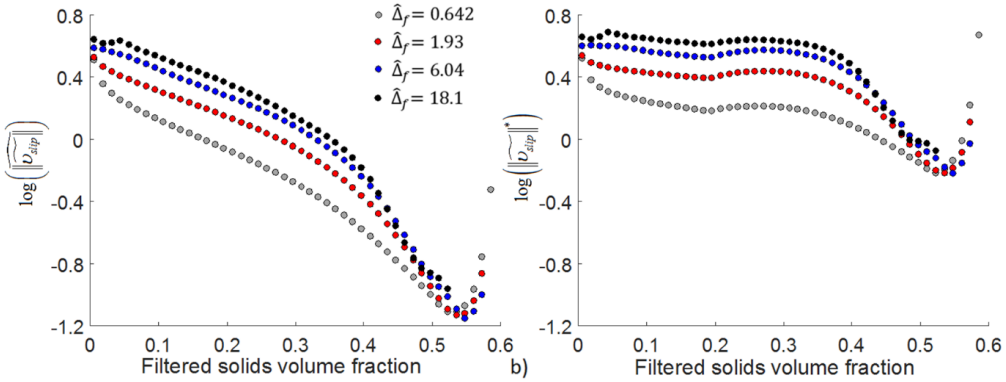

Figure 4 - Plots of a) the filtered slip velocity magnitude non-dimensionalized by the single particle terminal velocity and b) the filtered slip scaled by the steady state sedimentation velocity of a homogenous suspension as a function of the filtered solids volume fraction for different dimensionless filter sizes.

(ii) It was found that, at large filter sizes, a linear dependency exists between the scaled drag correction factor, defined as $-\log(C)$, and $\log(\|\widetilde{v_{slip}}^*\|)$. This dependency is illustrated in Figure 5.b, offering similar closure fitting advantages as the drift velocity (see Figure 3). Figure 5.a also illustrates a relatively simple volume fraction dependency, confirming the value of the much weaker correlation between the two markers enabled by the newly proposed second marker, $\|\widetilde{v_{slip}}^*\|$.

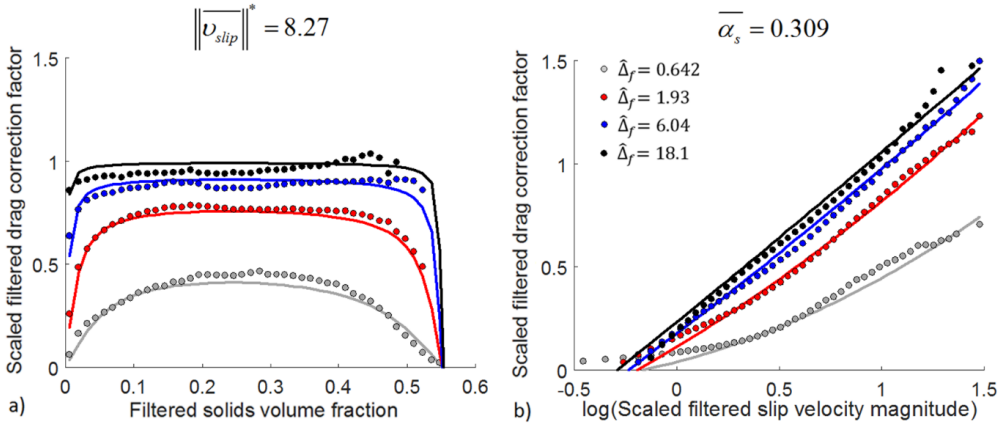

Figure 5 - The scaled filtered drag correction factor, $-\log(C)$, calculated based on the data for the direction of gravity as a function of a) the filtered solids volume fraction and b) the scaled slip velocity magnitude for different dimensionless filter sizes. The symbols show the binned data obtained from resolved simulations and the lines the model predictions.

Scaling the drag correction factor in this way provides an additional benefit: a maximum drag correction, as used in previous studies [13, 14], no longer needs to be specified. As the scaled filtered slip velocity magnitude increases, the drag correction factor will asymptotically approach zero due to the logarithmic definition of the scaled drag correction factor. This ensures that safe extrapolation to large filter sizes and slip velocities is possible.

The expression in Equation 45 is proposed to model the scaled drag correction factor. This formulation respects important physical limits, as discussed in Chapter 3.3.3. Also, the drag correction will saturate as the filter size approaches infinity.

$$-\log(C) = \operatorname{atan}\left(x_1\Delta_f^*\bar{\alpha}_s\right)\operatorname{atan}\left(x_2\Delta_f^* max(\bar{\alpha}_{\max} - \bar{\alpha}_s, 0)\right)\operatorname{atan}\left(x_3\Delta_f^*\right)\left(\frac{2}{\pi}\right)^3 \times \left(x_4 \log\left\|\widetilde{\upsilon_{slip}}^*\right\| + x_5{\Delta_f^*}^{x_6} + x_7\left(\log\left\|\widetilde{\upsilon_{slip}}^*\right\|\right)^2\left(1 - \frac{\operatorname{atan}\left(x_8\Delta_f^*\right)}{\pi/2}\right)\right) \quad \text{Equation 45}$$

$$\text{if} -\log(C) < 0 \qquad C = 1$$

A non-linear regression was performed, yielding an excellent fit to the binned data ($R^2 = 0.985$) for the following values of the coefficients: $x_1 = 36.6$, $x_2 = 22.6$, $x_3 = 1.68$, $x_4 = 0.835$, $x_5 = 0.140$, $x_6 = 0.188$, $x_7 = 1.33$, $x_8 = 3.28$ and $\bar{\alpha}_{max} = 0.551$. The fine grid dimensionless filter size was set to $\hat{\Delta}_{fine} = 0.1285$.

Figure 5 confirms that the proposed expression fits the binned data very well. It can also be noted that the binned data indicates that, at low slip velocities, the filtered drag force can be greater than the drag force predicted by the homogenous drag law, resulting in a negative scaled filtered drag correction factor (or drag correction factors greater than unity). For the present work, it is assumed that the effect of the filtered drag force at such small scaled slip velocities will be small, since it will

only serve to further reduce the slip and thereby also the drag force. For this reason, the data at scaled drag corrections smaller than zero were neglected during closure model fitting and the model is limited to not predict drag correction factors greater than unity.

3.4.2 Anisotropic filtered drag force closures

3.4.2.1 Directional dependence of the drag correction factor

As discussed in Chapter 3.4.1, the isotropic drag closure proposed in the previous section was derived based on the drag force in the direction aligned with gravity. This was motivated by the fact that this component of the drag force will be most important in a global sense due to gravity. Unfortunately, this argument does not hold when considering the statistics collected based on a finite filter size, $\hat{\Delta}_f$, as will be shown next.

Firstly, it can be established that the drag correction factor, C, is substantially different in the lateral and vertical directions: Figure 6.a and Figure 6.b compare the predictions on the basis of Equation 45 with the scaled filtered drag correction factors calculated based on the lateral direction drag force (i.e., the flow variables in the direction perpendicular to gravity). This shows that, quantitatively, the closure given by Equation 45 will substantially overpredict the drag force in the lateral directions when used in coarse grid simulations (note that $-log(C)$ is shown as the dependent variable in Figure 6.a and Figure 6.b). This effect is especially pronounced for large filter sizes and high particle concentrations.

Qualitatively, two significant differences can be observed between the lateral and vertical direction scaled drag correction factors: Firstly, at intermediate volume fractions, the vertical direction scaled drag correction tends to remain nearly constant, whereas the lateral direction scaled drag correction factor tends to increase with increasing filtered solids volume fraction. Secondly, at small scaled filtered slip velocity magnitudes, the vertical direction filtered drag force tends to be greater than that predicted by the microscopic drag law, whereas the drag is always substantially reduced in the lateral direction compared to the homogenous case. These qualitative differences imply a fundamental anisotropy in the filtered drag coefficient. Hence, a different functional form (than that shown in Equation 45) will be required when computing the filtered interphase force in planes perpendicular to gravity.

Previous studies have argued that the importance of the drag in the directions perpendicular to gravity is unimportant relative to the drag aligned with gravity. Next it is shown that this is not necessarily the case: the ratio of the slip velocity component aligned with gravity to the slip velocity component perpendicular to gravity is analysed in Figure 6.c and Figure 6.d. Specifically, it is found that, although the slip in the direction perpendicular to gravity is generally smaller, it is clearly not insignificantly. Thus, this indicates that the forces originating from the slip in the directions perpendicular to gravity are not insignificant in fTFMs, and hence necessitate a precise closure.

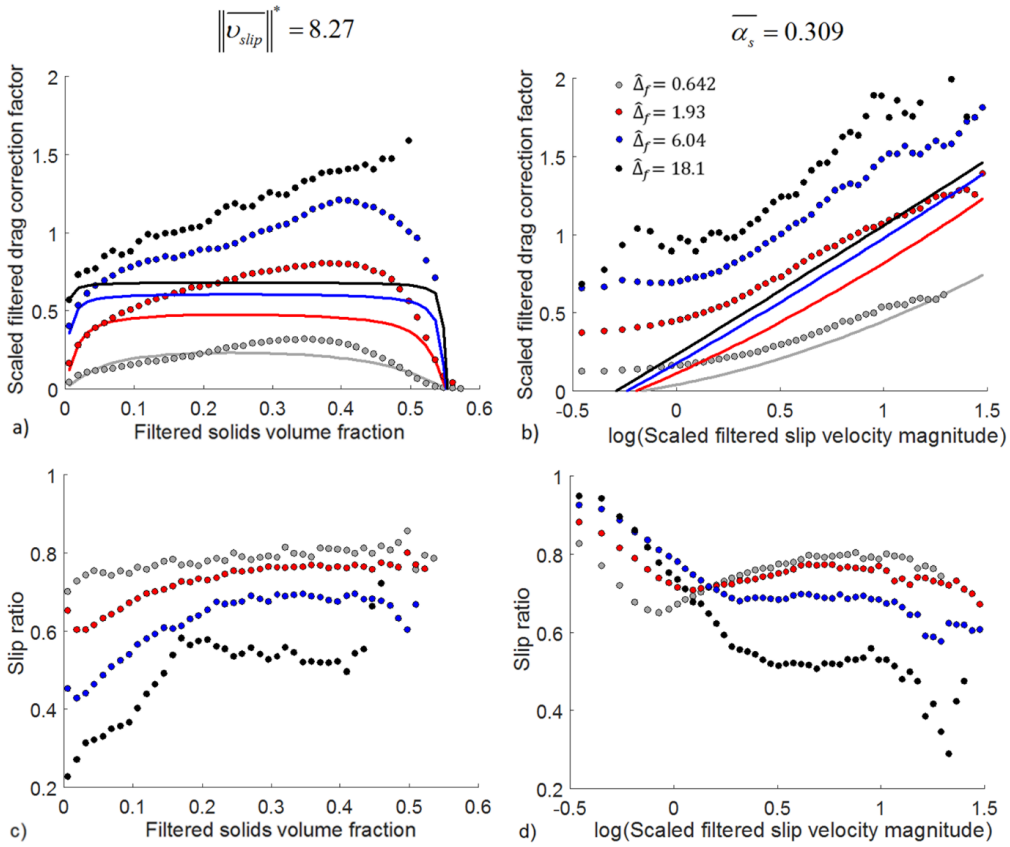

Figure 6 - The scaled filtered drag correction factor, $-log(C)$, calculated based on the lateral direction drag force (top) and the ratio of the lateral direction slip velocity to the vertical direction slip velocity (bottom) are plotted as a function of the filtered solids volume fraction (left) and the scaled filtered slip velocity magnitude (right) for different dimensionless filter sizes. In the top figures, the lines show the model predictions for the model based on the drag force in the direction aligned with gravity (vertical direction).

3.4.2.2 A revised formulation based on an adjusted slip velocity

Based on the encouraging results using the drift velocity as a second marker in Chapter 3.4.1.1, the drift velocity formulation proposed by the group of Prof. Simonin at INP Toulouse [17, 18] was further investigated. Applying some modifications to previous work, it was found that the filtered drag force in the direction *i* can be written as described in Equation 46 to Equation 50. The complete derivation is given in Appendix E.3. Note that only the filtered drag force will be discussed in this section. A separate closure for the mesoscale interphase force is proposed in Chapter 3.5.

$$\overline{K_{gs}\left(\upsilon_{g,i} - \upsilon_{s,i}\right)} = C_{NL} K_{gs,hom}\left(\tilde{v}_{g,i} - \tilde{v}_{s,i} - \upsilon_{d,i}\right) \qquad \text{Equation 46}$$

$$\upsilon_{d,i} = \frac{\overline{\alpha_g' \upsilon_{g,i}'}}{\bar{\alpha}_s \bar{\alpha}_g} \qquad \text{Equation 47}$$

$$C_1 = \frac{\overline{\frac{K_{gs}}{\alpha_s}(\alpha_s v_{g,\iota} - \alpha_s v_{s,\iota})}}{\overline{K_{gs}}\frac{(\alpha_s v_{g,\iota} - \alpha_s v_{s,\iota})}{\bar{\alpha}_s}} = \frac{\overline{K_{gs}(v_{g,\iota} - v_{s,\iota})}}{\overline{K_{gs}}(\tilde{v}_{g,i} - \tilde{v}_{s,i} - v_{d,i})} \quad \text{Equation 48}$$

$$C_2 = \frac{\overline{K_{gs}}}{K_{\mathrm{gs,hom}}} \quad \text{Equation 49}$$

$$C_{NL} = \mathrm{C}_1 C_2 \quad \text{Equation 50}$$

In Equation 46, the drift velocity, $v_{d,i}$, and the non-linearity correction factor, C_{NL}, require closure. Note that an opposite sign convention is used for the drift velocity compared to previous work from the INP Toulouse group [17, 18] and the definition used in Chapter 3.4.1.1. This convention ensures that the filtered slip velocity and the drift velocity will tend to mostly have the same sign. Also, the definition of the drift velocity (i.e., Equation 47) is different from the definition used in previous studies, where $v_{d,i} = \tilde{v}_{g,i} - \frac{\overline{\alpha_s v_{g,i}}}{\bar{\alpha}_s}$ when the sign convention of the present study is followed. As will be shown in Chapter 3.4.2.6, this allows a promising additional grid-based-marker to be identified for modelling the drift velocity.

Whereas in the isotropic formulation given by Equation 44 the filtered drag force is proportional to the filtered slip velocity, in the anisotropic formulation the filtered drag force is proportional to the difference between the filtered slip velocity and the drift velocity. Hence, this difference is referred to as the "adjusted slip velocity", $\tilde{v}_{adj,i}$. Similar to the observation for the slip velocity in Chapter 3.4.1.2, scaling the drift velocity and the adjusted slip velocity with the steady state sedimentation velocity also removes most of the volume fraction dependence of these quantities. It is therefore convenient to define the scaled adjusted slip velocity, $\tilde{v}^*_{adj,i}$, and the scaled drift velocity, $v^*_{d,i}$, as the respective velocities scaled by the steady state sedimentation velocity.

The benefits when adopting the above drift velocity formulation can be best demonstrated when considering the correlation of the filtered drag force with the scaled slip velocity, as well as the scaled adjusted slip velocity. This data is shown in Figure 7. First, panels a) and b) show that there is a large difference in the qualitative behaviour of the filtered drag force as a function of the slip velocity depending on the direction considered, as discussed in Chapter 3.4.2.1. Most importantly, the filtered drag force in the vertical direction tends to be positive at zero filtered slip velocities. A positive drag force is observed even at small negative slip velocities for this direction. In the isotropic drag correction factor framework, this would require setting C to very large values at small, positive slip velocities, and $C < 0$ for negative slip velocities. This discontinuity in C would be very challenging from a closure fitting point of view. Also, it is clear that very different functional forms of the drag correction factor would be required for the two directions.

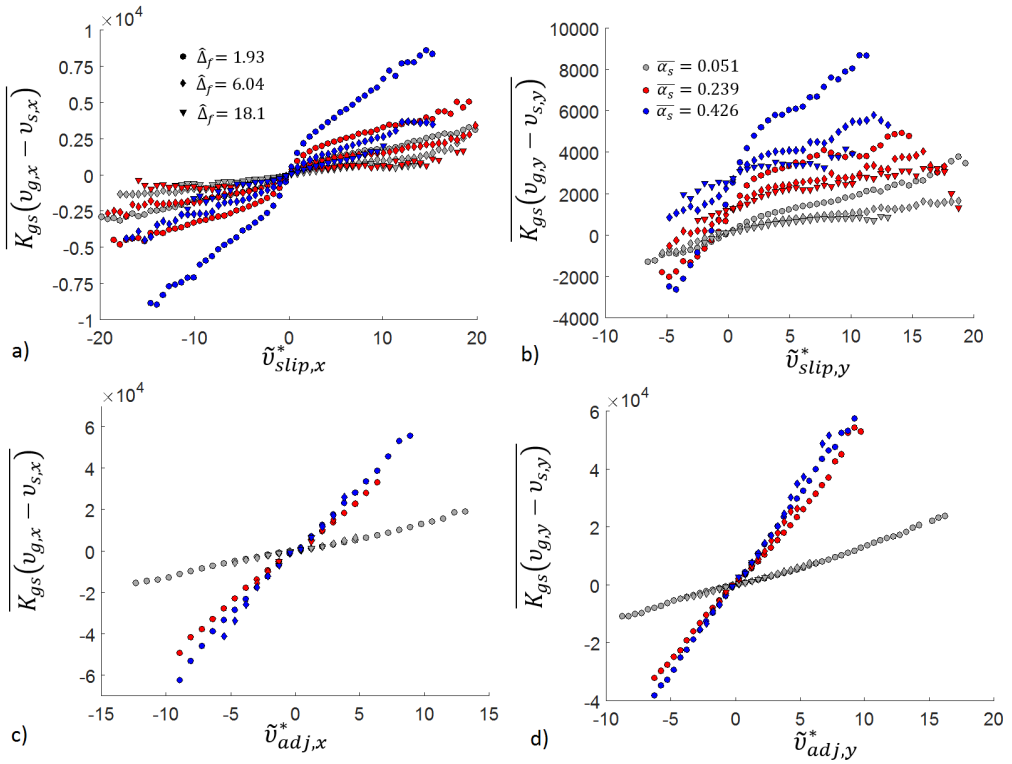

Figure 7 - The filtered drag force in the lateral (left) and the vertical (right) directions plotted against the scaled filtered slip velocity (top) and the scaled adjusted slip velocity (bottom)

Panels c) and d) in Figure 7 show that the filtered drag force is an almost linear function of the adjusted slip velocity that passes through the origin. The small deviations from a linear dependence are due to the assumptions used to derive the adjusted slip velocity formulation of the filtered drag force. This can be corrected for, as will be discussed later in this section. Additionally, the adjusted slip velocity formulation nearly collapses the different filter sizes onto the same line, implying that most of the filter size dependence of the filtered drag force comes from the closure for the drift velocity that is used to calculate the adjusted slip velocity (Equation 46). The qualitative behaviour of the filtered drag force dependency on the scaled adjusted slip velocity is very similar for the lateral and vertical directions. This implies that the anisotropy of the filtered drag force only has to be accounted for in the closure for the drift velocity. Chapter 3.4.2.4 will show that this can be done in a relatively simple manner.

Lastly, it can be noted that much larger filtered drag forces are observed in the bins when plotting against the scaled adjusted slip velocity. This means that the filtered drag force is much more sensitive to the adjusted slip velocity than to the filtered slip velocity. Furthermore, as shown in Figure 8, it is observed that the variance of the filtered drag force relative to the mean in each bin is about an order of magnitude larger when the data is binned as a function of the scaled slip velocity, than when it is binned as a function of the scaled adjusted slip velocity. Thus, the former binning strategy leads to small and large values in the bins cancelling out, leading to smaller values for the bin means. In contrast, binning as a function of the scaled adjusted slip velocity leads to a lower variance of filtered drag force data inside individual bins.

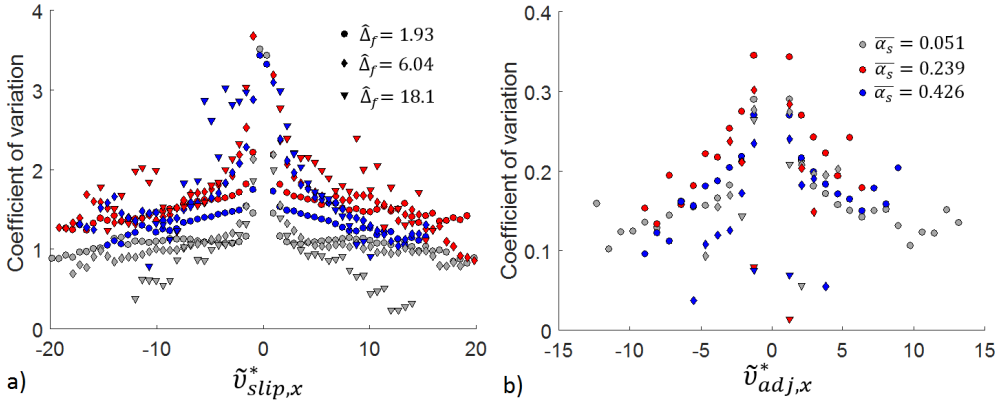

Figure 8 – The coefficient of variation (the standard deviation divided by the absolute of the mean) of the filtered drag force in each bin when using a) the scaled filtered slip velocity and b) the scaled adjusted slip velocity.

An important difference from previous work on the drift velocity-based drag closures [17, 18, 31, 32] is the presence of C_{NL} in Equation 46. C_{NL} compensates for errors introduced by two simplifying assumptions: (i) that the average of a product is equal to the products of the averages (Equation 48), and (ii) that the spatial average of the interphase momentum coefficient is set equal to the interphase momentum coefficient evaluated at the filtered volume fraction and the filtered slip velocity magnitude. Since both of these assumptions would be true if the involved functions (i.e., $\frac{K_{gs}}{\alpha_s}\left(\alpha_s v_{g,i} - \alpha_s v_{s,i}\right)$ in Equation 48 and K_{gs} in Equation 49) were linear, C_{NL} will be referred to as the non-linearity correction factor in the present study.

All earlier work on the drift velocity-based approach in fTFMs had assumed $\overline{K_{gs}\left(v_{g,\iota} - v_{s,\iota}\right)} = K_{gs,hom}(\tilde{v}_{g,i} - \tilde{v}_{s,i} - v_{d,i})$, therefore $C_{NL} = 1$. Data provided in a personal communication (Dr. Ozel, correspondence by e-mail, 24 August 2017) with one of the authors of a recent study [32] shows that there is indeed a very high correlation between $\overline{K_{gs}\left(v_{g,\iota} - v_{s,\iota}\right)}$ and $K_{gs,hom}(\tilde{v}_{g,i} - \tilde{v}_{s,i} - v_{d,i})$, as shown in Figure 9. However, the filter sizes evaluated in these previous studies were all very small, and, from the aforementioned data, the correlation coefficient appears to decrease linearly with the base-10 logarithm of the ratio of the filter size and the particle diameter. Two data points from the larger filter sizes evaluated in the present study matches the extrapolation from the given data and confirms that this trend continues at larger filter sizes. Thus, the correlation between $\overline{K_{gs}\left(v_{g,\iota} - v_{s,\iota}\right)}$ and $K_{gs,hom}(\tilde{v}_{g,i} - \tilde{v}_{s,i} - v_{d,i})$ supporting the traditional drift velocity-based approach degrades with increasing filter size. The assumption of $C_{NL} = 1$ therefore appears to weaken at the large filter sizes evaluated in the present study. Therefore, a closure for C_{NL} will be discussed in Chapter 3.4.2.3.

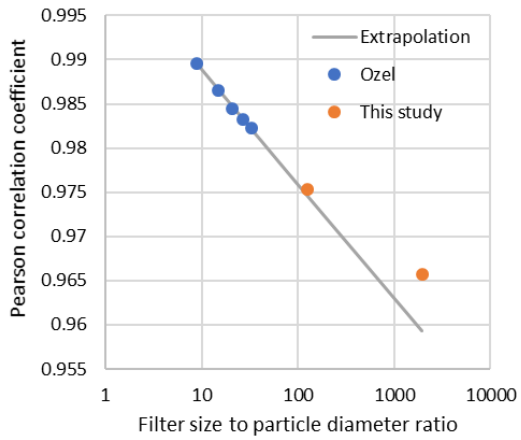

Figure 9 - Pearson correlation coefficient showing the correlation between $\overline{K_{gs}(v_{g,i} - v_{s,i})}$ and $K_{gs,hom}(\tilde{v}_{g,i} - \tilde{v}_{s,i} - v_{d,i})$. A value of 1 represents a perfect correlation.

The newly developed adjusted slip velocity-based formulation for the filtered drag force neatly separates three contributions that cause the filtered drag force to differ from the drag force predicted by the microscopic drag law: C_1, C_2 and $v_{d,i}$. To evaluate their relative importance, the contribution of the drift velocity is rearranged to yield a third correction factor:

$$C_3 = \frac{\tilde{v}_{g,i} - \tilde{v}_{s,i} - \dfrac{\overline{\alpha_g' v_{g,i}'}}{\bar{\alpha}_s \bar{\alpha}_g}}{\tilde{v}_{g,i} - \tilde{v}_{s,i}} \qquad \text{Equation 51}$$

Clearly, this correction factor is simply the ratio of the adjusted and the original filtered slip velocity. Also, it can be seen that $\overline{K_{gs}(v_{g,i} - v_{s,i})} = C_1 C_2 C_3 K_{gs,hom}(\tilde{v}_{g,i} - \tilde{v}_{s,i})$. Therefore, the product of the three contributions is equal to the drag correction factor defined in Equation 44 if the mesoscale interphase force was not lumped together with the filtered drag force.

Figure 10 compares the average values of the three drag correction factors in the drift velocity formulation as a function of the filter size and the filtered solids volume fraction. Considering that C_1 and C_3 are directionally dependent, data is shown for the vertical direction only. Similar conclusions will be drawn when considering the lateral direction. For this section regarding anisotropic drag closures, only the five largest filter sizes (i.e., $\hat{\Delta}_f \geq 1.93$.) in the range described in Chapter 3.2 will be considered for closure derivation. This is done because the assumption of negligible filtered kinetic theory stresses may no longer hold at smaller filter sizes, and the models developed in this study will start to become less accurate. Limiting the closure fitting to these filter sizes therefore simplifies the data analysis, while also ensuring that the closure models will be most accurate for the range of filter sizes where the closures are intended to be used. Despite this detail, using the scaled filter size in all closure models developed in the present study still ensures that the sub-grid contribution to the drag will go to zero as the filter size approaches the grid size at which the resolved simulations for model development were performed.

Figure 10.a shows that the assumption $\overline{\frac{K_{gs}}{\alpha_s}(\alpha_s v_{g,\iota} - \alpha_s v_{s,\iota})} = \overline{K_{gs}}\frac{(\overline{\alpha_s v_{g,\iota}} - \overline{\alpha_s v_{s,\iota}})}{\overline{\alpha_s}}$ would tend to overpredict the filtered drag force. Therefore, C_1 serves to reduce the filtered drag force by a factor of up to almost 2. The assumption $\overline{K_{gs}} = K_{\mathrm{gs,hom}}$ has the opposite effect, therefore C_2 acts to increase the filtered drag force by a factor of up to approximately 3 (Figure 10.b). The sudden change in the slope of the data at a filtered solids volume of fraction of 0.2, where the blending of the Wen-Yu and Gidaspow models occurs in the Huilin-Gidaspow drag model [36], suggests that C_2 is dependent on the choice of the microscopic drag law employed in the resolved simulations used for model development. The contributions originating from C_1 and C_2 are much smaller than the contribution from the drift velocity (see Figure 10.d). Clearly, the latter can reduce the filtered drag force by up to an order of magnitude. Finally, Figure 10.c shows that the contributions originating from C_1 and C_2 tend to cancel each other out to some degree. The effect of C_2 tends to be somewhat larger, with their combination, i.e., $C_{NL} = C_1 C_2$, taking on a maximum value of approximately 1.8. The effect of the non-linearity correction factor is therefore much smaller than that of the drift velocity, providing basis for the argument of previous works to neglect its effect. However, it is still clear from Figure 10.c that at filter sizes relevant to this study assuming $C_{NL} = 1$ would lead to a substantial underprediction of the filtered drag force at intermediate filtered volume fractions.

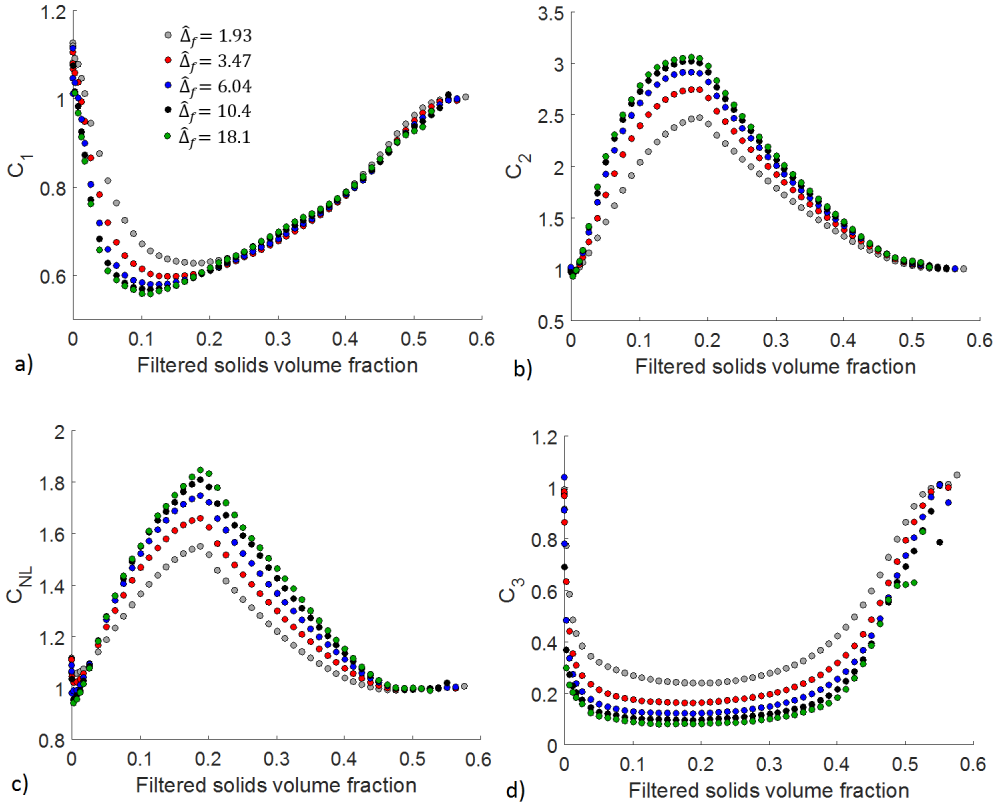

Figure 10 - Comparison of the three drag correction contributions in the adjusted slip velocity formulation of the filtered drag force in the vertical direction. Additionally, panel c) shows the combined contribution of C_1 and C_2.

3.4.2.3 Closure for the non-linearity correction factor

Evaluation of the non-linearity correction factor revealed that it could be closed using a 2-marker model similar to the isotropic drag closure discussed in Chapter 3.4.1.2. Furthermore, it was found that, when the data was binned as a function of the filtered solids volume fraction and the scaled filtered slip velocity magnitude, there was only a minor difference between values of C_{NL} calculated from the lateral and vertical direction data. Therefore, the closure model in this section is calibrated using the average of the lateral and vertical direction values.

Figure 11.a shows that, at low filtered solids volume fractions, C_{NL} increases with increasing solids volume fraction. At filtered solids volume fractions larger than 0.2, C_{NL} decreases again towards a value of 1. From Figure 11.b it can be seen that C_{NL} starts at a value greater than 1 when the scaled filtered slip velocity magnitude is equal to zero and then decreases with increasing slip velocity. Additionally, C_{NL} increases asymptotically with increasing filter size as can also be observed in Figure 10.c.

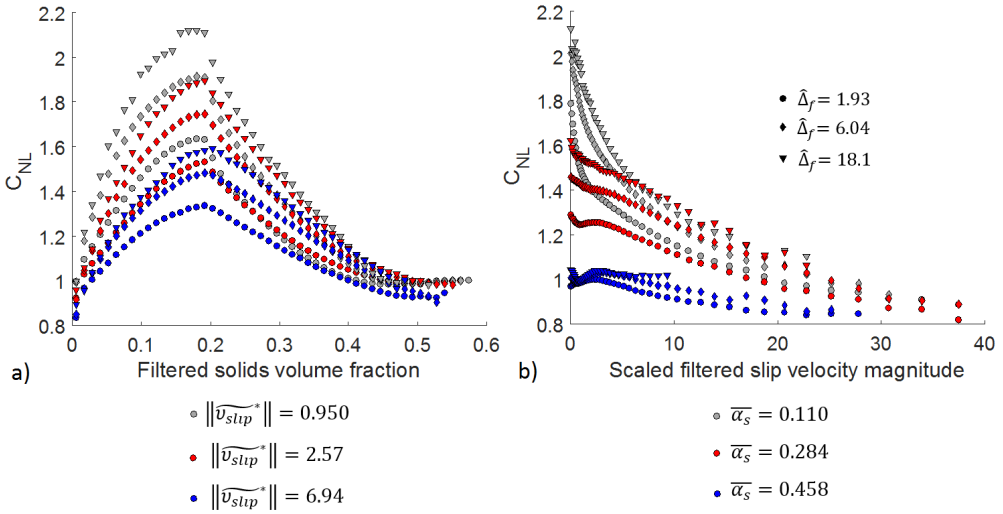

Figure 11 - The non-linear correction factor plotted against a) the filtered solids volume fraction and b) the scaled filtered slip velocity magnitude for different filter sizes.

It was found that these trends can be captured using the functional form shown in Equation 52 and the coefficients provided below. The closure for the non-linearity correction factor contains a part that is independent of the scaled filtered slip velocity magnitude (and proportional to x_5), as well as a part that decreases with increasing slip velocities (and proportional to x_9). Both parts contain a term that increases asymptotically with the filtered solids volume fraction, and a part that decreases with increasing solids volume fraction above a certain value. The coefficient x_2, with a value greater than unity, allows C_{NL} to become smaller than unity, as observed for certain combinations of large filtered solids volume fractions and large scaled filtered slip velocities. The last arctangent function ensures that the value of C_{NL} returns to unity in very dense regions. Lastly, the filter size dependencies of the coefficients ensure that the values of C_{NL} will reach a maximum at very large filter sizes.

$$C_{NL} = 1 + \left\{\left[\operatorname{atan}(x_1\overline{\alpha_s}) - x_2 \operatorname{atan}\left(x_3 \max(\overline{\alpha_s} - x_4, 0)\right)\right] x_5 + \left[\operatorname{atan}\left(x_6 \left\|\widetilde{v_{slip}}^*\right\|^{x_7} \overline{\alpha_s}\right) - \operatorname{atan}\left(x_8 \left\|\widetilde{v_{slip}}^*\right\|^{x_7} \max(\overline{\alpha_s} - x_4, 0)\right)\right] x_9 \left\|\widetilde{v_{slip}}^*\right\|^{x_{10}}\right\} \times \left(\frac{2}{\pi}\right)^2 \operatorname{atan}\left(x_{11} \max(\overline{\alpha_s} - x_{12}, 0)\right)$$

Equation 52

$x_1 = 23.5, x_2 = 1.29, x_3 = 7.73 - 2.17\left(\frac{2}{\pi}\right)\operatorname{atan}(0.194\Delta_{fil}^*), x_4 = 0.154,$
$x_5 = 2.04\left(\frac{2}{\pi}\right)\operatorname{atan}(0.710\Delta_{fil}^*), x_6 = 135, x_7 = -0.451, x_8 = 43.6,$
$x_9 = -0.547\left(\frac{2}{\pi}\right)\operatorname{atan}(0.825\Delta_{fil}^*), x_{10} = 0.390, x_{11} = 13.0$ and $x_{12} = 0.570.$

Using these coefficients, a fit with $R^2 = 0.980$ against the binned data was obtained. Figure 12 confirms that the closure in Equation 52 accurately approximates the binned data. Lastly, Figure 13 shows the model predictions against the binned data for the lateral and vertical directions separately, whereas previous plots showed the averages from these directions only. This confirms that using an isotropic closure for the non-linearity correction factor will only lead to minor errors.

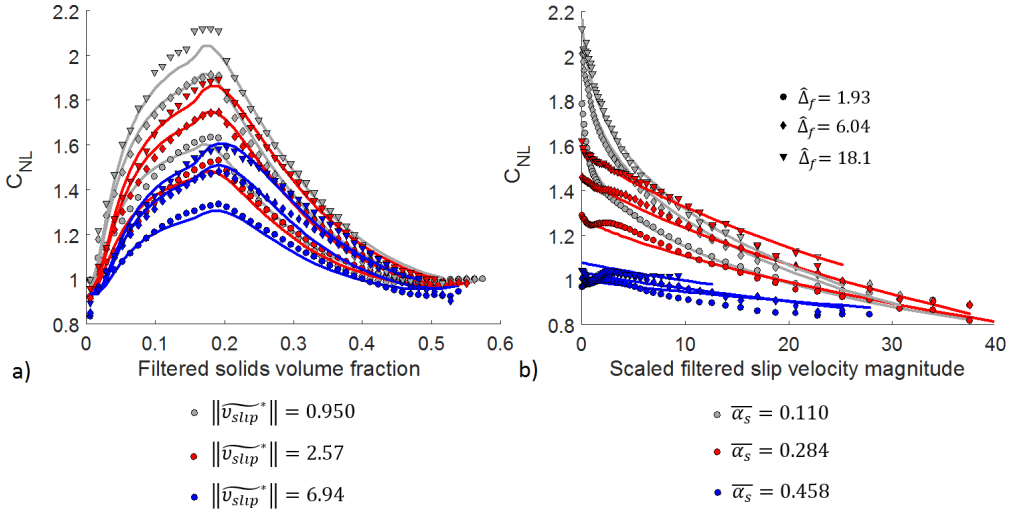

Figure 12 - The non-linear correction factor plotted against a) the filtered solids volume fraction and b) the scaled filtered slip velocity magnitude for different filter sizes. The symbols show the binned data and the lines the model predictions.

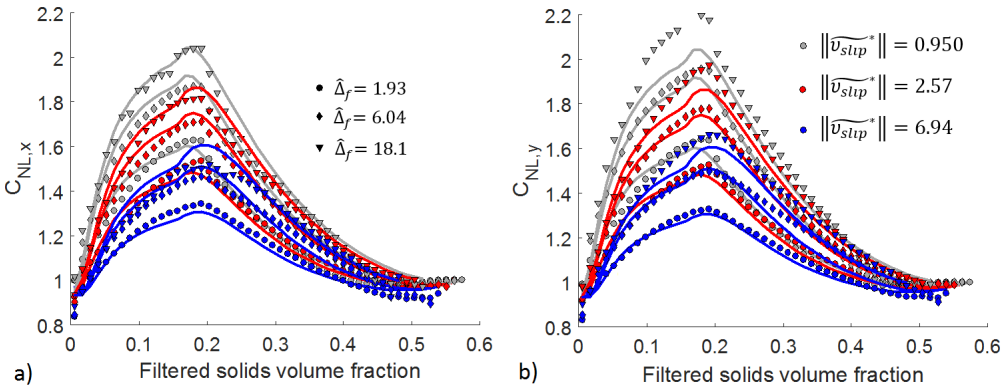

Figure 13 - The non-linear correction factor calculated from a) the lateral direction data and b) the vertical direction data plotted against the filtered solids volume fraction for different filter sizes and scaled filtered slip velocities. The symbols show the binned data and the lines the model predictions.

3.4.2.4 1-marker adjusted slip velocity closure

As a first step, the scaled adjusted slip velocity will be closed using a relatively simple 1-marker model, assuming a linear correlation of the drift velocity and the slip velocity. This is in line with the work of the Simonin group [17]. However, in contrast to this previous work, all velocities are scaled using the steady state sedimentation velocity due to the benefit of removing most of the filtered volume fraction dependency. Another important difference from earlier work is that the closure model is fitted to the scaled adjusted slip velocity, $v^*_{adj,i} = \tilde{v}^*_{slip,i} - v^*_{d,i}$, instead of the scaled drift velocity. As will be demonstrated in Chapter 3.4.2.5, the drift velocity is strongly correlated with the slip velocity, and can be almost as large as the slip velocity. This results in relatively small adjusted slip velocities for most situations, especially for large filter sizes. As a result, small relative changes in the drift velocity correspond to much larger relative changes in the adjusted slip velocity. Therefore, the effect of an independent variable on the drift velocity may appear negligible, but the effect on the adjusted slip velocity can be significant (this will be demonstrated later in the context of Figure 15). Similarly, errors in the predictions of the drift velocity may appear negligible, but may lead to substantial errors in the prediction of the adjusted slip velocity. Since the filtered drag force is proportional to the adjusted slip velocity, it is argued that it is essential that the predictions of the adjusted slip velocity are accurate. For this reason, this study will fit a closure for the adjusted slip velocity and, where possible, display binned data and model predictions for the adjusted slip velocity.

It is found that the scaled adjusted slip velocity can be accurately modelled using Equation 53 to Equation 56 and the coefficients given below. Similar to the work of the Simonin group, the drift velocity in direction i is found to be proportional to the filtered slip velocity in direction i (this is reflected by the second term on the right-hand side of Equation 54). However, it is found that there are substantial differences between the adjusted slip velocity in the lateral and the vertical directions, which can be explained by an additional term in the drift velocity closure that is independent of the filtered slip velocity and only acts in the direction aligned with gravity (k_1 in Equation 54). Therefore, it can be argued that the drift velocity originates from differences in the velocities of the phases in the direction considered, or from a driving force component such as gravity. The latter may be referred to

as the "gravitational contribution" to the drift velocity, and will be further discussed in Chapter 3.4.2.5. It can be isolated simply by considering the drift velocity parallel and perpendicular to gravity.

The gravitational contribution (denoted as k_1 below) increases approximately quadratically with increasing filtered solids volume fraction up to a certain point, after which it returns to zero in very dense regions. The slip velocity contribution, $\tilde{v}^*_{slip,i}(1-10^{-k_2})$, is formulated in such a way that k_2 is analogous to the scaled drag correction factor, i.e., $-\log(C)$ in the isotropic drag closure in Equation 45, giving similar advantages as those discussed in Chapter 3.4.1.2. The slip velocity contribution, k_2, is zero in the very dilute and very dense limits, and reaches a maximum at intermediate filtered solids volume fractions. The filter size dependencies of the coefficients ensure that both contributions to the drift velocity will tend to saturate at very large filter sizes.

$$v^*_{adj,i} = \tilde{v}^*_{slip,i} - v^*_{d,i} \qquad \text{Equation 53}$$

$$v^*_{d,i} = k_1 + \tilde{v}^*_{slip,i}(1-10^{-k_2}) \qquad \text{Equation 54}$$

$$k_1 = x_1\left(\frac{2}{\pi}\right)(\overline{\alpha_s}^{x_2})\,\mathrm{atan}\left(x_3\max(x_4-\overline{\alpha_s},0)\right) \qquad \text{Equation 55}$$

$k_1 = 0$ if i is in the direction perpendicular to gravity

$$k_2 = \left(\frac{2}{\pi}\right)^2 \mathrm{atan}(x_5\overline{\alpha_s})\,\mathrm{atan}\left(x_3\max(x_4-\overline{\alpha_s},0)\right)(x_6\overline{\alpha_s}^{x_7}) \qquad \text{Equation 56}$$

$x_1 = -3.44,\ x_2 = 2.09,\ x_3 = 21.6\left(\frac{2}{\pi}\right)\mathrm{atan}(0.216\Delta^*_{fil}),\ x_4 = 0.559,\ x_5 = 99.7{\Delta^*_{fil}}^{3.31},\ x_6 = 2.19$ and $x_7 = 1/(2.08{\Delta^*_{fil}}^{0.246})$.

Using the coefficients above, a fit with $R^2 = 0.990$ is obtained against the binned data. Since the filtered slip velocity is not used as a marker in the binning procedure, the mean filtered slip velocity in each bin is used in Equation 54 when calibrating the parameters of the closure model. Since each bin does not have a fixed filtered slip velocity value, the binned data for the 1-marker model is best displayed in the form $-\log(1-v^*_{d,i}/\tilde{v}^*_{slip,i})$, as shown in Figure 14. From the binned data, it is clear that this scaled ratio of the drift velocity to the filtered slip velocity is dependent on the direction considered. More importantly, it can be seen that the 1-marker model proposed in this section accurately predicts the binned data in both directions. Furthermore, the drift velocity correctly goes to zero in the limits of dilute and dense filtered solids volume fractions.

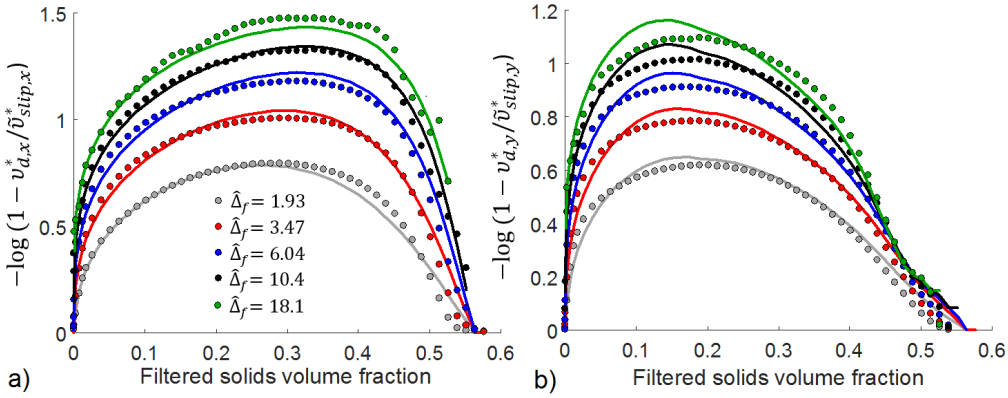

Figure 14 – The average value of $-\log(1-v^*_{d,i}/\tilde{v}^*_{slip,i})$ plotted against the filtered solids volume fraction for a) the lateral direction and b) the vertical direction. Symbols show the binned observation and lines the closure model predictions.

It can be added that the closure model in this section is not truly a 1-marker model, since Equation 54 assumes a correlation to the scaled filtered slip velocity in the direction considered and the binned values of the filtered slip velocities are used during model fitting. However, it can be noted that, in the case where the gravitational contribution is zero and the non-linearity correction factor is equal to unity, $\overline{K_{gs}\left(v_{g,i}-v_{s,i}\right)} = 10^{-k_2}K_{gs,hom}(\tilde{v}_{g,i}-\tilde{v}_{s,i})$ for this closure model. Hence, 10^{-k_2} is analogous to the drag correction factor, C, and k_2 is analogous to the scaled drag correction factor, $-\log(C)$, in the isotropic drag closure discussed in Chapter 3.4.1.2. Since k_2 is only a function of the filtered solids volume fraction, the closure model developed in this section is henceforth referred to as the anisotropic 1-marker drag closure. This also serves to distinguish it from the closure model in the following section where k_2 is also a function of the scaled filtered slip velocity.

3.4.2.5 2-marker adjusted slip velocity closure

For the 2-marker model presented in this chapter, the scaled adjusted slip velocity is binned as a function of the filter size, the filtered solids volume fraction and the filtered slip velocity in the direction considered. Having the filtered slip velocity as an additional independent variable allows the data to be visualized in ways that help to explain some of the concepts discussed in Chapter 3.4.2.4.

Firstly, the scaled drift velocity in the lateral direction is plotted against the scaled slip velocity in the lateral direction in Figure 15.a and Figure 15.b for the smallest and largest filter sizes evaluated. These figures show the proportionality between the drift velocity and the slip velocity for the direction considered (the same proportionality is observed in the vertical direction). It can also be seen than the value of the drift velocity is very close to that of the slip velocity, little dependence on the filtered solids volume fraction can be observed, and the proportionality appears almost linear, especially for the largest filter size considered.

On the contrary, considering the scaled adjust slip velocity (see Figure 15.c and Figure 15.d) shows a significantly non-linear correlation between the slip velocity and the adjusted slip velocity (and therefore also the drift velocity). Additionally, significant filtered solids volume fraction dependencies can be observed. These examples demonstrate how the adjusted slip velocity (and therefore also the filtered drag force) is extremely sensitive to changes in the drift velocity. This is due to the very strong

correlation between the drift velocity and the slip velocity. As discussed in Chapter 3.4.2.4, this shows why it is important to perform model fitting and data evaluation based on the adjusted slip velocity, instead of the drift velocity.

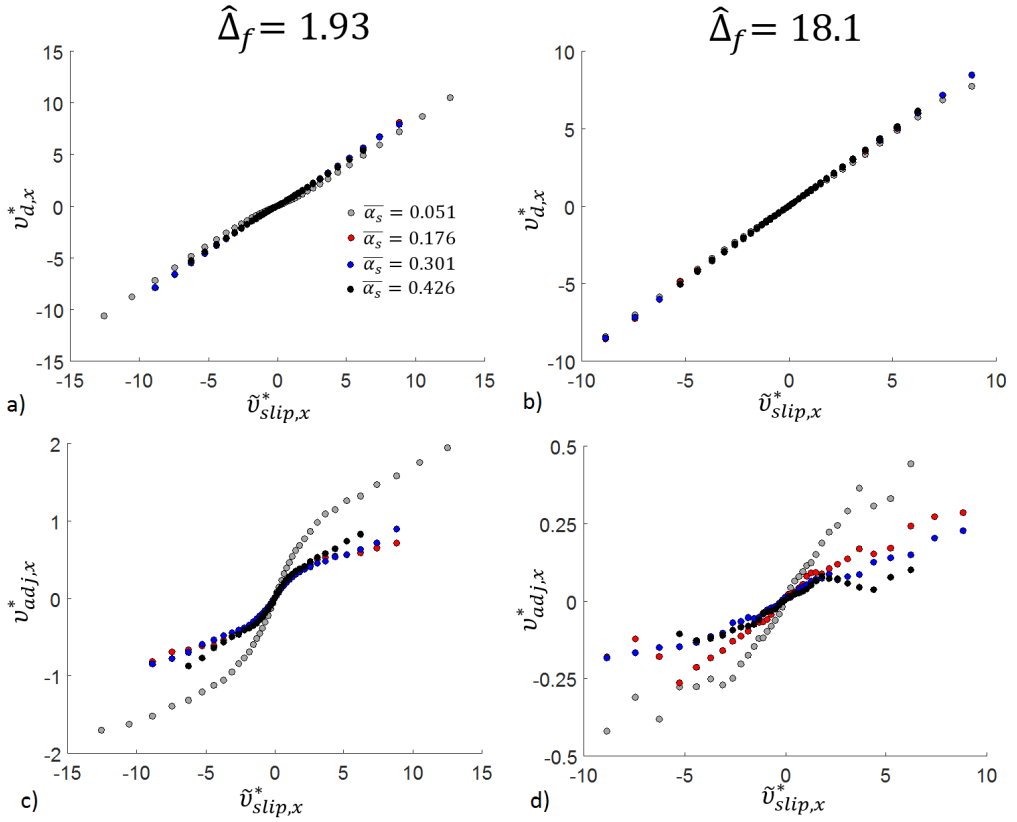

Figure 15 – The scaled drift velocity (top) and the scaled adjusted slip velocity (bottom) plotted against the scaled filtered slip velocity for the lateral direction data for filter sizes of $\hat{\Delta}_f = 1.93$ (left) and $\hat{\Delta}_f = 18.1$ (right).

Next, the scaled adjusted slip velocity in the vertical direction is shown in Figure 16 for situations in which the filtered slip velocity in the vertical direction is zero. This shows that there exists a positive drag force in the vertical direction at zero filtered slip velocity, which, as discussed in Chapter 3.4.2.4, stems from the presence of the gravitational force in that direction. This gravitational contribution increases with filter size, and reaches a maximum just below a filtered solids volume fractions of 0.5. This justifies the functional form for the gravitational contribution shown in Equation 55. It is also clear that this contribution is substantial relative to the scaled adjusted slip velocities reported for the lateral direction, as shown in Figure 15.c and Figure 15.d.

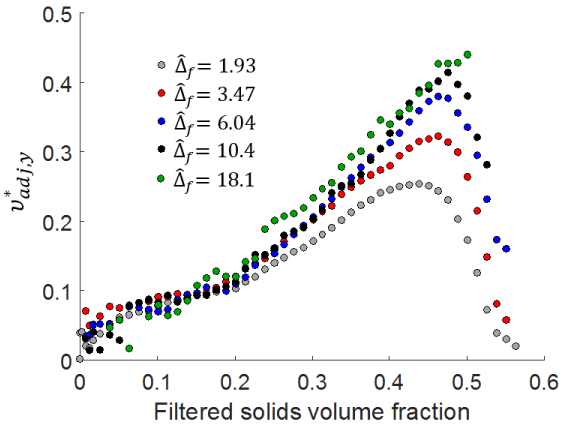

Figure 16 - The scaled adjusted slip velocity in the vertical direction for situations in which the filtered slip velocity in the vertical direction is zero.

Using a 2-marker closure model, the scaled adjusted slip velocity can be closed using Equation 57 to Equation 60 and the coefficients below. Similar to the 1-marker model presented in Chapter 3.4.2.4, the anisotropy of the drift velocity is accounted for via the gravitational contribution, k_1, which is independent of the filtered slip velocity. The only difference is that now the proportionality of the drift velocity to the filtered slip velocity is also a function of the filtered slip velocity in the direction considered, as implied by Equation 60. As with $-\log(C)$ in the isotropic drag closure, it is found that k_2 is also proportional to $log|\tilde{v}^*_{slip,i}|$. This is because k_2 is defined in a way that is analogous to the use of $-\log(C)$ in the isotropic drag closure. The addition of the slip velocity dependent term in k_2 ensures that the adjusted slip velocity will start to flatten out at large filtered slip velocities, as observed from the binned data in Figure 15.c and Figure 15.d. Also, it is found that the dependency of k_2 on the filtered slip velocity ceases at combinations of small slip velocities and dilute flows, which is accounted for by using $\left(\frac{2}{\pi}\right)\text{atan}\left(x_9\overline{\alpha_s}^{x_{10}}|\tilde{v}^*_{slip,i}|\right)$ in Equation 60.

$$v^*_{adj,i} = \tilde{v}^*_{slip,i} - v^*_{d,i} \qquad \text{Equation 57}$$

$$v^*_{d,i} = k_1 + \tilde{v}^*_{slip,i}(1 - 10^{-k_2}) \qquad \text{Equation 58}$$

$$k_1 = x_1\left(\frac{2}{\pi}\right)(\overline{\alpha_s}^{x_2})\,\text{atan}\left(x_3\max(x_4 - \overline{\alpha_s}, 0)\right) \qquad \text{Equation 59}$$

$k_1 = 0$ if i is in the direction perpendicular to gravity

$$k_2 = \left(\frac{2}{\pi}\right)^2 \text{atan}(x_5\overline{\alpha_s})\,\text{atan}\left(x_3\max(x_4 - \overline{\alpha_s}, 0)\right)\left(x_6\overline{\alpha_s}^{x_7} + x_8\left(\frac{2}{\pi}\right)\text{atan}\left(x_9\overline{\alpha_s}^{x_{10}}|\tilde{v}^*_{slip,i}|\right) log|\tilde{v}^*_{slip,i}|\right) \qquad \text{Equation 60}$$

$x_1 = -1.40$, $x_2 = 1.38$, $x_3 = 48.5\left(\frac{2}{\pi}\right)\text{atan}(0.235\Delta^*_{fil})$, $x_4 = 0.553$, $x_5 = 333{\Delta^*_{fil}}^{1.92}$,

$x_6 = 1.76\left(\frac{2}{\pi}\right)\text{atan}(1.29\Delta^*_{fil})$, $x_7 = 1/(2.40{\Delta^*_{fil}}^{0.234})$, $x_8 = 1/\left(2.44\left(\frac{2}{\pi}\right)\text{atan}(1.92\Delta^*_{fil})\right)$,

$x_9 = 25.6\Delta^*_{fil}$ and $x_{10} = 1.56$.

Using this closure model, an excellent fit, i.e., $R^2 = 0.977$, is obtained against the binned data. This is demonstrated in Figure 17. It can be noted that, in the lateral direction, the scaled adjusted slip velocity is symmetrical around values of zero filtered slip velocity. However, in the vertical direction, due to the presence of gravity, the adjusted slip velocity tends to be biased towards positive values (see data for zero filtered slip velocity in panels b) and d) of Figure 17). Also, it can be seen from panels b) and d) that the effect of the gravitational contribution in the vertical direction becomes more significant at larger filter sizes. Lastly, in the dilute and dense volume fraction limits, the drift velocity is zero, therefore the adjusted slip velocity becomes equal to the filtered slip velocity.

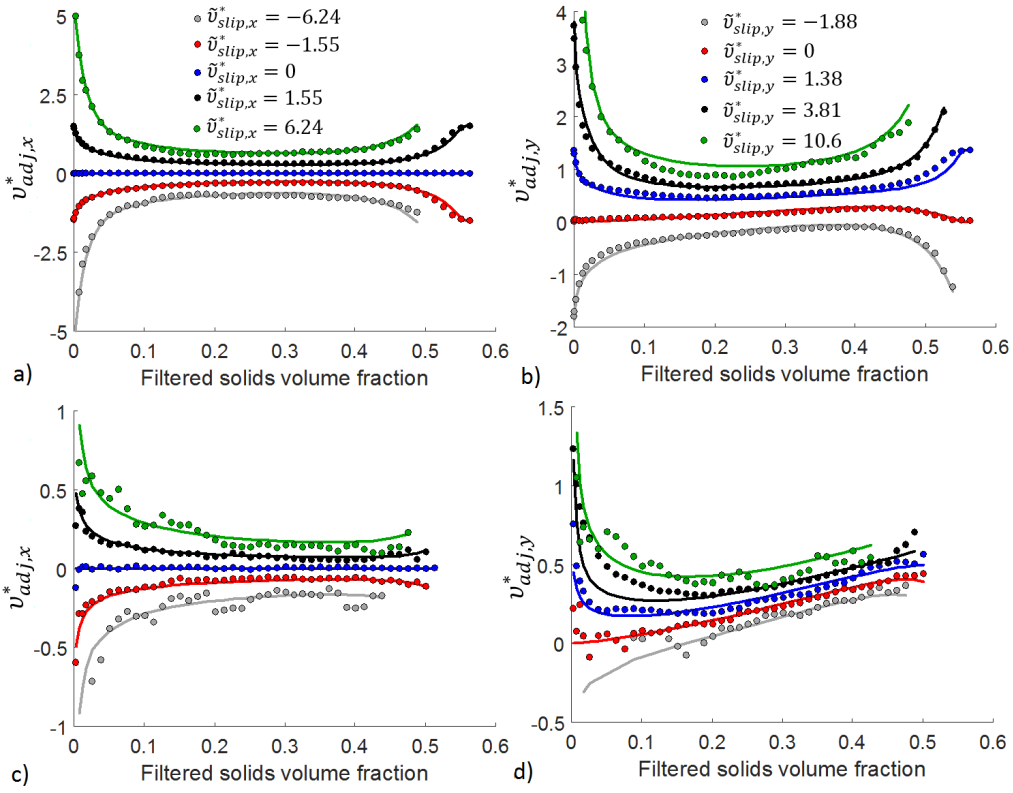

Figure 17 – The scaled adjusted slip velocity for the lateral direction (left) and vertical direction (right) plotted against the filtered solids volume fraction and at $\hat{\Delta}_f = 1.93$ (top) and $\hat{\Delta}_f = 18.1$ (bottom).

3.4.2.6 3-marker adjusted slip velocity closure

When investigating anisotropic closures for the solids mesoscale stresses (presented later in Chapter 3.6.3), it was found that a filtered variance quantity in the form of $\overline{X'Y'}$ can be modelled by a marker of the form $M = (\frac{d\tilde{x}}{dx}\frac{d\tilde{y}}{dx} + \frac{d\tilde{x}}{dy}\frac{d\tilde{y}}{dy})$, referred to as the "gradient product marker" (GPM). This approach can similarly be applied to the definition of the drift velocity, $v_{d,i} = \frac{\overline{\alpha'_g v'_{g,i}}}{\overline{\alpha}_s \overline{\alpha}_g}$, as used in the present study to obtain a promising third marker. Applying the GPM concept to the scaled drift velocity, the "drift GPM" in the direction i becomes:

$$\mathrm{M}_{drift,i} = \frac{\left(\frac{d\overline{\alpha_g}}{dx}\frac{d\bar{v}_{g,i}}{dx} + \frac{d\overline{\alpha_g}}{dy}\frac{d\bar{v}_{g,i}}{dy}\right)}{\overline{\alpha_s}\,\overline{\alpha_g}\bar{v}_{ss\_slip}} \qquad \text{Equation 61}$$

In the present study, the drift GPM is non-dimensionalized as $\widehat{\mathrm{M}}_{drift,i} = \mathrm{M}_{drift,i}\frac{v_t^4}{g^2}$. Additionally, since the GPM is highly dependent on the filter size, the following scaling is applied for the binning process to ensure a better distribution of data through the parameter space:

$$M^*_{drift,i} = \frac{\widehat{\mathrm{M}}_{drift,i}}{a\Delta_f^{*(b+c\Delta_f^*)}} \qquad \text{Equation 62}$$

Where $a = 3.28$, $b = -1.81$ and $c = -0.0120$. $M^*_{drift,i}$ will henceforth be referred to as the scaled drift GPM. A potential issue with using the drift GPM is that, as can be noted from Equation 61, the definition of the drift GPM requires the algebraic average of the gas velocities in the filter region. However, the filtered momentum transport equations, discussed in Chapter 2.2.2.2, solve for the phase-weighted gas velocities. From the derivation of the newly proposed adjusted slip velocity formulation in Appendix E.3, it is found that the algebraic average of the gas velocity can be calculated as:

$$\overline{v_{g,i}} = \tilde{v}_g - \bar{\alpha}_s v_{d,i} \qquad \text{Equation 63}$$

It is therefore clear that the model prediction for the drift velocity (which requires the drift GPM to be known) is required to calculate $\overline{v_{g,i}}$, which is necessary to calculate the drift GPM. Thus, the algebraic averages of the velocities are implicitly defined. Fortunately, this can easily be solved via a simple iteration loop: For the current iteration, the value of the drift velocity from the previous iteration is used to calculate $\overline{v_{g,i}}$, the drift GPM and the filtered drag force, in that order. For the first iteration of the simulation the $\overline{v_{g,i}}$ can simply be approximated as $\tilde{v}_{g,i}$ to calculate the drift GPM.

Furthermore, two additional factors ensure that this process is robust. Firstly, as shown in Table 3, $\overline{v_{g,i}}$ is highly correlated with $\tilde{v}_{g,i}$, even at large filter sizes. Therefore, a very good approximation of the drift GPM could be obtained even if $\tilde{v}_{g,i}$ was used in Equation 61. Secondly, because of the very strong correlation between the drift velocity and the filtered slip velocity in Table 3, the drift velocity can be predicted to a high degree of precision using the 3-marker closure model derived later in this section. This is in contrast to the adjusted slip velocity, which is much more difficult to predict precisely, as will be discussed in Chapter 3.4.3. It can also be seen that the correlation between observed values and model predictions for the drift velocity increases at large filter sizes, when the correlation between the drift velocity and the filtered slip velocity is even stronger. As a result of these two factors and the iterative procedure followed, the estimate of $\overline{v_{g,i}}$ used to calculate the drift GPM will always be very accurate.

Table 3 – Coefficient of determination (R^2) for the correlation of $\overline{v}_{g,i}$ and $\widetilde{v}_{g,i}$ as observed in the resolved simulations, as well as for the correlation between observed values and model predictions (using the 3-marker closure) for the drift velocity, $v_{d,i}$. Results are shown for two filter sizes.

$\hat{\Delta}_f$	Correlation between $\overline{v}_{g,i}$ and $\widetilde{v}_{g,i}$		Correlation between observed and predicted values for $v_{d,i}$	
	Lateral direction	Vertical direction	Lateral direction	Vertical direction
1.93	0.9991	0.9990	0.8481	0.8712
18.1	0.9973	0.9931	0.9865	0.9920

For the 3-marker closure proposed in this section, the adjusted slip velocity is binned for each filter size as a function of the filtered solids volume fraction, the scaled slip velocity in the direction considered and the scaled drift GPM in the direction considered. The binned data for the scaled adjusted slip velocity is shown in Figure 18 plotted against the scaled drift GPM. It is clear that there is a strong dependence of the adjusted slip velocity with respect to the drift GPM at both small and large filter sizes. The drift GPM dependence appears to be of similar importance as the filtered slip velocity dependence.

Specifically, increasing drift GPM values lead to smaller adjusted slip velocities, and therefore also smaller filtered drag forces. At the smaller filter size considered, the scaled adjusted slip velocity tends to flatten out at large absolute values of the drift GPM. At the larger filter size considered, such a trend cannot be clearly distinguished. However, this is most likely due to the fact that large enough GPMs do not occur in the resolved simulations: All other filter sizes, for which the results are not shown here, confirm that the adjusted slip velocity becomes independent of the drift GPM at large absolute values of the drift GPM. Lastly, it is noted that there appears to be some correlation between the filtered slip velocity and the drift GPM for a specific direction. As seen from Figure 18, the drift GPM tends to be positive at large positive slip velocities and negative at large negative slip velocities.

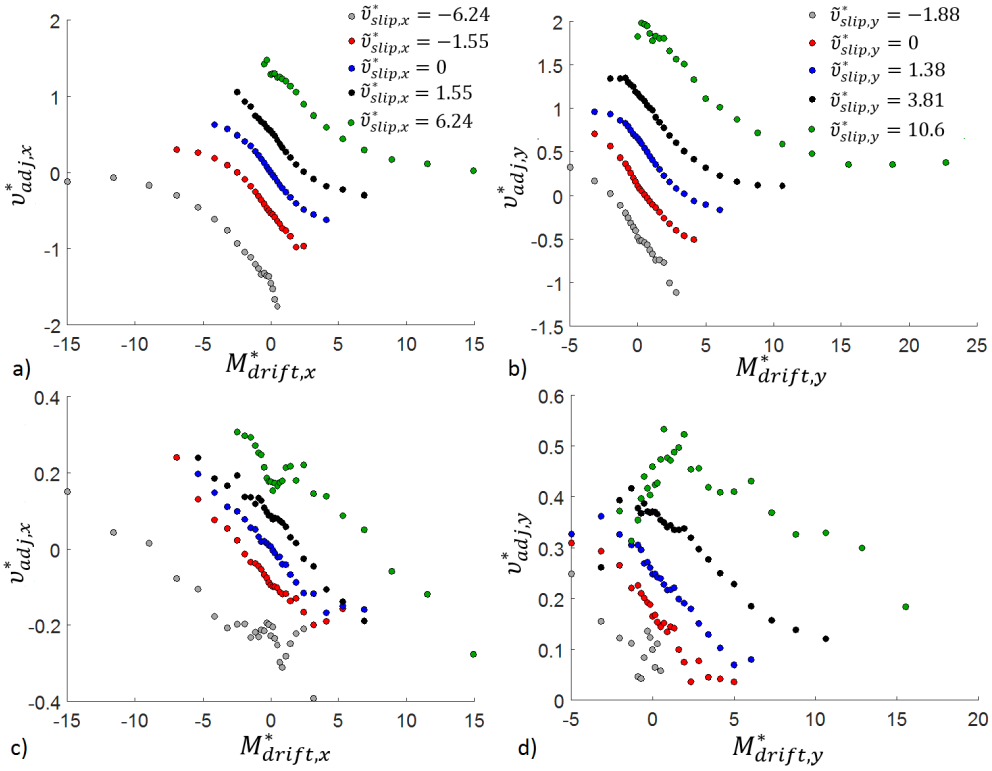

Figure 18 - The scaled adjusted slip velocity for the lateral direction (left) and vertical direction (right) plotted against the scaled drift GPM at $\hat{\Delta}_f = 1.93$ (top) and $\hat{\Delta}_f = 18.1$ (bottom). The data shown is for an intermediate filtered solids volume fraction, $\overline{\alpha_s} = 0.251$.

Through a rigorous analysis of the binned data, it was found that the scaled adjusted slip velocity could be closed using the 3-marker model in Equation 64 and Equation 68 and the coefficients below. The third marker adds a substantial amount of complexity to the closure fitting process. This is due to (i) the large increase in the number of bins caused by the added dimension in the binned data, and (ii) due to the complex interactions between the different markers. The process that was used to overcome this complexity is described in more detail in Appendix D.1 for the interested reader.

Compared to the 2-marker model, it can be seen that the gravitational and slip velocity contributions (i.e., k_1 and $\tilde{v}^*_{slip,i}\left(1 - 10^{-k_2}\right)$, respectively) remain similar, with only minor changes in the filter size dependencies of the coefficients. Most important, it is found that the effect of the drift GPM can be included as an additional term k_3, which is denoted as the "gradient contribution term" in what follows. Therefore, gradients in the flow (specifically in the filtered gas volume fraction and in the algebraically averaged gas velocity field) can be identified as an additional source of drift velocity. It can be physically understood that large drift GPMs in a coarse grid filtered simulation indicates the presence of a cluster interface, which cannot be well resolved on a coarse grid. It is well known that poor cluster interface resolution overpredicts gas-solid contact, leading to overpredictions of interphase mass, momentum and energy transfer. The use of the drift GPM as marker allows the model to directly address this overprediction of momentum transfer.

In the gradient contribution, i.e., k_3 in Equation 68, the first two arctangent functions ensure that the gradient contribution to the drift velocity is zero at the dilute and dense limits. The third arctangent function, i.e., $atan\left(x_{13}\widehat{\mathrm{M}}_{drift,i}\right)$, causes the gradient contribution to saturate at large absolute values of the drift GPM, as observed in the binned data. The filter size dependency of x_{13} compensates for the fact that the dimensionless drift GPM decreases rapidly with increasing filter size. Therefore, at large filter sizes, the gradient contribution saturates at smaller drift GPM values.

The next three terms identify different parts of the gradient contribution. The first part (proportional to x_{14}) is due to only the drift GPM and takes the sign of the drift GPM. The second part (proportional to $\left(x_{16}\left|\overline{\alpha_s}-\frac{x_4}{2}\right|^{x_{17}}+x_{18}\right)$) is due to the interaction of the drift GPM and the filtered slip velocity, since it is observed that the gradient contribution increases at large absolute slip velocities. It is found that this part has a minimum effect at intermediate volume fractions, but the effect increases towards the dilute and dense limits. However, it can be noted that the first two arctangent functions still ensure that this part goes to zero at the dilute and dense limits. Furthermore, this GPM-slip interaction part of the gradient contribution takes the sign of the drift GPM and its absolute value is symmetrical around a drift GPM of zero.

The third part of the gradient contribution (proportional to x_{19}) is an asymmetrical GPM-slip interaction part, since it is observed that near the dilute and dense limits there is an additional effect in case the drift GPM and the filtered slip velocity has opposite signs. This asymmetrical effect can clearly be seen in Figure 19, where the drift GPM dependence is compared at dilute and intermediate volume fractions. The asymmetrical GPM-slip interaction part has no effect at intermediate volume fractions, but the effect increases towards the dilute and dense limits, similarly to the symmetrical GPM-slip interaction part. In the closure model, by using $\min\left(sign\left(\tilde{v}^*_{slip,i}\widehat{\mathrm{M}}_{drift,i}\right),0\right)$, this part is defined in such a way that it only has an effect in case the drift GPM and the filtered slip velocity has opposite signs. Also, this part has the opposite sign as the drift GPM. The asymmetrical interaction part therefore has an effect in the opposite direction as the symmetrical interaction part.

$$v^*_{adj,i}=\tilde{v}^*_{slip,i}-v^*_{d,i} \qquad \text{Equation 64}$$

$$v^*_{d,i}=k_1+\tilde{v}^*_{slip,i}\left(1-10^{-k_2}\right)+k_3 \qquad \text{Equation 65}$$

$$k_1=x_1\left(\frac{2}{\pi}\right)\left(\overline{\alpha_s}^{x_2}\right)\operatorname{atan}\left(x_3\max(x_4-\overline{\alpha_s},0)\right) \qquad \text{Equation 66}$$

$k_1=0$ if i is in the direction perpendicular to gravity

$$k_2=\left(\frac{2}{\pi}\right)^2\operatorname{atan}(x_5\overline{\alpha_s})\operatorname{atan}\left(x_3\max(x_4-\overline{\alpha_s},0)\right)\left(x_6\overline{\alpha_s}^{x_7}+x_8\left(\frac{2}{\pi}\right)\operatorname{atan}\left(x_9\overline{\alpha_s}^{x_{10}}\left|\tilde{v}^*_{slip,i}\right|\right)log\left|\tilde{v}^*_{slip,i}\right|\right) \qquad \text{Equation 67}$$

$$k_3 = \left(\frac{2}{\pi}\right)^3 \operatorname{atan}(x_{11}\overline{\alpha_s}) \operatorname{atan}\left(x_{12}\max(x_4 - \overline{\alpha_s}, 0)\right) atan\left(x_{13}\widehat{\mathrm{M}}_{drift,i}\right)\left\{x_{14} + \left|\tilde{v}^*_{slip,i}\right|^{x_{15}}\left[\left(x_{16}\left|\overline{\alpha_s} - \frac{x_4}{2}\right|^{x_{17}} + x_{18}\right) + \min\left(sign\left(\tilde{v}^*_{slip,i}\widehat{\mathrm{M}}_{drift,i}\right), 0\right) x_{19}\left|\overline{\alpha_s} - \frac{x_4}{2}\right|^{x_{17}}\right]\right\} \quad \text{Equation 68}$$

$x_1 = -1.74\left(\frac{2}{\pi}\right) atan\left(1.71\Delta^*_{fil}\right)$, $x_2 = 1.54$, $x_3 = 21.8\left(\frac{2}{\pi}\right) atan\left(0.708\Delta^*_{fil}\right)$, $x_4 = 0.558$,

$x_5 = 45.6{\Delta^*_{fil}}^{2.10}$, $x_6 = 2.09\left(\frac{2}{\pi}\right) atan\left(0.331\Delta^*_{fil}\right)$, $x_7 = 0.248$, $x_8 = 0.308$, $x_9 = 6.35\Delta^*_{fil}$,

$x_{10} = 1.22$, $x_{11} = 4030$, $x_{12} = 194$, $x_{13} = 0.0742{\Delta^*_{fil}}^{1.89}$, $x_{14} = 1/\left(3.53\left(\frac{2}{\pi}\right) atan\left(0.303\Delta^*_{fil}\right)\right)$,

$x_{15} = 1/\left(1 + 4.69\left(\frac{2}{\pi}\right) atan\left(0.0604\Delta^*_{fil}\right)\right)$, $x_{16} = 9.18$, $x_{17} = 2.84$, $x_{18} = 1/\left(2.24\Delta^*_{fil}\right)$ and

$x_{19} = 1/\left(0.0742\left(\frac{2}{\pi}\right) atan\left(0.419\Delta^*_{fil}\right)\right)$.

The closure model presented in this section yields an excellent fit to the binned data over all filter sizes with $R^2 = 0.979$. This is demonstrated for the intermediate filter size in Figure 20, where the scaled adjusted slip velocity is plotted against the filtered solids volume fraction at different filtered slip velocities and scaled drift GPM values. Additionally, Figure 19 shows how the closure models capture the drift GPM dependency to predict the scaled adjusted slip velocity.

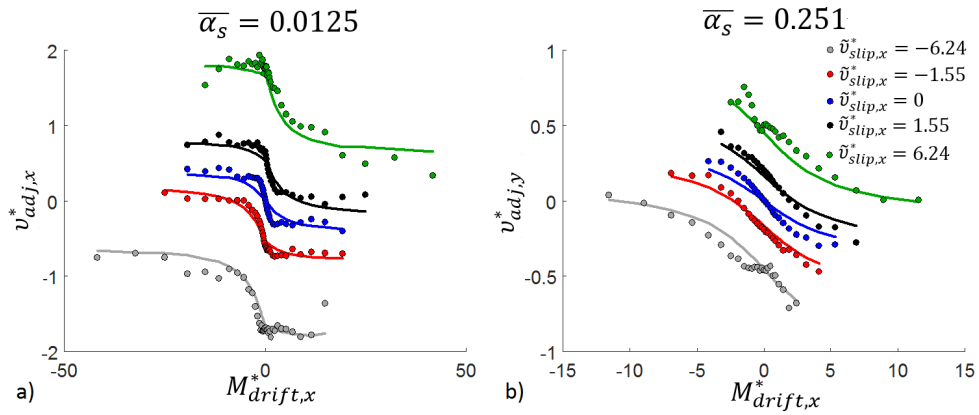

Figure 19 - The scaled adjusted slip velocity for the lateral direction plotted against the scaled drift GPM at $\hat{\Delta}_f = 5.91$ for a) a dilute filtered solids volume fraction, $\overline{\alpha_s} = 0.0125$ and b) an intermediate filtered solids volume fraction, $\overline{\alpha_s} = 0.251$.

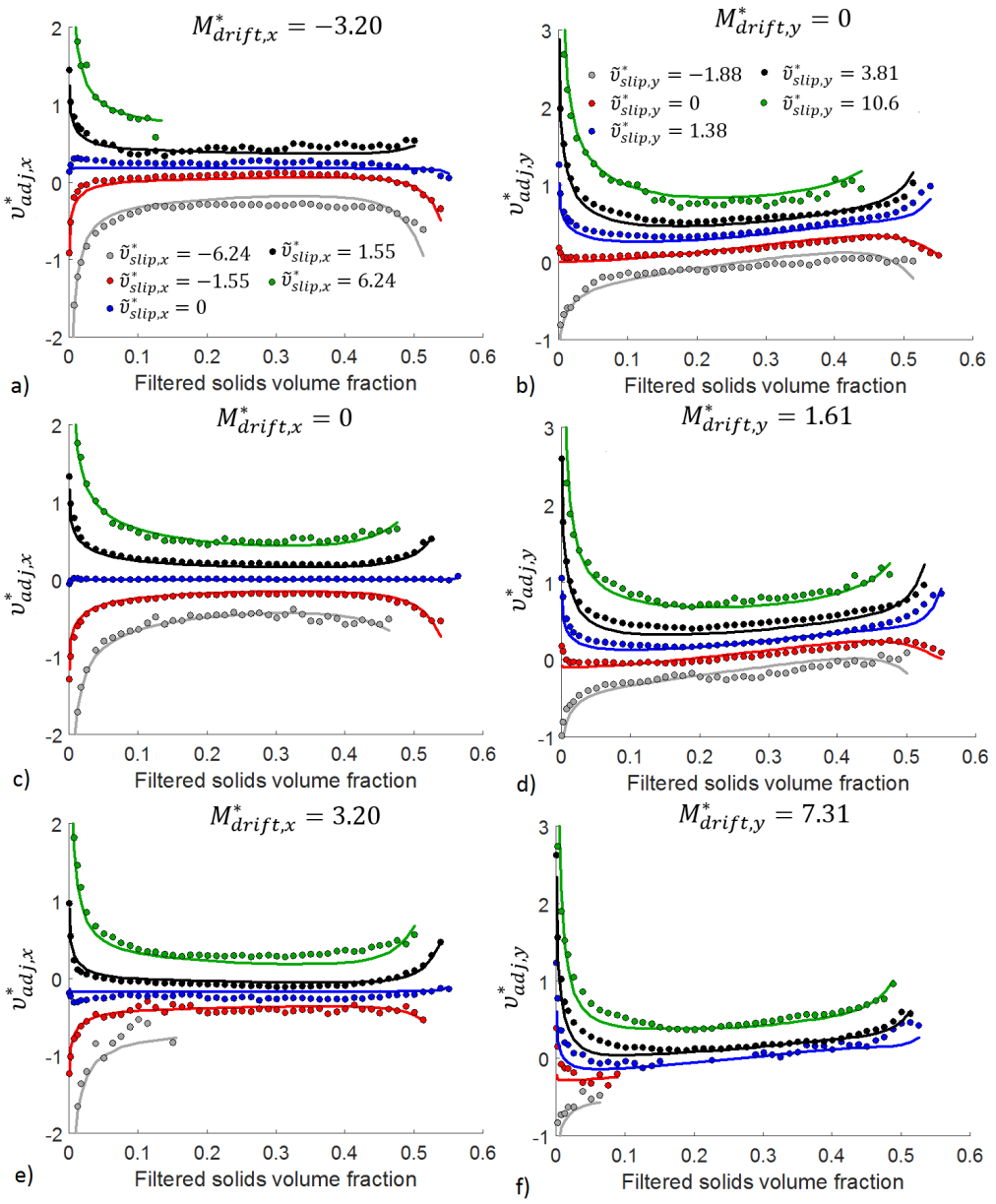

Figure 20 - The scaled adjusted slip velocity for the lateral direction (left) and the vertical direction (right) plotted against the filtered solids volume fraction at $\hat{\Delta}_f = 5.91$ for different scaled drift GPMs (top, centre and bottom rows).

3.4.3 *A priori* analysis of the filtered drag closures

In this section, the resolved simulation data used for model derivation is used to compare the observed values to the predicted values when using a specific closure model for the filtered drag force. The correlation of the observed and predicted values is then expressed using the coefficient of

determination (R^2) as discussed in Chapter 3.2. An R^2 value of unity corresponds to a perfect correlation, whereas the model predictions increasingly differ from the observed values as the R^2 value decreases. An R^2 value of zero corresponds to using the mean of the observations as the model prediction.

It can be noted that the R^2 values in this section, determined by comparing observations and predictions for individual data samples, are significantly lower than those reported in Chapter 3.4.1 and Chapter 3.4.2. This is because in these chapters model predictions were compared to the binned observed values, i.e., conditional averages. This means that there is a large amount of scatter of the data characterized by these conditional averages, which is averaged out in the bin and not explained directly by the closure model. Such a large amount of averaging reduces the capability of the model to accurately predict flow situations that may differ substantially from the average conditions of the resolved simulations from which the models were derived. For example, validation of fTFM closures from literature performed early in this study [50] showed that a one-marker model [16, 19] failed completely by its inability to predict large enough drag corrections for the case under consideration. On the contrary, a two-marker model [13], which explains more of the variance in the sample data, could predict these flow conditions reasonably well. Additionally, one-marker models derived from periodic simulations are known to fail in wall-bounded flows without wall correction functions [25], whereas two-marker models have been shown to perform reasonably well also in wall-bounded flows without additional wall corrections [13, 26]. It is therefore valuable to develop closure models that can explain as much as possible of the variance in the resolved simulation data without averaging these results in the bins, thereby making the models more generally applicable. For this reason, this section compares the R^2 values determined from the same set of resolved data for the different filtered drag force closures developed, as a measure of their relative predictive capabilities.

It can be noted that the isotropic closure presented in Chapter 3.4.1.2 was derived for the combined filtered drag and mesoscale interphase forces. To be able to compare it directly with the anisotropic closures for the filtered drag force presented in Chapter 3.4.2, the isotropic closure is rederived for the filtered drag force only. It is found that the same expression as in Equation 45 can be used by only changing the coefficient values. This new closure model is provided in Appendix F.1.

Figure 21 summarises the results when comparing the observations and predictions for samples in the resolved simulation data. Clearly, the models perform substantially better in the vertical direction than in the lateral direction. This is especially evident for the isotropic closure, which makes reasonable predictions at the smallest filter size, but deteriorates rapidly as the filter size increases. Although not all the data is shown, it can be noted that $R^2 = -1.12$ for the isotropic model in the lateral direction and for the largest filter size considered. The isotropic model therefore completely fails in predicting the filtered drag force in the lateral direction when large filter sizes are considered. The reason for this was observed earlier in Figure 6, where it was clearly seen that the assumption of an isotropic drag correction factor becomes poorer at larger filter sizes.

In contrast, the anisotropic models perform much better in predicting the lateral filtered drag force, although the predictive capability of the models clearly decrease with increasing filter size. This is expected as there will be more sub-grid variability when using larger filter sizes, and it appears that this variability will be difficult to predict. Furthermore, it is observed that the model predictions are

significantly improved as the number of markers in the anisotropic closure is increased. Most important, there is a substantial improvement at all filter sizes when increasing from 2 to 3 markers.

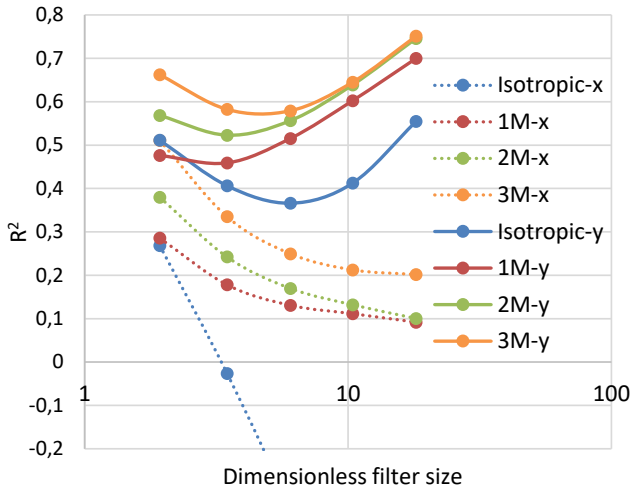

Figure 21 – The coefficient of determination as a function of the dimensionless filter size for the lateral and vertical direction and for the four different closures developed for the filtered drag force.

In the vertical direction, several surprising observations can be made. Firstly, the isotropic closure (based on 2-markers) performs poorer than the 1-marker anisotropic closure (in combination with the 2-marker closure for the non-linearity correction factor). This is especially pronounced at larger filter sizes. Closer analysis of the sample data confirmed that this is due to the isotropic closure not accurately accounting for the gravitational contribution to the filtered drag, since the formulation in Equation 119 (see Appendix F.1) limits the filtered drag force to be proportional to the filtered slip velocity. It therefore is clear that the adjusted slip velocity formulation of the filtered drag force in Equation 46 is an improved method for closing the filtered drag force, compared to using an isotropic drag correction factor.

The second interesting observation is that the correlation between the observations and predictions in the vertical direction improves with increasing filter size at large filter sizes. This is contrary to the notion that predictions will become more difficult as the sub-grid variability increases with increasing filter size. The third observation is that the effect of the number of markers in the adjusted slip velocity closures becomes smaller at larger filter sizes.

The trends in the R^2 values can be explained based on the following hypothesis: There is less variability in the gravitational contribution to the drift velocity than in the slip and gradient contributions, therefore the portion of the filtered drag force resulting from the effect of gravity can be explained with a high coefficient of determination. Since there is no gravitational contribution in the lateral direction, this would explain why the R^2 values in the lateral direction are substantially lower than those in the vertical direction. Furthermore, since the proportion of the gravitational contribution to the filtered drag force in the vertical direction increases with increasing filter size (see Figure 16 and Figure 17), this is also a possible explanation for the reversal of the trend for the R^2 values at intermediate filter sizes. Lastly, since the gravitational contribution is a function of the volume fraction only, this explains why there is little difference in the performance of the 1-marker, 2-marker and 3-

marker models in the vertical direction at large filter sizes: in these situations, the contribution of the gravitational part to the filtered drag force is dominating, and captured reasonably well already with a 1-marker-based, anisotropic drag closure.

In conclusion, it can be noted that the anisotropic closures clearly outperform the isotropic closure, with the 3-marker model also offering a clear improvement in predictive capability compared to the simpler anisotropic closures. However, from Chapter 3.4.2.6, it is also clear that including the gradient contribution to the adjusted slip velocity closure substantially complicates the derivation process, as well as the resulting closure expression. The verification exercises in Chapter 5.1 and Chapter 5.2 will therefore further evaluate whether the more complex 3-marker drag closure results in any practical improvements in coarse grid simulations.

3.5 Mesoscale interphase force closures

3.5.1 Anisotropic closure for the mesoscale interphase force

The contribution from the pressure gradient fluctuations (last term on the right of Equation 15), has been referred to as the buoyancy force [18, 20] or as a mesoscale added-mass force [51-53] in the literature. Following these detailed studies [51-53], it is noted that this force originates from the redistribution of the pressure gradient over the mesoscale structures. On the contrary, the filtered drag force, the other interphase transfer force in the filtered momentum transport equations, is a force acting on the microscale (i.e., at the particle level) which is averaged over the mesoscale structures. To highlight this important difference, the pressure gradient fluctuation contribution is simply referred to as the mesoscale interphase force in the present study.

While the more detailed studies [51-53] found the mesoscale interphase force to be of significant importance, other studies have reported that it can be neglected [18, 20] for certain applications. To investigate the importance of the mesoscale interphase force, the absolute values of the filtered drag force and the mesoscale interphase force is binned as a function of the filtered solids volume fraction and the absolute filtered slip velocity in the direction considered. The relative contribution (in a percentage) of the mesoscale interphase force to the total filtered interphase force is then defined as:

$$MIF\% = \frac{-\overline{\alpha_s{}' \frac{dp'}{di}}}{\left(\overline{K_{gs}(v_{g,i}-v_{s,i})}-\overline{\alpha_s{}' \frac{dp'}{di}}\right)} \times 100\%.$$

Figure 22 shows that, although the mesoscale interphase force is on average smaller than the filtered drag force, its contribution to the filtered interphase momentum transfer is significant in both directions. The contribution of the mesoscale interphase force tends to increase with increasing filter size and reaches a maximum at intermediate volume fractions and small slip velocities. For the filter sizes shown, the contribution can be up to 33% of the combined filtered interphase momentum transfer force.

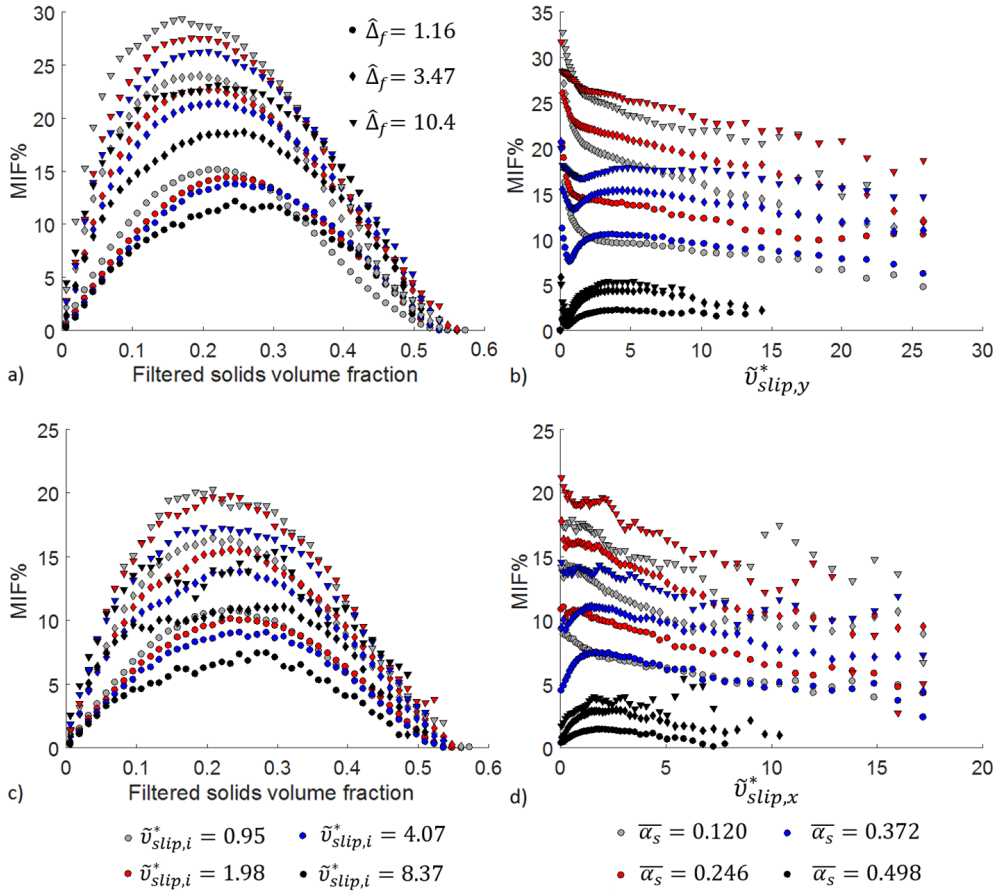

Figure 22 – The percentage contribution of the mesoscale interphase force to the sum of the filtered drag force and the mesoscale interphase force as a function of the filtered solids volume fraction (left) and the filtered slip velocity in the direction considered (right) for the vertical (top) and the lateral (bottom) directions at different filter sizes.

Due to the apparent significance of the mesoscale interphase force, a simple anisotropic closure is derived in this section, to be used in combination with the anisotropic filtered drag force closures presented in Chapter 3.4.2. Using the definition $F_{M,i} = -\overline{\alpha_s{}' \frac{\partial p'}{\partial \iota}}$, the mesoscale interphase force is non-dimensionalised as follows, using characteristic quantities similar to those used in the fTFM literature [12]. Specifically, $\hat{F}_{M,i} = F_{M,i}/(\rho_g g)$.

It can be noted that, similarly to the anisotropic drag closures, only filter sizes larger than $\hat{\Delta}_f \geq 1.93$ are considered for deriving the closure for the mesoscale interphase force in this section. Analysis of the mesoscale interphase force showed that it is correlated with the filtered slip velocity in the direction considered, as shown for the lateral direction in Figure 23. From the binned data, it can be seen that the mesoscale interphase force tends to be proportional to the filtered slip velocity, but the dependency tends to flatten out at large values for the filtered slip velocity. Additionally, the mesoscale interphase force tends to be zero at the dilute and dense volume fraction limits, and has a maximum at intermediate particle volume fractions. Lastly, the magnitude of the mesoscale interphase force

tends to decrease with increasing filter size. Interestingly, it can be noted that, since it was observed in Figure 22 that the contribution of the mesoscale interphase force increases relative to the filtered drag force with increasing filter size, it can be concluded that the filtered drag force decreases at a faster rate than the mesoscale interphase force with increasing filter sizes.

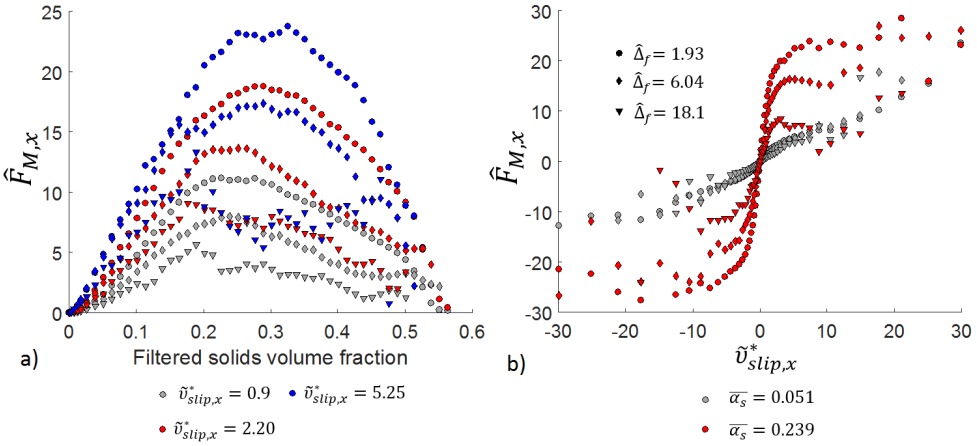

Figure 23 - The dimensionless interphase mesoscale force in the lateral direction as a function of a) the filtered solids volume and b) the scaled filtered slip velocity in the lateral direction for three filter sizes.

For the vertical direction, as with the filtered drag force, it is found that there exists a positive force at zero filtered slip velocities, as seen in Figure 24. This contribution increases with the filter size and appears to saturate at large filter sizes.

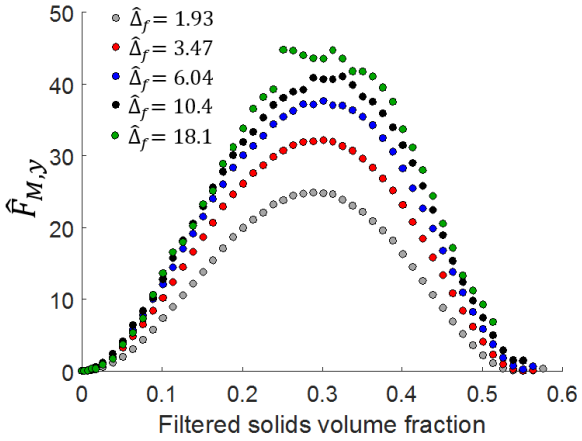

Figure 24 - The dimensionless interphase mesoscale force in the vertical direction as a function of the filtered solids volume fraction for all filter sizes considered conditioned on a vertical filtered slip velocity of zero.

Based on these previous observations, it is found that the mesoscale interphase force can be closed in a similar way as the 2-marker anisotropic drag closure reported in Chapter 3.4.2.5. The mesoscale interphase force is divided into two parts: one part, k_1, that is due to a gravitational contribution and

only acts in the vertical direction, and a second part, k_2, that is correlated with the filtered slip velocity in the direction considered. The proposed closure model is provided in Equation 69 to Equation 71, with the optimised coefficients reported below. Both contributions peak at intermediate volume fractions and have a zero value at the dilute and dense filtered volume fraction limits. From the filter size dependencies of x_1 and x_6, it can be seen that both contributions will saturate at very large filter sizes. However, the gravitational contribution will tend to increase with increasing filter sizes, whereas the slip contribution decreases with increasing filter size. The gravitational contribution is, as with the filtered drag force, independent of the filtered slip velocity. On the other hand, the slip contribution takes the sign of the slip velocity and its absolute value increases with increasing absolute values of the filtered slip velocity in the direction considered. The arctangent function, $atan\left(x_9\tilde{v}^*_{slip,i}\right)$, ensures that the slip contribution reaches a plateau at large absolute values of the filtered slip velocity.

$$\hat{F}_{M,i} = k_1 + k_2 \qquad \text{Equation 69}$$

$$k_1 = x_1\left(\frac{2}{\pi}\right)\overline{\alpha_s}^{x_2}\, atan\left(x_3 max(\overline{\alpha_s} - x_4, 0)^{x_5}\right) \qquad \text{Equation 70}$$

$k_1 = 0$ if i is in a direction perpendicular to gravity

$$k_2 = x_6\left(\frac{2}{\pi}\right)^3 atan(x_7\overline{\alpha_s})\, atan\left(x_8\, max(x_4 - \overline{\alpha_s}, 0)\right) atan\left(x_9\tilde{v}^*_{slip,i}\right) \qquad \text{Equation 71}$$

$x_1 = 29000\left(\frac{2}{\pi}\right)\text{atan}\left(0.690\Delta^*_{fil}\right)$, $x_2 = 185$, $x_3 = 0.168$, $x_4 = 0.551$, $x_5 = 1.43$,
$x_6 = 92.4 - 65.4\left(\frac{2}{\pi}\right)\text{atan}\left(0.167\Delta^*_{fil}\right)$, $x_7 = 5.65$, $x_8 = 7.06$ and $x_9 = 0.475$.

Using the proposed model, a good fit ($R^2 = 0.948$) is obtained against the binned data, as shown in Figure 25. Some minor deviations of the model predictions from the binned data can be discerned, for example in the lateral direction and for large filtered slip velocities. In these situations, the interphase mesoscale force is somewhat overpredicted. Therefore, it can be concluded that the approach of dividing the force into a gravitational and a slip contribution does not work quite as well as for the 2-marker anisotropic drag closure. In general, however, the model appears to capture the trends in the data sufficiently well, especially considering that the mesoscale interphase force is generally of lesser importance than the filtered drag force.

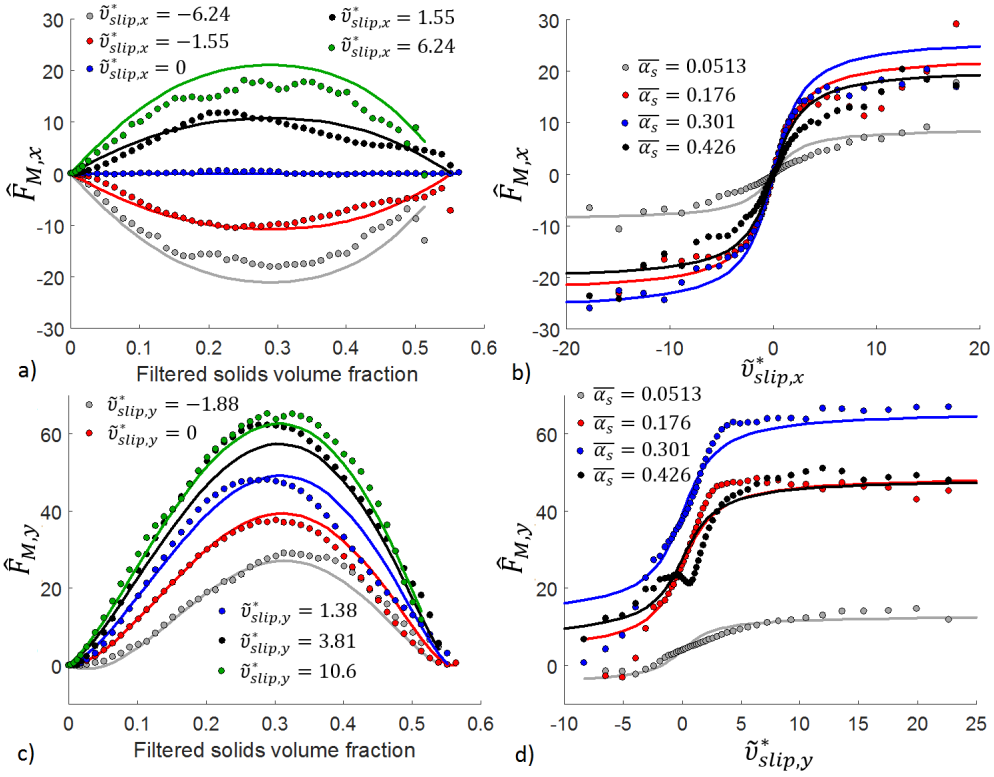

Figure 25 - The dimensionless mesoscale interphase force for the lateral (top) and vertical (bottom) directions plotted against the filtered solids volume fraction (left) and the scaled filtered slip velocity in the direction considered (right) at $\hat{\Delta}_f = 5.91$.

3.5.2 *A priori* analysis of the mesoscale interphase force closures

In this section, the performance of the anisotropic closure for the mesoscale interphase force proposed in the previous section is evaluated by comparing observed values in the resolved simulations to model predictions. To provide context for the performance of the anisotropic model, the mesoscale interface force predicted by the isotropic closure is evaluated in the same way. This is done by subtracting the force predicted by the isotropic closure for the filtered drag force (Equation 119 in Appendix F.1) from the combined filtered interphase force predicted by the isotropic closure in Chapter 3.4.1.2.

Figure 26 shows that the isotropic approach performs very poorly in predicting the mesoscale interphase force observed in the resolved simulations. The complete failure in the lateral direction can be expected, since the isotropic closure is derived only from the vertical direction data. The poor performance in the vertical direction is due to the fact that the larger filtered drag force is weighted more in the isotropic closure for the combined filtered drag and mesoscale interphase force. Since the two forces show different qualitative behaviours with respect to the markers, the isotropic closure will tend to follow the trend of the filtered drag force. This leads to a poorer performance in predicting the mesoscale interphase force individually.

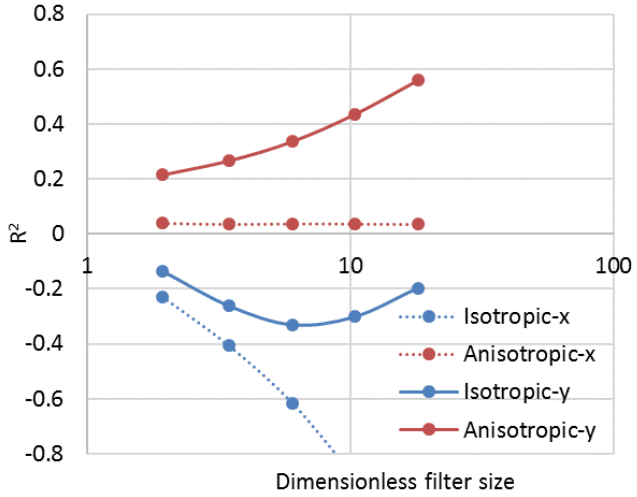

Figure 26 – The coefficient of determination as a function of the dimensionless filter size for the lateral and vertical directions and for the isotropic and anisotropic approaches for calculating the mesoscale interphase force.

A significant improvement in performance is noted for the anisotropic closure compared to the isotropic approach in a combined closure. However, the R^2 values are still substantially lower than those reported for the filtered drag force in Chapter 3.4.3. This observation seems to indicate that the filtered slip velocity may not be the optimum second marker for closing the mesoscale interphase force. Based on the excellent performance of the GPM type markers reported in Chapter 3.4.2 and Chapter 3.6.3 when closing filtered co-variance terms, such a GPM-based approach can be recommended for future studies that aim on improving mesoscale interphase force predictions. Also, it can be noted that, similar to the case of the filtered drag force, the closure performs better in the vertical direction, where, surprisingly, the R^2 value increases with increasing filter size. Again, this can be explained based on the hypothesis that the gravitational contribution to the mesoscale interphase force can be more precisely predicted. Since the gravitational contribution will become relatively more important at larger filter sizes, the overall fidelity of the prediction increases as well.

It should be noted that, although the R^2 values reported for the anisotropic model is quite low, the model still accurately predicts the mean effect of the mesoscale interphase force, as shown in Figure 25. The anisotropic closure should therefore be able to reasonably account for the effect of this force component. Also, this closure offers a clear improvement compared to the common approach in literature of closing the mesoscale interphase force in combination with the filtered drag force. Hence, it will be considered for the verification studies performed in Chapter 4, Chapter 5.1 and Chapter 5.2.

3.6 Solids mesoscale stress closures

The solids mesoscale stresses result from the sub-grid solids velocities due to mesoscale structures and increases the dispersive momentum transport in the system. These stresses have traditionally been closed based on the Boussinesq approximation [13-15, 18, 20]. This section will first evaluate the traditional Boussinesq-based approach, and then propose and evaluate an alternative, anisotropic approach. It can be noted that it has recently been suggested [20] that the solids mesoscale stresses

originate from large scale shear rates or from interfacial work (i.e., drag). The present study will, as most previous studies, focus on the shear rate contribution [13-15, 18, 20], as it appears to lead to substantially larger solids mesoscale stresses than the drag contribution [20]. Also, the present study will analyse how the shear rate contribution can be more accurately modelled. Future work will consider adding the interfacial work contribution to the anisotropic mesoscale stress closure developed in this section.

3.6.1 Isotropic closure models for the solids mesoscale stresses

In recent literature [13, 14, 20] the approach for closing the solids mesoscale stress tensor, $\bar{\bar{\Sigma}}_{s,fil}$, has been to model the mean of the components on the diagonal as an isotropic filtered solids pressure:

$$p_{s,fil} \approx \frac{1}{3} tr\left(\bar{\bar{\Sigma}}_{s,fil}\right) \qquad \text{Equation 72}$$

The deviatoric components have been modelled via a classical Boussinesq ansatz that relies on a filtered solids viscosity, $\mu_{s,fil}$. The latter has been calculated from the solids mesoscale deviatoric stress tensor, $\bar{\bar{\tau}}_{s,fil}$, as follows:

$$\mu_{s,fil} \approx \frac{\sqrt{\bar{\bar{\tau}}_{s,fil} : \bar{\bar{\tau}}_{s,fil}}}{2\overline{\alpha_s}\sqrt{\bar{\bar{S}}_{s,fil} : \bar{\bar{S}}_{s,fil}}} \qquad \text{Equation 73}$$

$$\bar{\bar{\tau}}_{s,fil} = \bar{\bar{\Sigma}}_{s,fil} - \frac{1}{3} tr\left(\bar{\bar{\Sigma}}_{s,fil}\right)\bar{\bar{I}} \qquad \text{Equation 74}$$

$$\bar{\bar{S}}_{s,fil} = \frac{1}{2}\left(\nabla\tilde{\vec{v}}_s + \nabla\tilde{\vec{v}}_s^{\,T}\right) - \frac{1}{3}\nabla\cdot\tilde{\vec{v}}_s\bar{\bar{I}} \qquad \text{Equation 75}$$

Recent studies [13, 14] have used simple Smagorinsky-type models to close the filtered solids pressure and viscosity using the dimensionless filter size, the filtered solids volume fraction and the filtered deviatoric shear rate magnitude (henceforth abbreviated as the SRM, see below for its definition) as independent variables. Since the SRM is a scalar quantity, the models presented in the current section are referred to as the isotropic solids mesoscale stress closures in the rest of the study. A more complex equation closure strategy will be used in this study compared to earlier work, adding additional coefficients and dependencies to the Smagorinsky equation form. The reasoning for this more complex form is that, in the presented 2D study, the focus is on evaluating different modelling approaches. The error associated with the fit of the model to the binned data will therefore be minimized to allow a more direct comparison of the modelling approaches. However, since the mesoscale stresses can vary over several orders of magnitude, 15 coefficients are necessary to establish a good fit over all filter sizes and flow conditions. It should however be noted that reasonably good closure model fits (i.e., with $R^2 > 0.95$) can still be obtained with comparably simple functional forms (e.g., using six coefficients). The equations proposed below could therefore be modified at a later stage to simpler, more user-friendly forms for specific applications, for example when only a certain range of filter sizes needs to be considered, as demonstrated for the anisotropic solids mesoscale stress closure in the next section.

When using the SRM, defined as $\|S_{s,fil}\| = \sqrt{2\bar{\bar{S}}_{s,fil} : \bar{\bar{S}}_{s,fil}}$, as the second marker, a poor distribution of samples in the parameter space occurs. This is since $\|S_{s,fil}\|$ tends to decrease with increasing filter size and increasing filtered solids volume fraction. The physical reason for this behaviour is that (i) the domain-averages shear (i.e., that at very large filter size) is zero due to the periodic setup, and (ii) velocity fluctuations will be dampened more quickly in dense suspensions. Consequently, to obtain a more even distribution of samples, and therefore also a better model fit, $\|S_{s,fil}\|$ is scaled in a similar manner as done by Milioli [14] for the binning procedure:

$$\|S^*_{s,fil}\| = \frac{\|\hat{S}_{s,fil}\|}{a\overline{\alpha_s}^b \hat{\Delta}_f{}^c} \qquad \text{Equation 76}$$

Here the SRM is non-dimensionalized via $\|\hat{S}_{s,fil}\| = \|S_{s,fil}\| \frac{v_t}{g}$. In this study, the following values were found for the coefficients: $a = 1.056$, $b = -0.208$ and $c = -0.580$.

The following functional form is used to model the mesoscale stresses in this section:

$$\hat{\tau}_{s,fil} = \frac{2}{\pi} x_1 \overline{\alpha_s}^{x_2} \operatorname{atan}\left(x_3 {\Delta_f^*}^{x_4} \|\hat{S}_{s,fil}\|^{x_5} \max(x_6 - \overline{\alpha_s}, 0)\right) {\Delta_f^*}^{x_7} \|\hat{S}_{s,fil}\|^{x_8 + x_9 {\Delta_f^*}^{x_{10}}} + \frac{2}{\pi} x_{11} \overline{\alpha_s}^{x_{12}} \operatorname{atan}(x_{13} \max(x_{14} - \overline{\alpha_s}, 0)) {\Delta_f^*}^{x_{15}} \qquad \text{Equation 77}$$

, where $\hat{\tau}_{s,fil} = \frac{\tau_{s,fil}}{\rho_s v_t^2}$. The definition of the scaled filter size, $\Delta_f^* = 0.1285$, is discussed in Chapter 3.3.3.

The form of Equation 77 is based on the Smagorinsky-type models previously used in the fTFM literature [13-15], but with the following modifications: The mesoscale stresses tend to increase with increasing solids volume fraction, until they start to decrease above a critical volume fraction. The arctangent function captures this effect, which is found to be a function of the filter size and $\|\hat{S}_{s,fil}\|$. This volume fraction dependency is different from that reported by the Princeton group [13, 14], where the mesoscale stresses continue to increase with increasing solids volume fraction in dense regions. However, from a physical understanding it is expected that, in very dense regions, the solids velocity distribution would become more uniform, leading to a reduction in solids velocity fluctuations. Since mesoscale stresses decrease with decreasing velocity fluctuations by definition, mesoscale stresses must approach zero in the limit of high solids volume fractions. It was previously found that the reduction in the mesoscale stresses with increasing solids volume fractions starts at lower solids volume fractions when the effect of frictional pressure is included in the resolved simulations, as discussed in Appendix B. Therefore, it is expected that this effect will be more important in the present study compared to the work of the Princeton group, since frictional stresses were not considered in the latter.

The filter size dependency is obtained by using the scaled dimensionless filter size, Δ_f^*, which will ensure zero solids mesoscale stresses if the model is applied at the same grid size as used in the resolved simulations. Furthermore, it was found that the model fit could be significantly improved by making the exponent to which $\|\hat{S}_{s,fil}\|$ is raised a function of the filter size. Lastly, the second term in Equation 77 (with different coefficients for the volume fraction and filter size dependencies) is included since, similarly to Schneiderbauer [20], non-zero solids mesoscale stresses were observed at zero

values of $\|\hat{S}_{s,fil}\|$ in the present simulations. The physical reason for this observation is that, even in the absence of mean shear, mesoscale velocity fluctuations in sedimenting gas-particle suspensions persist due to the well-known instability mechanism [54, 55]. Hence, a no-shear mesoscale stress limit must be considered when closing fTFMs for sedimenting suspensions.

More information regarding the model fit for the filtered solids pressure and filtered solids viscosity is presented in Appendix F.2.1 and Appendix F.2.2. This is since, in most aspects, these models are similar to that reported previously in the literature [13-15].

Apart from models for the isotropic filtered solids pressure and the filtered solids viscosity, an anisotropic model was also established for the individual diagonal components of the solids mesoscale stress tensor (i.e., the normal stresses) by setting $p_{fil,s,x} \approx \rho_s\overline{\alpha_s u_s'' u_s''}$ and $p_{fil,s,y} \approx \rho_s\overline{\alpha_s v_s'' v_s''}$. This is similar to the ideas recently published by Sarkar et al. [13]. As shown by the latter authors, it was also found that the model is largely similar in shape to the isotropic filtered solids pressure model, except that the mesoscale stresses aligned with gravity ($\rho_s\overline{\alpha_s v_s'' v_s''}$) tend to be greater in magnitude. These anisotropic normal stress models will be used in the subsequent analysis. Therefore, the coefficients for the corresponding closure models are also included in Appendix F.2.3 and Appendix F.2.4.

3.6.2 *A priori* analysis of the isotropic solids mesoscale stress closures

The closure models using the SRM as a marker will be evaluated next. First, consider the Boussinesq ansatz:

$$\rho_s\overline{\alpha_s v_{s,i}'' v_{s,j}''} \approx p_{s,fil}\delta_{ij} - \overline{\alpha_s}\mu_{s,fil}\left(\frac{\partial\widetilde{v_i}}{\partial x_j} + \frac{\partial\widetilde{v_j}}{\partial x_i} - \frac{2}{3}\frac{\partial\widetilde{v_k}}{\partial x_k}\delta_{ij}\right) \quad \text{Equation 78}$$

Here, $\partial\widetilde{u_k}/\partial x_k$ implies the sum of the terms on the diagonal of the strain rate tensor. From this, it follows that the individual components of the solids mesoscale stress tensor are modelled as:

$$\rho_s\overline{\alpha_s u_s'' u_s''} \approx p_{s,fil} - \overline{\alpha_s}\mu_{s,fil}\left(\frac{4}{3}\frac{\partial\tilde{u}_s}{\partial x} - \frac{2}{3}\frac{\partial\tilde{v}_s}{\partial y}\right) \quad \text{Equation 79}$$

$$\rho_s\overline{\alpha_s v_s'' v_s''} \approx p_{s,fil} - \overline{\alpha_s}\mu_{s,fil}\left(\frac{4}{3}\frac{\partial\tilde{v}_s}{\partial y} - \frac{2}{3}\frac{\partial\tilde{u}_s}{\partial x}\right) \quad \text{Equation 80}$$

$$\rho_s\overline{\alpha_s u_s'' v_s''} = \rho_s\overline{\alpha_s v_s'' u_s''} \approx -\overline{\alpha_s}\mu_{s,fil}\left(\frac{\partial\tilde{u}_s}{\partial y} + \frac{\partial\tilde{v}_s}{\partial x}\right) \quad \text{Equation 81}$$

From these definitions, and by considering the filtered solids momentum equations in Equation 16 and Equation 17, it can be deduced that the forces due to the solids mesoscale stresses are modelled as follows in the *x*- and *y*-directions, respectively:

$$\frac{\partial(\rho_s\overline{\alpha_s u_s'' u_s''})}{\partial x} + \frac{\partial(\rho_s\overline{\alpha_s u_s'' v_s''})}{\partial y} \approx \frac{\partial p_{s,fil}}{\partial x} - \frac{\partial\left(\overline{\alpha_s}\mu_{s,fil}\left(\frac{4}{3}\frac{\partial\tilde{u}_s}{\partial x} - \frac{2}{3}\frac{\partial\tilde{v}_s}{\partial y}\right)\right)}{\partial x} - \frac{\partial\left(\overline{\alpha_s}\mu_{s,fil}\left(\frac{\partial\tilde{u}_s}{\partial y} + \frac{\partial\tilde{v}_s}{\partial x}\right)\right)}{\partial y} \quad \text{Equation 82}$$

$$\frac{\partial(\rho_s\overline{\alpha_s v_s'' v_s''})}{\partial y}+\frac{\partial(\rho_s\overline{\alpha_s u_s'' v_s''})}{\partial x}$$
$$\approx \frac{\partial p_{s,fil}}{\partial y}-\frac{\partial\left(\overline{\alpha_s}\mu_{s,fil}\left(\frac{4}{3}\frac{\partial \tilde{v}_s}{\partial y}-\frac{2}{3}\frac{\partial \tilde{u}_s}{\partial x}\right)\right)}{\partial y}-\frac{\partial\left(\overline{\alpha_s}\mu_{s,fil}\left(\frac{\partial \tilde{u}_s}{\partial y}+\frac{\partial \tilde{v}_s}{\partial x}\right)\right)}{\partial x} \quad \text{Equation 83}$$

Based on Equation 79 to Equation 83, several comparisons between the resolved simulation results and the model predictions can be made to evaluate the performance of the modelling approach using the SRM as the second marker. A summary of these comparisons is presented in Figure 27 in the form of R^2 values (calculated according to the procedure outlined in Chapter 3.2) as a function of the filter size. It should be noted that the R^2 values in Figure 27 represent the correlation of model predictions to individual samples from the resolved TFM data, and not to the conditionally-averaged (i.e., binned) data that was used to establish the closure models.

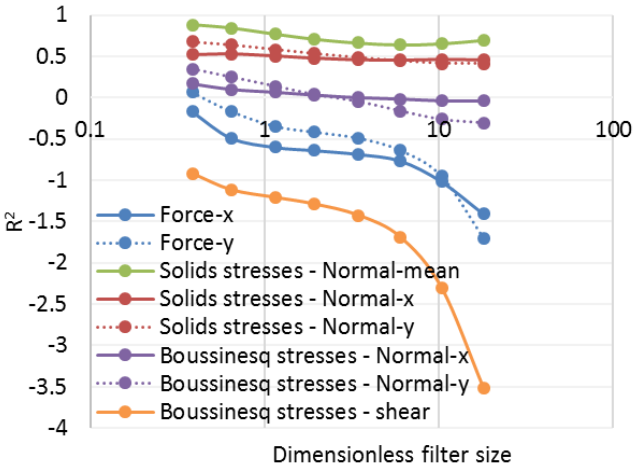

Figure 27 - R^2 values as a function of the dimensionless filter size when comparing model predictions with the SRM as marker to observed values for various quantities relevant to the solids mesoscale stresses.

Firstly, the accuracy of modelling the volumetric force due to the solids mesoscale stresses in both momentum equations is evaluated (therefore, the left- and right-hand sides obtained from Equation 82 and Equation 83 are considered). This comparison is given by the blue lines in Figure 27 and clearly shows that the current approach performs poorly at predicting the forces resulting from the solids mesoscale stresses. At small filter sizes, the model only achieves $R^2 \approx 0$ and the performance deteriorates at large filter sizes (i.e., R^2 decreases with increasing filter size, and may reach large negative values). It is therefore clear that this modelling approach performs poorly when predicting the sub-grid effects due to the solids mesoscale stresses and that further investigation is required to determine the cause of this poor performance.

In the next two steps, the performance of models for the normal solids mesoscale stresses are evaluated when using the filtered deviatoric shear rate magnitude as the second marker. Firstly, isotropic normal mesoscale stresses are assumed and the mean normal stresses are compared. This means that $\frac{1}{3}(\rho_s\overline{\alpha_s u_s'' u_s''}+\rho_s\overline{\alpha_s v_s'' v_s''})$ is compared to the model prediction for $p_{s,fil}$, calculated

using Equation 77 and the coefficients given in Appendix F.2.1. From the green line in Figure 27, it can be seen that an average R^2 of roughly 0.73 is obtained, indicating a good representation of the sample data by the closure model. This means that this approach performs very well in predicting the mean normal solids mesoscale stresses.

However, models were also derived for the individual normal components of the solids mesoscale stresses (i.e., $\rho_s\overline{\alpha_s u_s'' u_s''}$ and $\rho_s\overline{\alpha_s v_s'' v_s''}$) using the SRM as the marker (coefficients used in Equation 77 for these models are given in Appendix F.2.3 and Appendix F.2.4). When comparing the corresponding closure model predictions to the solids mesoscale stresses observed in the resolved TFM simulations, a significantly lower, although still reasonable, average R^2 of 0.50 is obtained. This is shown by the red lines in Figure 27.

An explanation for the poorer performance when comparing to individual normal stress components can be obtained by evaluating the correlation between values of $\rho_s\overline{\alpha_s u_s'' u_s''}$ and $\rho_s\overline{\alpha_s v_s'' v_s''}$. This was done for a large number of samples, and the result is shown in Figure 28. From this comparison, it is clear that there is a very poor correlation between $\rho_s\overline{\alpha_s u_s'' u_s''}$ and $\rho_s\overline{\alpha_s v_s'' v_s''}$. Therefore, the assumption of isotropic mesoscale fluctuations is clearly incorrect. Subsequently, this means that the accuracy of closure models employing the filtered deviatoric shear rate magnitude as a marker will be limited, since the SRM is a scalar quantity and can therefore not accurately capture the differences in the normal stress components.

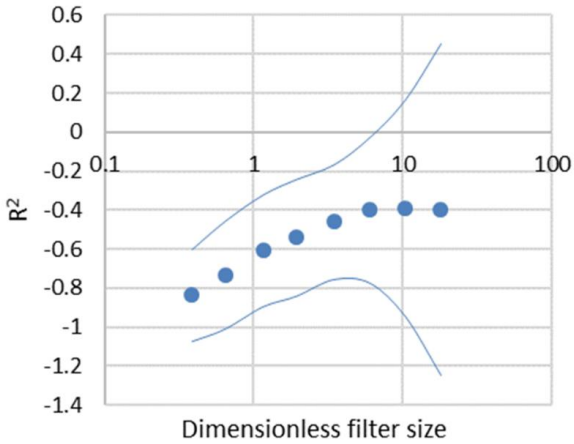

Figure 28 - Coefficients of determination as a function of the dimensionless filter size when evaluating the correlation between the two diagonal components of the solids mesoscale stresses. The symbols show the mean values and the lines the 95% confidence interval.

Furthermore, it can be seen that the fluctuations tend to become more isotropic (i.e., the correlation coefficient R^2 increases) as the filter size is increased. This is expected since a larger number of the mesoscale structures (i.e., clusters and bubbles) will be smaller than the averaging volume for large filter sizes, leading to more isotropic behaviour. Clearly, extremely large filter sizes would have to be considered for the mesoscale fluctuations to become truly isotropic. Also, the data shown in Figure 28 suggests that the increase in R^2 values with increasing filter size halts at large filter sizes. Thus, such an asymptotic isotropic behaviour may even not exist. However, this flattening trend is uncertain due to rapidly widening 95% confidence bounds of the data set.

Another perspective is offered in Figure 29 where plots of $\rho_s\overline{\alpha_s u_s'' u_s''}$ against $\rho_s\overline{\alpha_s v_s'' v_s''}$ are presented at different filter sizes for samples randomly selected over all flow conditions. It is immediately clear that no correlation (and hence no isotropy) exists at small filter sizes, but some correlation starts to become visible at the largest filter size.

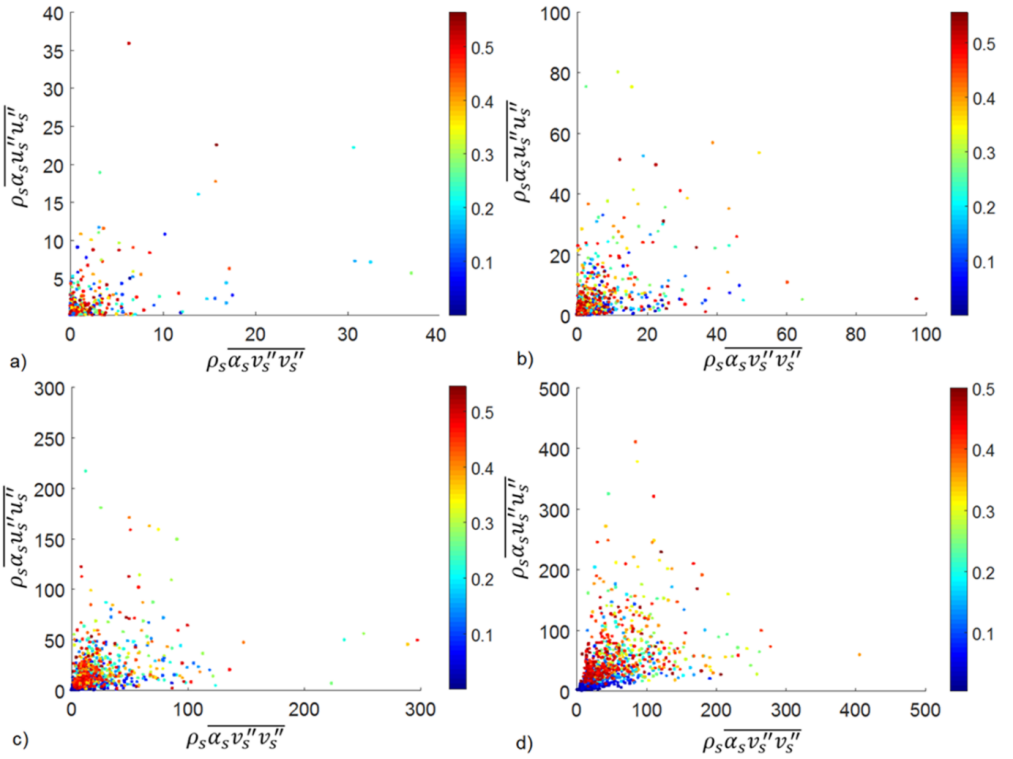

Figure 29 - Plots of $\rho_s\overline{\alpha_s v_s'' v_s''}$ against $\rho_s\overline{\alpha_s u_s'' u_s''}$ for dimensionless filter sizes of a) 0.643, b) 1.93, c) 6.04 and d) 18.1. The colour key shows different values of the filtered solids volume fraction.

However, even though the isotropic SRM marker is clearly not ideal for predicting the observed anisotropy of the normal mesoscale stresses, the R^2 values for these stresses remain reasonable in both the lateral and vertical directions (see Figure 27). Another reason will therefore have to be found for the poor predictions of the total forces resulting from the solids mesoscale stresses.

Next, the performance of the Boussinesq approximation is evaluated, firstly by looking at the normal stresses. Thus, the left- and right-hand sides are compared for each component of the normal stress approximation, i.e., that of Equation 79 and Equation 80. The purple lines in Figure 27 show that, when the normal components of the mesoscale solids stresses are modelled by the Boussinesq approximation, there is a large decrease in the R^2 values (to an average value of approximately 0.02) compared to when these stresses are modelled directly, as done in the previous two steps. Applying the Boussinesq approximation for modelling the normal mesoscale solids stresses therefore clearly worsens the comparison of closure model predictions with observed values.

Finally, the performance of the closure model for the mesoscale shear stresses can be evaluated by comparing the left and the right-hand sides of Equation 81. From the orange line in Figure 27, it can be

seen that that R^2 values of less than zero are obtained in this comparison for all filter sizes, with large negative R^2 values at large filter sizes. If the approach of modelling the off-diagonal mesoscale stress components with the Boussinesq ansatz would be correct, at least some of the variance in the sample values of $\rho_s\overline{\alpha_s u_s{}'' \mathrm{v}_s''}$ would be explained by $-\overline{\alpha_s}\mu_{s,fil}\left(\frac{\partial \widetilde{u_s}}{\partial y}+\frac{\partial \widetilde{v_s}}{\partial x}\right)$. Clearly, this is not the case since R^2 can become as low as -3.51 (see Figure 27).

The challenge of modelling $\rho_s\overline{\alpha_s u_s{}'' \mathrm{v}_s''}$ lies therein that the off-diagonal component of the solids mesoscale stress tensor, unlike the diagonal components, can assume both positive and negative values. By using the viscosity analogy, one thereby assumes a linear dependency between $\rho_s\overline{\alpha_s u_s{}'' \mathrm{v}_s''}$ and $-\left(\frac{\partial \widetilde{u_s}}{\partial y}+\frac{\partial \widetilde{v_s}}{\partial x}\right)$. However, from Figure 30 it is evident that no such trend exists.

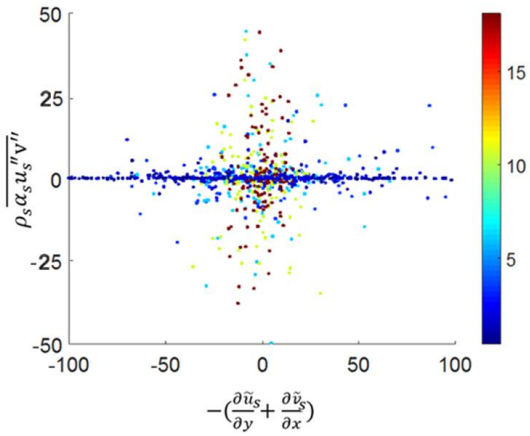

Figure 30 – A Plot of $\rho_s\overline{\alpha_s u_s{}'' v_s''}$ against $-(\frac{\partial \widetilde{u_s}}{\partial y}+\frac{\partial \widetilde{v_s}}{\partial x})$. The colour map shows different dimensionless filter sizes.

From the results presented in this section, it is therefore evident that a new method should be formulated for modelling the off-diagonal component of the mesoscale stresses $\left(\rho_s\overline{\alpha_s u_s{}'' \mathrm{v}_s''}\right)$. Also, it was shown that there is room for improvement when modelling the anisotropic normal mesoscale stresses, i.e., $\rho_s\overline{\alpha_s u_s{}'' u_s{}''}$ and $\rho_s\overline{\alpha_s v_s{}'' v_s{}''}$. These topics will be addressed in the following section.

3.6.3 Anisotropic closure model for the solids mesoscale stresses

By rigorously screening potential markers to correlate the mesoscale stresses with, it was found that, in general, a filtered variance quantity in the form of $\overline{\alpha X'' Y''}$ can be modelled by a marker of the form $\bar{\alpha}\left(\frac{d\hat{X}}{dx}\frac{d\hat{Y}}{dx}+\frac{d\hat{X}}{dy}\frac{d\hat{Y}}{dy}\right)$. In what follows, the latter is called the gradient product marker (GPM). Most importantly, it will be shown below that the GPM appears to correlate well with all solids mesoscale stress components. Therefore, each component of the solids mesoscale stress tensor can be modelled as:

$$\hat{\Sigma}_{s,fil,ij}=f\left(\hat{\Delta}_f,\overline{\alpha_s},\widehat{M}_{ij}\right) \qquad \text{Equation 84}$$

, where:

$$M_{xx} = \overline{\alpha_s}\left(\left(\frac{d\widetilde{u_s}}{dx}\right)^2 + \left(\frac{d\widetilde{u_s}}{dy}\right)^2\right) \quad \text{Equation 85}$$

$$M_{xy} = \overline{\alpha_s}\left(\frac{d\widetilde{u_s}}{dx}\frac{d\widetilde{v_s}}{dx} + \frac{d\widetilde{u_s}}{dy}\frac{d\widetilde{v_s}}{dy}\right) \quad \text{Equation 86}$$

$$M_{yy} = \overline{\alpha_s}\left(\left(\frac{d\widetilde{v_s}}{dx}\right)^2 + \left(\frac{d\widetilde{v_s}}{dy}\right)^2\right) \quad \text{Equation 87}$$

and the GPM is non-dimensionalized using $\widehat{\mathrm{M}}_{ij} = \mathrm{M}_{ij} v_t^2/g^2$.

Figure 31 qualitatively illustrates that there is a good correlation between the individual components of the mesoscale stresses and their respective GPMs for an intermediate domain-averaged volume fraction and filter size. This correlation is strong even without considering an additional marker, e.g., the filtered solids volume fraction (included in panel a) in Figure 31). Also, it is clear from Figure 31 that large values for the two different normal stresses appear in different regions, again emphasising the need for different markers for the individual stress components.

The good performance of the GPM rests on the fact that, in one-dimensional space, the quantity $\overline{X'Y'}$ can be exactly described as $k\frac{d\bar{X}}{dx}\frac{d\bar{Y}}{dx}$ if both variables vary linearly inside the averaging region. In this case X' and Y' are the differences from the algebraic averages of X and Y and k is a proportionality factor. In the case of such a linear variation $k = \frac{dx^2}{12}(n+1)(n-1)$, where dx is the cell size and n is the number of cells in the averaging region. It was also found that when phase-weighted variables are considered, as in the case of the solids mesoscale stresses, $k\bar{\alpha}\frac{d\tilde{X}}{dx}\frac{d\tilde{Y}}{dx}$ is a very good approximation of $\overline{\alpha X''Y''}$, where X'' and Y'' are the fluctuations of the quantities X and Y around their Favre averages. Naturally, this approximation will degrade in situations where the quantities of interest do not vary linearly inside the averaging region. Hence, it may be expected that this approximation will perform better for small filter sizes (i.e., in situations where the averaging region is smaller than the typical mesoscale structures), and will gradually worsen as the filter size is increased.

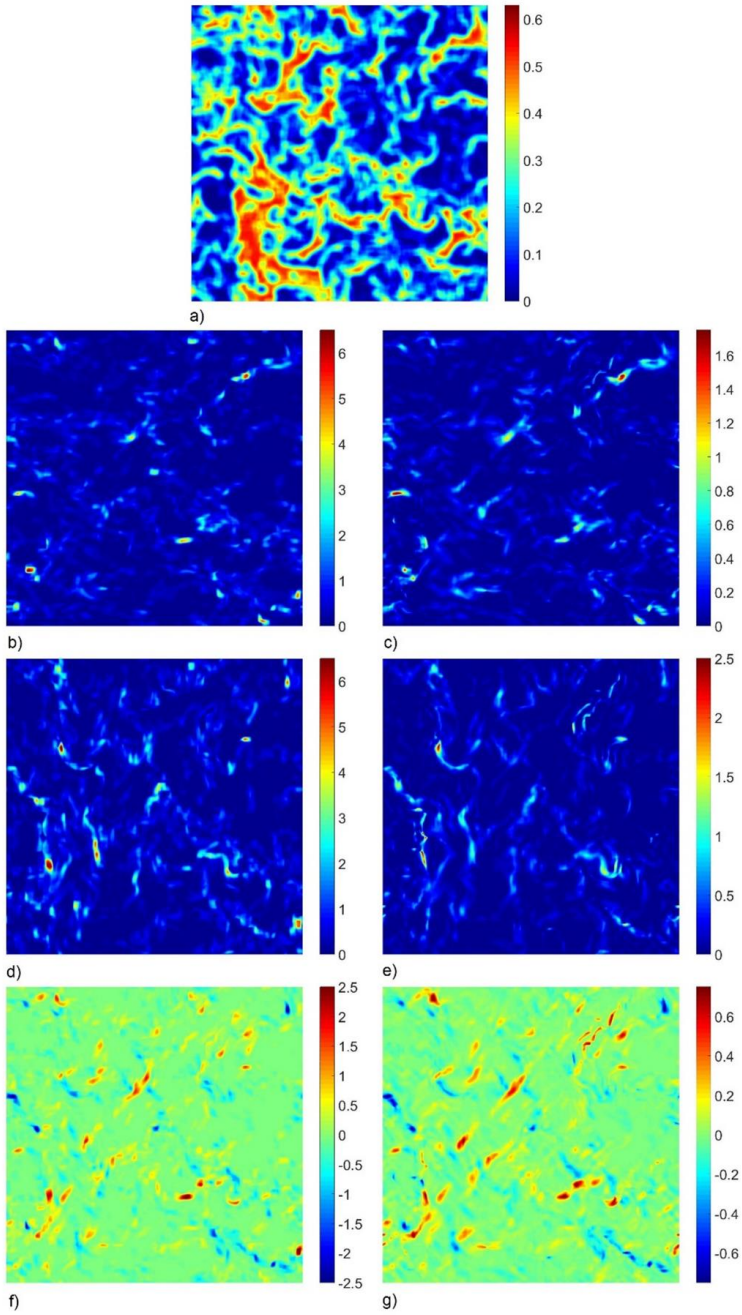

Figure 31 - A comparison of the solids mesoscale stress components to their respective GPMs for a domain-averaged solids volume fraction of 0.2 and a dimensionless filter size of 3.47. In general, the dimensionless stresses are shown on the left and the corresponding dimensionless GPM on the right. Specifically, plots are shown for a) the filtered solids volume fraction, b) $\widehat{\Sigma}_{s,fil,xx}$, c) $\widehat{M}_{xx}$, d) $\widehat{\Sigma}_{s,fil,yy}$, e) $\widehat{M}_{yy}$, f) $\widehat{\Sigma}_{s,fil,xy}$ and g) $\widehat{M}_{xy}$.

Similar to the SRM, the GPM rapidly decreases with filter size, leading to a poor distribution of the samples in the bins. For this reason, the GPM is scaled for the binning process as follows:

$$M_{ij}^{*} = \frac{\widehat{M}_{ij}}{a\hat{\Delta}_f^{(b+c\hat{\Delta}_f)}} \qquad \text{Equation 88}$$

The following values were obtained for the coefficients. For M_{xx}^{*}: $a = 0.291$, $b = -1.11$ and $c = -0.0117$. For M_{xy}^{*}: $a = 0.177$, $b = -1.16$ and $c = -0.0154$. For M_{yy}^{*}: $a = 0.362$, $b = -1.12$ and $c = -0.0163$.

From an analysis of the binned data it was found that the following general expression can be used to model the individual components of the solids mesoscale stress tensor:

$$\begin{aligned}\hat{\Sigma}_{s,fil,ij} = {} & sign(\widehat{M}_{ij})\left(\frac{2}{\pi}\right)^2 x_1 \operatorname{atan}\left(x_2 {\Delta_f^{*}}^{x_3} {\widehat{M}_{ij}}^{x_4}(\overline{\alpha_s} + x_5)\right) \\ & \times \operatorname{atan}\left(x_6 {\Delta_f^{*}}^{x_7} {\widehat{M}_{ij}}^{x_8} \max(x_9 - \overline{\alpha_s}, 0)\right) {\Delta_f^{*}}^{x_{10}} {\widehat{M}_{ij}}^{x_{11}+x_{12}{\Delta_f^{*}}^{x_{13}}} \\ & + D\left(\frac{2}{\pi}\right)^2 x_{14} \operatorname{atan}(x_{15}\overline{\alpha_s}) \operatorname{atan}(x_{16} \max(x_{17} - \overline{\alpha_s}, 0))\, {\Delta_f^{*}}^{x_{18}}\end{aligned} \qquad \text{Equation 89}$$

Apart from using the GPM as the second marker, the shape of the equation is similar to that of Equation 77. This is because, similarly to the shear rate magnitude-based closure models, the mesoscale stresses tend to increase with increasing values of the GPM and reach a maximum at an intermediate filtered solids volume fraction. However, a change in the volume fraction dependency is introduced. It was found that the reduction of the mesoscale stresses towards low solids volume fractions could be better captured by using an arctangent function. Similar to the arctangent that causes the reduction in the mesoscale stresses at very high volume fractions, the rate of the reduction in the stress with changing volume fraction is a function of the filter size and the value of the GPM.

It should be noted that the stress does not become zero when the filtered solids volume fraction tends to zero, as can be noted from the binned data shown in Figure 33. To include this effect, the coefficient x_5 is added to the filtered solids volume fraction within the arctangent used in Equation 89. It should be noted that, despite this addition, the physical limit of zero mesoscale solids stresses at a filtered solids volume fraction of zero is still obeyed. Specifically, if the filtered solids volume fraction is zero, the second term in Equation 89 will vanish. Furthermore, since the filtered solids volume fraction is zero, the GPM will also have a zero value, resulting in the first term in Equation 89 also vanishing. As a result, the correct limit for dilute flows is obeyed in the developed closure model.

It should be noted that, as for the isotropic model presented in Chapter 3.6.1, the complex form of Equation 89 with many coefficients is used to minimize the error in the model fit, allowing a clear comparison of the two modelling approaches investigated for the solids mesoscale stresses. However, to demonstrate that a simpler closure could also accurately predict the solids mesoscale stresses, an anisotropic closure using fewer coefficients than the one discussed in this section is presented in Appendix F.2.5. The relative performance of these two closure models will be assessed in the next section.

A benefit of using the GPM as the second marker was identified when analysing the binned results: separate models were not necessary for the different components of the solids mesoscale stresses as

long as the GPM is calculated using appropriate gradients (as shown in Equation 85 to Equation 87) and $D = 1$ for the normal components and $D = 0$ for the off-diagonal components of the solids mesoscale stress tensor. Therefore, the normal solids mesoscale stresses contain an additional contribution that is independent of the GPM that is not present in the shear components (second term in Equation 89). This contribution is due to other sources of the solids mesoscale stresses than the solids velocity gradients, for example the interfacial work as discussed by Schneiderbauer [20], that is not accounted for in the present model. It can be noted that the additional contribution is likely also present in the shear mesoscale stresses, but negative values and positive values tend to cancel each other around GPM values of zero, causing the mean shear mesoscale stresses to be zero at zero GPMs, as seen later in Figure 33.

Based on the finding above, a single model was therefore fitted to the binned data for all components of the solids mesoscale stress tensor. This resulted in a fit with $R^2 = 0.989$ using the following coefficient values: $x_1 = 0.542$, $x_2 = 2.53$, $x_3 = 0.102$, $x_4 = -0.460$, $x_5 = 0.0400$, $x_6 = 3.66$, $x_7 = 0.876$, $x_8 = 0.213$, $x_9 = 0.685$, $x_{10} = 1.75$, $x_{11} = 0.80$, $x_{12} = 0.593$, $x_{13} = -0.218$, $x_{14} = 56.0$, $x_{15} = 2.61$, $x_{16} = 0.00743$, $x_{17} = 0.601$ and $x_{18} = 1.03$. It can be noted that, in the first term of Equation 89, the exponent of the filter size factor (x_{10}) is 1.75, which is slightly lower than the exponents of around 2 that has been reported in literature [13-15, 20] for the SRM-based filtered solids pressure closures. The exponent of the GPM factor ($x_{11} + x_{12}\Delta_f^{*\,x_{13}}$) ranges from 1.60 at the smallest filter size and 1.12 at the largest filter size considered in this study. Noting that the GPM is comparable to the SRM squared, the GPM exponent is therefore only slightly larger than the SRM exponents of around 2 reported in literature [13-15] at the larger filter sizes considered. An example of the model fit is given for the vertical direction normal solids mesoscale stresses in Figure 32 and for the absolute value of the shear solids mesoscale stresses in Figure 33.

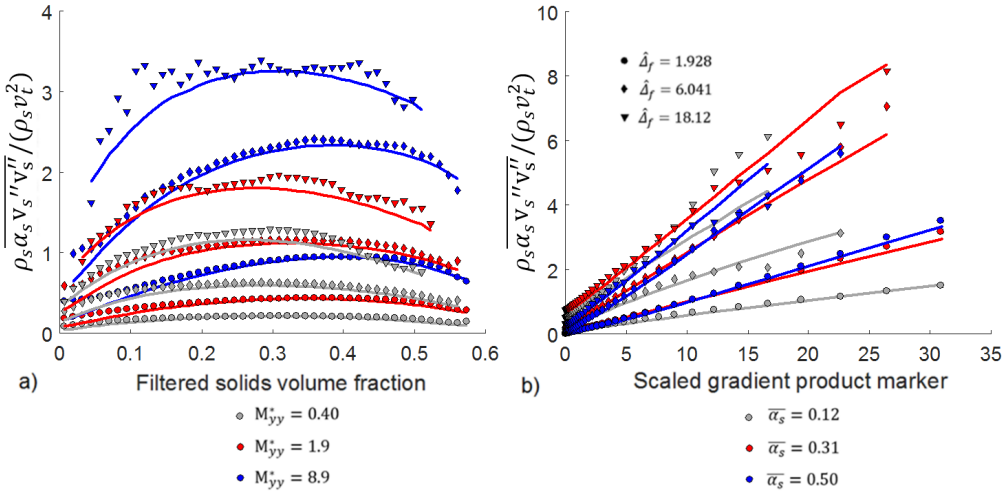

Figure 32 - Comparison of the binned data (symbols) to the model fit (lines) for the dimensionless y-direction diagonal component of the solids mesoscale stress as a function of a) the filtered solids volume fraction and b) the scaled gradient product marker.

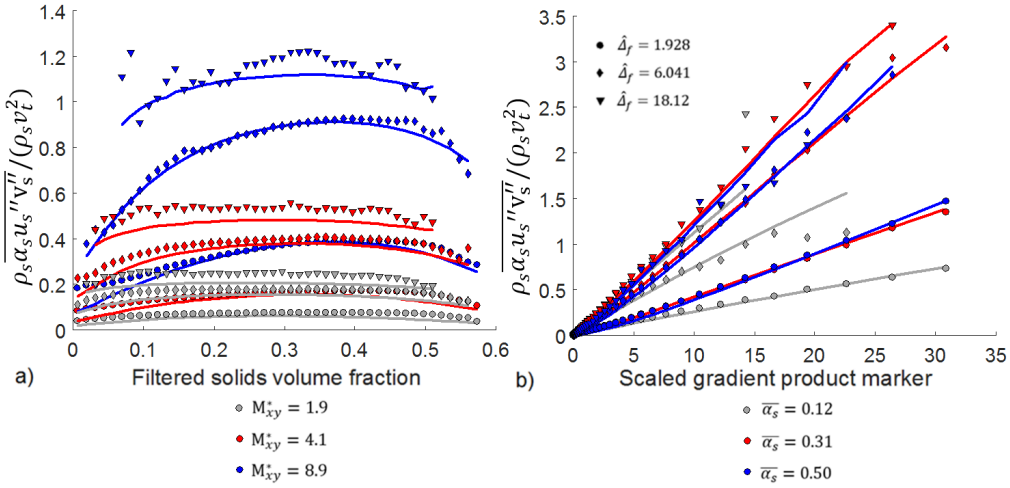

Figure 33 - Comparison of the binned data (symbols) to the model fit (lines) for the dimensionless off-diagonal component of the solids mesoscale stress as a function of a) the filtered solids volume fraction and b) the scaled gradient product marker.

As can be seen from the binned data in Figure 32 and Figure 33, the proposed closure model is able to accurately capture the general trends in the data, as well as the difference in the normal and the shear components by setting the second term in Equation 89 to zero when predicting the shear solids mesoscale stresses. It should be noted that although only the data for positive shear GPMs are shown in Figure 33, if the GPM had a negative sign, the stress would be equal in magnitude, but also take on a negative sign. For this reason, the first term in Equation 89 is multiplied by the sign of the GPM. Since, from the definitions in Equation 85 and Equation 87, the normal GPMs are always positive, the predicted normal solids mesoscale stresses will also always be positive, as observed in the binned data.

3.6.4 *A priori* analysis of the anisotropic solids mesoscale stress closure

Using the proposed anisotropic solids mesoscale stress closure, a similar comparison as in Chapter 3.6.1 can be performed for the closure model predictions and the observations in the resolved TFM simulation data. Similar comparisons to that in Figure 27 are made in Figure 34, except that the comparison of the average of the normal mesoscale stresses to the model predictions is excluded. This is because the earlier results showed that the normal fluctuations are highly anisotropic, therefore evaluating the performance of the model in predicting the average of the normal stresses is meaningless since these normal stresses are evaluated in different momentum equations. From inspecting the R^2 values summarized in Figure 34 for the prediction of the volumetric force due to the solids mesoscale stresses (blue lines), it is clear that the model using the anisotropic GPM compares substantially better to the sample data from resolved simulations than the model using the isotropic SRM as marker that was presented previously. Over all filter sizes, the GPM model shows good performance with an average R^2 of 0.620. A still reasonable minimal value of R^2 (i.e., 0.47) for the vertical direction force at the largest filter size further illustrates the robustness of the GPM-based closure model.

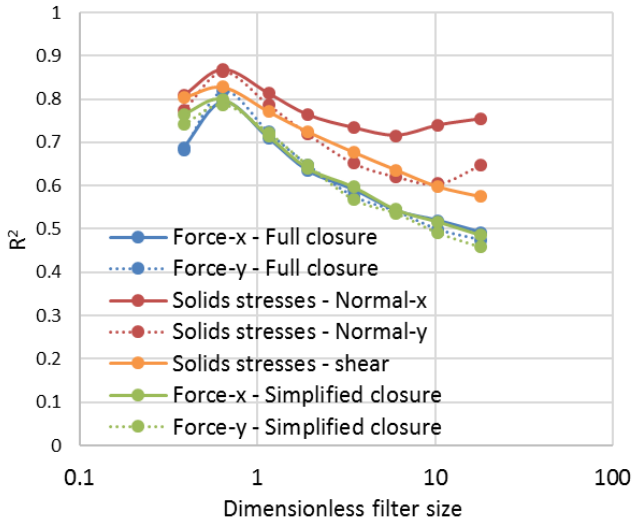

Figure 34 - R^2 values as a function of the dimensionless filter size when comparing model predictions with the anisotropic GPM as marker to observed values for various components of the solids mesoscale stress tensor.

The average R^2 for the normal solids mesoscale stresses (red lines in Figure 34) is 0.74, which is a significant improvement over the value of 0.50 that was obtained when using the isotropic SRM as marker to model the individual components of the normal mesoscale solids stresses. It is therefore clear that, by accounting for the anisotropy of the normal components of the solids mesoscale stresses by using an anisotropic marker, substantially more of the variance in the resolved simulation data can be explained. However, it is in the prediction of the shear mesoscale stress (orange line in Figure 34) that the largest improvement is made. Whereas the solids viscosity approach detailed in Chapter 3.6.1 failed in predicting $\rho_s\overline{\alpha_s u_s'' v_s''}$ correctly, the closure model predictions for the solids mesoscale shear stress component based on the GPM are much more reasonable. Specifically, a similar accuracy (average $R^2 = 0.70$) to that observed for the normal components can be demonstrated. Again, this is because there is a clear correlation between $\rho_s\overline{\alpha_s u_s'' v_s''}$ and the GPM, which can also adequately predict the sign of $\rho_s\overline{\alpha_s u_s'' v_s''}$. An example of this correlation is provided for the largest filter size (i.e., the most challenging situation) in Figure 35.

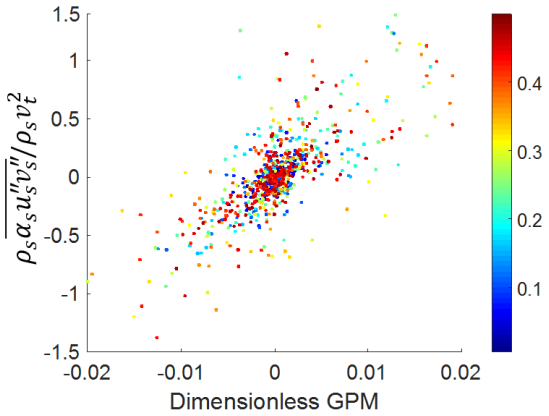

Figure 35 - The dimensionless off-diagonal solids mesoscale stress plotted against the dimensionless gradient product marker. The colour key shows the filtered solids volume fraction.

From Figure 34, it can be noted that there is a general decrease in the model performance as the filter size is increased. As explained earlier, this is because the GPM marker works best in predicting the velocity fluctuations when the gradient inside the filtered region is relatively uniform. However, as the filter size increases, some of the structures (bubbles and clusters) will become smaller than the averaging region. This means that the mean gradient over the filter can deviate substantially from the gradient at specific regions within the filter, leading to a poorer performance of the GPM. Future work can potentially look at markers that can improve the model performance at large filter sizes, although the proposed model already represents a large improvement over the current state of the art.

It can be noted that the sudden deviation from the trend of better model performance at smaller filter sizes at the smallest filter size is simply because the model fit to the binned data becomes relatively poorer at small filter sizes, when the stresses also become small. Despite this, the model fit over the large spectrum of filter sizes appears acceptable. It is expected that, in general, the ability of GPM-based models to predict the solids mesoscale stresses will improve as the filter size becomes smaller, therefore very accurate models could be derived specifically for small filter sizes.

As mentioned earlier, a simplified version of the anisotropic solids mesoscale stress closure was also derived, only considering $\hat{\Delta}_f \geq 1.93$ for the model fit and reducing the number of coefficients from 18 to 11. This closure model is given in Appendix F.2.5. From Figure 34, it can be seen that the simplified closure model (green lines) predicts the forces resulting from the solids mesoscale stresses to a similar accuracy as the more elaborate closure model for the larger filter sizes (i.e., those used in the derivation of the simplified closure model). At the second smallest filter size considered, the simplified closure model performs slightly poorer. However, surprisingly, the simplified closure model performs better at the smallest filter sizes. Therefore, it appears that by using the scaled filter size in the closure model, the closure model can be accurately extrapolated to the limit of having the filter size equal to the grid size in the resolved simulations. Based on this excellent performance of the simplified closure model, it can be argued that, if necessary, the closure model can still be further simplified compared to Equation 121, while maintaining acceptable accuracy.

In general, it can be concluded from this section that it is essential to model the solids mesoscale stresses in a way that accounts for the anisotropy of the sub-grid solids velocity fluctuations. While the

correlation with the data in the resolved simulations has been improved substantially by accounting for the anisotropy of the stresses, the verification performed in Chapter 4, Chapter 5.1 and Chapter 5.2 will evaluate the practical benefits of this improvement in coarse grid simulations.

3.7 Frictional stress closures

It was found in the investigation discussed in Appendix B, that the qualitative behaviour of the sub-grid contributions that require closure in fTFMs change when frictional stresses are included in the resolved simulations used for model derivation. This is because the frictional stresses cause the dense regions to become more homogenous, thereby reducing the effect of mesoscale structures in very dense regions. Based on this finding, a closure for predicting the frictional pressure was included in the resolved simulations to account for this physical behaviour of fluidized beds.

It was found that, at large filtered solids volume fractions, the filtered frictional pressure became significant compared to the solids mesoscale stresses. The filtered frictional stresses will therefore tend to prevent the coarse grid simulations from entering very dense regions that did not occur in the resolved simulations. Since most of the fTFM closures change rapidly near the dense volume fraction limit, it was deemed necessary to include a closure for the filtered frictional pressure.

3.7.1 Filtered frictional pressure closure

It was found that the filtered frictional pressure could be modelled as a function of the filtered solids volume fraction and the filtered deviatoric shear rate magnitude (SRM), as defined in Chapter 3.6.1. Since the filtered frictional pressure is an isotropic quantity, the use of the scalar-valued SRM as an independent variable will not pose a problem. From the expression given in Equation 90, it can be seen that the closure for the filtered frictional pressure contains two parts: one that is correlated to the SRM and another that is independent of the SRM. Both parts increase with the filter size, although the rate of increase with the filter size is greater for the first, SRM dependent term. Additionally, both terms increase exponentially with the filtered solids volume fraction. However, the SRM independent term is defined in such a way that it increases extremely rapidly towards the dense volume fraction limit beyond a certain solids volume fraction, specified by x_{12}.

$$\frac{\bar{p}_{s,fric}}{\rho_s v_t^2} = \bar{\alpha}_s^{\,x_1} \Delta_f^{*\,x_2 + x_3 \Delta_f^{*\,x_4}} \left(x_5 \left\| \hat{S}_{s,fil} \right\|^{x_6 + x_7 \Delta_f^{*\,x_8}} \Delta_f^{*\,x_9} + x_{10} \frac{e^{x_{11} \max(\bar{\alpha}_s - x_{12}, 0)}}{(\alpha_{s,\max} - \bar{\alpha}_s)^{x_{13}}} \right) \qquad \text{Equation 90}$$

The proposed closure yields a good fit to the binned data (i.e., $R^2 = 0.965$) with the following coefficients: $x_1 = 2.78$, $x_2 = 1.00$, $x_3 = -0.0726$, $x_4 = 0.722$, $x_5 = 0.124$, $x_6 = 2.00$, $x_7 = -0.0689$, $x_8 = 0.684$, $x_9 = 0.807$, $x_{10} = 7.38 \times 10^{-6}$, $x_{11} = 36.0$, $x_{12} = 0.485$, $x_{13} = 3.64$ and $\alpha_{s,\max} = 0.63$ (the latter is the maximum packing specified in the resolved simulations).

Figure 36 shows the model predictions compared to the binned data for the filtered frictional pressure. By comparing the dimensionless filtered frictional pressure values to the normal mesoscale stresses in Figure 32, it can be seen that, although smaller, the filtered frictional pressure may have a significant contribution at large filtered solids volume fractions. The binned data also shows that substantial filtered frictional pressures may occur significantly below a solids volume fraction of 0.5, where frictional stresses start in the resolved simulations. This is because a filtered region, especially at large filter sizes, may be at an intermediate filtered solids volume fraction, but may still contain very dense

regions where frictional stresses occur. It is found that such situations are more likely to occur at large filtered shear rates, therefore the correlation with the SRM appears reasonable. Lastly, it can be seen that, although the filtered frictional pressures tend to increase with the filter size, large filtered frictional pressures are not observed for the largest filter size. This is because the maximum filtered solids volume fraction, as well as the average SRM, in the binned data from the resolved simulations tend to decrease with increasing filter sizes.

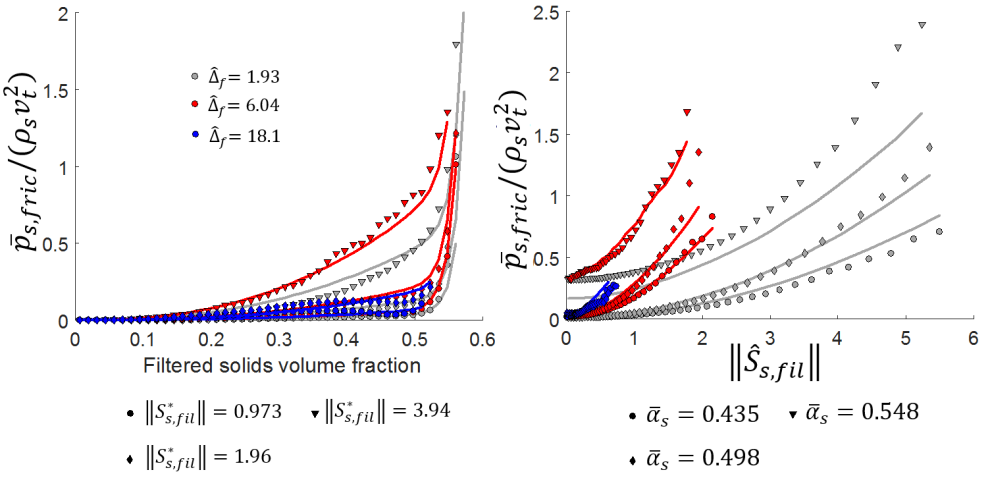

Figure 36 - The filtered frictional pressure as a function of a) the filtered solids volume fraction and b) the dimensionless filtered deviatoric shear rate magnitude for different filter sizes. The symbols show the binned data and the lines the model predictions.

3.7.2 *A priori* analysis of the filtered frictional pressure closure

As in previous sections, the coefficient of determination is calculated by comparing the model predictions to the observed values. This is done for both (i) the resolved data for the filtered frictional pressure, and (ii) for the volumetric forces resulting from the filtered frictional pressure. The results in Figure 37 show that the model for the filtered frictional pressure explains a large amount of variance in the resolved simulation data at the smaller filter sizes considered. However, the correlation coefficient decreases rapidly with increasing filter size, therefore the predictive capability of the proposed model decreases at large filter sizes. As previously noted, the binned data suggests that the filtered frictional pressure becomes less important at larger filter sizes, therefore the decrease in the R^2 values at large filter sizes may not have a substantial effect on the model accuracy in coarse grids simulations. Also, even at the minimum R^2 value of around 0.1, the model can be expected to reasonably predict the mean effects of the filtered frictional pressure. The proposed model can therefore be expected to adequately fulfil the required purpose, namely to prevent very dense regions from occurring in coarse grid simulations.

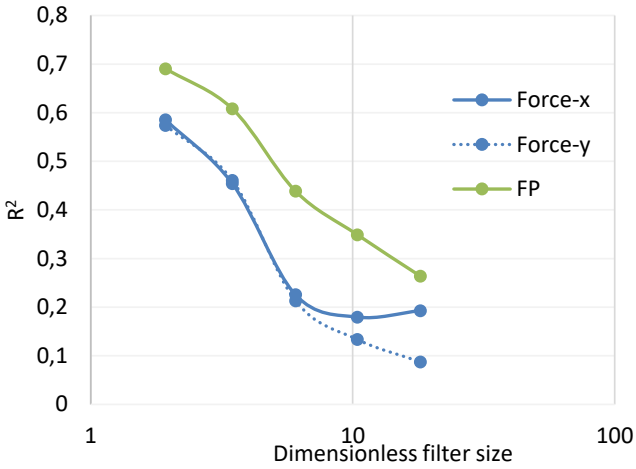

Figure 37 - R^2 values as a function of the dimensionless filter size when comparing model predictions with the observed values for various quantities relevant to the filtered frictional pressure.

3.7.3 Filtered frictional viscosity

From Equation 16 and Equation 17 it can be seen that the frictional viscosity is multiplied with the deviatoric shear rate before averaging. This results in three different, anisotropic quantities that have to be closed to include the effects of the frictional viscosity in the coarse grid simulations. From experience, closing anisotropic quantities is a much more complex task than closing isotropic quantities, such as the filtered frictional pressure. Therefore, it can be expected that closing the filtered frictional viscosity contributions would be a time consuming and complex task.

Fortunately, the resolved simulation data suggests that the filtered frictional viscosity contributions are significantly smaller than the filtered frictional pressure. Furthermore, the contribution of the frictional viscosity decreases with increasing filter size. The absolute value of the forces resulting from the filtered frictional viscosity contributions are on average approximately 3.5 times smaller than the absolute values of the forces resulting from the filtered frictional pressure when $\hat{\Delta}_f = 1.93$, and about 5 times smaller when $\hat{\Delta}_f = 18.2$. It addition, the forces due to the frictional pressure are already significantly smaller than those arising from the filtered drag force, the solids mesoscale stresses and the mesoscale interphase force. Experience with performing coarse grid simulations also indicated that the closure for the filtered frictional pressure has only a minor effect for the cases considered in the present study. Based on these findings, it is concluded that for the filter sizes that are of significance for the present study, little additional accuracy would be achieved by closing the filtered frictional viscosity contributions. Such a closure is therefore not developed.

It should be noted, however, that, in specific cases where large, dense, frictional regions are present, closures for the filtered frictional contributions may be more important than in the present study. Furthermore, it is known that the accuracy of the frictional pressure and viscosity models used in this study is debatable and more realistic models have been proposed more recently [56, 57]. Therefore, it is suggested that if fTFM closures are required for a case where the frictional stresses are of critical importance, new resolved simulations should be performed with more advanced frictional stress models to generate data for closure development.

3.8 Species transport closures

3.8.1 Mesoscale species dispersion rate closures

In the filtered species transport equation (Equation 19), $\overline{\alpha_g X_A'' \vec{v}_g''}$ requires closure. In the present study, the fTFM closure model developed by Agrawal et al. [27], where the mesoscale species dispersion is modelled as an added species diffusivity, is used. Since analysis of the closure model in the verification study in Chapter 4.1.3 showed that the mesoscale species dispersion had only a minor effect on the overall reactant conversion, no attempt was made to develop an improved closure model in the present study.

However, it can be speculated that the mesoscale species dispersion could potentially be closed using a similar approach as for the solids mesoscale stresses (see Chapter 3.6.3). Thus, a GPM-based marker could be used to refine the fidelity of the closure for the mesoscale dispersion rate. In this case, the GPM would then be the product of the filtered species mass fraction and the filtered gas phase velocity gradients. Such an approach will be investigated in future studies.

3.8.2 Filtered reaction rate closures

In this section, the filtered reaction rate in Equation 19, $k_A \rho_g \overline{\alpha_s X_A}$, will be closed as follows:

$$k_A \rho_g \overline{\alpha_s X_A} = \mathrm{R} k_A \rho_g \overline{\alpha_s} \tilde{X}_A \qquad \text{Equation 91}$$

Due to mass transfer limitations imposed by the mesoscale structures, the filtered reaction rate is reduced compared to the reaction rate evaluated as the filtered values, i.e., $k_A \rho_g \overline{\alpha_s} \tilde{X}_A$. This effect is therefore compensated for in the coarse grid simulations by deriving a closure model for the reaction rate correction factor, R, defined as follows:

$$\mathrm{R} = \frac{\overline{\alpha_s X_A}}{\overline{\alpha_s} \tilde{X}_A} \qquad \text{Equation 92}$$

This methodology is analogous to the use of the drag correction factor presented in Chapter 3.4.1. Nevertheless, it should be noted that, since the filtered reaction rate is a scalar quantity, this approach does not suffer from the same issues as those associated with the filtered drag force.

In the periodic simulations used for data generation, a problem is faced in calculating the filtered reaction rate correction in that X_A tends to zero as the reactant is converted. For this reason, the reactant mass fraction is scaled with the domain-averaged reactant mass fraction to produce a scaled reactant mass fraction, $\kappa_A = X_A / \langle X_A \rangle_d$. Based on this scaled variable, the reaction rate correction factor can then be redefined as:

$$\mathrm{R} = \frac{\overline{\alpha_s \kappa_A}}{\overline{\alpha_s} \tilde{\kappa}_A} \qquad \text{Equation 93}$$

The only fTFM closure for the reaction rate in literature [28] follows a somewhat different approach, where the filtered reaction rate is corrected for non-local effects. It should be noted that such an approach was first followed in this study as well. A closure derived based on such a non-locally corrected reaction rate correction factor is presented in Appendix F.3.1. This model was used in initial

verification studies in partially-periodic domains presented in Chapter 4, where there was not a clear difference in the performance of the non-locally corrected closure and the closure using the definition in Equation 92. However, in a later verification study in a wall-bounded domain, it was found that, when the hydrodynamics were correctly predicted, the non-locally corrected closure tended to overpredict the conversion. In this case, the definition in Equation 92 yielded better results, and will therefore be focussed on in what follows.

Similar to the work of Holloway & Sundaresan [28], it was found that the reaction rate correction is a strong function of the filtered solids volume fraction, and that the largest reduction in the reaction rate occurs at intermediate filtered solids volume fractions. No correction is necessary at the dilute and dense volume fraction limits, as expected. Furthermore, it was found that the reaction rate correction factor depends on the scaled slip velocity magnitude, as defined in Chapter 3.4.1.2. Specifically, the reduction in the reaction rate tends to increase with increasing scaled slip velocity magnitude because the slip velocity is correlated with the amount of sub-grid heterogeneity.

It should also be noted that the closure model developed by Holloway & Sundaresan [28] also included a mesoscale Thiele modulus (i.e., a scaled reaction rate) and the Schmidt number as independent variables. In the present study, the focus is placed on determining (i) how accurately the reaction rates can be predicted on coarse grids, and (ii) how the hydrodynamic fTFM closures influence the reactive predictions on coarse grids. To limit the scope, the present study therefore only considers a single reaction rate constant, k_A, and species mass diffusivity, D, given in Table 2. The reaction rate constant is specified such that the mesoscale Thiele modulus, $\varphi = \sqrt{k_A d_p^2/D} = 0.16$. The closure model in this study is therefore derived specifically for verification purposes and will be extended in the future to be of practical used for large scale, non-isothermal fluidized bed reactor studies.

Based on the binned data, it is found that the reaction rate correction factor can be closed as in Equation 94. It can be noted that a scaled version of the reaction rate correction factor is used in the closure expression. As with the drag correction factor in Chapter 3.4.1, when the reduction of the filtered reaction rate is large, i.e., R is small, the filtered reaction rate is sensitive to small changes in the value of R. Using the scaled reaction rate correction factor, $-\log(R)$, more emphasis is placed on these areas of large correction to ensure that the closure model is accurate in these critical regions.

In Equation 94, the first two arctangent functions ensure that there is no correction in the reaction rate at the dilute and dense volume fraction limits and that the correction reaches a maximum at intermediate filtered volume fractions. The rate at which the correction reduces towards the dilute and dense volume fraction limits is additionally a function of the filter size. Next, two terms contribute towards the reaction rate correction. The first is proportional to the base-10 logarithm of the scaled filtered slip velocity magnitude and independent of the filter size. This contribution tends to disappear as small filtered slip velocities. The second contributing term is independent of the scaled filtered slip velocity magnitude. Additionally, this term increases with the filter size and plateaus for very large filter sizes.

$$-\log(R) = \left(\frac{2}{\pi}\right)^3 \operatorname{atan}\left(x_1 \Delta_f^{*\,x_2} \bar{\alpha}_s\right) \operatorname{atan}\left(x_3 \Delta_f^{*\,x_4} \max(\mathrm{x}_5 - \bar{\alpha}_s, 0)\right) \times \left(x_6 \operatorname{atan}\left(x_7 \left\|\widetilde{v_{slip}}^*\right\|\right) \log\left\|\widetilde{v_{slip}}^*\right\| + x_8 \operatorname{atan}(x_9 \Delta_f^*)\right) \quad \text{Equation 94}$$

The fit to the binned data shown in Figure 38 is achieved with the following coefficients: $x_1 = 5.66$, $x_2 = 0.0118$, $x_3 = 25.0$, $x_4 = 0.232$, $x_5 = 0.559$, $x_6 = 0.341$, $x_7 = 0.380$, $x_8 = 1.09$ and $x_9 = 0.683$. The binned data also clearly show the importance of accounting for the effect of the filtered slip velocity magnitude in the closure model.

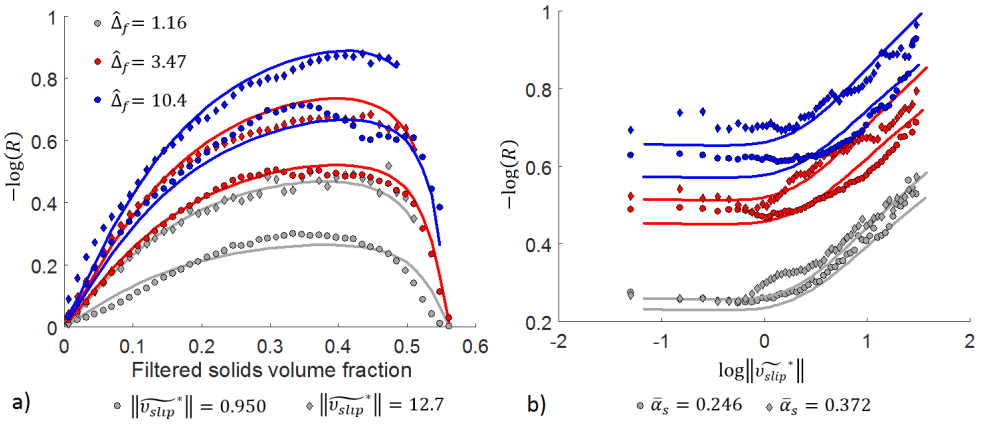

Figure 38 - The scaled reaction rate correction factor, $-log(R)$, as a function of a) the filtered solids volume fraction and b) the scaled filtered slip velocity magnitude. The symbols show the binned data from the resolved simulations and the lines the model predictions.

3.8.3 *A priori* analysis of the filtered reaction rate closures

As with the previous closure models, the performance of the filtered reaction rate closure will next be analysed by comparing observed values in the resolved simulation data to model predictions. Here the scaled filtered reaction rate, $k_A \rho_g \overline{\alpha_s \kappa_A}$, is considered. To give context to the performance of the closure model developed in this section, a simple 1-marker was derived as well for the reaction rate correction factor. The information for this closure model is given in Appendix F.3.2. It can further be noted that these closures, developed during the early stages of the present study, consider filter sizes from $\hat{\Delta}_f = 0.643$ to $\hat{\Delta}_f = 10.4$. However, the performance of the closure models will still be evaluated for $\hat{\Delta}_f \geq 1.93$, the filter sizes that are considered most relevant for industrial scale simulations.

Figure 39 compares the performance of the 1-marker and 2-marker closure models for predicting the filtered reaction rate. The 2-marker closure performs slightly better for most filter sizes, but the mean R^2 for the 1-marker model always falls within the 95% confidence interval of the 2-marker model. Therefore, adding the scaled filtered slip velocity magnitude as the second marker does not substantially improve the predictive capability of the closure model. Future work should therefore consider alternative second markers that may lead to larger improvements in the closure model performance. However, it should be noted that the R^2 values calculated for the filtered reaction rate is significantly higher than those of all hydrodynamic closures considered earlier in this chapter. It therefore appears that the variability of the effect of the mesoscale structures on the filtered reaction rate is relatively small. Both closure models should therefore be able to precisely predict the filtered reaction rate in coarse grid simulations. Due to the minor difference in the R^2 values when using the 1-marker and 2-marker closures, their relative performance will not be further considered during the

verification studies in Chapter 4, Chapter 5.1 and Chapter 5.2. Therefore, the 2-marker closure model is used for the rest of this study.

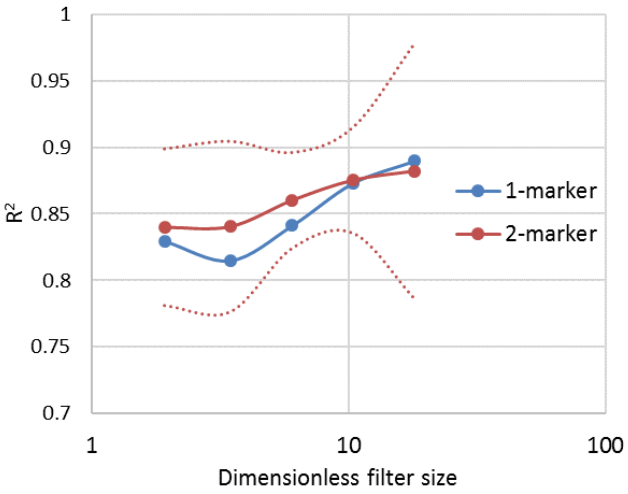

Figure 39 – The R^2 when comparing the observed and predicted values of the scaled filtered reaction rate, $k_A \rho_g \overline{\alpha_s \kappa_A}$, as a function of the dimensionless filter size. The dotted lines show the 95% confidence interval for the 2-marker model.

Chapter 4: Verification of fTFM closures in a partially-periodic domain

In this chapter, the closure models derived in the previous chapter will be evaluated in an *a posteriori* manner: by comparing the results of coarse grid simulations employing the fTFM closures to benchmark results from resolved simulations. These verification studies will help to improve the understanding of how the different closures behave, reveal the progress that was made with the closures developed in this study and help to identify limitations of the existing closures that will be addressed in future studies.

It should be noted that for this entire chapter, as well as in Chapter 5.1 and Chapter 5.2, the same particle and fluid properties as presented in Chapter 3.1.3, i.e., those used for deriving the fTFM closures, are used. Additionally, to allow the detailed verification performed in the present chapter, all simulations are performed in 2D. As previously discussed, development and verification in 2D allows a more detailed analysis of the closure performance with current computational resources. The improved understanding developed in this study can then be applied in the future to develop closure models from 3D resolved simulation data.

Early 1-marker fTFMs [16, 19] developed from periodic simulations are known to fail in wall-bounded domains without dedicated wall-correction functions. Later 2-marker-based closure models [13, 14] have been shown to offer improved performance in wall-bounded domains, and it has been speculated that these more advanced closure models may not require wall-corrections [13, 26]. However, this claim has not been deeply analysed in the literature. Due to the uncertainty regarding the ability of fTFMs to accurately predict the sub-grid corrections in near-wall regions, the verification in this chapter aims to minimise the effect that wall-regions have on the simulations. These preliminary verification cases were used to assess the performance of existing fTFMs in literature to better understand the improvements that are necessary, as well as to test closures during the development phase in the present study.

4.1.1 Simulation setup

Coarse grid simulations using fTFM closures are performed using grid sizes of 20 mm ($267d_p$), 40 mm ($533d_p$) and 80 mm ($1067d_p$). In the present study, such simulations will be referred to as “filtered simulations”, since they solve the transport equations of the filtered variables given in Chapter 2.2. A resolved TFM simulation, used as benchmark to assess the performance of fTFM closures, is performed on a grid of 0.884 mm ($11.8d_p$). It should be noted, that due to the large domain considered in this section, it was computationally infeasible to use the same grid size for the benchmark resolved simulations as was used in the fully-periodic simulations used for model development, i.e., 0.625 mm ($8.33d_p$). However, it was tested that the solution of the verification case only changed slightly when refining the grid from 1.25 mm to 0.884 mm (see Figure 40). Therefore, the solution is expected to change even less when refining to 0.625 mm. Considering this, for the preliminary evaluation purposes of the verification performed in this chapter, a grid size of 0.884 mm for the benchmark resolved simulations is a reasonable compromise between accuracy and computational cost.

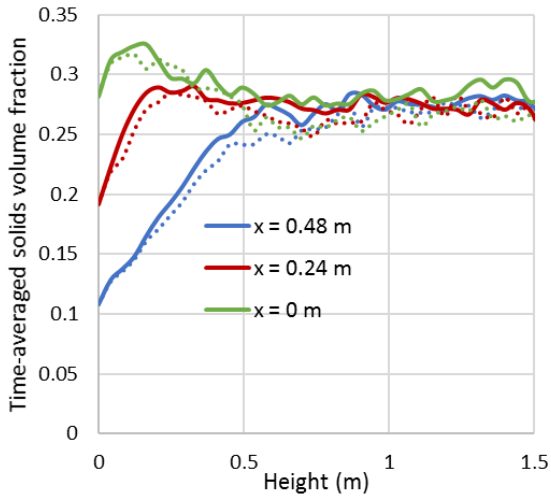

Figure 40 - Analysis of the grid dependence of the results for the bubbling verification case. The solid lines show the time-averaged solids volume fraction for a 0.884 mm grid, and the dotted lines for a 1.25 mm grid. The different colours show the vertical profiles at three different lateral positions.

In this section, a rectangular region (referred to as the "fluidization region") is considered, with an inlet at the bottom and periodic boundaries at the sides. The size and the aspect ratio of this region changes for the three cases considered in this section, as described in Table 4. Periodic boundaries are selected to eliminate uncertainties arising from wall effects in this preliminary verification, since the closure models evaluated in this study were derived from data collected from fully-periodic simulations. To prevent numerical instabilities due to backflow, walls slope at 45° from the top of the rectangular region towards an outlet with a width of 0.08 m. The solids boundary conditions at the walls are specified as free-slip to prevent backflow into the fluidization region and thereby minimize the effect of the walls on the flow in this region. The simulated domains can be seen in Figure 43 to Figure 45.

Table 4 - Description of the configuration for the three verification cases

Case	Fluidization region height (m)	Fluidization region width (m)	Average gas superficial velocity (m/s)
Bubbling	1.6	0.96	0.468
Turbulent	2.26	0.679	2.07
Fast fluidization	3.2	0.48	5.01

Three cases, operated in different fluidization regimes, are considered in this chapter to thoroughly test the generality of the filtered models derived in this study. The average superficial inlet gas velocity is chosen to be at the geometric centre of the bubbling fluidization and turbulent fluidization regimes, according to Bi and Grace [58], and quarter way between the transitions to core-annular dilute phase flow and homogenous dilute phase transport for the fast fluidization case. A solids flux of 150 kg/m^2s is specified for all three cases. Additionally, non-uniform boundary conditions, illustrated in Figure 41, are specified at the inlet to allow faster cluster formation in the absence of walls. The gas and solids velocities are set equal at the inlet and are specified to be half the mean superficial gas velocity at the sides and then increase linearly towards the centre. The solids volume fraction is set to half of the mean solids volume fraction at the centre and increases linearly towards the sides. The flow at the

inlet therefore changes from fast and dilute at the centre to denser and slower at the sides of the domain. Additionally, the reactant is injected with a mass fraction of 1 at the centre of the inlet and decreases linearly towards 0 at the sides.

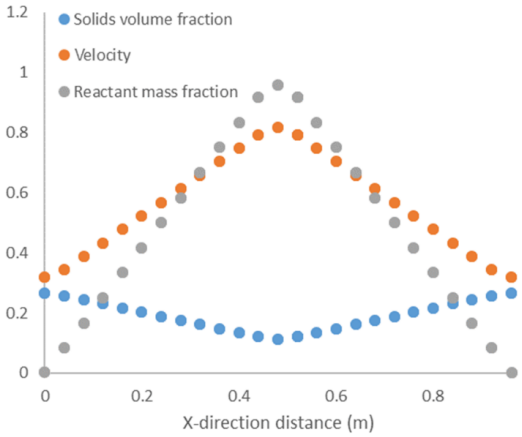

Figure 41 - Non-uniform inlet boundary conditions for the partially-periodic verification cases.

4.1.2 Preliminary hydrodynamic verification of fTFMs from literature

In this section, the performance of three fTFM closure models from literature was evaluated: The 1-marker closure models from Igci [16], the 2-marker closure models from Milioli [14] and the 2-marker closure models from Sarkar [13]. Additionally, an early version of the isotropic drag closure from Chapter 3.4.1.2, used in combination with the solids mesoscale stress closure from Sarkar [13], is evaluated. This model is here referred to as the Cloete model, but will not be discussed in detail, since later sections will discuss more complete fTFMs from the present study in greater detail. Filtered simulations were performed on 20 mm grid cells, specifying the filter size used in the fTFM closures as twice the grid size, as is common practice [17, 19, 26]. The simulations were allowed to run for 10 s to reach a pseudo-steady state, after which time-averaging was performed for 30 s.

An overall impression of model performance is provided in Figure 42. The bars represent the percentage deviation in terms of the time-averaged solids holdup in the fluidization region from the fine-grid simulations for the three different fluidization regimes. A positive deviation implies that too much solids is present in the domain, most likely caused by an underprediction of the drag force. A negative deviation indicates too little solids resulting from an overpredicted drag force.

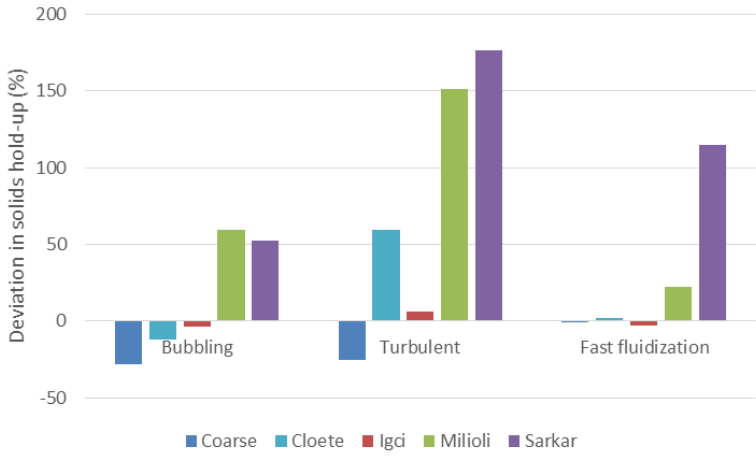

Figure 42 - Deviation in the overall solids holdup from the resolved simulation for several different model setups. Coarse: no fTFM closures; Cloete: Similar to Chapter 3.4.1.2; Igci: [16]; Milioli: [14]; Sarkar: [13]. All simulations were carried out on a grid with a mesh size of 20 mm (i.e., approximately 23 times larger than the fine grid simulations).

The importance of a filtered closure models is clearly visible in the coarse grid simulations without fTFM closures for the bubbling and turbulent regimes shown in Figure 42. In both these cases, a significant negative deviation (i.e., ca. 25%) in the overall solids holdup is observed, indicating that clustering is not sufficiently resolved to accurately predict the momentum coupling between gas and solids. As a result, the momentum coupling term is overpredicted, resulting in an underprediction of the solids holdup. This is not observed in the fast fluidization case, simply because clustering only took place in a relatively small region of the domain (see Figure 45).

Of the four different fTFMs employed, the Igci model consistently showed the best performance. This is the original filtered model, using only the filtered volume fraction as a marker for both the drag and the stresses. Also, the Igci model has been derived from 2D simulations. Unfortunately, this model is not suitable as a general solution for large-scale fluidized bed reactor modelling because of two important limitations: (i) it requires specialized wall functions to give reliable predictions in wall-bounded domains [25], and (ii) it cannot create sufficiently large drag corrections to predict flows in domains with very large cell sizes [50].

The more complex two-marker closure models, which employ the filtered slip velocity magnitude as an additional marker for the drag and the filtered deviatoric shear rate magnitude as an additional marker for the solids mesoscale stresses, proved to be less reliable. These closure models are required to overcome the fundamental limitations of the one-marker closure outlined above, but it is clear that additional work is required to improve performance to the point where these models can be safely employed for large-scale fluidized bed reactor simulations.

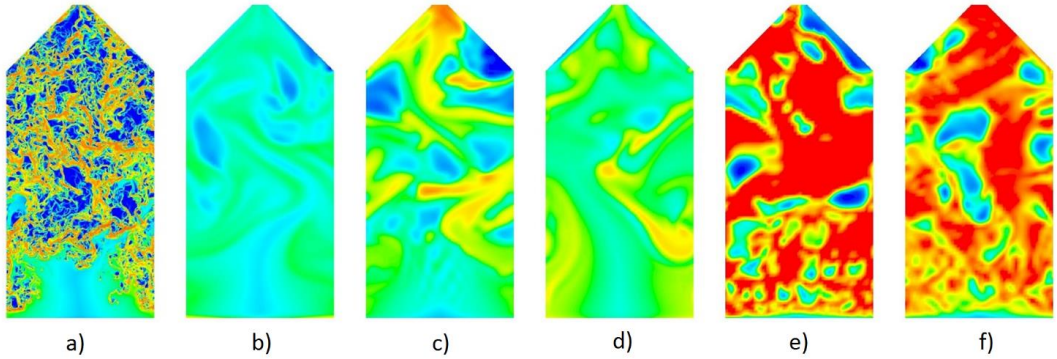

Figure 43 - Instantaneous solids volume fraction contours arranged from left to right for the (a) Resolved, (b) Coarse, (c) Cloete, (d) Igci, (e) Milioli and (f) Sarkar models in the bubbling regime. The closure models are referenced in the caption of Figure 42.

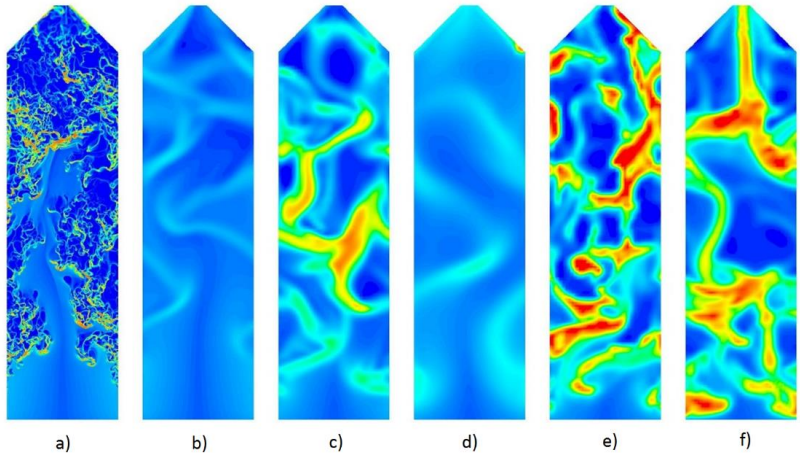

Figure 44 - Instantaneous solids volume fraction contours arranged from left to right for the (a) Resolved, (b) Coarse, (c) Cloete, (d) Igci, (e) Milioli and (f) Sarkar models in the turbulent regime. The closure models are referenced in the caption of Figure 42.

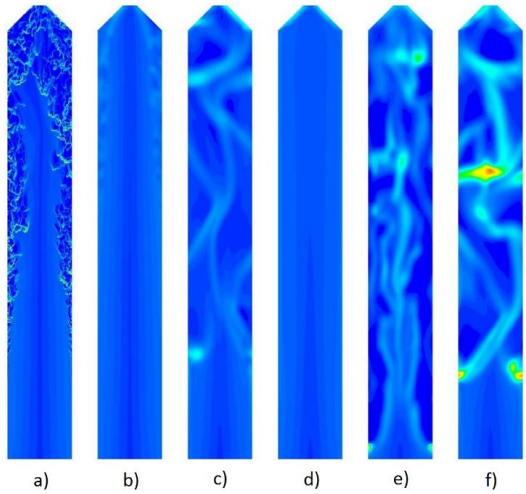

Figure 45 - Instantaneous solids volume fraction contours arranged from left to right for the (a) Resolved, (b) Coarse, (c) Cloete, (d) Igci, (e) Milioli and (f) Sarkar models in the fast fluidization regime. The closure models are referenced in the caption of Figure 42.

As shown in Figure 43, Figure 44 and Figure 45, both the Milioli and Sarkar closure models lead to large inaccuracies when compared to the resolved simulation. Not only is the solids holdup much too high, also the bottom region where no clustering takes place is not captured correctly. Given that the Sarkar model was derived for 3D flows, it is understandable that the drag force is underpredicted, since the reduction in drag resulting from the mesoscale structures are expected to be larger in 3D. However, such a clear reason for the discrepancy cannot be identified for the Milioli closure.

The Cloete closure model in this section was tested in combination with the solids mesoscale stress closures from all of the literature fTFMs investigated. Figure 46 shows that the solids mesoscale stress closure has a significant impact on the solids holdup and the general flow behaviour in the filtered simulation. Therefore, there is a large amount of uncertainty regarding the choice of the solids mesoscale stress closure.

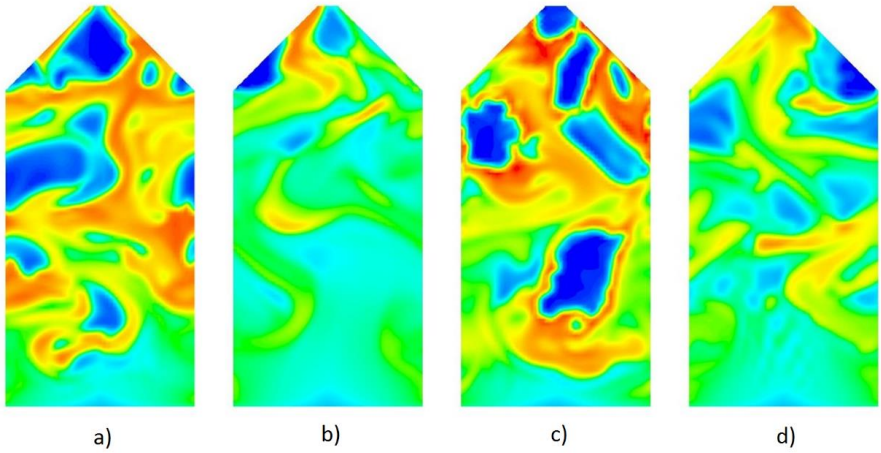

Figure 46 - Instantaneous solids volume fraction contours for the Cloete filtered drag model with (a) no filtered stress modelling, (b) Igci filtered stresses, (c) Milioli filtered stresses and (d) Sarkar filtered stresses in the bubbling regime.

The verification results in this section clearly show that there is a large amount of uncertainty regarding the performance of the literature models investigated. The only model that yielded reasonable results was the fTFM from Igci, which, as discussed earlier, has been shown in validation studies to have important limitations for practical use. These findings triggered a more detailed analysis of the filtered data from the resolved simulations, which eventually led to the development of the anisotropic closures in Chapter 3.4.2 and Chapter 3.6.3. These anisotropic closures will be evaluated in subsequent verification sections.

4.1.3 Preliminary reactive verification

This section will briefly discuss an important finding from an early reactive verification study [59] that formed part of the present study. This investigation evaluated the reactive predictions on coarse grids in the bubbling case when using preliminary formulations of the isotropic drag closure (Chapter 3.4.1.2), the Boussinesq-based solids mesoscale stress closure (Chapter 3.6.1), the filtered frictional pressure (Chapter 3.7.1) and the non-locally corrected filtered reaction rate closure (Appendix F.3.1). Since a more detailed reactive verification will be performed for the partially-periodic bubbling case in Chapter 4.1.4, the results from this investigation will not be detailed here. However, one finding will be pointed out: Figure 47 shows that accounting for the mesoscale species dispersion rate had little effect on the overall conversion rate for this case. It can be seen that the effect of the mesoscale species dispersion increases with filter size, but remains relatively small even at the largest filter size considered here. Based on this finding, an improved closure model was not investigated in this study and the existing closure model of Agrawal et al. [27] was used for all reactive filtered simulations.

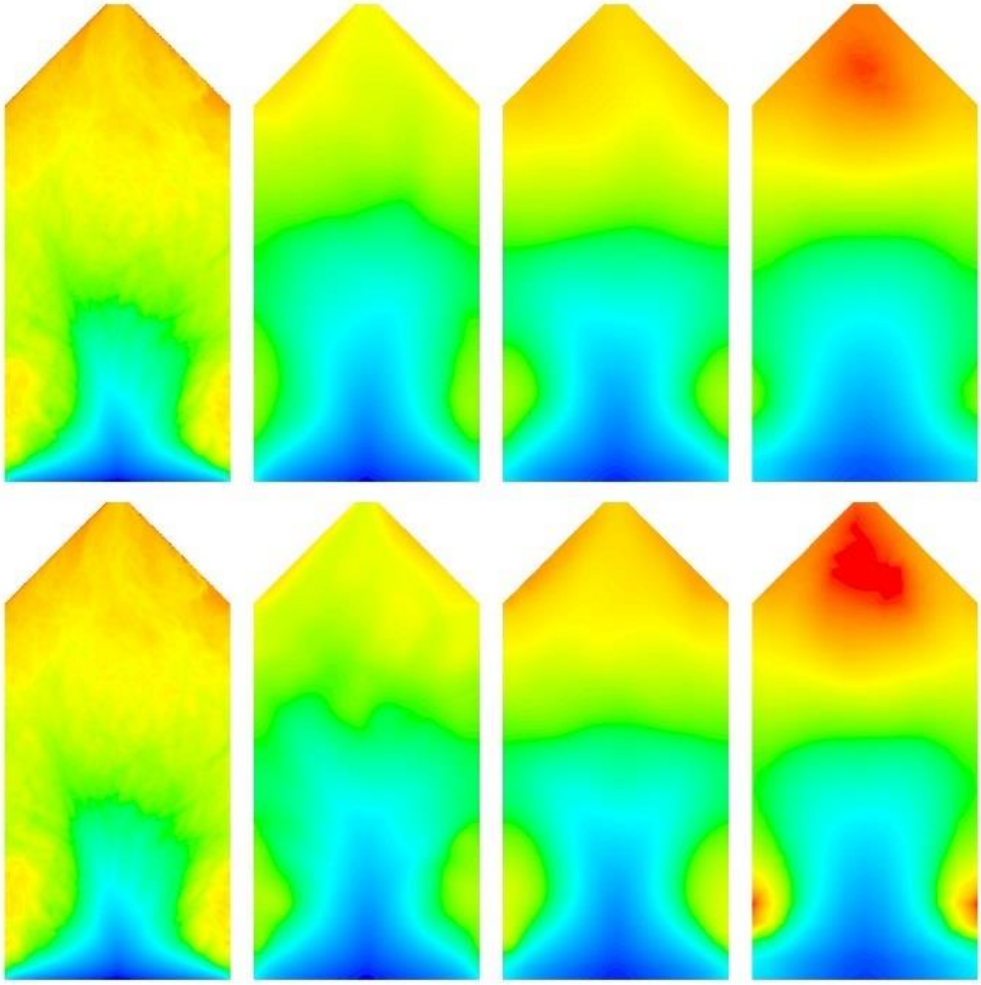

Figure 47 - Time-averaged contours of the scaled reactant conversion $(-log(X_A))$. Top row: with mesoscale species dispersion rate closure [27]. Bottom row: without mesoscale species dispersion rate closure. Each row shows the resolved simulation on the left and then the coarse grid simulations on grids with a mesh size of 20, 40 and 80 mm. The blue-red colour map spans a range of 0-6.

4.1.4 Detailed verification for the bubbling case

In this section, a detailed hydrodynamic and reactive verification of the partially-periodic bubbling case is performed. Four possible combinations of the anisotropic and isotropic closures for the filtered interphase momentum exchange and the solids mesoscale stresses are evaluated at three different grid sizes of 20 mm, 40 mm and 80 mm. Time-averaged vertical profiles of relevant quantities are then compared to the results of the resolved simulation to assess the performance of the different closures. The following closures are investigated: (D+) Anisotropic filtered interphase forces using the non-linearity correction factor closure (Chapter 3.4.2.3), the 3-marker adjusted slip velocity closure (Chapter 3.4.2.6) and the anisotropic mesoscale interphase force closure (Chapter 3.5.1). (D-) Isotropic filtered interphase forces using the isotropic drag correction closure (Chapter 3.4.1.2). (S+) Anisotropic

solids mesoscale stress closure (Chapter 3.6.3). (S-) Isotropic solids mesoscale stress closures based on the Boussinesq approximation (Chapter 3.6.1). To be more concise, these closures are referred to as the anisotropic drag, isotropic drag, anisotropic stress and isotropic stress models, respectively. All filtered simulations use the filtered frictional pressure closure (Chapter 3.7.1) and the non-locally corrected filtered reaction rate closure (Appendix F.3.1). It can be noted that the filter size in the closure models are set equal to the grid size in the coarse grid simulations in this section.

4.1.4.1 Inlet effect

The non-uniform inlet conditions shown in Figure 41 was specified to introduce a mean gradient in the flow field, in the absence of walls for most of the domain, thus providing more interesting verification data. However, this boundary condition also introduced some uncertainty due to the region of uniform intermediate volume fraction that can be observed at the bottom of the domain in Figure 48. In filtered simulations, a region of intermediate volume fraction is generally associated with significant clustering, leading to significant corrections for drag, stresses and reaction rates. As a result, the filtered simulations generally predicted significant sub-grid corrections in the uniform inlet region where no correction should actually be imposed since no clustering takes place.

This is clearly observed in the slip velocity prediction along vertical lines in the centre and at the side of the domain shown in Figure 49. It is shown that the match between the resolved and coarse grid simulations is generally very good, except in the lower region on the centre line. This is the region of intermediate volume fraction where the models predict a correction, while no correction should be imposed. Due to this uncertainty in the central region of the domain, the rest of the paper will present results on the side periodic boundaries where clustering takes place along the entire height of the domain.

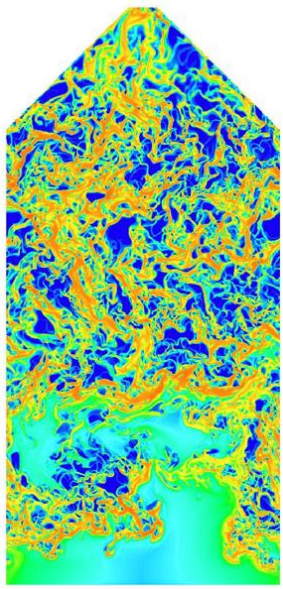

Figure 48 – Contour plot of the instantaneous solids volume fraction from the resolved TFM simulations.

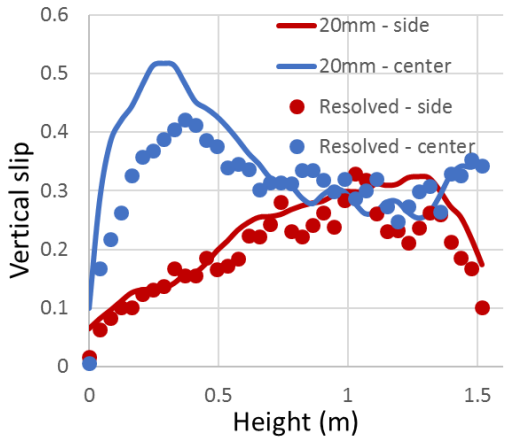

Figure 49 – Comparison of time-averaged vertical profiles of the vertical slip velocity along lines at the centre and at the side of the domain. Coarse grid simulations are performed on a 20 mm grid and using anisotropic closures for both the filtered interphase forces and the solids mesoscale stresses.

It should be noted that fTFM closures in literature are generally expected to perform poorly in such cases with homogenous regions at intermediate volume fractions, since all the proposed closures make use of algebraic equations. Solving transport equations for markers that affect the closures is a possible strategy to allow a more accurate modelling of such cases on coarse grids. Such models have been proposed [20], but were subsequently simplified to algebraic relations before application. This was done to eliminate the complexity of solving additional transport equations. In practical applications, clustering general occurs rapidly at the boundaries, and such homogeneous regions at intermediate volume fractions are negligibly small. As a result, this weakness of algebraic fTFM closures is not expected to cause significant errors in most practical applications.

It can be noted that the fTFM closures investigate here accurately predicted the solids holdup in the turbulent and fast fluidization cases described in Chapter 4.1.1. However, an unusual periodic behaviour was obtained for all fTFMs considered, which does not match the resolved simulation behaviour. Some evidence of this can be seen in Figure 44.d. This is also expected to be an effect of the inlet boundary conditions and the absence of walls that cannot be captured by the algebraic fTFM closures employed in the present study. For this reason, the partially-periodic turbulent and fast fluidization cases are not further considered for detailed verification.

4.1.4.2 Solids volume fraction

The model predictions of time-averaged solids volume fraction along a vertical line on the side periodic boundary of the domain is shown in Figure 50. Clearly, all models return reasonable predictions of this quantity, but the cases with anisotropic solids mesoscale stress modelling generally produce a closer match to the resolved simulation data. Anisotropic solids mesoscale stress modelling also appears to be important for good grid independence behaviour, especially when transitioning from the 40 mm to the 80 mm grid. The anisotropic drag model also appears to outperform the isotropic drag model, except for the coarsest grid.

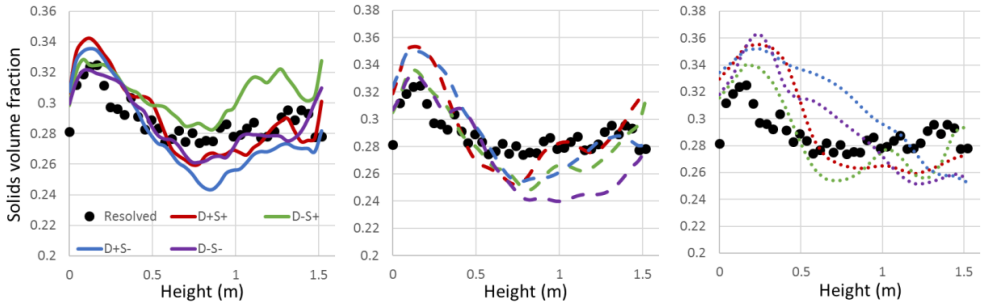

Figure 50 - Time-averaged vertical profiles of the solids volume fraction along the side boundary. From left to right the coarse grid simulations are performed on grids of 20 mm, 40 mm and 80 mm.

4.1.4.3 Vertical direction slip velocity

The insights from the solids volume fraction profiles in Figure 50 are also reflected in the slip velocity predictions plotted on Figure 51. Once again, the anisotropic stress model appears to be important for ensuring good predictions, especially on coarser grids. In this case, no clear improvement from the anisotropic drag closure model can be observed when used in combination with the anisotropic stress model. However, in combination with the isotropic stress model, the anisotropic drag model performs better on the two smaller grid sizes.

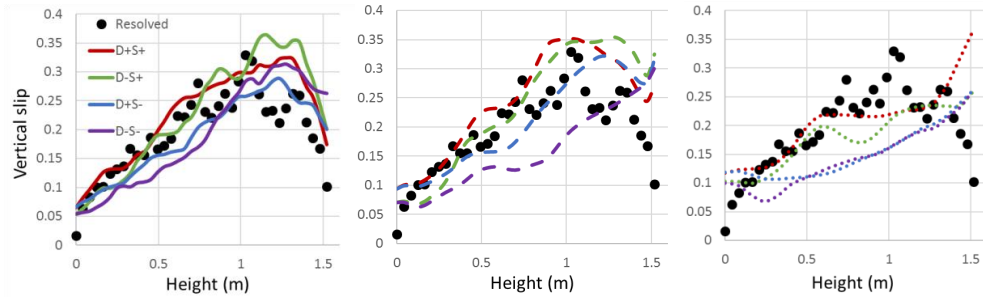

Figure 51 - Time-averaged vertical profiles of the vertical slip velocity along the side boundary. From left to right the coarse grid simulations are performed on grids of 20 mm, 40 mm and 80 mm.

4.1.4.4 Volume fraction variance

As may be expected, Figure 52 shows that all coarse grid simulations predict a significantly lower solids volume fraction variance than the resolved simulations, especially as the grid is coarsened. Figure 53 offers a graphical illustration of this effect. However, it is clearly shown that the anisotropic stress closure significantly increases the degree of solids volume fraction variance resolved on the coarse grids. The anisotropic drag model also resolved greater flow details on the coarser grids.

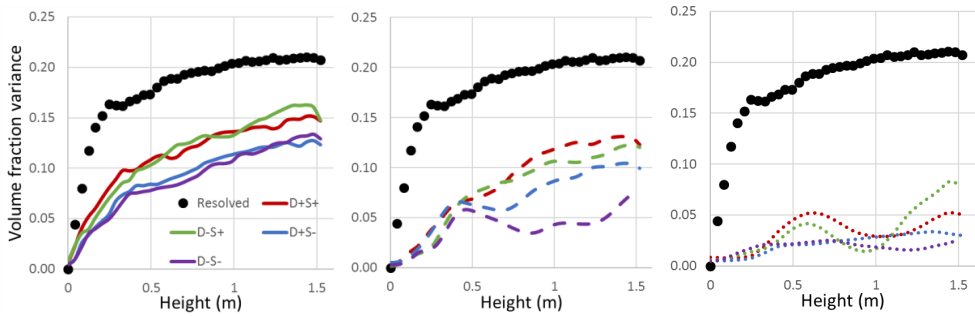

Figure 52 - The vertical profiles of the solids volume fraction variance along the side boundary. From left to right the coarse grid simulations are performed on grids of 20 mm, 40 mm and 80 mm.

The improved performance of the anisotropic stress closures can be explained based on the macro-scale structure resolution: From Figure 53 it can be seen that the isotropic stress models predict less distinct macro-scale 'clusters' and 'bubbles'. More gas flow will then tend to pass through these macro-clusters, whereas more of the gas flow will tend to slip around the more resolved macro-clusters predicted by the anisotropic mesoscale stress closure. As a result, the vertical drag is increased when using the isotropic solids mesoscale stress closure, leading to underpredictions in the vertical slip velocity (Figure 51) and the solids volume fraction (Figure 50, with the exception of the coarsest grid).

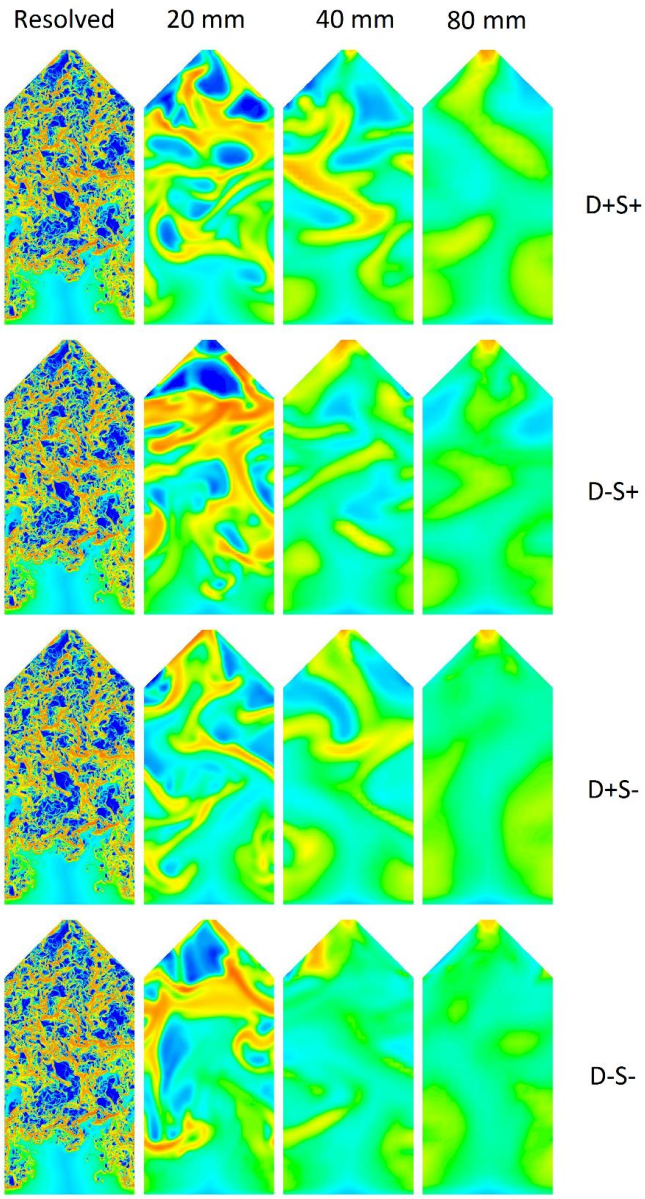

Figure 53 - Comparison of the instantaneous volume fraction contours for the resolved simulations and for the different closure combinations at different coarse grid sizes.

4.1.4.5 Conversion rate

Finally, the performance of the filtered reaction rate closure is displayed in Figure 54. Once more, the anisotropic stress closure appears to be critical for attaining accurate results on the coarser meshes. This result illustrates the importance of accurate resolution of the hydrodynamic flow details when

completing reactive fluidized bed simulations. In this case, the effect of the anisotropic drag closure was insignificant.

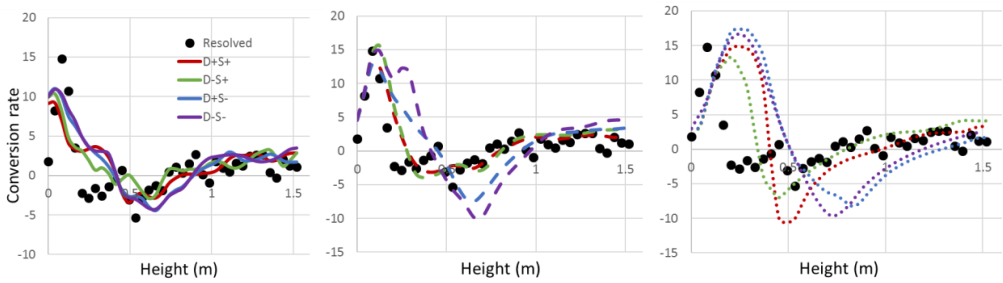

Figure 54 - The time-averaged vertical profiles of the conversion rate ($\frac{d(-log(X_A))}{dy}$) along the side boundary. From left to right the coarse grid simulations are performed on grids of 20 mm, 40 mm and 80 mm.

To put the reactive results in context, coarse grid simulations were also performed with the fTFM closures from Igci [16], which performed the best of the literature models evaluated in Chapter 4.1.2, for the hydrodynamics. The closure of Holloway [28] was used for the filtered reaction rate. In these simulations, the filter size is set to twice the grid size, as recommended by Igci [19]. This setup is referred to as the Princeton model. From Figure 55, it can be seen that the Princeton model overpredicts the conversion rate in the bottom region and underpredicts the conversion rate at intermediate heights when using 20 mm and 40 mm cells. Surprisingly, the results using 80 mm cells matches the resolved simulation results reasonably well. However, this can be considered to be coincidental, since the filtered simulations should become more accurate as the grid is refined. In general, the closures developed in the present study predicts the conversion rate more accurately and it can therefore be concluded that the closure models from the present study represent a significant advancement in the ability to predict reactive behaviour on coarse grids.

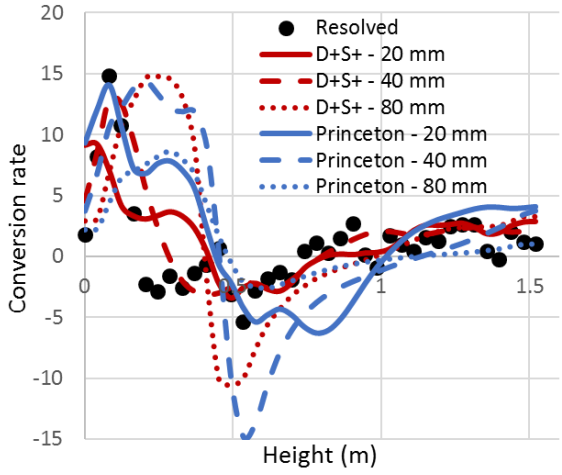

Figure 55 - The time-averaged vertical profiles of the conversion rate ($\frac{d(-log(X_A))}{dy}$) along the side boundary. The performance of the anisotropic closures from the present study is compared to that of the Princeton model on grids of 20 mm, 40 mm and 80 mm.

However, a final set of simulations was performed with the anisotropic closures from the present study for the hydrodynamics, but with the closure from Holloway [28] for the filtered reaction rate. Figure 56 shows that there is little difference between the predictions whether closing the filtered reaction rate with the closure developed in the present study or with the closure from literature. It can therefore be concluded that the improved closures for the filtered drag force and the solids mesoscale stresses are primarily responsible for the improved predictions of the conversion rate. On the contrary, improvements in the filtered reaction rate closure has a negligible effect. This is in agreement with the *a priori* assessment of the filtered reaction rate closure in Chapter 3.8.3, which indicated that even a simple 1-marker closure model could yield a very strong correlation with the observed values in the resolved simulations data. It therefore appears that much more complex closures are required for the filtered interphase forces and for the solids mesoscale stresses than for the filtered reaction rate.

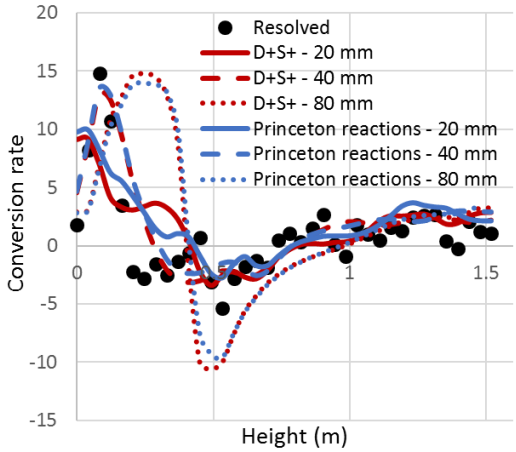

Figure 56 - The time-averaged vertical profiles of the conversion rate ($\frac{d(-log(X_A))}{dy}$) along the side boundary. The performance of the filtered reaction rate closure developed in the present study and that from the Princeton group is compared on grids of 20 mm, 40 mm and 80 mm. All simulations use the anisotropic closures developed in the present study for the hydrodynamics.

Chapter 5: Further verification and validation of fTFM closures

The a posteriori assessments presented in this chapter was carried out in collaboration with Dr. Schalk Cloete from SINTEF Materials and Chemistry, who performed the coarse grid simulations, analysed the data and disseminated the results for submission as journal papers. The author of the present thesis developed the fTFM closures that are evaluated here, implemented the newly developed and literature closures in ANSYS FLUENT, performed the resolved simulations that serve as benchmark in the verification, provided insight into the behaviour of the different closure models and contributed to the dissemination of the results.

5.1 Verification in a fully-periodic domain

Due to the issues regarding the boundary conditions in the verification cases considered in Chapter 4, new cases are considered in this section for a more detailed verification of the closure models developed in the present study. Here, the fTFM closures outlined in Chapter 3 will be implemented in a periodic case similar to the resolved simulations from which the closures were derived. This is the most direct model verification test available. It is also a very challenging verification exercise given that there are no walls, inlet or outlet boundaries to constrain the solution within certain bounds. Therefore, such a periodic verification study is a good place to get a first impression of model performance.

The results presented in this section will focus only on the hydrodynamic closures (i.e., filtered drag force, mesoscale interphase force, solids mesoscale stresses, filtered frictional stresses and filtered KTGF stresses) and quantify model performance via the vertical direction domain-averaged slip velocity: this velocity is the time average of the difference between the Favre-averaged gas and solids velocities over the entire domain. In all cases, the simulation was run for 5 s to reach a pseudo-steady state, followed by 5 s of averaging.

Aside from the different closure combinations, the most important independent variable in this study is the filter size to grid size ratio (henceforth denoted as filter/grid ratio). A filter/grid ratio of 2 is commonly suggested in fTFM studies [17, 19, 26]. This ratio is, however, not well understood at present and is often used as a tuning parameter in fTFM simulations. In the previous verification in Chapter 4, it was found that excellent results could be achieved by setting the filter size in the closure models equal to the grid size used in the coarse grid simulations. The filter/grid ratio is therefore evaluated in detail here to better understand how it influences the coarse grid simulations and what the correct ratio should be. Ideally, grid independence would also be tested, but cell sizes larger than 10 mm could not be simulated without the resolved macro-clusters occasionally spanning across the entire periodic domain. As shown in Figure 57, larger cells resulted in larger macro-scale clusters, thus increasing the likelihood of such a macro-cluster spanning the entire height or width of the periodic domain. This unwanted phenomenon introduces significant uncertainty in the simulation data, and hence needs to be avoided.

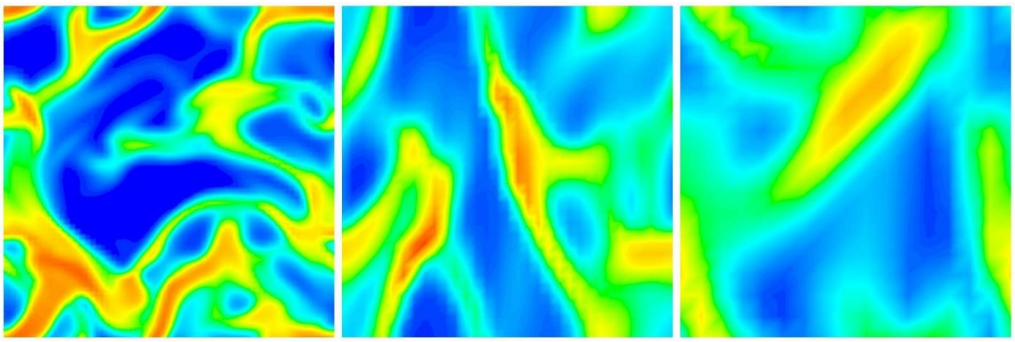

Figure 57 - Instantaneous contours of solids volume fraction on grids of 10 mm, 20 mm and 40 mm with a filter/grid ratio of 1 and a domain-averaged solids volume fraction of 0.2. The blue-red colourmap range is 0-0.6 and the complete fTFM model, described as Case 1 later in this section, is used.

Thus, the 10 mm cell size was selected as a good compromise between computational affordability for the large number of simulations to be completed, and the avoidance of domain-size effects caused by macro-clusters spanning horizontally or vertically across the entire domain. Grid independence has been considered in Chapter 4.1.4 and will be further investigated in detail in other verification cases reported in Chapter 5.2.

Table 5 - Different case setups investigated in this section.

Case	Filtered drag force	Solids mesoscale stresses	Mesoscale interface force	Filtered frictional stress	Granular temperature
1	3-marker	Anisotropic	Included	Filtered pressure	Complete
2	3-marker	Anisotropic	Excluded	Filtered pressure	Complete
3	2-marker	Anisotropic	Included	Filtered pressure	Complete
4	1-marker	Anisotropic	Included	Filtered pressure	Complete
5	Isotropic	Anisotropic	Included in drag model	Filtered pressure	Complete
6	3-marker	Boussinesq	Included	Filtered pressure	Complete
7	3-marker	None	Included	None	Complete
8	3-marker	Anisotropic	Included	Unfiltered pressure and viscosity	Complete
9	3-marker	Anisotropic	Included	Filtered pressure	Algebraic
10	3-marker	Anisotropic	Included	Filtered pressure	None

A similar challenge was encountered in the 10 mm cases, especially in the cases with large domain-averaged slip velocities (mostly the cases with larger filter/grid ratios and lower domain-averaged volume fractions). In these cases, a vertical channel occasionally formed across the domain, allowing the gas to slip rapidly past the solids. These instances created erroneous data and it was therefore decided to double the height of the simulation domain compared to that used for model

derivation in Chapter 3.1. This modification of the domain successfully removed this problem, but naturally introduces a new uncertainty. This uncertainty is shown to be negligibly small in the first subsection below.

The subsections that follow will investigate the performance of various fTFM closure combinations at four filter/grid ratios (0.707, 1, 1.414 & 2) and three domain-averaged solids volume fractions (0.1, 0.2 & 0.3). The ten different cases simulated are summarized in Table 5.

5.1.1 Case 1: Complete model

Case 1 represents the most complete set of closures available in this study. As shown in Figure 58, the model performs well when the filter/grid ratio is at unity or slightly below. For perspective, cases run without any fTFM closures are also included (see green bars), showing the expected large underpredictions of the domain-averaged slip velocity, especially at larger domain-averaged volume fractions.

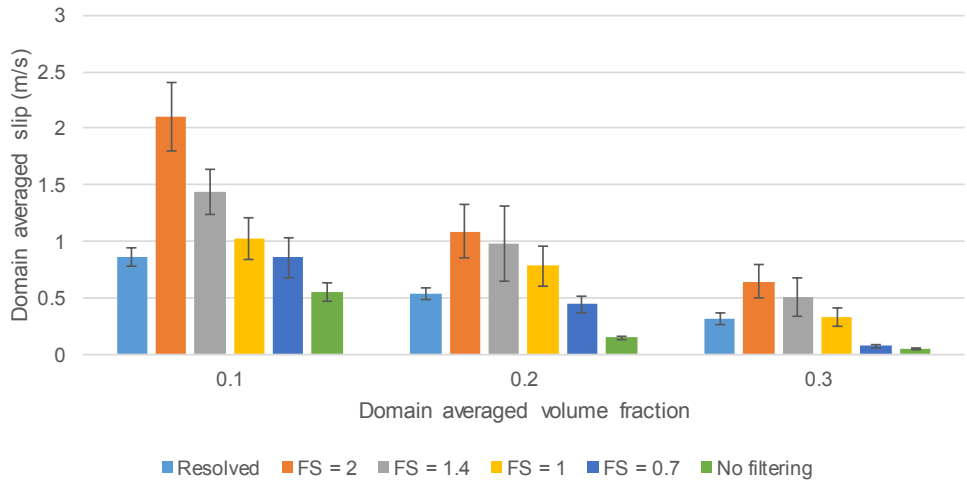

Figure 58 - Domain-averaged slip velocity results from Case 1 in Table 5. The error bars represent the standard deviation in the temporal variation of the slip velocity over the averaging period. FS = filter/grid ratio.

Clearly, larger filter/grid ratios significantly overpredict the slip between the phases. A filter/grid ratio of 2 returns a slip velocity more than double the value obtained in the resolved simulations. This is a significant finding because larger filter/grid ratios are often employed in the literature. Arguably, a filter/grid ratio close to unity makes more sense given that the model will then explain only phenomena occurring on a scale smaller than the computational cells employed.

Figure 58 also shows that the standard deviation of the average slip velocity over the 5 s time averaging period is substantially larger than was the case in the resolved simulation. This is due to the large macro-clusters being resolved in the filtered simulations, increasing the amplitude of the slip velocity oscillations in the geometry. Figure 59 illustrates the difference in the size and morphology of the resolved structures between the filtered and resolved simulations.

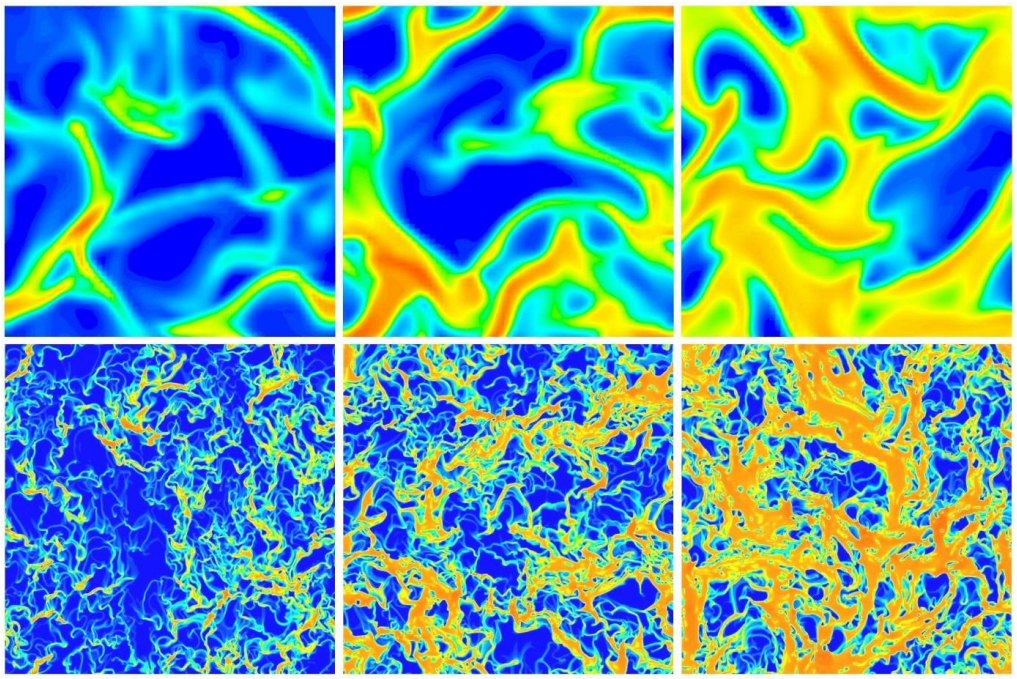

Figure 59 - Comparison of the resolved solids volume fraction field in the filtered coarse grid simulations (top) and the resolved fine grid simulations (bottom) for the three domain-averaged volume fractions considered. The blue-red colourmap range is 0-0.6.

As outlined earlier, the results in Figure 58 were generated from a domain that is twice as long as the square domain used in the resolved simulations to prevent the occasional formation of vertical gas channels. Since these channels mostly occurred in cases with larger filter/grid ratios, simulations could be carried out in the regular square domain for a filter/grid ratio of 1. Figure 60 adds these results to the data in Figure 58. Clearly, the difference between the green and yellow bars in Figure 58 is well within the standard deviations indicated on the graphs. No systematic difference is present with the domain-averaged slip velocity being slightly smaller in one case and slightly larger in the other two. Hence, it can be concluded that the decision to use a taller periodic domain does not introduce significant uncertainty into the study.

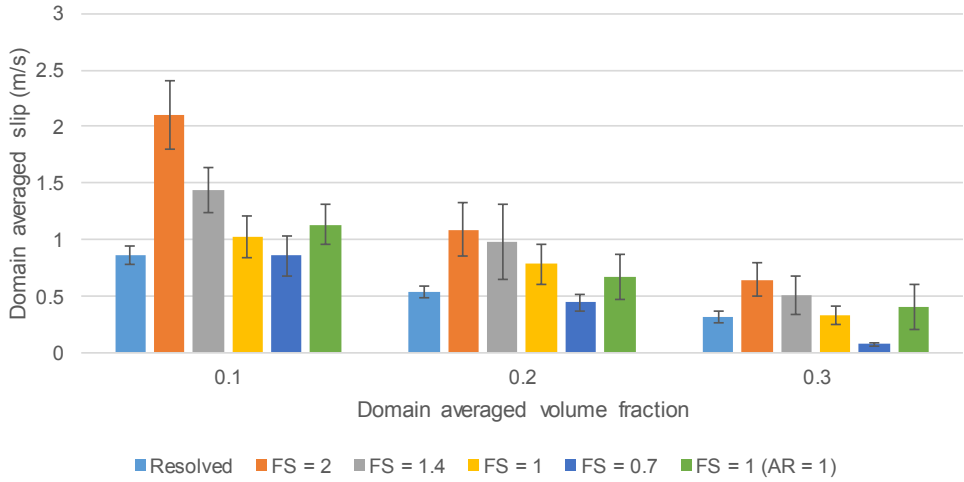

Figure 60 - Domain-averaged slip velocity results from Case 1 including cases completed in the original square geometry (AR = 1). The error bars represent the standard deviation in the temporal variation of the slip velocity over the averaging period. FS = filter/grid ratio.

Despite the good performance of the model at a filter/grid ratio around unity, comparisons between the volume fraction field in the filtered simulations and the filtered volume fraction field from the resolved simulations show significant qualitative differences. As shown in Figure 61, the filtered simulations generally give smoother and larger structures than the filtered resolved simulation data. This discrepancy is to be expected because a large portion of the variance in the filtered data is not explained by the models, as seen from the R^2 values substantially below unity during the *a priori* analyses performed in Chapter 3. Despite the qualitative differences in Figure 61, the predictive performance of the filtered model remains admirable, especially considering a simulation speedup factor in the order of 10^4 for the case considered in this section.

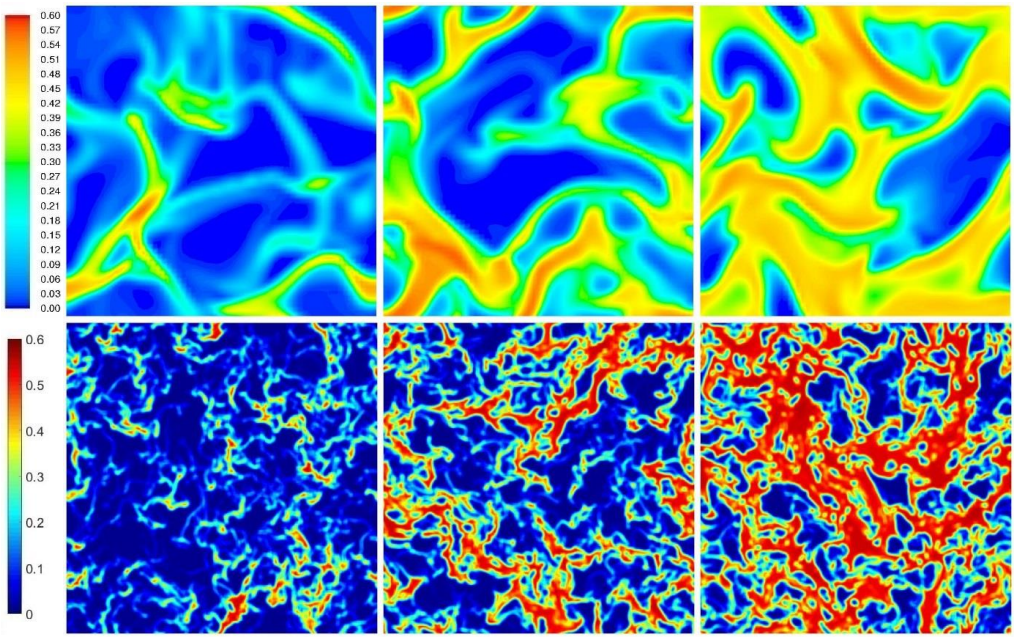

Figure 61 – Instantaneous solids volume fraction fields from the coarse grid simulation using the complete set of fTFM closures (top) and the resolved simulation results that were filtered (bottom) for domain-averaged solids volume fractions of 0.1 (left), 0.2 (middle) and 0.3 (right).

5.1.2 Case 2: Exclusion of the mesoscale interphase force

The mesoscale interphase force is generally accepted to be of lesser importance than the drag correction. In some cases [15, 18, 20] it is even neglected completely. As shown in Figure 62, for the case considered here this seems to be a reasonable assumption, although it may lead to moderate underpredictions of the interphase momentum exchange in dilute cases (e.g. filter/grid ratios of 1 and 1.4 for the domain-averaged volume fraction of 0.1). However, it should be noted that in Chapter 3.5 it was found that the relative importance of the mesoscale interphase force compared to the filtered drag force increased with increasing filter size. Therefore, the mesoscale interphase force may be of greater importance when coarser grids than 10 mm are considered.

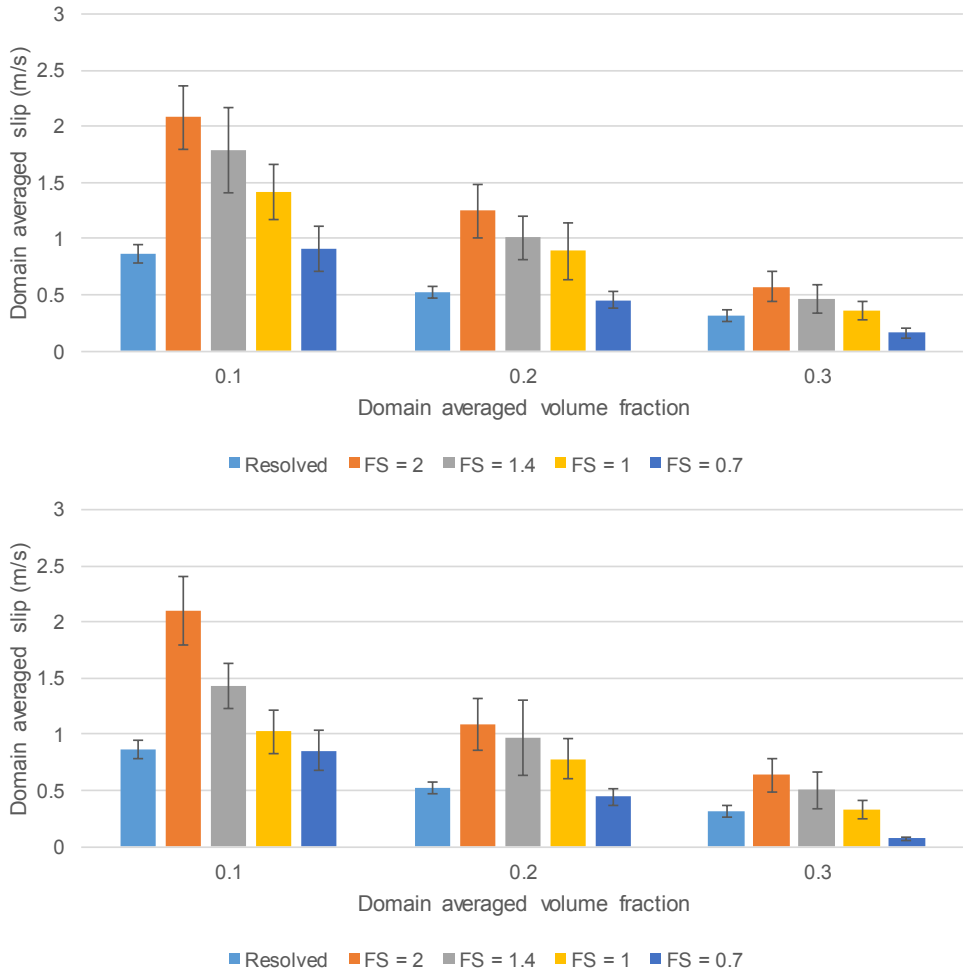

Figure 62 - Top: Domain-averaged slip velocity results from Case 2 in Table 5. The error bars represent the standard deviation in the temporal variation of the domain-averaged slip velocity over the averaging period. FS = filter/grid ratio. Bottom: Results from Case 1 for perspective.

5.1.3 Case 3: 2-marker drag model

As outlined in 3.4.2.5, the 2-marker closure for the adjusted slip velocity excludes the drift GPM used in the 3-marker closure. It is immediately evident from Figure 63 that this simplification has a large impact on model performance. Clearly, the 2-marker model predicts significantly smaller interphase momentum exchange than the 3-marker model, and substantially overpredicts the domain-averaged slip velocity even when the filter/grid ratio is smaller than unity.

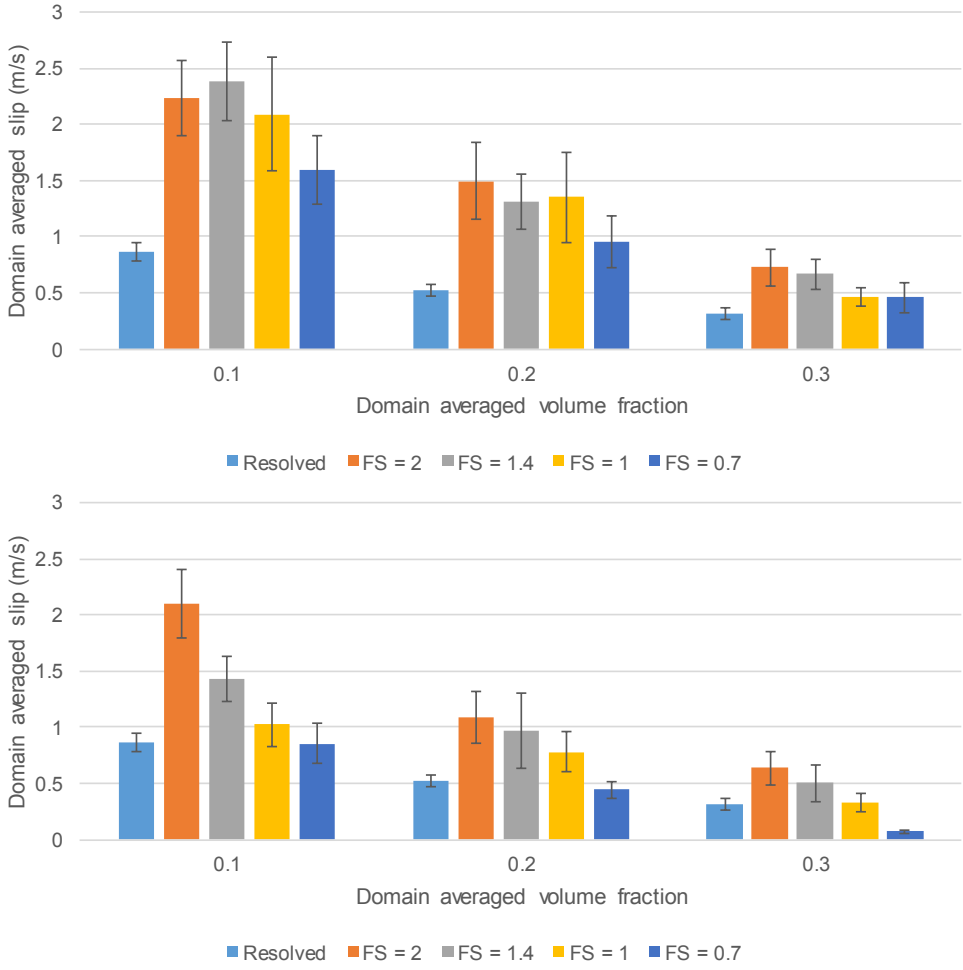

Figure 63 - Top: Domain-averaged slip velocity results from Case 3 in Table 5. The error bars represent the standard deviation in the temporal variation of the domain-averaged slip velocity over the averaging period. FS = filter/grid ratio. Bottom: Results from Case 1 for perspective.

The following explanation may be offered for the large decrease in the model performance when the drift GPM is neglected as independent variable: In general, the effect of an increasing drift GPM is to decrease the filtered drag force. The large difference in the performance of the 2- and 3-marker closures may therefore be related to the drift GPM being smaller in the filtered simulations than in the filtered data from the resolved simulation. This notion is confirmed in Figure 64 where it is shown that the drift GPMs calculated in the coarse grid simulations are generally substantially smaller than those from the filtered resolved simulation data.

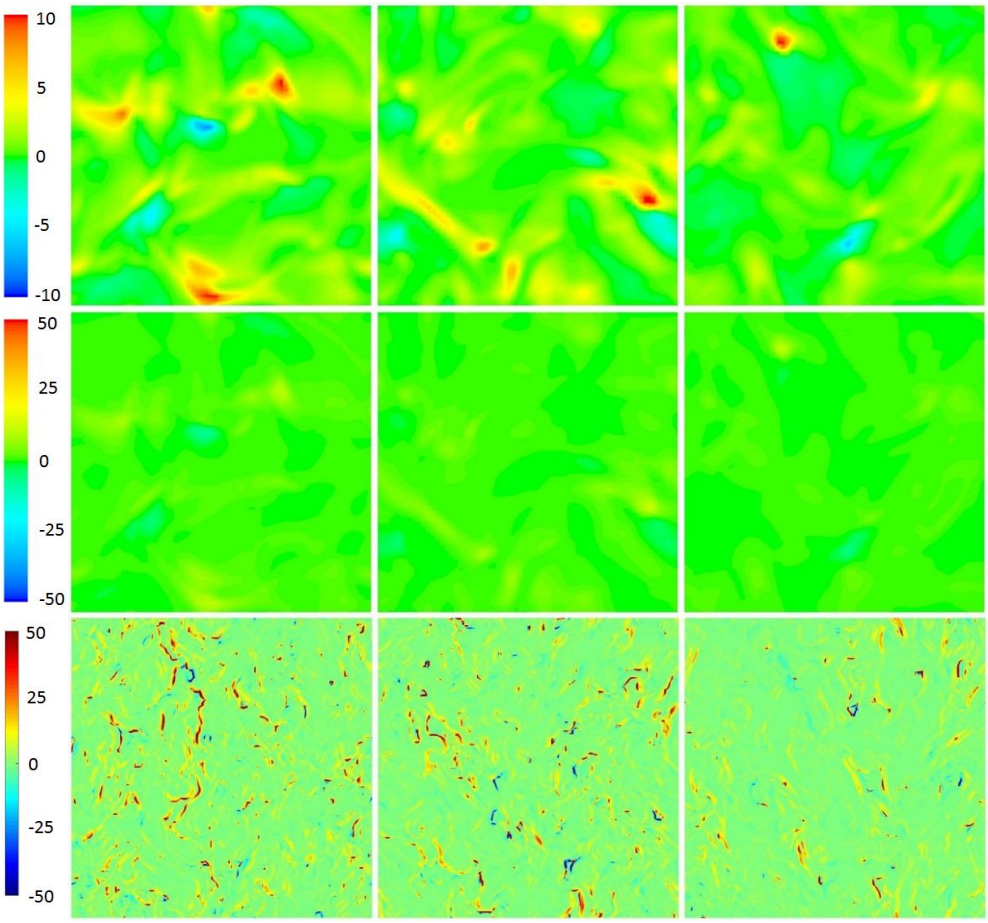

Figure 64 - Comparison of instantaneous vertical direction dimensionless drift GPMs from the coarse grid simulations (top two rows) and from the filtered resolved data (bottom row) for the same three instances as shown in Figure 61. The two rows of coarse grid images show the same data, but only using colourmaps of different ranges for better visualization.

The smaller drift GPM values observed in the coarse grid simulations must be due to the filtered models not explaining all the variance in the resolved simulation data, as discussed in Chapter 5.1.1. The filtered volume fraction field from the resolved simulations appears to be significantly more detailed with sharper gradients than the coarse grid simulations. The third marker (i.e., the drift GPM) therefore appears to be important to adjust for the inability of the filtered models to capture all the details in the filtered resolved data. In essence, the 2-marker model assumes the lower drag force that would occur in a situation with high volume fraction and velocity gradients, even when such large gradients are not resolved in the coarse grid simulation. This leads to an underprediction of the interphase momentum exchange rate.

5.1.4 Case 4: 1-marker drag model

As shown in Figure 65, the performance of the 1-marker model is much closer to the 3-marker model than the 2-marker model. Even though the slip prediction is still significantly larger in the most dilute case, the prediction is similar in the two denser cases.

This result questions the attractiveness of the filtered slip velocity as a marker. One potential challenge with this marker is that it removes most of the self-correcting nature of the drag force; i.e. larger slip velocities lead to larger drag forces, which then reduce the slip velocity. When the slip velocity is used as a marker, the binned data from resolved simulations suggests that the drag force becomes only weakly dependent on the slip velocity. This means that a small error in the model could potentially lead to a large error in the slip velocity. In this periodic case, for example, even a small error in the drag closure would require a large change in slip velocity to restore the balance between drag and gravity.

Furthermore, whereas the physical arguments for using the solids volume fraction and drift GPM are clear, it is more difficult to formulate a strong physical argument for using the slip velocity as marker. The solids volume fraction is a good marker because clustering can only occur at intermediate filtered volume fractions. Similarly, a large drift GPM indicates that the given cell is on the edge of a poorly resolved macro-cluster where the closure model should reduce the drag force. As discussed earlier (see Chapter 3.4.1.1), the filtered slip velocity correlates well with the drag correction, since they both result from the same physical mechanism of the gas tending to slip around dense solids clusters. As a result of this good correlation, it has been common practice to use the filtered slip velocity as a marker for the drag correction. However, given that larger filtered slip velocities are a result of drag reduction from the sub-grid clustering phenomena, rather than the cause, it is not technically suitable for use as an independent variable in the filtered drag closure. With regards to this, it can be noted that when a closure for the drag reduction resulting from clustering is derived from theoretical principles [20], it does not contain the filtered slip velocity as an independent variable. Future work will therefore explore a 2-marker model using the solids volume fraction and drift GPM as markers or other formulations that do not use the filtered slip velocity as a marker.

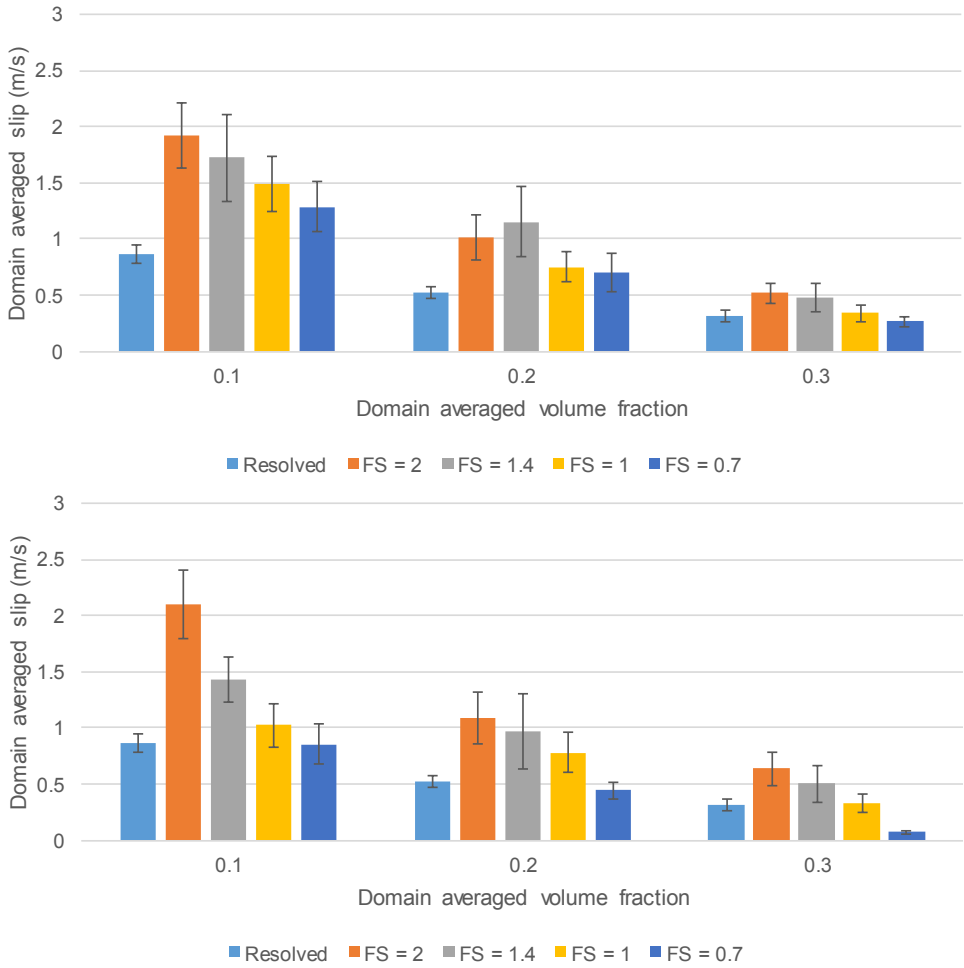

Figure 65 - Top: Domain-averaged slip velocity results from Case 4 in Table 5. The error bars represent the standard deviation in the temporal variation of the domain-averaged slip velocity over the averaging period. FS = filter/grid ratio. Bottom: Results from Case 1 for perspective.

5.1.5 Case 5: Isotropic drag model

Figure 66 shows that the isotropic drag model behaves similarly to the 2-marker model. This should be expected given that both models use the filtered solids volume fraction and filtered slip velocity as markers. The speculation about the risks of using the slip velocity as marker from the previous section therefore also applies to this model.

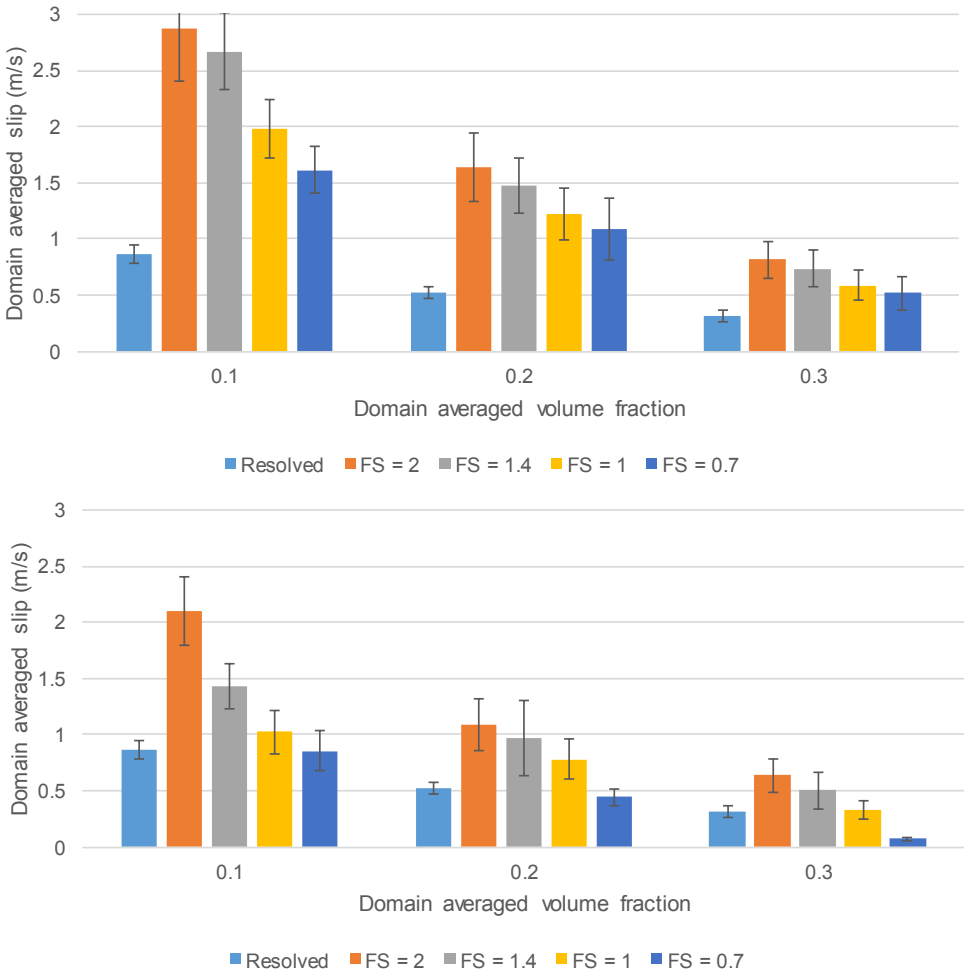

Figure 66 - Top: Domain-averaged slip velocity results from Case 5 in Table 5. The error bars represent the standard deviation in the temporal variation of the domain-averaged slip velocity over the averaging period. FS = filter/grid ratio. Bottom: Results from Case 1 for perspective.

Given that the isotropic model strongly overpredicts the drag in the lateral direction (see Figure 6), it was expected that this model would predict somewhat lower slip velocities than the 2-marker model. However, a comparison of Figure 63 and Figure 66 shows that the slip velocities from the isotropic model are even slightly higher than those from the 2-marker model. This implies that some other aspect of the model formulation more than cancels out the significant overprediction of the lateral direction drag.

Aside from using anisotropic closures, the 2-marker closure model also uses the adjusted slip velocity formulation with separate models for the nonlinearity correction factor, the adjusted slip velocity and the mesoscale interphase force. This more complex formulation therefore appears to improve the model performance slightly. Figure 67 illustrates the difference in the filtered interphase force prediction of these two models. The figure shows that the filtered slip velocity dependence of the

isotropic drag closure becomes weaker at higher slip velocities, which might explain the even larger overpredictions of the slip velocity compared to the 2-marker model.

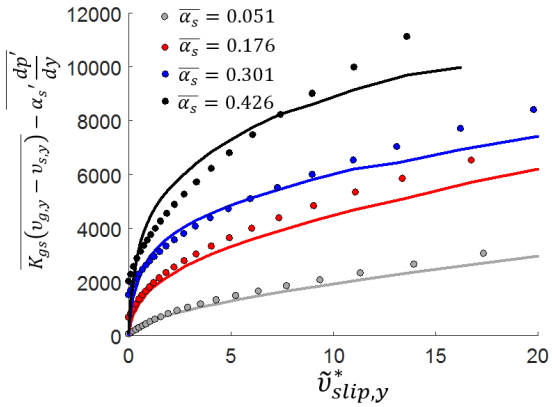

Figure 67 - Comparison of the vertical direction filtered interphase force (sum of the filtered drag and mesoscale interphase forces) predictions from the 2-marker anisotropic (circles) and isotropic (lines) drag closures as a function of scaled filtered slip velocity in the vertical direction.

5.1.6 Case 6: Boussinesq-based solids mesoscale stresses

As discussed in 3.6.2, use of the Boussinesq approximation to model the deviatoric component of the solids mesoscale stress tensor is an erroneous assumption. Even though this approach shows a negative coefficient of determination compared to the sample data, the slip velocity comparison in Figure 68 does not show such a large mismatch with the anisotropic stress closure. This could simply be due to the relatively small (10 mm) cell size employed in these simulations. The solids mesoscale stresses increase super-linearly with filter size, whereas the filtered drag force decreases with filter size, implying that the effect of the solids mesoscale stress closure will become more apparent at larger cell sizes.

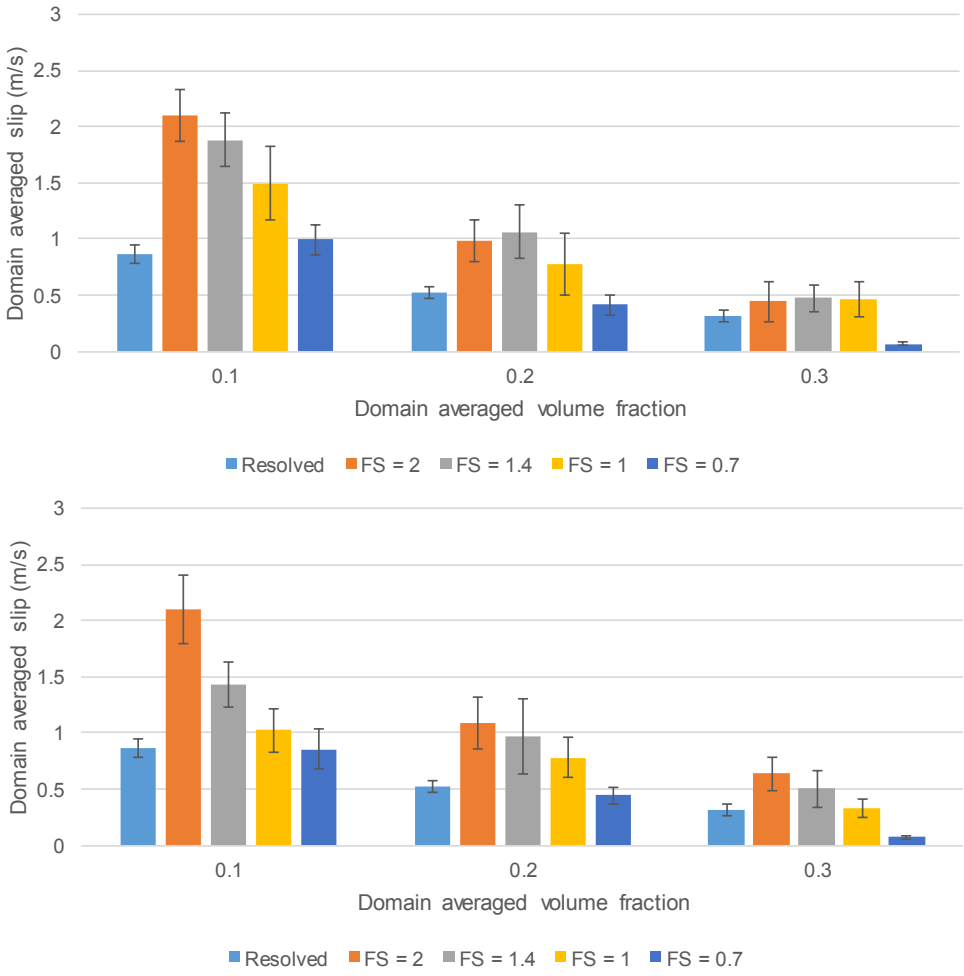

Figure 68 - Top: Domain-averaged slip velocity results from Case 6 in Table 5. The error bars represent the standard deviation in the temporal variation of the domain-averaged slip velocity over the averaging period. FS = filter/grid ratio. Bottom: Results from Case 1 for perspective.

It can be noted that even though the overall effect of the solids mesoscale stress closure appears to be significantly smaller than the filtered drag force closure, the dynamic behaviour of the clusters changed significantly when the Boussinesq approximation was employed. As may be expected, the flow behaviour became more viscous with the Boussinesq-based closure due to the added solids viscosity, although macro-scale clusters were resolved with similar sharpness as when the anisotropic solids mesoscale stress closure was used.

5.1.7 Case 7: No filtered stresses

A simple test of the effect of solids mesoscale stress closures is to simply neglect these models. Figure 69 shows that removal of the mesoscale stress model only slightly increased the slip velocity. As discussed in the previous section, it is likely that the effect of mesoscale stresses is relatively small on this cell size and may be substantially larger on coarser grids. In any case, an increase in domain-

averaged slip velocity when solids stresses are neglected may be expected given that the lack of momentum dispersion would allow the gas to more easily slip around the macro-clusters.

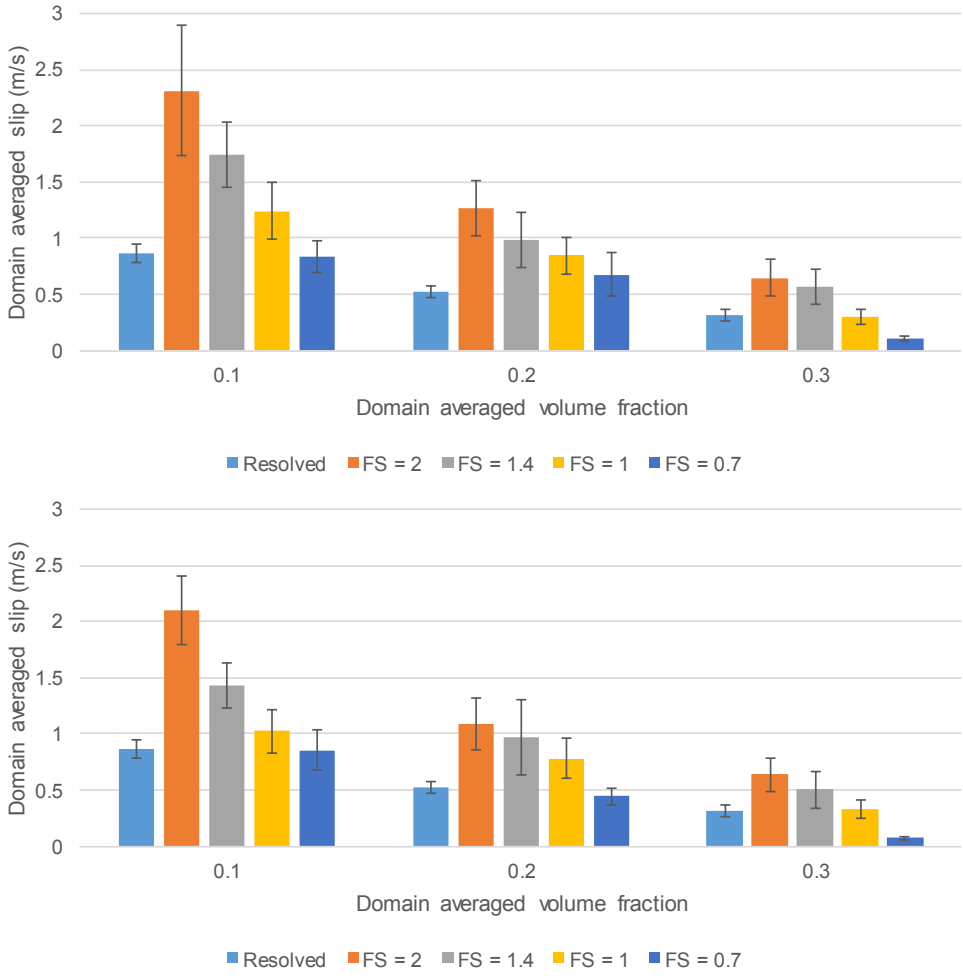

Figure 69 - Top: Domain-averaged slip velocity results from Case 7 in Table 5. The error bars represent the standard deviation in the temporal variation of the domain-averaged slip velocity over the averaging period. FS = filter/grid ratio. Bottom: Results from Case 1 for perspective.

5.1.8 Case 8: Standard frictional pressure and viscosity models

The lack of a filtered model for the deviatoric component of the frictional stress tensor is a shortcoming of the present model formulation. As explained in Chapter 3.7.3, deriving such a model could be difficult considering the limited impact that such a closure is expected to have in most cases. To test this assumption, the simulations were run using the standard (not filtered) closures for frictional pressure and viscosity [35, 42]. This would be another option when filtered closures for the frictional stresses are not available. Figure 70 confirms that the effect of frictional stress modelling is indeed relatively small.

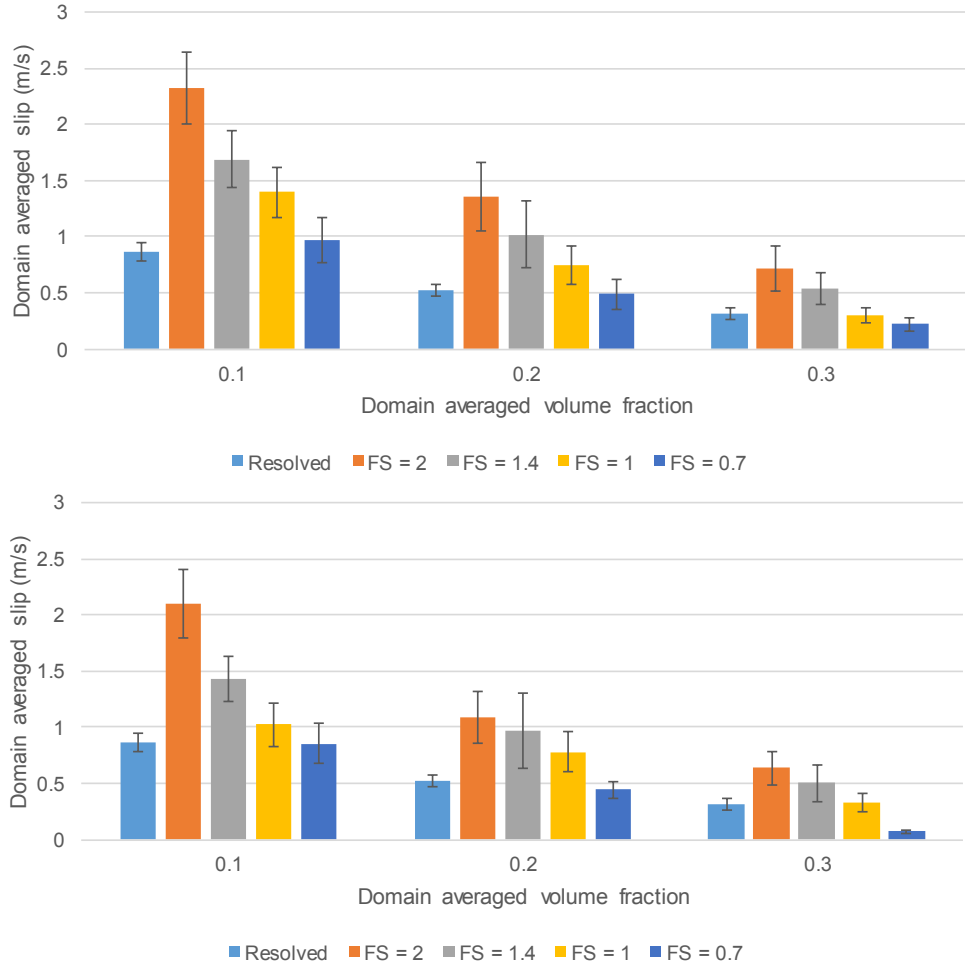

Figure 70 - Top: Domain-averaged slip velocity results from Case 8 in Table 5. The error bars represent the standard deviation in the temporal variation of the domain-averaged slip velocity over the averaging period. FS = filter/grid ratio. Bottom: Results from Case 1 for perspective.

5.1.9 Cases 9 & 10: Effect of granular temperature modelling

In the present study, the filtered kinetic theory stresses are approximated using the microscopic closures used in the resolved simulations with the unfiltered granular temperature. This is done under the assumption that the effect of the filtered kinetic theory stresses will be small for the filter sizes considered in the present study. To quantify the effect of incorporating the KTGF stresses in this way, simulations were run with commonly used approximations of the granular temperature: neglecting convection and diffusion of granular temperature (see the second term on the left-hand side and the second term on the right-hand side of Equation 6) to turn the conservation equation into an algebraic formulation (Case 9), and completely neglecting the KTGF (Case 10). As illustrated in Figure 71, the effect of KTGF stresses was insignificantly small, even in this case using a relatively small cell size.

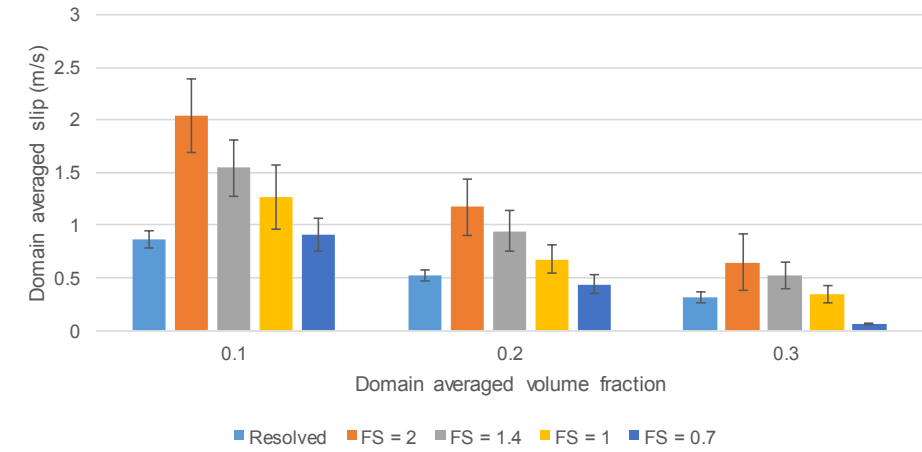

.

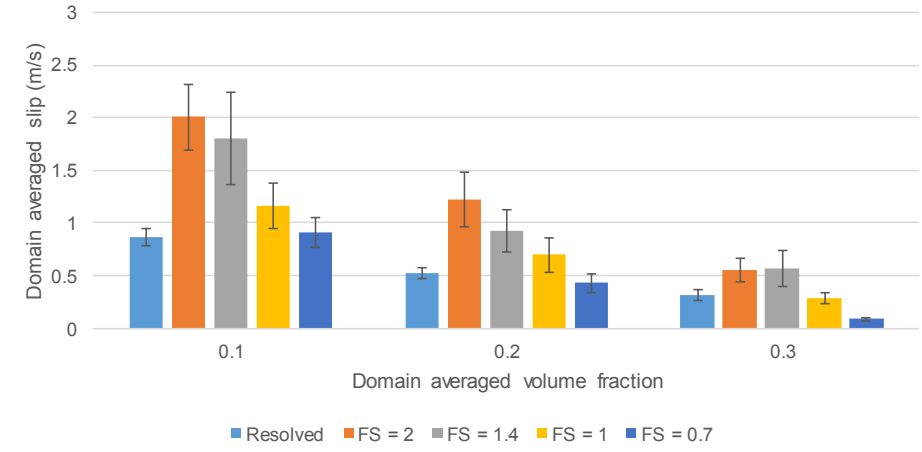

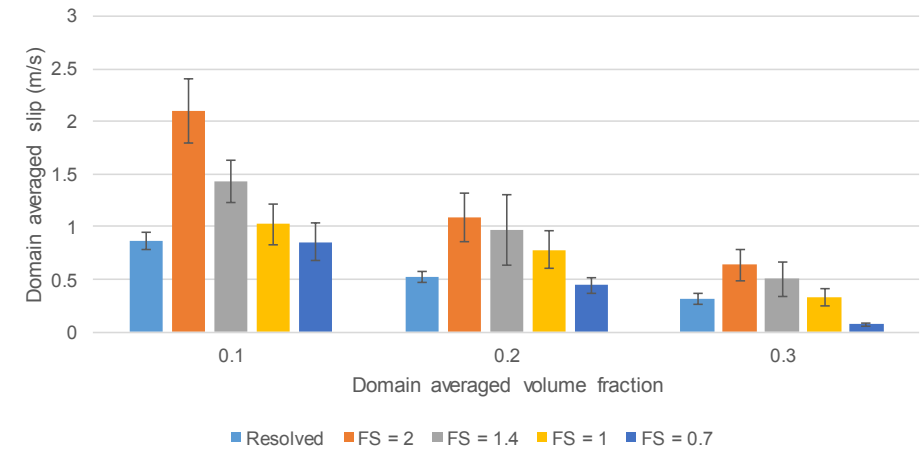

Figure 71 - Domain-averaged slip velocity results from Case 9 (middle) and Case 10 (top) in Table 5. The error bars represent the standard deviation in the temporal variation of the domain-averaged slip velocity over the averaging period. FS = filter/grid ratio. Bottom: Results from Case 1 for perspective.

Interestingly, the case implementing the granular temperature conservation as an algebraic formulation was the most stable numerically, suggesting that this should be the preferred KTGF option in filtered simulations

5.2 Verification in wall-bounded domains

In this section, the fTFM closures developed in this study, which were derived from resolved simulations performed in fully-periodic domains, were also verified against dedicated resolved simulations carried out in wall-bounded domains. Two resolved simulations were completed using the same cell size (0.625 mm) as the periodic resolved simulations:

1. A bubbling fluidized bed where the fluidization velocity (0.086 m/s) was taken as the geometric mean between the minimum fluidization velocity and the critical fluidization velocity (where turbulent fluidization starts) [58]. This geometry was 0.48 m wide and 0.8 m tall.
2. A turbulent fluidized bed where the fluidization velocity (1.171 m/s) was set equal to the critical velocity [58]. This geometry was 0.32 m wide and 1.2 m tall.

Both geometries were simple rectangles with a velocity inlet on the bottom face, a pressure outlet on the top face, and walls on the side faces. For the turbulent case, a significant amount of solids reached the outlet in some cases and these solids were recirculated back to the inlet at the bottom of the domain to keep the mass in the fluidized bed constant. At the walls, a no-slip boundary condition is specified for the gas phase and a free-slip boundary condition for the solids phase. The presence of a wall has an important effect on the mesoscale structures by confining the flow and thereby altering the heterogeneity. The purpose of the verification in this section is to test whether the closure models developed in the present study are able to accurately predict the flow behaviour under such conditions. Consequently, a free-slip wall will be sufficient to include the confining effect of the walls.

Different combinations of the fTFM closures developed in this study were tested in these two geometries on three different computational cell sizes: 10 mm, 20 mm and 40 mm. In order to simplify the comparison, the filter/grid ratio was adjusted for each case so that the bed expansion of the bubbling case on the 10 mm grid matched well with the resolved simulation. This same filter/grid ratio was then also used on the other grids and the turbulent case to evaluate model generality. The different cases with their respective filter/grid ratios are summarized in Table 6. It should be noted that the 1-marker, 2-marker and 3-marker filtered drag force closures refer to the anisotropic adjusted slip velocity closures developed in Chapter 3.4.2. The non-linearity correction factor closure of the Chapter 3.4.2.3 and the mesoscale interphase force closure of Chapter 3.5.1 are used in combination with these filtered drag force closures.

All cases were run with the filtered frictional pressure closure, except for Case 6 where all filtered stresses were deactivated. In all cases the filtered KTGF stresses were approximated by using the same closures as in the resolved simulations in combination with the PDE for the unfiltered granular temperature.

After attaining a pseudo-steady state, the bubbling cases were averaged for 30 s and the turbulent cases for 15 s. Time averages for velocities and reactant concentrations were phase-weighted in both the resolved and coarse grid simulations to correctly assign more weight to instances with high volume fractions and allow a direct comparison between the resolved and filtered simulation results.

Table 6 - Summary of the cases investigated in the wall-bounded verification study.

Case	Filtered drag force closure	Solids mesoscale stress closure	Filter/grid ratio
1	3-marker	Anisotropic	1.8
2	2-marker	Anisotropic	1.0
3	1-marker	Anisotropic	1.1
4	Isotropic	Anisotropic	2.3
5	3-marker	Boussinesq	2.5
6	3-marker	None	1.7
7	Isotropic	Boussinesq	3.0

5.2.1 Case 1: Complete model

The performance of the complete model in the bubbling case is summarized in Figure 72. A distinct feature of this case is the asymmetric flow pattern that developed in the geometry where the gas prefers to rise on one side of the domain. This behaviour persisted for long simulation times and is likely related to the dimensions of the geometry. This asymmetric flow pattern is also predicted by the filtered simulations.

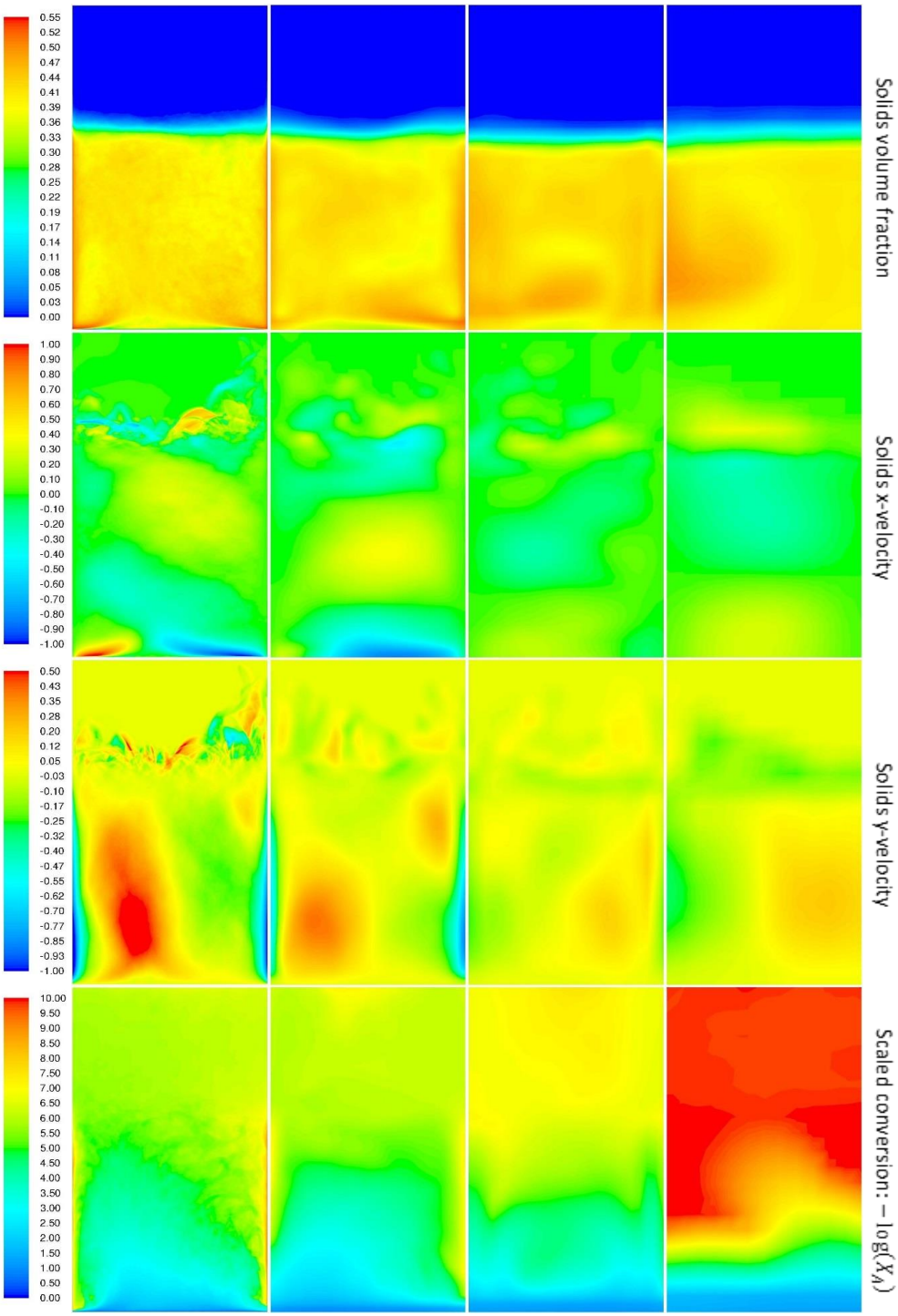

Figure 72 - Time-averaged contour plots for Case 1 (bubbling). In each row, the contours from left to right represent the resolved case, the 10 mm grid, the 20 mm grid, and the 40 mm grid.

In general, the bed expansion is predicted very well on all grids, indicating good grid independence behaviour. However, the reactant conversion is increasingly overpredicted on coarser grids. The erroneous prediction of the reactions show the importance of resolving at least some of the macro-scale flow behaviour. It is clear from the y-velocity profiles that the coarser grids no longer resolve the large downwards velocities taking place at the walls. This back-mixing behaviour forces the gas to rise more rapidly in the centre of the domain, thus shortening the gas residence time. If this macro-scale flow pattern is no longer captured, the gas residence time is overpredicted, leading to a significant overprediction in reactant conversion. It can therefore be concluded that in some cases it may be required to refine the grid for specific regions in coarse grid simulations to capture the macro-scale flow features, even in case good fTFM closures are being used. However, it should also be noted that the free-slip boundary condition for the solids phase specified for these verification simulations over emphasises the effect of the downflow near the wall. More realistic partial-slip boundary conditions would alleviate this problem to some degree, but this was not explored in the present study.

Despite the inaccuracy on the coarsest grids, the performance of the complete model setup shown in Figure 72 is very good. The 10 mm grid shows an especially close match in all the time-averaged contour plots. As mentioned in Chapter 5.1, this fTFM simulation already allows for a speedup (in terms of computation time) in the order of 10^4. The two further doublings of the cell size from this benchmark each bring about one order of magnitude of additional speedup. The imperfect performance of the 40 mm grid is also understandable given that this geometry contains only 240 computational cells.

Further perspective is given by Figure 73 where the model behaviour without any fTFM closures is illustrated. The complete failure of the simulations without fTFM closures is immediately evident. Almost no clustering behaviour could be resolved, leading to a very large overexpansion of the bed and overprediction of the reactant conversion. This result confirms the critical importance of fTFM closures in coarse grid simulations of Geldart A powders.

Model performance in the turbulent fluidization regime is summarized in Figure 74. Note that, due to time constraints, the resolved simulation in this case could only be averaged for 4 s, whereas the coarse grid simulations were averaged for 15 s. Reasonable agreement with the resolved simulation data is observed, indicating that the fTFM closures scale well to this much more dilute flow situation. It is possible that the time-averaged y-velocity contours will become more uniform with 15 s of averaging to produce a closer match with the coarse grid simulations.

The coarse grid simulations also show good grid independence behaviour in the turbulent case, although the 40 mm case again fails to resolve the large downflows at the walls. A slight underprediction in the bed expansion ratio and reactant conversion is observed, which might be related to the effect of the geometry width on the required filter/grid ratio as discussed next.

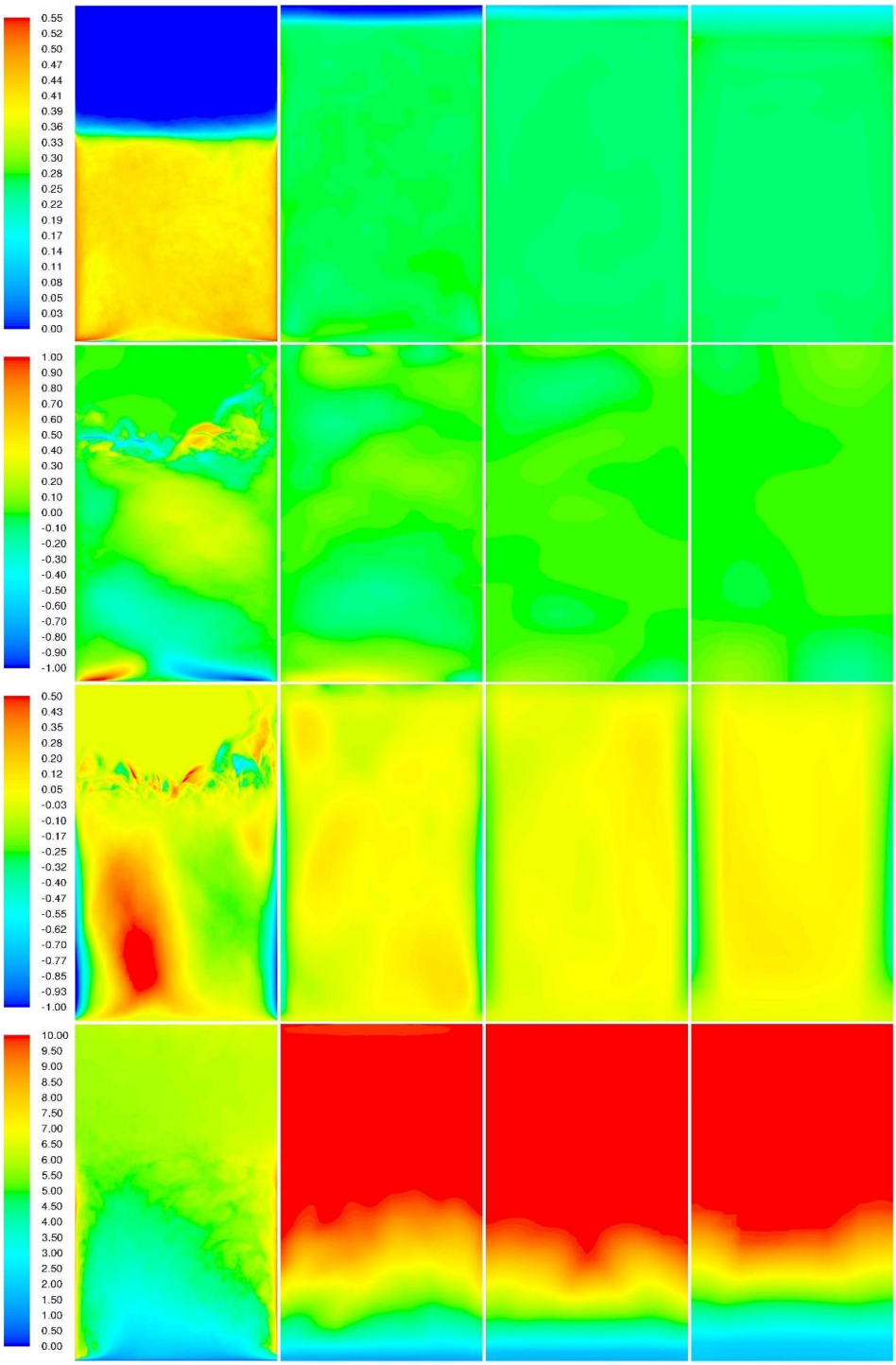

Figure 73 - Time-averaged contour plots without using fTFM closures (bubbling regime). In each row, the contours from left to right represent the resolved case, the 10 mm grid, the 20 mm grid, and the 40 mm grid.

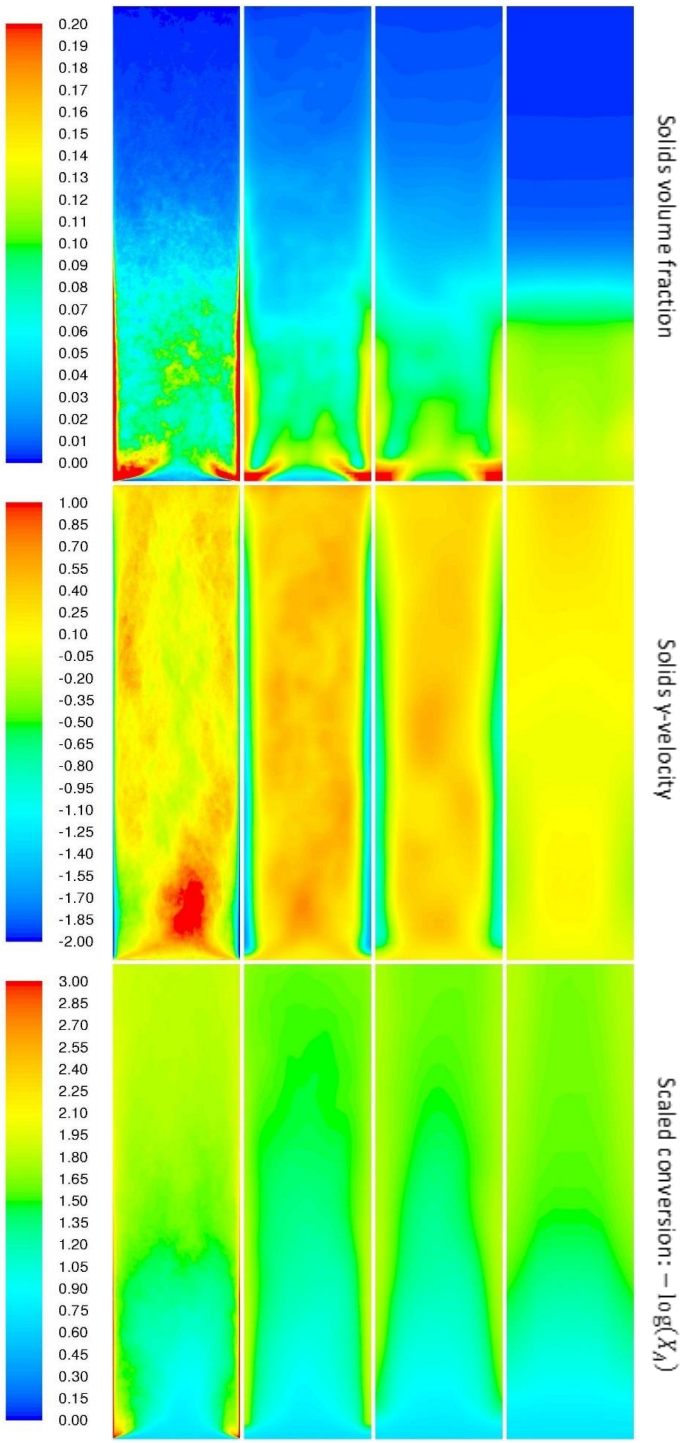

Figure 74 - Time-averaged contour plots for Case 1 (turbulent regime). In each row, the contours from left to right represent the resolved case, the 10 mm grid, the 20 mm grid, and the 40 mm grid.

One interesting feature of these results is that a larger filter/grid ratio (i.e., 1.8) was required to obtain good results compared to the filter/grid ratio around unity recommended in Chapter 4.1.4 and Chapter 5.1. Use of a filter/grid ratio of unity results in significant overexpansion of the bed. This feature is also shared by the other cases to be presented later in this section.

To shed further light on this issue, Figure 75 compares data from the turbulent wall-bounded case to two periodic cases carried out using the same model setup, cell size and filter/grid ratio, as well as a similar domain-averaged volume fraction (0.1) as the bed region of the verification case. Clearly, the width of the fully-periodic domain has a large impact on the degree of resolution of the macro-clusters in the filtered simulations. Macro-clusters in the narrow periodic domain are generally less dense (as observed from the instantaneous solids volume fraction contours), resulting in a lower root mean square error (RMSE) of the solids volume fraction.

The domain-averaged vertical direction slip velocity in the narrow periodic domain (1.08 m/s) is also much lower than in the standard periodic case (1.88 m/s). Interestingly, the slip velocity in the narrow periodic domain with a filter/grid ratio of 1.8 is close to the slip velocity of 1.02 m/s in the wider geometry at a filter/grid ratio of 1 (see Figure 58). This gives further confidence that the increase in filter/grid ratio is required primarily because of the narrower geometry.

The effect of the domain width on the degree of macro-cluster resolution is related to the size of the macro-clusters. From the wider periodic domain in Figure 75, it can be observed that the macro-clusters can become larger than the width of the narrower domain. This implies that, in the narrower domain, the gas path through the resolved solids flow field is constrained so that gas often has to pass through the macro-clusters instead of around them. Naturally, this artificially increases the degree of momentum coupling, thus requiring more filtering (a larger filter/grid ratio) to compensate.

It is important to note that this is not a wall effect, but rather an effect of the relative size of the macro-clusters to the domain width. Since the filtered closures were derived in a wider domain than the domain used in the verification case, this effect became significant. Further studies, such as a filtering the resolved data from the wall-bounded verification case and analysing it in detail, will be required to fully understand this effect.

Given that the clusters in the narrower periodic domain are still more resolved than the lower region of the wall-bounded turbulent case, it may be that the boundary conditions also have an effect. For example, the macro-clusters forming in the periodic case have (theoretically) an infinite amount of time to develop, whereas the macro-clusters in the wall-bounded case are continuously influenced by the solid walls and the uniform gas inlet. Again, further work will be required to better understand this effect.

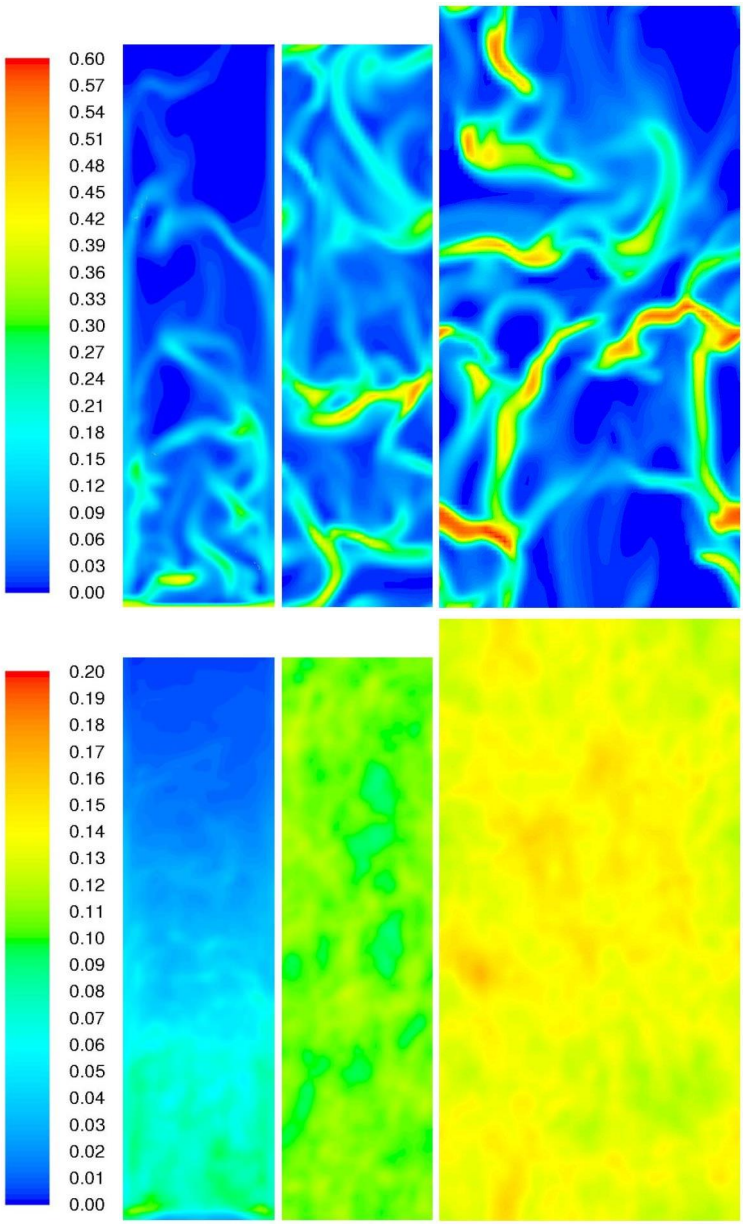

Figure 75 - Top row: Instantaneous solids volume fraction contours illustrating macro-cluster formation in three cases: the turbulent wall-bounded verification case (left), a fully-periodic simulation using the same domain size as the turbulent verification case (middle), and the domain used in the fully-periodic verification study in Chapter 5.1 (right). All simulations were run on a 10 mm cell size with a filter/grid ratio of 1.8. Bottom row: Root mean square error (RMSE) contours determined over 15 s of averaging in the same three cases.

5.2.2 Case 2: 2-marker drag model

The performance of the 2-marker drag model in the bubbling verification case is summarized in Figure 76. Similar to the 3-marker model, this model also shows good grid independence behaviour and

captures the asymmetric flow pattern developing in the bed. One significant difference is the higher reactant conversion resulting from the smaller filter/grid ratio that had to be employed in this case.

The explanation behind the smaller filter/grid ratio required by the 2-marker model relative to the 3-marker model is the same as outlined in Chapter 5.1.3 for the periodic verification study. Low drift GPMs were observed in the filtered cases, leading to a higher drag force prediction by the 3-marker model. However, the large drift GPMs from the resolved periodic simulations are averaged into the 2-marker closure model, causing an underprediction of the drag in cases where the drift GPM is low.

Figure 77 displays the performance of the 2-marker model in the turbulent case. Although reasonable grid independence behaviour is observed, a significantly denser bed is predicted than for the 3-marker model in Figure 74. This results in a somewhat less accurate comparison to the resolved case. Specifically, the resolved simulation predicts an average solids volume fraction of 0.108 in the bottom quarter of the domain. The 2-marker and 3-marker models, respectively, predict values of 0.116 and 0.104 on the 10mm grid and values of 0.128 and 0.108 on the 20mm grid. The more dilute turbulent case therefore appears to emphasize model shortcomings more strongly than the denser bubbling case.

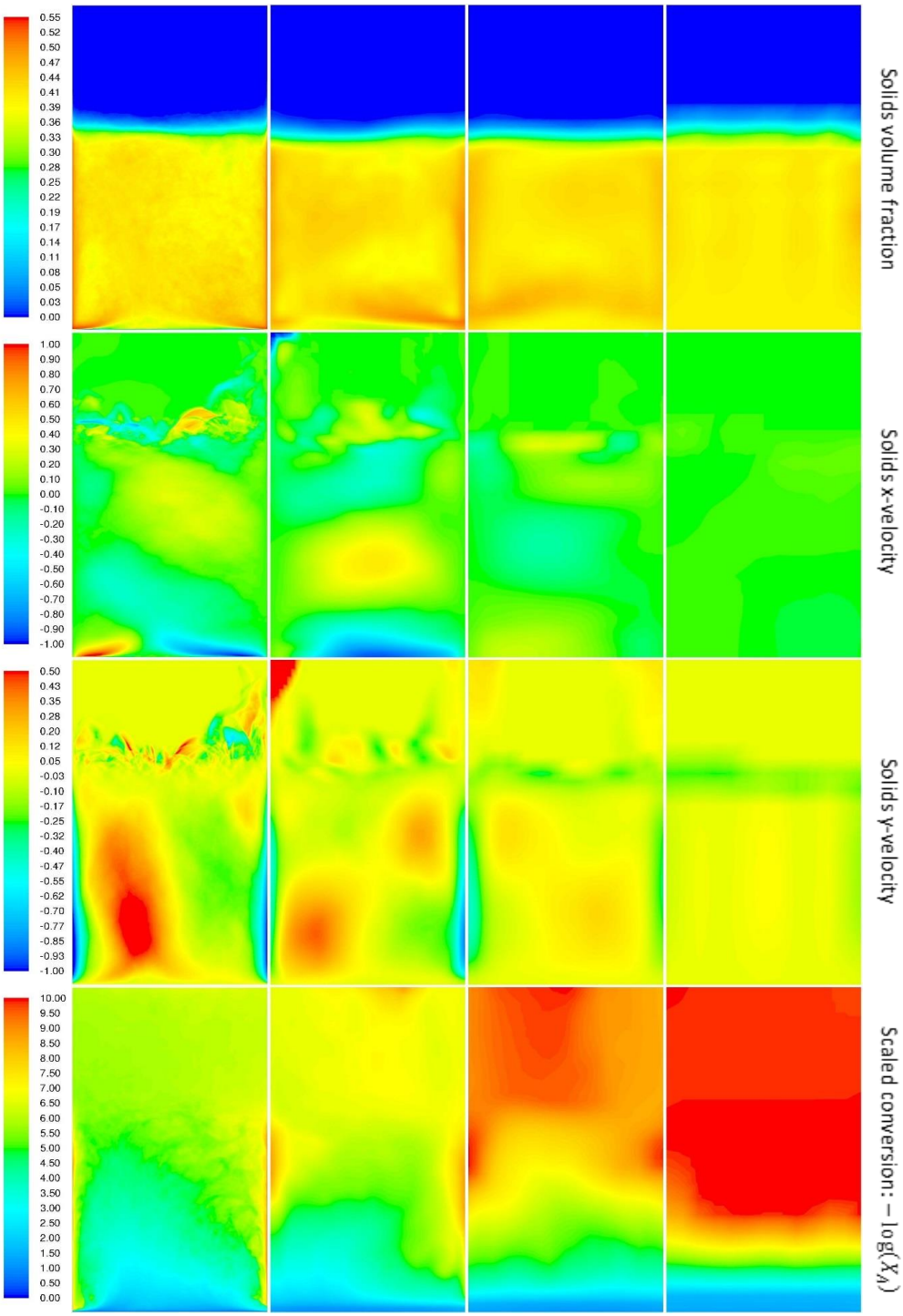

Figure 76 - Time-averaged contour plots for Case 2 (bubbling regime). In each row, the contours from left to right represent the resolved case, the 10 mm grid, the 20 mm grid, and the 40 mm grid.

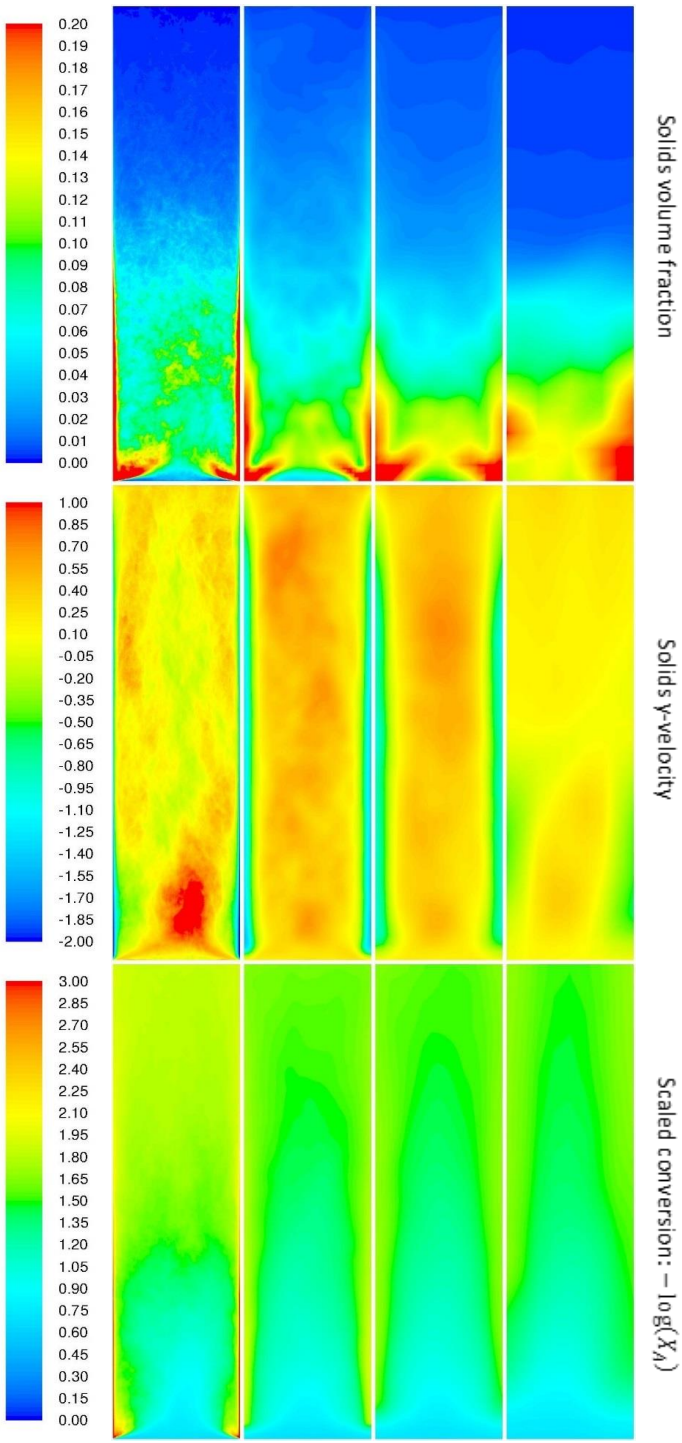

Figure 77 - Time-averaged contour plots for Case 2 (turbulent regime). In each row, the contours from left to right represent the resolved case, the 10 mm grid, the 20 mm grid, and the 40 mm grid.

5.2.3 Case 3: 1-marker model

Figure 78 illustrates the performance of the 1-marker model in the bubbling case. Similar to the other two anisotropic drag models, grid independence behaviour is good for the bed expansion, but the reactant conversion is increasingly overpredicted on coarser grids as the downward flow at the walls is no longer resolved.

This model required a filter/grid ratio just marginally higher than the 2-marker model and significantly lower than the 3-marker model. The same explanation is valid for this case where the large drift GPMs in the resolved periodic simulations are also averaged into the model, leading to underpredictions of the filtered drag force when the drift GPM is low.

The turbulent case in Figure 79 shows a high degree of similarity with the 3-marker model (Figure 74), except on the coarsest mesh where a substantially larger bed expansion is predicted. Overall, the 1-marker model outperforms the 2-marker model in this verification test. As discussed in Chapter 5.1.4, this result questions the attractiveness of the filtered slip velocity as a second marker for the filtered drag force closure, suggesting that a 2-marker closure using the filtered solids volume fraction and the drift GPM may be an interesting topic for future work.

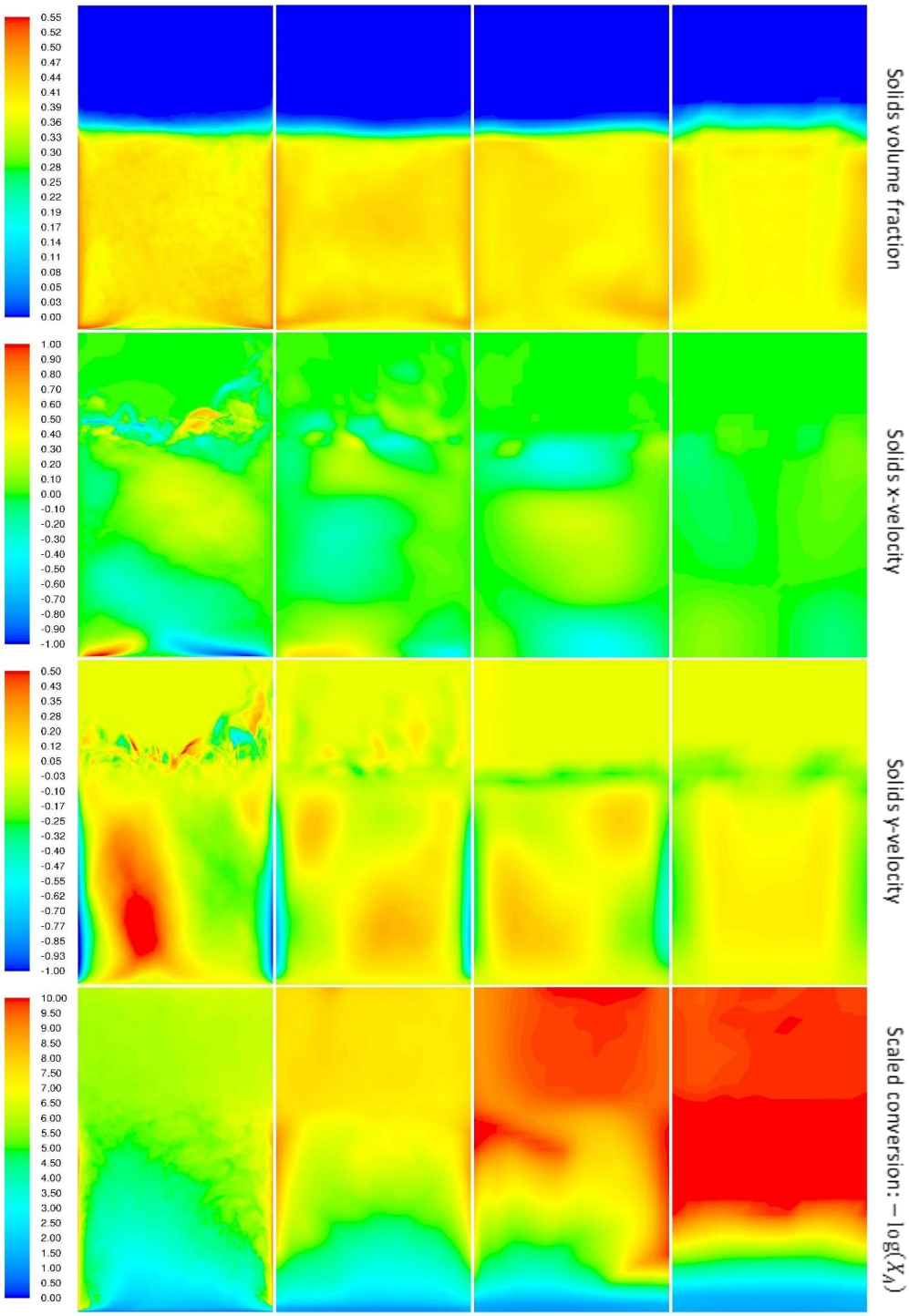

Figure 78 - Time-averaged contour plots for Case 3 (bubbling). In each row, the contours from left to right represent the resolved case, the 10 mm grid, the 20 mm grid, and the 40 mm grid.

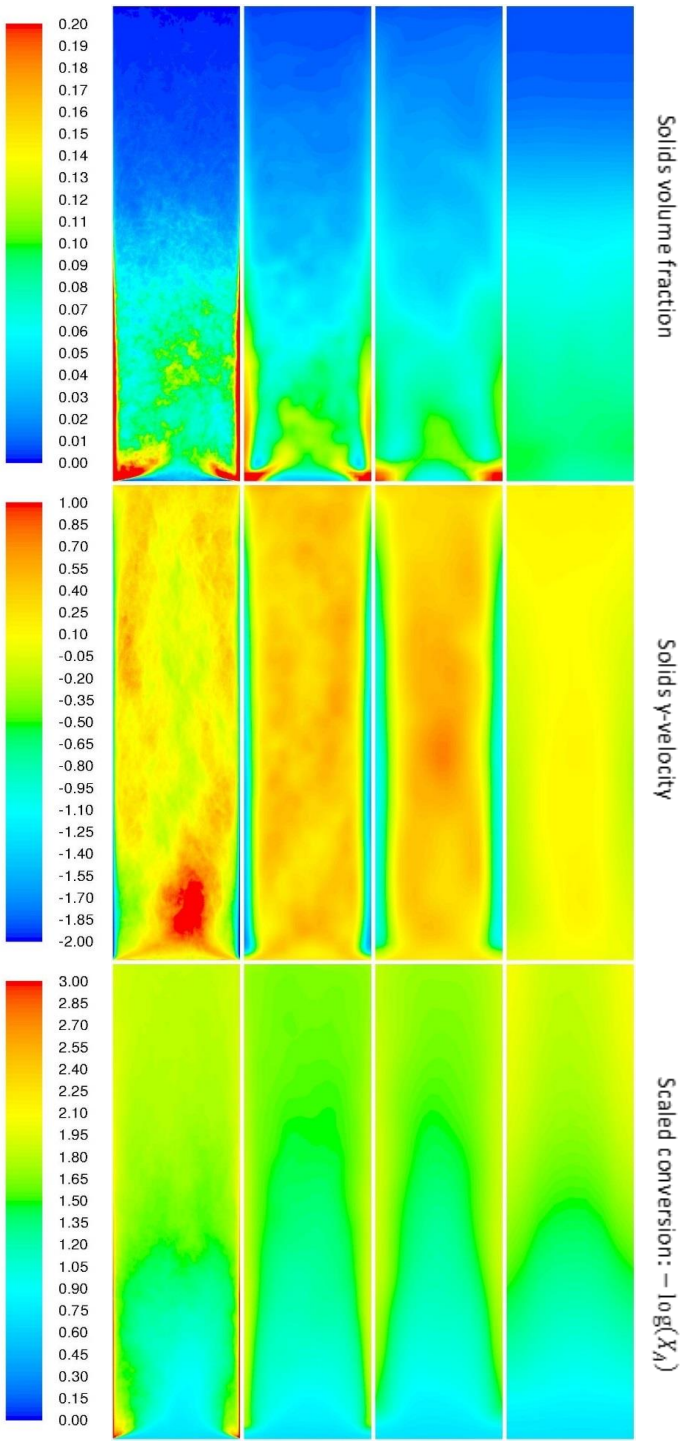

Figure 79 - Time-averaged contour plots for Case 3 (turbulent). In each row, the contours from left to right represent the resolved case, the 10 mm grid, the 20 mm grid, and the 40 mm grid.

5.2.4 Case 4: Isotropic drag model

As shown in Figure 80 and Figure 81, the isotropic drag model shows a gradual expansion of the bed with increasing grid size. Clearly, grid independence behaviour is significantly worse than the anisotropic drag models discussed in the previous three sections. A possible explanation for this is because, as discussed in Chapter 3.4.2.1, the isotropic drag closure will tend to increasingly overpredict the filtered drag force in the lateral directions as the filter size is increased. This increase in lateral drag forces makes it more difficult for the gas to slip around macro-clusters, resulting in proportionally more gas passing through the macro-clusters in the vertical direction. This then increases the effective vertical drag, explaining the increase in the bed expansion with increasing grid size seen in Figure 80 and Figure 81.

The generalizability between the bubbling and turbulent cases is also significantly worse than for the anisotropic models. This is especially evident in the 10 mm case where the bed expansion is strongly underpredicted in the turbulent case. The grid dependency improves the bed expansion prediction as the grid is coarsened. Finally, the 10 mm bubbling case showed a highly skewed flow behaviour that differs significantly from the resolved simulation. This is because the bubbling case experiences a strong circulating flow pattern with significant lateral velocities observed. Since the isotropic drag closure will poorly predict the lateral direction drag forces, which are highly significant in this case, the isotropic drag model cannot accurately predict this circulating flow behaviour.

Another interesting point is the very large difference in the filter/grid ratio required in this case (2.3) and in the periodic case (where even a filter/grid ratio of 0.7 overpredicted the slip velocity by more than 100% as shown in Figure 66). In comparison to the anisotropic drag models, this difference in the required filter/grid ratios is much larger, further increasing the uncertainty related to this model parameter.

Overall, these results clearly illustrate the merits of the anisotropic adjusted slip velocity formulation for the filtered drag force outlined in Chapter 3.4.2.2. In comparison to the conventional isotropic drag approach, all three anisotropic formulations considered in this study offer clear improvements in terms of accuracy and generality with regard to grid size and flow situation.

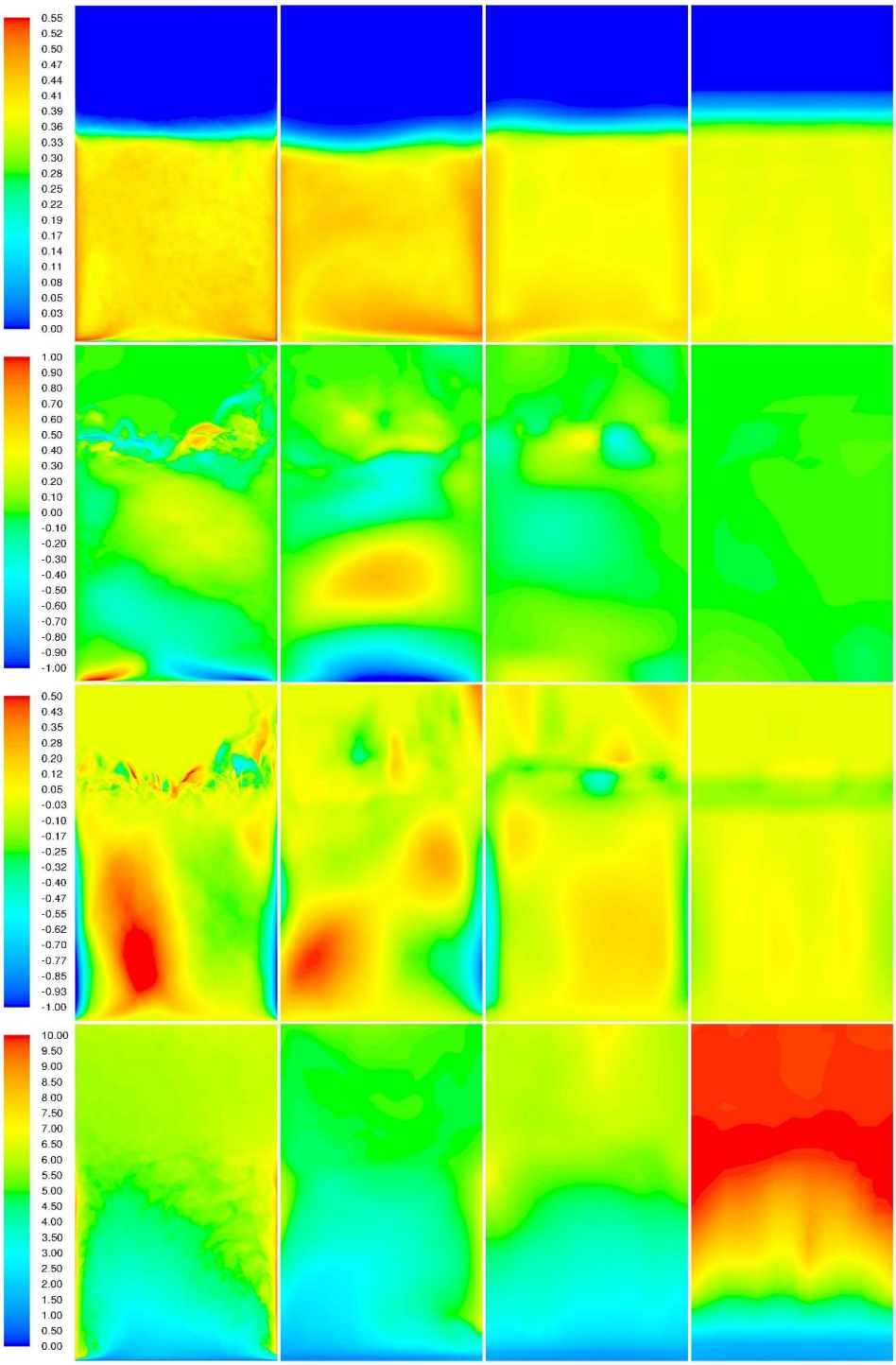

Figure 80 - Time-averaged contour plots for Case 4 (bubbling). In each row, the contours from left to right represent the resolved case, the 10 mm grid, the 20 mm grid, and the 40 mm grid.

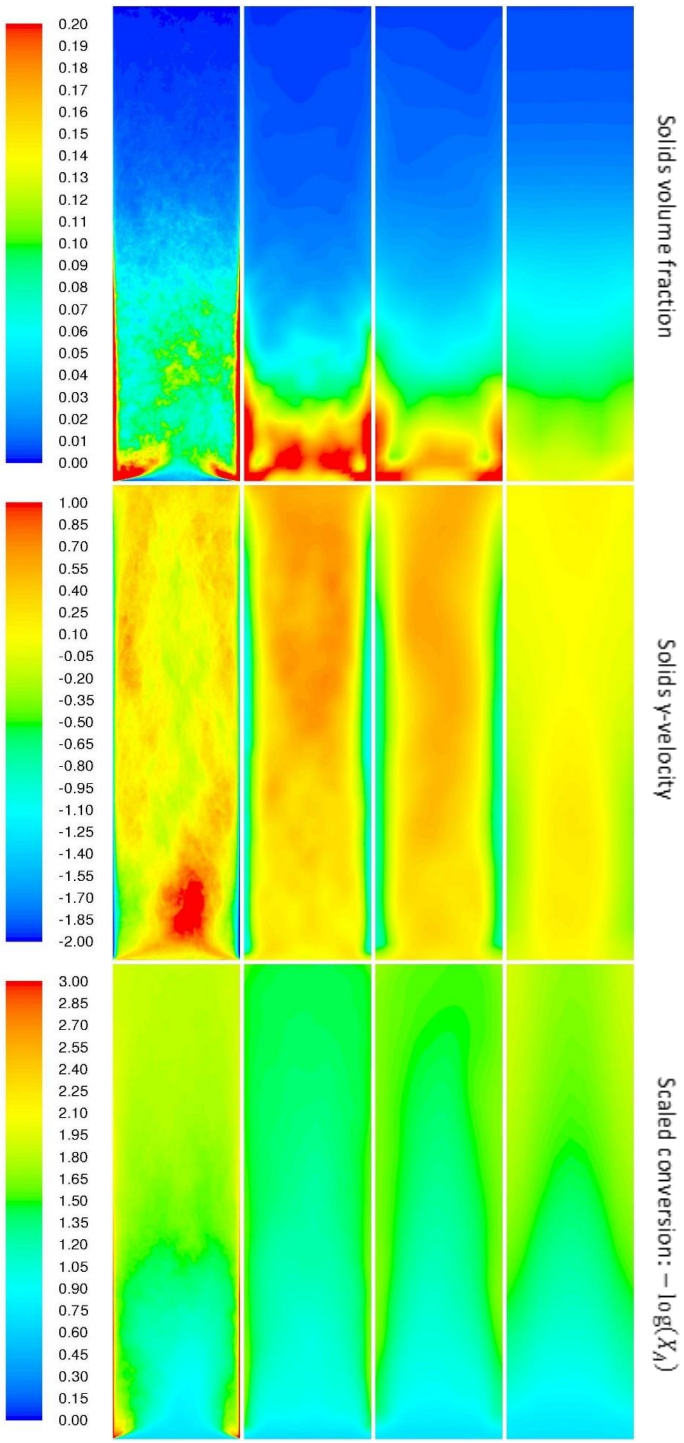

Figure 81 - Time-averaged contour plots for Case 4 (turbulent). In each row, the contours from left to right represent the resolved case, the 10 mm grid, the 20 mm grid, and the 40 mm grid.

5.2.5 Case 5: Boussinesq-based solids mesoscale stress closure

Figure 83 shows that the use of the Boussinesq-based solids mesoscale stresses result in reasonable predictions in the bubbling case. A slight decrease in the bed expansion is observed as the grid is coarsened, but this effect is relatively small.

A much larger impact is observed in the turbulent case shown in Figure 84. Here, the bed expansion is strongly overpredicted on the 10 mm grid and strongly underpredicted on the 40 mm grid. Another perspective is provided in Figure 82 where the instantaneous volume fraction contours of the cases with the anisotropic and Boussinesq-based solids mesoscale stress closures are compared. The comparison of the 10 mm cases shows the more intuitive behaviour: the viscosity introduced in the Boussinesq assumption caused a greater amount of momentum dispersion, resulting in less clustering and greater gas-solids momentum transfer, ultimately leading to an overprediction of the bed expansion.

As the grid is coarsened, however, this trend is reversed, with the Boussinesq-based stresses underpredicting the bed expansion. This is due to the viscosity in the bed becoming so large that the dense macro-clusters forming at the side of the domain become unphysically immobile, allowing the gas to rise more easily through the centre of the domain. This causes the bed to collapse near the walls. If the viscosity was not as large, these macro-clusters would frequently move into the rising gas stream to be swept upwards, thus increasing bed expansion.

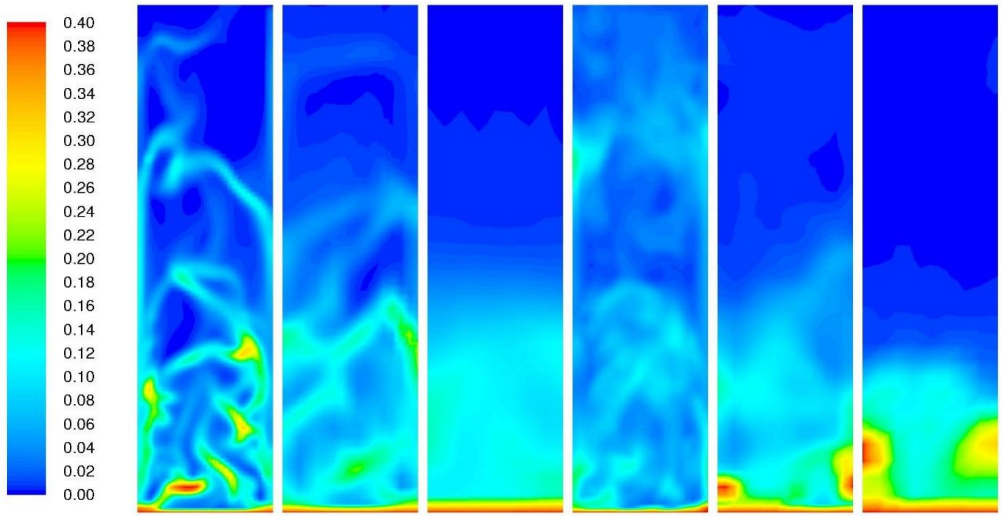

Figure 82 - Instantaneous solids volume fraction contours showing the impact of solids mesoscale stress modelling. The three images on the left are the 10, 20 and 40 mm grid sizes using the anisotropic solids mesoscale stress closure, and the three images on the right are the 10, 20 and 40 mm grid sizes using the Boussinesq-based solids mesoscale stress model.

This result clearly illustrates the merits of the anisotropic solids mesoscale stress closure and shows that using the Boussinesq approximation to close the solids mesoscale stresses can result in large predictive errors in certain cases.

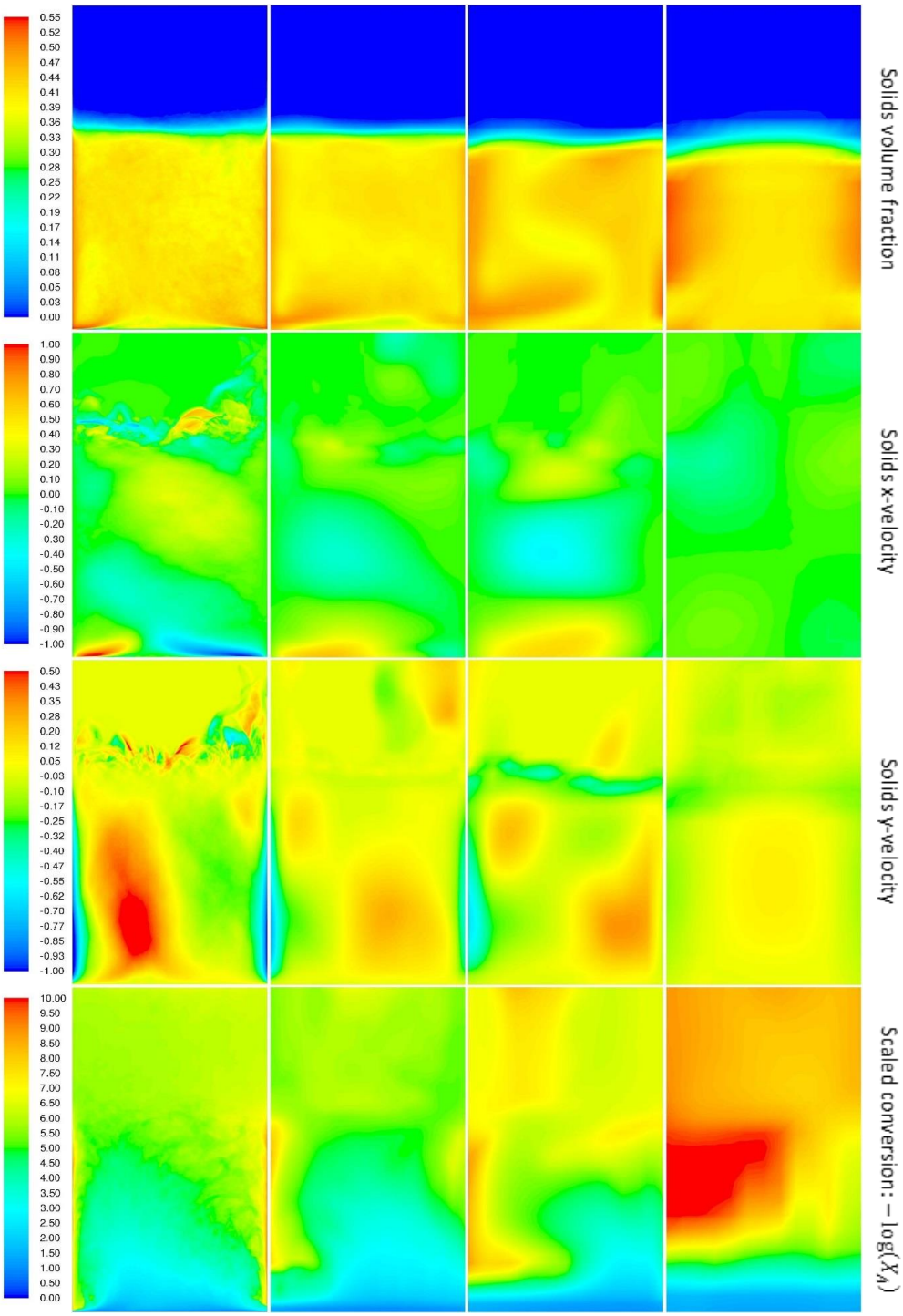

Figure 83 - Time-averaged contour plots for Case 5 (bubbling regime). In each row, the contours from left to right represent the resolved case, the 10 mm grid, the 20 mm grid, and the 40 mm grid.

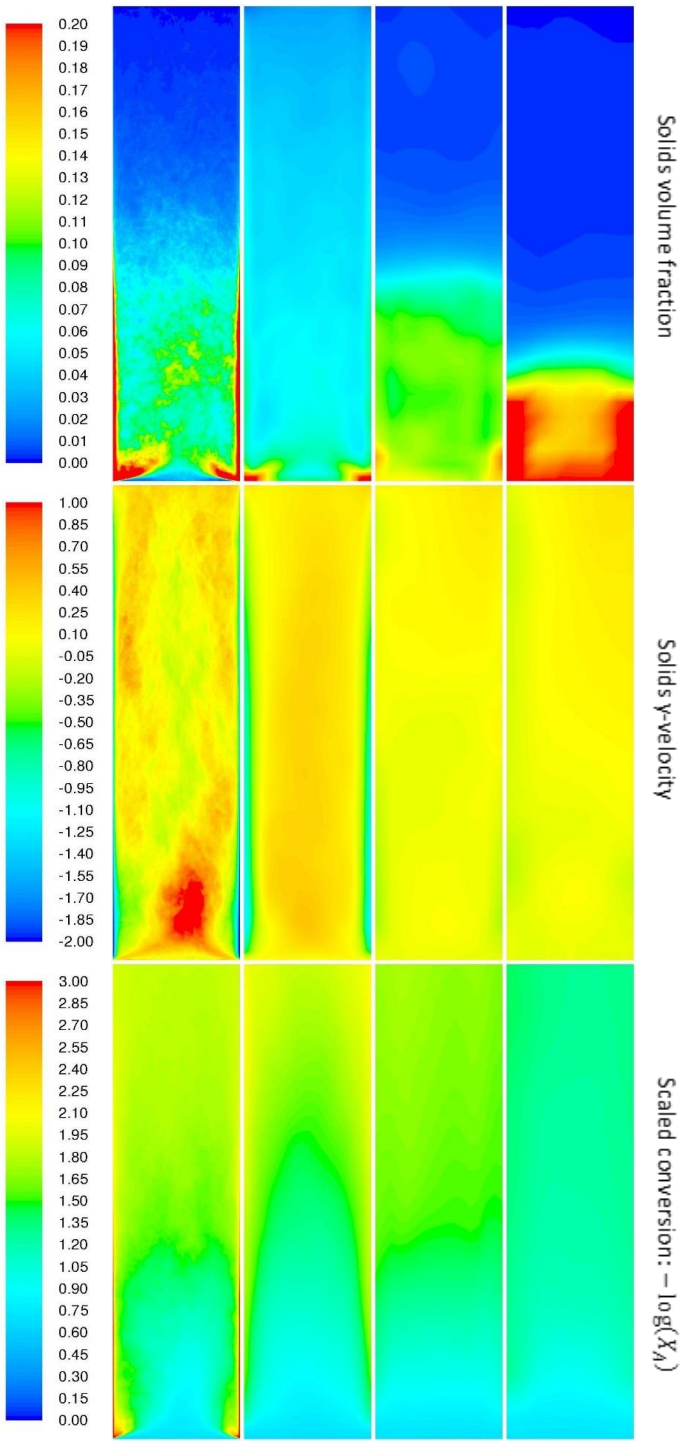

Figure 84 - Time-averaged contour plots for Case 5 (turbulent regime). In each row, the contours from left to right represent the resolved case, the 10 mm grid, the 20 mm grid, and the 40 mm grid.

5.2.6 Case 6: No filtered stresses

Figure 85 and Figure 86 show that the case without any modelling for the solids mesoscale stresses or the filtered frictional stresses behaves quite similarly to the complete case (Case 1: Figure 72 and Figure 74). The selected filter/grid ratio is also similar to the complete case (1.7 instead of 1.8). The biggest difference is shown in the bed expansion ratio for the turbulent case where the lack of solids stresses caused a greater underprediction of the bed expansion. This result is expected given the momentum dispersion effect of the solids mesoscale stresses. Without this effect, the gas is able to slip around the macro-clusters more easily, reducing the degree of gas-solids momentum transfer and creating a more compact bed.

In general, however, the results show that completely neglecting the solids mesoscale stresses yields better performance than using the Boussinesq approximation in the closure model. This is also suggested by the large negative coefficient of determination (R^2) at larger filter sizes in Figure 27. A negative R^2 implies that a simple average of all the data would be a better model than the proposed correlation.

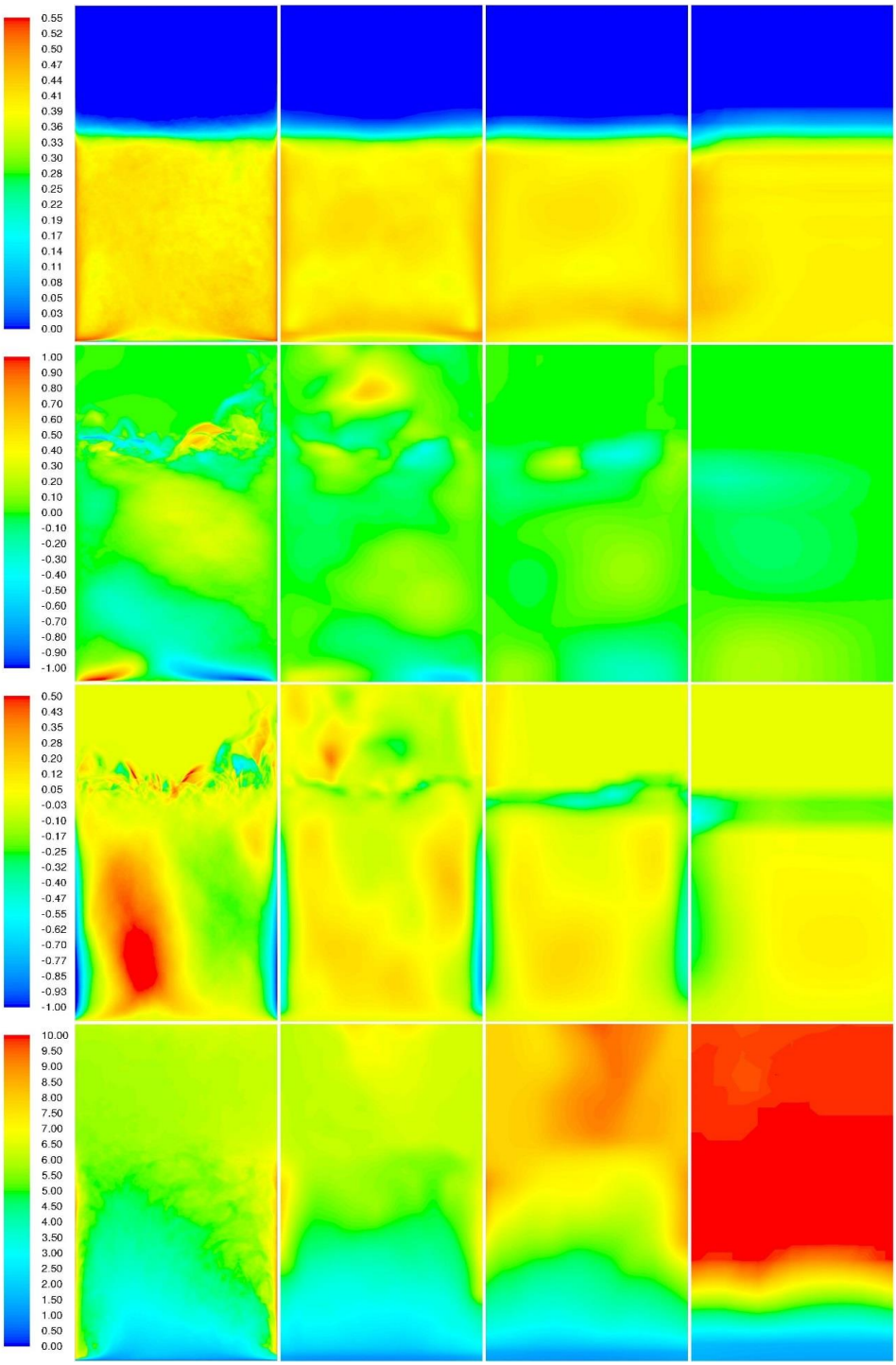

Figure 85 - Time-averaged contour plots for Case 6 (bubbling regime). In each row, the contours from left to right represent the resolved case, the 10 mm grid, the 20 mm grid, and the 40 mm grid.

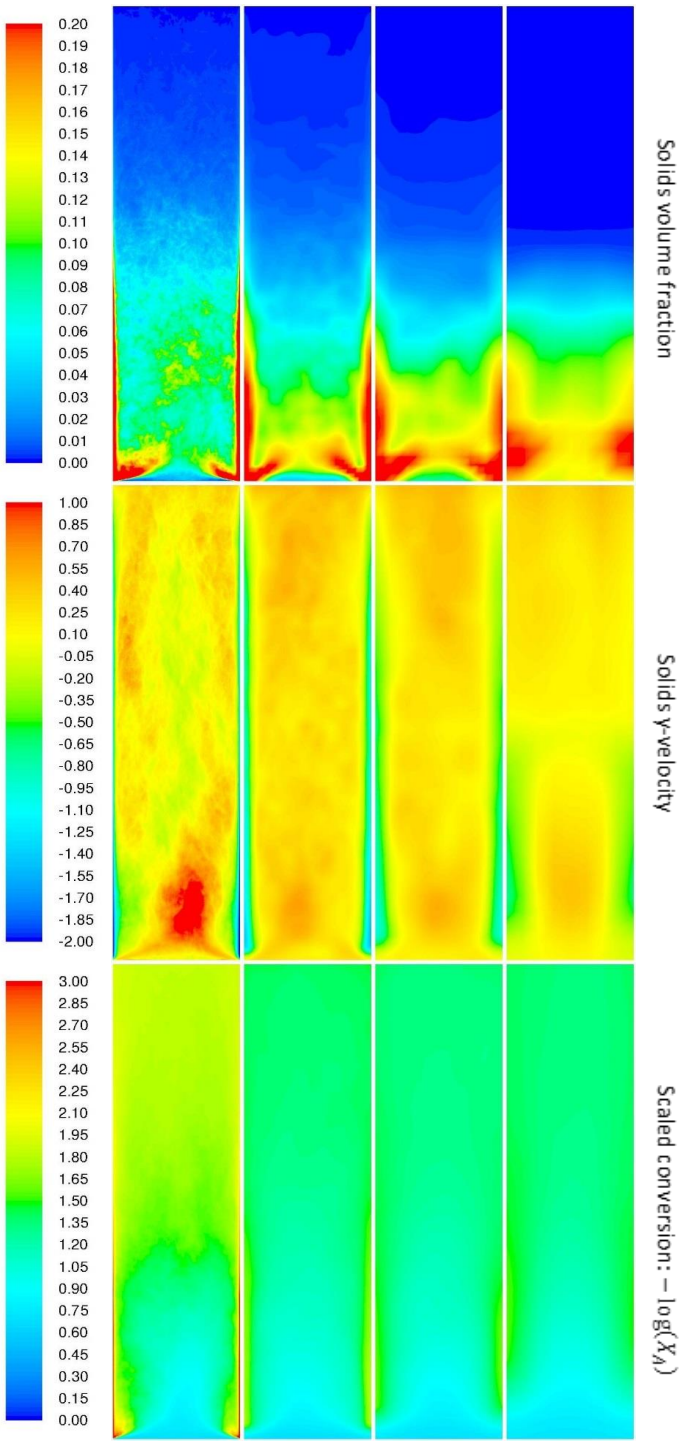

Figure 86 - Time-averaged contour plots for Case 6 (turbulent regime). In each row, the contours from left to right represent the resolved case, the 10 mm grid, the 20 mm grid, and the 40 mm grid.

5.2.7 Case 7: Isotropic drag and Boussinesq stresses

This final case was included to illustrate the performance of the current state of the art closures: isotropic drag combined with solids mesoscale stresses with an isotropic filtered solids pressure and Boussinesq-based filtered solids viscosity. Figure 87 and Figure 88 both show that the inaccuracies of these drag and stress approaches discussed in Chapter 5.2.4 and Chapter 5.2.5 cancel each other out to a certain degree. Specifically, the isotropic drag closure tended to increase the bed expansion with increasing grid size, while the Boussinesq stresses tended to decrease the bed expansion. In the bubbling case (Figure 87), this led to an increase in the bed expansion from the 10 mm to the 20 mm grid, followed by a decrease to the 40 mm grid. In the turbulent case (Figure 88), the effect of the stresses dominated, causing a consistent decrease in the bed expansion as the grid is coarsened.

Another interesting feature is the highly skewed flow pattern developing on the 10 mm grid in the bubbling case (Figure 87). This is similar to the skewed flow pattern in Figure 80 (isotropic drag and anisotropic stresses), but appears to be even more accentuated by using Boussinesq-based solids mesoscale stress closure.

It should also be noted that this case required the largest filter/grid ratio (3) – nearly double that of the cases with anisotropic drag and solids mesoscale stress models. In general, it is preferable to limit the reliance on the filtered closures and rely more on the directly resolved flow field to limit uncertainty from the imperfect sub-grid closures. Filtered models that perform well at a lower grid/filter ratio are therefore preferred.

Overall, these results show that the use of current state of the art isotropic filtered closures certainly achieves great improvements relative to the case without filtering (shown in Figure 73). However, the anisotropic approaches proposed in the present study appear to offer substantial benefits in terms of generality, grid independence and good performance at lower filter/grid ratios.

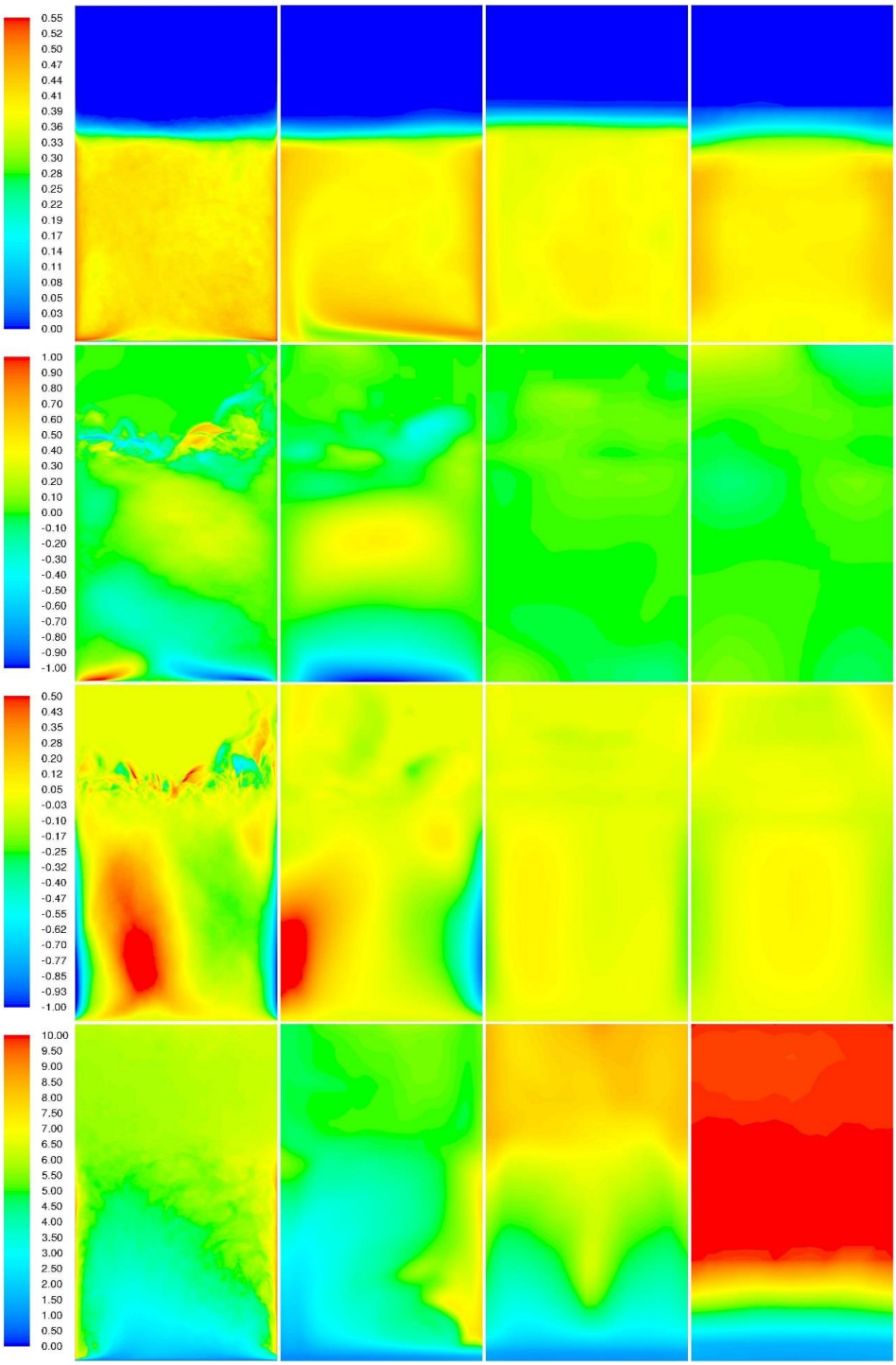

Figure 87 - Time-averaged contour plots for Case 7 (bubbling). In each row, the contours from left to right represent the resolved case, the 10 mm grid, the 20 mm grid, and the 40 mm grid.

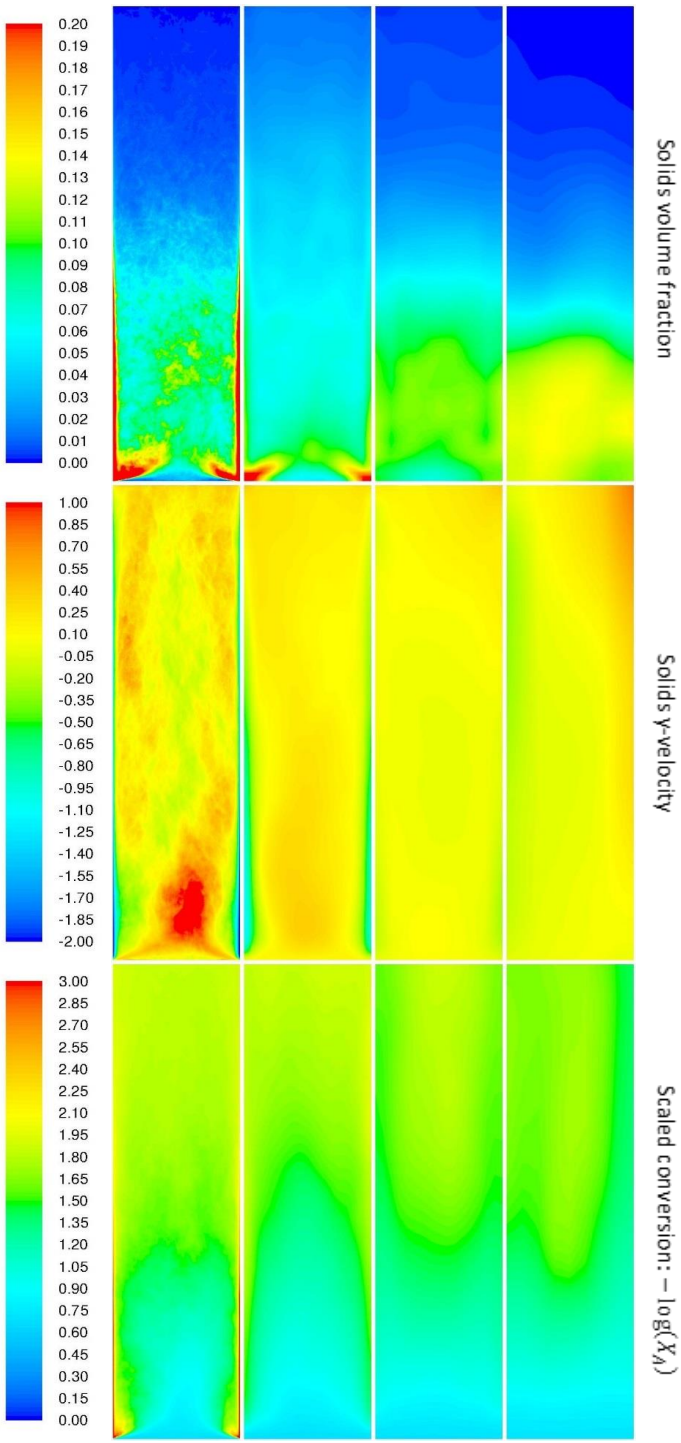

Figure 88 - Time-averaged contour plots for Case 7 (turbulent). In each row, the contours from left to right represent the resolved case, the 10 mm grid, the 20 mm grid, and the 40 mm grid.

5.2.8 Case 1 with no-slip walls

A final test was done where the bubbling bed from Case 1 (complete model) was run with no-slip walls. Note that, as with the turbulent case, the resolved simulation for this case could only be time-averaged for 18 s due to time constraints.

As shown in Figure 89, the model also performs well in this case. When comparing with the free-slip case shown in Figure 72, it is clear that the transition from free-slip to no-slip boundaries did not have a large impact on the fluidized bed behaviour. The flow remains skewed and the biggest discrepancy remains the reactant conversion in the coarse grid case.

The most prominent difference created by the no-slip boundary conditions is a significant reduction in the lateral direction velocities at the bottom of the domain where the downward flow at the walls reach the distributor. A comparison of Figure 89 and Figure 72 shows that this effect is well captured on the 10 mm grid, although this flow detail could not be resolved on the coarser grids.

Given the relative insensitivity of the bubbling case to changes in the model formulation, it is likely that a larger effect of no-slip boundaries may be observed in the turbulent case. Unfortunately, time constraints did not allow for a no-slip resolved simulation of the turbulent case.

In cases where the wall friction boundary condition is much more important than observed in Figure 89, a partial-slip boundary condition may need to be employed. In the coarse grid simulations, this will add the complication that a closure for the filtered shear stress at the walls will be required. Such a closure should compensate for i) the effect of the sub-grid mesoscale structures at the wall on the non-linear shear stress, ii) the fact that the filtered granular temperature, used in wall shear stress closures for partial-slip boundary conditions, is not known, and iii) an accurate estimate of the solids slip velocity at the walls will be difficult to obtain on coarse grids. Given the substantial additional modelling effort that this entails, it is advisable to first determine the importance of the wall boundary condition by comparing free-slip to no-slip cases.

Narrow risers with rapidly rising particle flows represent the most likely case where partial-slip boundary conditions may be important. A study was completed early in the present work to show that the conventional Johnson and Jackson boundary condition [35] performs poorly in such a case, since it requires the specularity coefficient to be tuned for the flow situation considered. A more recent formulation proposed by Schneiderbauer [34] significantly improved the generality of the wall boundary condition, since a single set of parameters could accurately be used for a large range of flow conditions. The Schneiderbauer model is therefore recommended for cases requiring a partial-slip boundary condition. More details of this study can be found in Appendix C. Therefore, future work can be suggested to developed a sub-grid closure based on this boundary condition for use in coarse grid simulations when the particle-wall boundary condition is of importance.

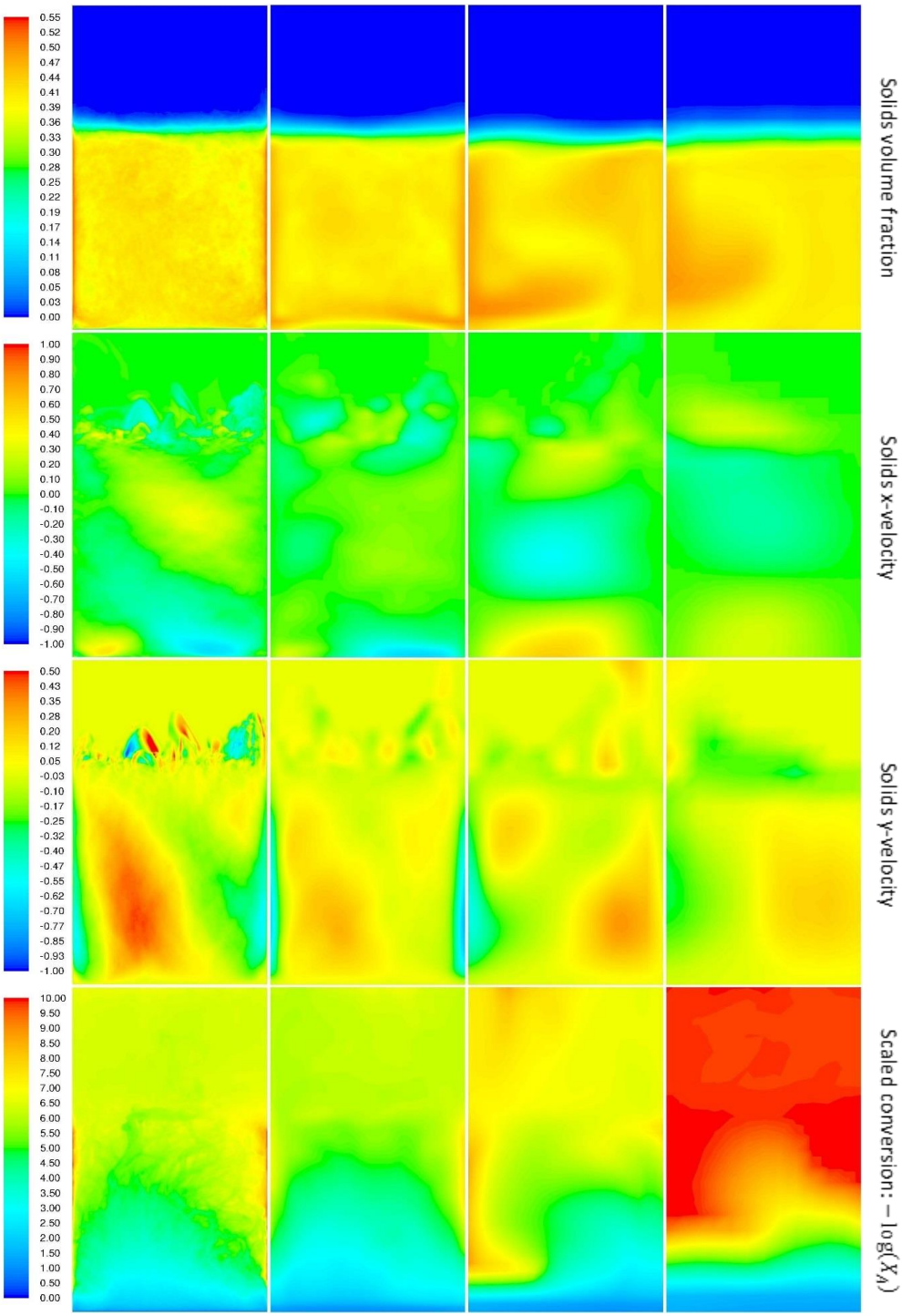

Figure 89 - Time-averaged contour plots for Case 1 with no-slip walls (bubbling). In each row, the contours from left to right represent the resolved case, the 10 mm grid, the 20 mm grid, and the 40 mm grid.

5.3 Validation of fTFM closures

In this chapter, some of the fTFM closures developed in Chapter 3 is validated by comparing filtered simulation results to experimental results from literature. The primary experimental data set is from a lab scale fluidized bed [60, 61]. In addition, the larger NETL Challenge problem [62] is also considered briefly. From this study earlier versions of isotropic drag closure and the anisotropic solids mesoscale stress closure, henceforth referred to as the NTNU model, are considered. The formulation of closures used (see Appendix G.1) are slightly different from those reported in Chapter 3.4.1.2 and Chapter 3.6.3, but the closure predictions are expected to be nearly identical. Additionally, to serve as benchmark, two fTFMs from literature are also considered: Those of Igci [16, 19] and Sarkar [13]. The closures used for these two fTFMs are detailed in Appendix G.2 and Appendix G.3. It can be noted that for all fTFMs the approach of setting the filter size in the closures to twice the grid size, as is commonly used in literature [17, 19, 26], is followed. This filter/grid ratio is close to the ratio of 2.3 that was found to be the optimal value for the wall-bounded verification in Chapter 5.2 when using an isotropic drag closure in combination with the anisotropic solids mesoscale stress closure.

Unfortunately, validation has not yet been performed for the anisotropic filtered interphase force closures developed in Chapter 3.4.2 and Chapter 3.5. This will be considered in future studies. However, based on the verification results in Chapter 4 and Chapter 5, especially those in the wall-bounded domain, it can be expected that the anisotropic filtered interphase force closures will further improve the performance of the closures reported in this chapter.

5.3.1 Simulation geometry, initial and boundary conditions

5.3.1.1 Lab scale experiments

The geometry selected for this study is a lab scale 0.267 m ID fluidized bed with a tall freeboard section expanding to 0.667 m ID to prevent particle elutriation as reported by Zhu *et al.* [60, 61]. The fluidized bed section is 2.5 m in height and the freeboard extends to a height of 4.2 m. The geometry was meshed with a structured Cartesian cut-cell mesh using three different cell sizes: 1 cm, 1.41 cm and 2 cm, corresponding to $154d_p$, $217d_p$ and $308d_p$, respectively. To put this into perspective, for TFM simulations without sub-grid closures, grid sizes of approximately 10 particle diameters are typically required for accurate results. Since the bed generally did not expand significantly into the freeboard region, a coarser mesh was employed in the freeboard. An example of the meshed geometry is displayed in Figure 90.

Gas was injected uniformly though a velocity inlet on the bottom face of each reactor. Four fluidization velocities were investigated: 0.06, 0.4, 0.9 and 1.4 m/s. Gas exited at the top of the reactor though a pressure outlet at 0 Pa gauge pressure. A no-slip boundary condition was specified at the walls for the gas phase, while a partial-slip boundary condition was specified for the solids. The model of Johnson and Jackson [35] was used for the solids boundary condition with a specularity coefficient of 0.001 describing the wall roughness. This value depends on the reactor material and particle properties and is therefore not known. The low value given above indicates an almost free-slip boundary condition and was found to give acceptable results in the current case.

Geldart A-type [63] powder was used in the experiments with a density of $1780\ kg/m^3$ and a mean diameter of $65\ \mu m$ [60]. Standard air at room temperature was used as the fluidizing gas. The

simulations were initialized with a static bed height of 0.9 m replicating the experiments. The solids volume fraction in this initial static bed was set to 0.6. All simulations were time-averaged for 30 s after reaching a statistical steady state. The statistical steady state was identified by monitoring the average solids velocity magnitude in the domain.

Figure 90 - The geometry with the 2 cm mesh used in this study. The inlet is indicated in blue and the outlet in red.

5.3.1.2 NETL Challenge problem

An additional validation was performed for the NETL challenge problem [62] in a bubbling bed with a diameter of 0.91 m (more than 3 times larger than the primary validation case). The fluidization velocity employed was 0.6 m/s, and the particle size and density were $79\ \mu m$ and $1489\ kg/m^3$ respectively.

A rather complex sparger is used for gas injection. However, given the almost perfectly linear pressure gradient that developed in the bed, it appears that this complex inlet condition did not have a large

impact on the macro-scale bed behaviour. For this reason, the bed was simulated as a simple cylinder with a uniform velocity inlet on the bottom face and a pressure outlet on the top face. The cylinder was specified to be 0.91 m in diameter and 6.3 m in height. The geometry was meshed with three different cell sizes; 3.5 cm, 5 cm and 7 cm, to evaluate grid independence behaviour.

The bed was initialized with 1510 kg of particle and a boundary condition was implemented to reinject the small amount of solids reaching the outlet at the velocity inlet. Simulations were time-averaged for 90 s of flow time after a pseudo-steady state condition was identified by monitoring the average solids velocity magnitude.

5.3.2 Results and discussion

Results will be presented and discussed in four sections. Firstly, a qualitative comparison between the three filtered models will be presented to give a visual impression of model behaviour. Secondly, a quantitative comparison against experimental data will be presented. The final two sections will individually explore the impact of models for filtered interphase momentum exchange and solids mesoscale stresses.

5.3.2.1 Qualitative comparison

A first impression of model behaviour is given in Figure 91. In general, the NTNU model appears to create a more resolved flow than the other models. For the slowest fluidization velocity, the Sarkar model does not predict any fluidization, mainly because the drag correction does not disappear in the limit of very dense flows where no clustering can take place (to be discussed later around Figure 96).

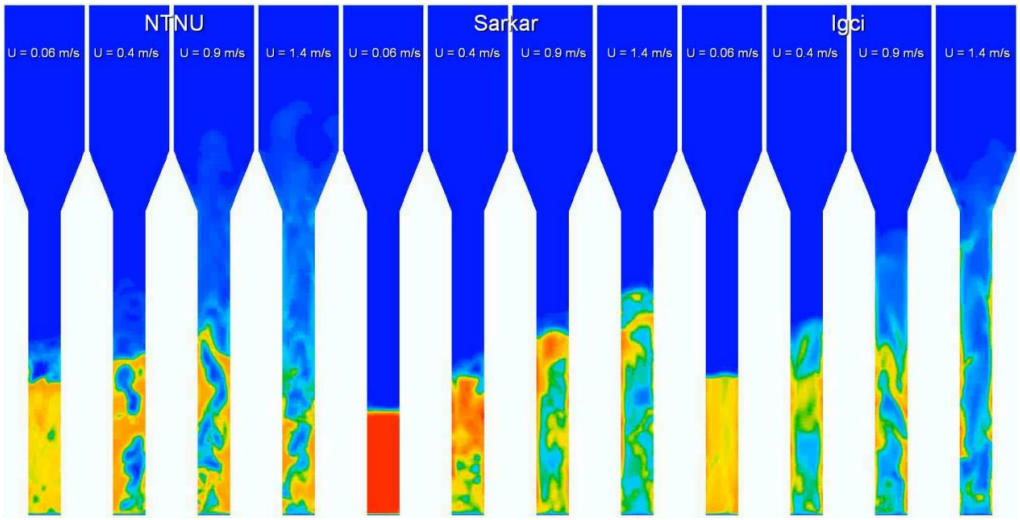

Figure 91 - Instantaneous solids volume fraction contours from the three fTFM approaches evaluated in this study for four different fluidization velocities. Contours are displayed on a central plane through the axis of the geometry in Figure 90 for the 2 cm grid size. The blue-red colourmap ranges from zero to 0.63 (maximum packing).

Qualitative behaviour of the three different models on the three different grid sizes considered in this study is displayed in Figure 92. The figure shows that the NTNU model generally predicts similar dynamics and overall expansion of the dense bed region, while the bed becomes denser with grid

refinement for the other two approaches. A slight grid dependency effect can be observed for the NTNU model in the dilute region above the dense bed where less particle entrainment to the freeboard is observed on finer grids.

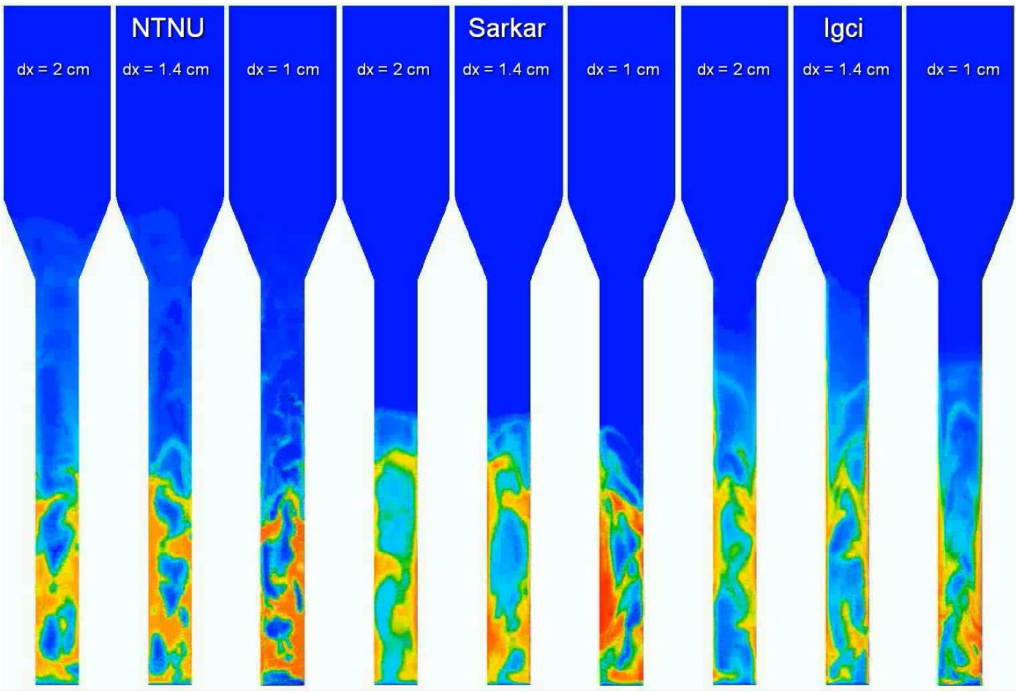

Figure 92 - Instantaneous solids volume fraction contours from the three fTFM approaches evaluated in this study for three different grid sizes. Contours are displayed on a central plane through the axis of the geometry in Figure 90 for a fluidization velocity of 0.9 m/s. The blue-red colourmap ranges from zero to 0.63 (maximum packing).

5.3.2.2 Quantitative comparison

The first comparison to experimental results is presented in the form of axial pressure gradient to assess the ability of the model to accurately predict the amount of bed expansion. As shown in Figure 93, all models provide at least reasonable comparisons to the experimental data, although the pressure drop is significantly overpredicted in some cases. It is important to keep in mind that, if no filtering was employed, the model would predict an axial pressure gradient of about half the experimental values [25].

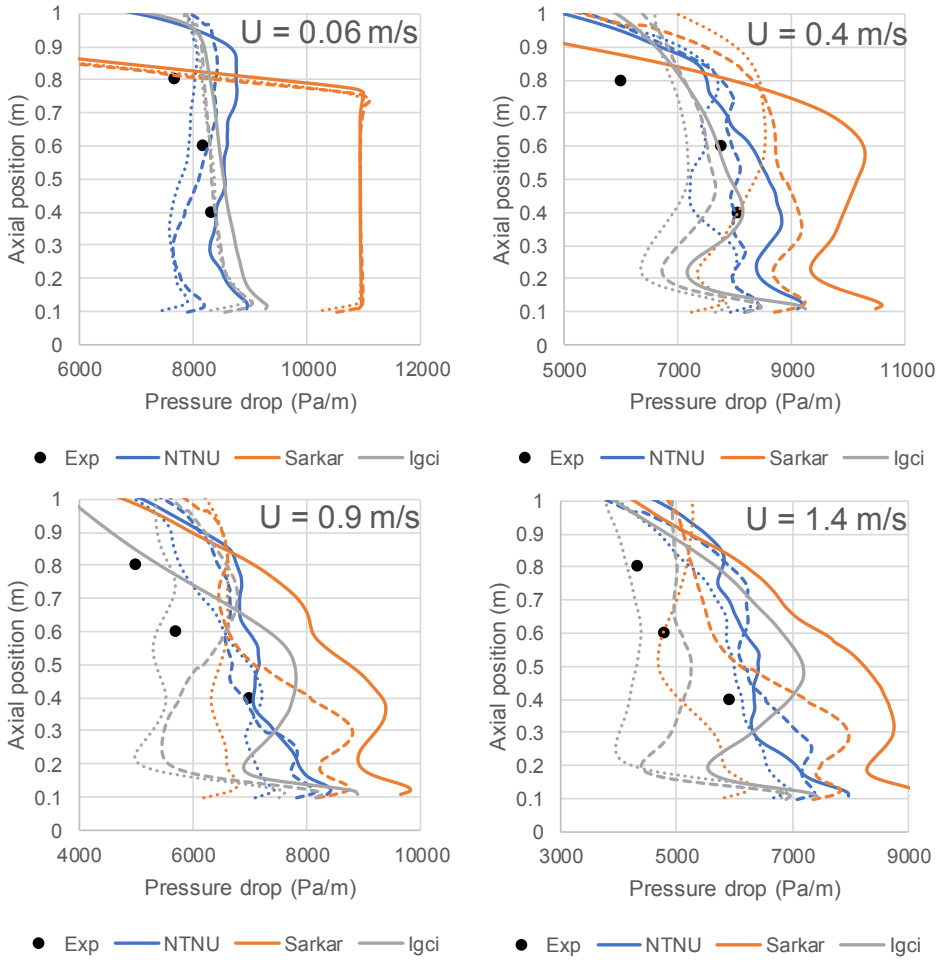

Figure 93 - Comparison of the time-averaged axial pressure gradient predicted by the three different filtered models for three different grid sizes. The pressure gradient was calculated over an axial distance of 20 cm as was the case in the experiments [61]. For each model, the dotted line represents the 2 cm grid, the dashed line the 1.4 cm grid, and the solid line the 1 cm grid.

Figure 93 also confirms the observation from Figure 92 that the NTNU model generally shows the best grid independence behaviour, while the other two models generally lead to denser beds as the grid is refined. Only in the case with the slowest fluidization velocity (U = 0.06 m/s) does the Igci model provide a better fit to the experimental data.

Grid dependency effects shown by the Igci model are most likely due to the lack of a filter size dependency of the wall corrections employed in the simulation (Equation 157 to Equation 160). As observed in the prior validation study, these wall corrections are very important for ensuring accurate results with this model [25], but the wall corrections should disappear in the limit of very small grid sizes. Grid dependency of the Sarkar model may be due to challenges with filter-size dependency, model scaling and wall corrections as will be further discussed in the next two sections.

Figure 94 shows the comparison to radial solids volume fraction measurements. The radial volume fraction profile is generally well captured by all models, with the exception of the case at 0.4 m/s where the models fail to capture the relatively uniform radial profile. The experimental profile was averaged from three measurements, where one was significantly different from the other two due to a swirling phenomenon observed only at this fluidization velocity [60, 61]. This unique effect could not be captured by the models, all of which consistently predicted the expected higher solids concentration towards the wall.

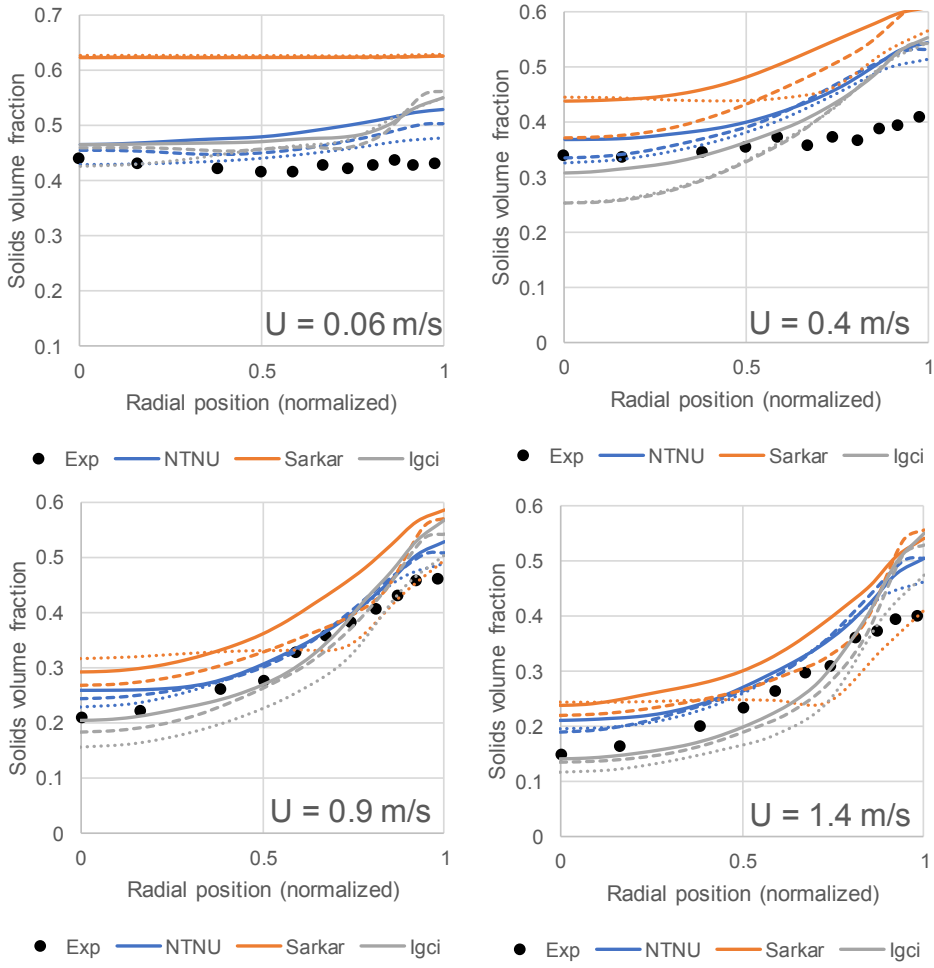

Figure 94 - Comparison of the time-averaged radial solids volume fraction predicted by the three different filtered models for three different grid sizes. Results were collected at a bed height of 0.6 m as measured in the experiments [61]. For each model, the dotted line represents the 2 cm grid, the dashed line the 1.4 cm grid, and the solid line the 1 cm grid.

As can be deduced from the pressure drop measurements at a height of 0.6 m reported in Figure 93, the NTNU model marginally overpredicts the average solids volume fraction at this height and the Sarkar model shows greater overpredictions. The denser bed predicted by the Sarkar model is due to a substantially larger drag correction as will be discussed in the next section.

Finally, Figure 95 displays the comparison of solids volume fraction standard deviation at the same measurement locations as Figure 94. In general, model predictions show the correct trend: higher standard deviation in the centre of the geometry where most bubbles are rising and lower standard deviation at the walls. Although perfect grid independence is not achieved, the NTNU model again shows the smallest grid dependency except in the case with the lowest fluidization velocity (0.06 m/s). Results also confirm that the NTNU model resolves more flow details, as could be qualitatively observed in Figure 91 and Figure 92.

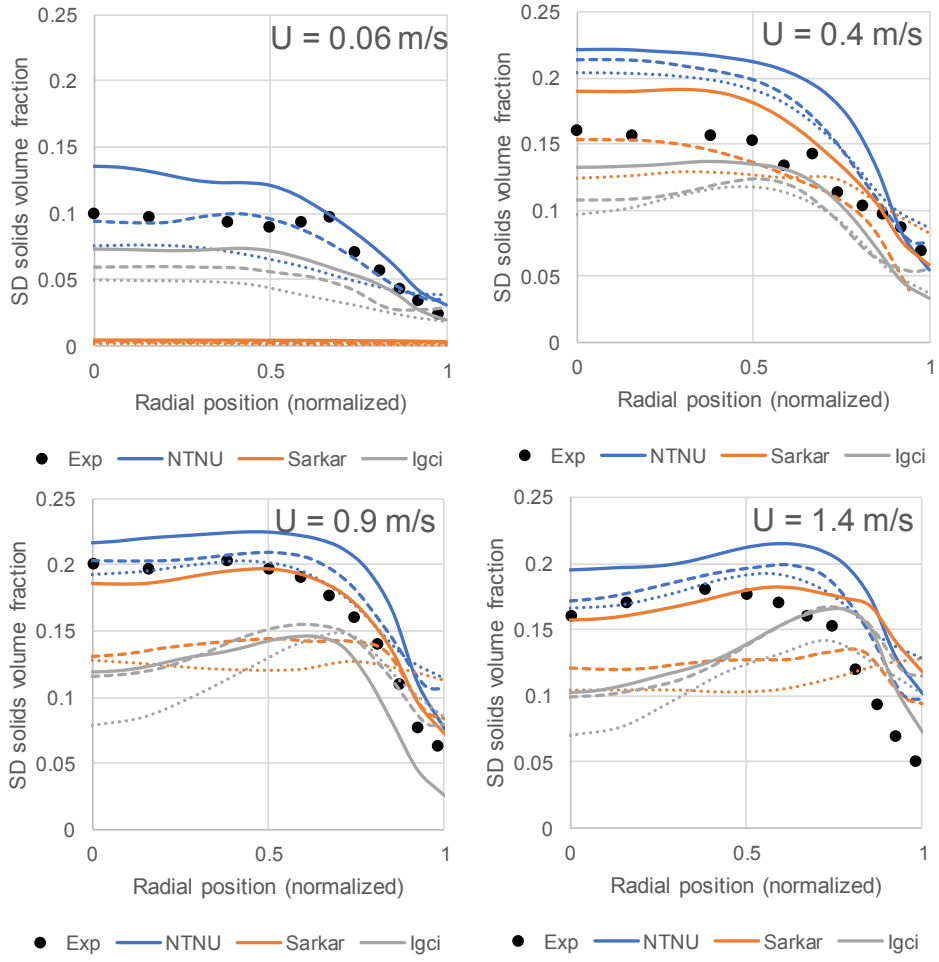

Figure 95 - Comparison of radial profiles of the standard deviation of solids volume fraction measurements predicted by the three different filtered models for three different grid sizes. Results were collected at a bed height of 0.6 m as measured in the experiments [61]. For each model, the dotted line represents the 2 cm grid, the dashed line the 1.4 cm grid, and the solid line the 1 cm grid.

The fluidization velocity of 0.4 m/s once again shows the greatest deviations. In particular, the NTNU model and the finest grid simulation with the Sarkar model substantially overpredict the solids volume fraction standard deviation. This may also be due to the swirling phenomenon observed in the experiments that could not be successfully reproduced by the models.

5.3.2.3 Drag model comparison

As alluded to in the previous section, the Sarkar model generally overpredicts the solids bed density, especially for finer grid sizes (which should be more accurate than coarser grids). Given that this model is the only one in this study that was derived in 3D, it can be intuitively expected to be the most accurate. However, Figure 96 shows that the Sarkar model predicts substantially larger drag corrections (i.e., smaller drag forces) than the NTNU model, thus offering a simple explanation for the overprediction of the bed density. The hard limit imposed at a drag correction factor of $C = 0.03$ in the Sarkar model is also visible for the highest slip velocity in Figure 96. Such a limit is avoided in the NTNU model by scaling the drag correction factor as $-\log(C)$ to allow for a more natural treatment of regions with a large drag correction, as discussed in Chapter 3.4.1.2.

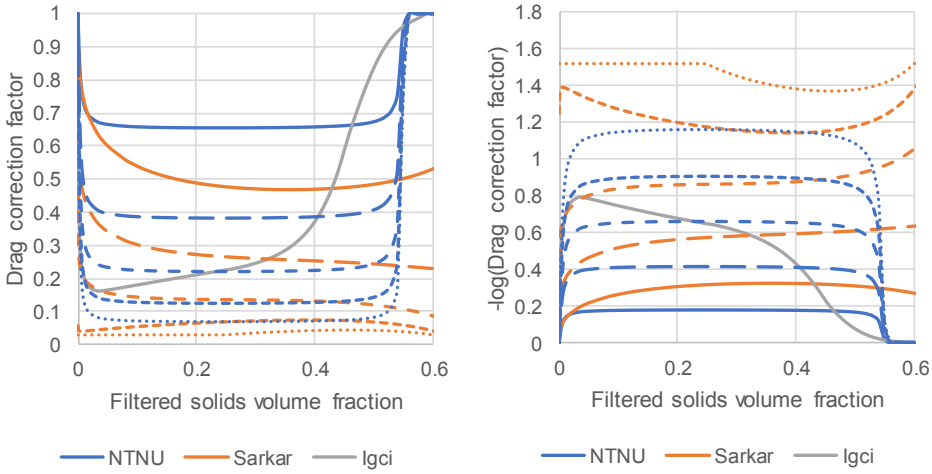

Figure 96 - Comparison of drag correction factors for the three filtered drag closures investigated in this study. For the NTNU and Sarkar models, different slip velocities are included, scaled by the steady state sedimentation velocity (Equation 138). The scaled velocity ranges from 1 (solid line) through 2, 4 and 8 to 16 (dotted line). The left-hand graph shows the drag correction factor (C in Equation 124, Equation 142 and Equation 151), and the right-hand side shows a scaled drag correction factor ($-log(C)$) to better portray the regions where the drag correction has a large impact (small C).

Part of the reason for the overprediction of the drag correction in the Sarkar model is related to the scaling from the particles where the model was derived (150 µm and 441 kg/m^3) to the particles used in the experiments for this study (65 µm and 1780 kg/m^3). The NTNU and Igci models were derived for particles that are closer to the experimental case (75 µm and 1500 kg/m^3), thus requiring less scaling than the Sarkar model.

Incidentally, the commonly used scaling parameter, the particle terminal velocity, is fairly similar between the particles used in the derivation of the different models: 0.2697 m/s for the Sarkar model and 0.2297 m/s for the NTNU and Igci models. It can therefore be expected that the uncertainties introduced by scaling the model to a new system should be small. In addition, Sarkar et al. [13] investigated the scalability of their model to the particle conditions under which the NTNU and Igci models were derived and concluded that the model scaled quite well. However, significant overprediction of the drag correction was observed at larger slip velocities (see Fig. 16 in [13]). In this

study, the average ratio between the drag correction factors from the Sarkar and NTNU models ranges from 0.765 at a scaled slip velocity of 1 to 0.436 at a scaled slip velocity of 16, reflecting a similar trend.

Despite these differences, the Sarkar model was validated [13] for a Geldart A particle system (NETL challenge problem [62]) similar to the one investigated in this study. Successful validation of the Sarkar and NTNU models in this alternative (larger) case was confirmed in Figure 97 (a brief description of this simulation case is given in Chapter 5.3.1.2). Unlike the results presented thus far, the Sarkar model also shows good grid independence behaviour in this case.

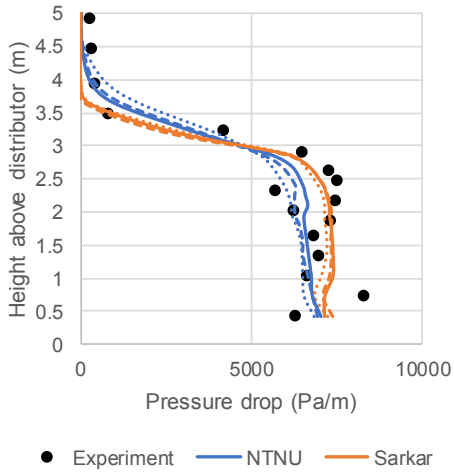

Figure 97 - Comparison of simulation predictions from two filtered models to the pressure drop measurements in the NETL challenge problem [62]. For each model, the dotted line represents a 7 cm grid, the dashed line a 5 cm grid, and the solid line a 3.5 cm grid.

An important reason for the similar performance of the NTNU and Sarkar models in this case is that the NTNU model is closer to the Sarkar model for the larger cell sizes required (i.e., 3.5 - 7 cm) than for the cell sizes used in the validation study presented in the previous sections (i.e., 1 - 2 cm). As shown in Figure 98, the Sarkar model saturates already at very small cell sizes, whereas the NTNU model saturates much more slowly. Based on the good grid independence behaviour of the NTNU in both validation cases, the filter size dependency in the NTNU appears to be more realistic.

The most likely explanation for this large difference in filter size dependency is that the Sarkar model was derived from resolved simulations on a small 3D domain (13.5 dimensionless units), whereas the NTNU model was derived from a much larger 2D domain (132 dimensionless units). Given that the particle properties are similar for the validation case from Zhu *et al.* [60, 61] and the NETL challenge problem [62], but the Sarkar model performs much better in the challenge problem where larger filter sizes are used (Figure 98), it appears that the effect of the domain size used for model derivation is of greater importance than the uncertainty related to scaling the particle properties discussed earlier.

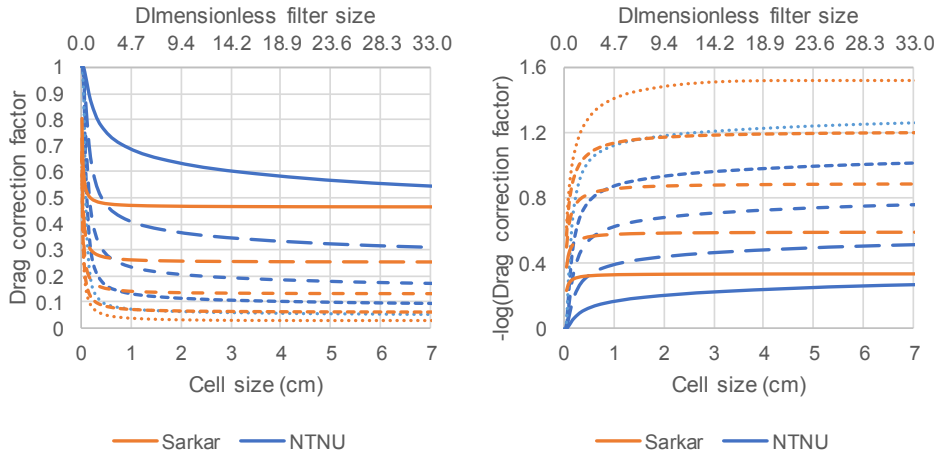

Figure 98 - Comparison of the drag correction factor from the NTNU and Sarkar models employed on different cell sizes at an intermediate solids volume fraction of 0.3. As in Figure 96, five different scaled slip velocities are shown, ranging from 1 (solid line) through 2, 4 and 8 to 16 (dotted line). As outlined in the caption of Figure 96, the left-hand figure shows the drag correction factor (C) and the right-hand figure shows the scaled drag correction factor $(-log(C))$.

5.3.2.4 The effect of solids mesoscale stress modelling

Finally, the influence of the solids mesoscale stress model in the NTNU model is investigated by replacing it with the Sarkar stress model. Specifically, Equation 124 to Equation 138 are used for the interphase momentum exchange and Equation 143 to Equation 150 are used for the solids stresses. A qualitative impression of the effect of this blended model is shown in Figure 99. It is clear that the bed expands much more than in the case of the individual NTNU and Sarkar models, while also resolving less flow detail.

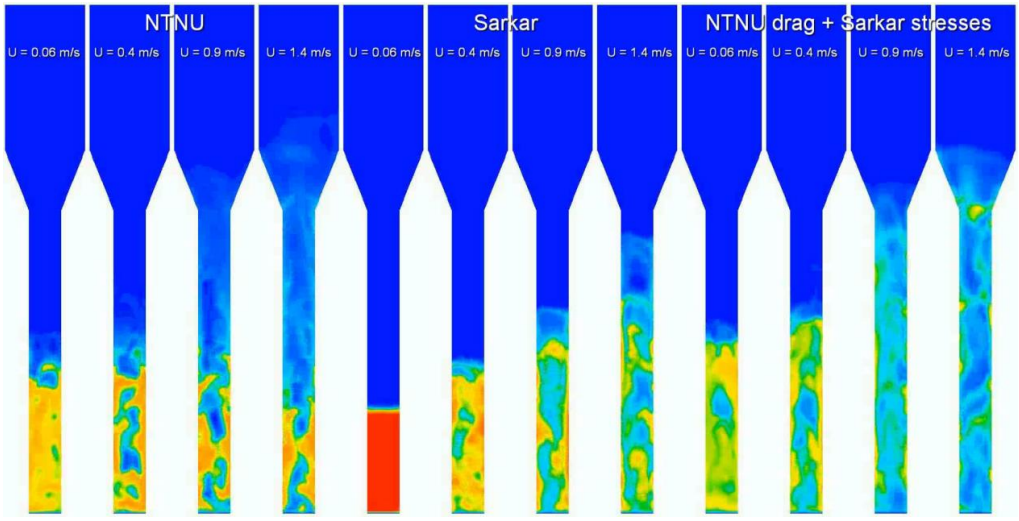

Figure 99 - Instantaneous solids volume fraction contours similar to Figure 91, only replacing the Igci model with a blend of the NTNU and Sarkar models.

Figure 100 gives a qualitative impression of the grid independence behaviour of this blended model. Large grid dependence effects are visible, with finer grids resulting in a much denser bed.

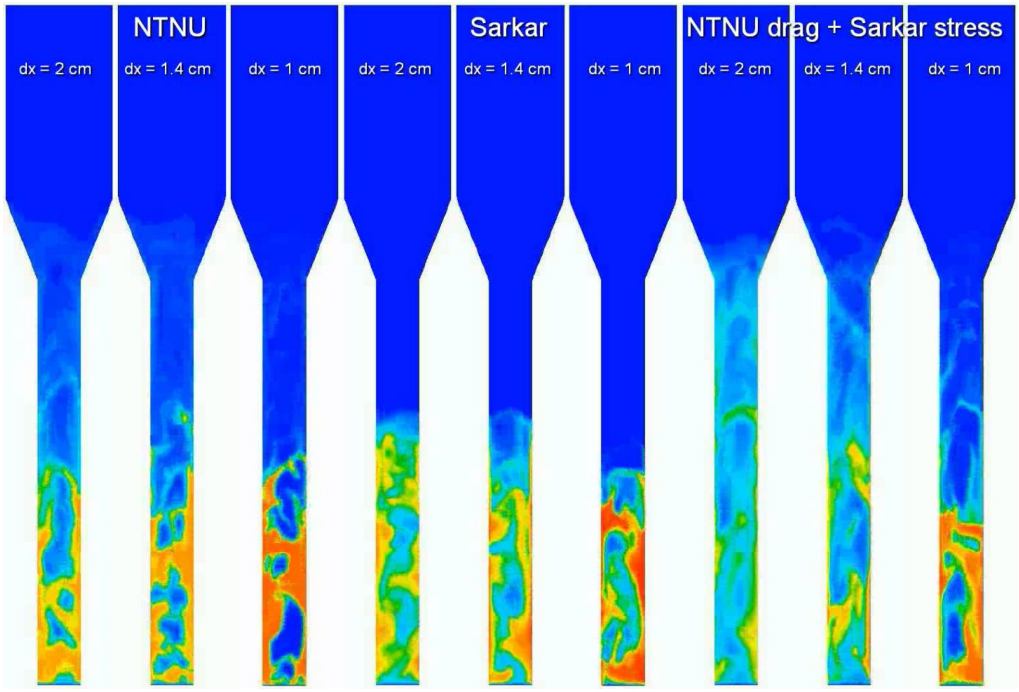

Figure 100 - Instantaneous solids volume fraction contours similar to Figure 92, only replacing the Igci model with a blend of the NTNU and Sarkar models.

These results are quantified via the axial pressure drop comparisons in Figure 101. The qualitative observations from Figure 99 and Figure 100 are confirmed by the data. In general, the blended model predicts a more dilute bed than both (i) the individual NTNU and (ii) Sarkar model, and also shows large grid dependencies. It is only on the finest grid (1 cm) that the blended model predicts similar results as the NTNU model. These results therefore confirm the finding in Chapter 5.2.6 that using isotropic, Boussinesq-based closures for the solids mesoscale stresses, similar to those in the Sarkar model, introduces a substantial error in the model predictions. As discussed in Chapter 3.6.2, modelling the deviatoric component of the solids mesoscale stress tensor through the Boussinesq approximation fails to capture the direction of the resulting force. As a result, modelling these stresses as a solids viscosity leads to a force of the correct magnitude, but often in the incorrect direction. In contrast, the anisotropic solids mesoscale stress closure used in the NTNU model can accurately predict the forces resulting from the solids mesoscale stresses.

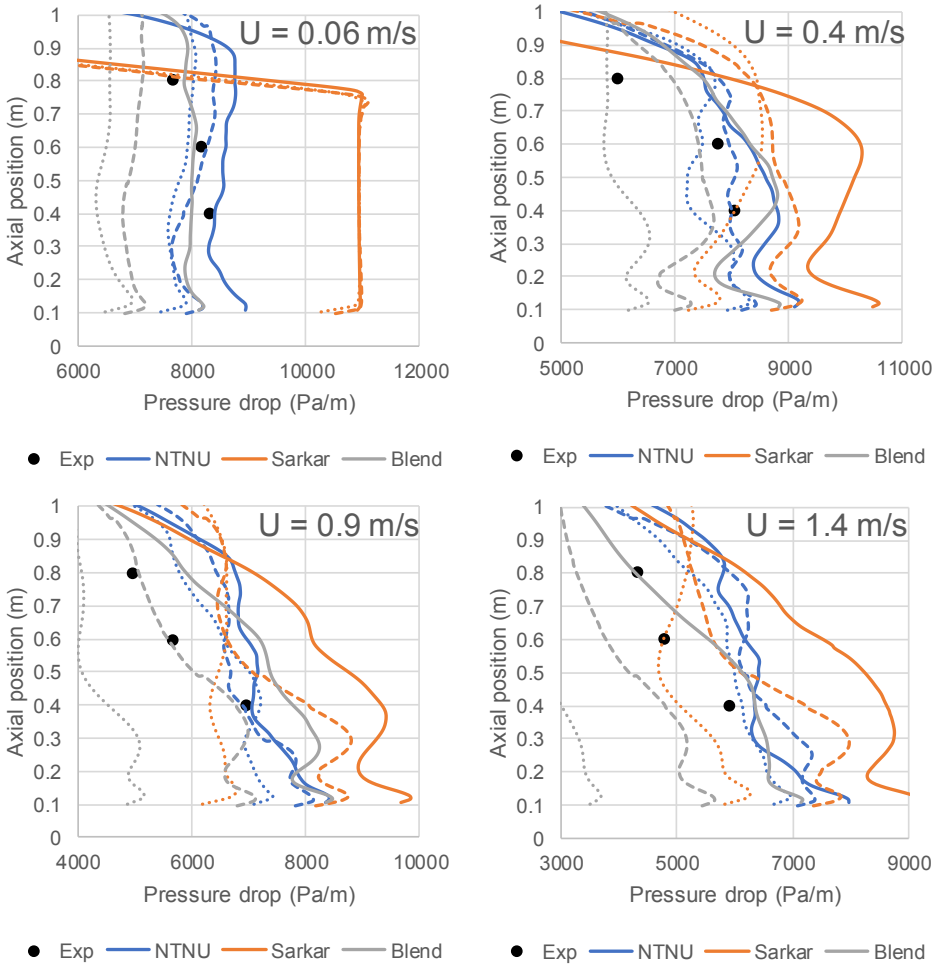

Figure 101 - Comparison of the time-averaged axial pressure gradient similar to Figure 93, only replacing the Igci model with a blend of the NTNU and Sarkar models. For each model, the dotted line represents the 2 cm grid, the dashed line the 1.4 cm grid, and the solid line the 1 cm grid.

It can further be noted that anisotropy in the solids mesoscale stresses becomes especially important in domains where walls have a large influence, as in the lab scale fluidized bed under consideration. It is well known in the field of single-phase turbulence that turbulent fluctuations become highly anisotropic in regions close to the wall. It has recently been shown that this is also the case for the solids mesoscale stresses and that it is important to account for this anisotropy at the walls in coarse grid simulations [64]. It is therefore likely that the importance of walls in this validation study emphasized the large grid dependency effects shown in Figure 101, since the Boussinesq-based solids mesoscale stress closure using isotropic independent variables in the Sarkar model is expected to perform especially poorly in highly anisotropic situations. This notion is supported by a worsening in the grid dependency behaviour as the fluidization velocity is increased.

Chapter 6: Conclusions

The primary conclusion from the present study is that fTFM performance can be improved substantially by correctly accounting for anisotropy in the closures for the filtered interphase forces and the solids mesoscale stresses. Newly proposed anisotropic filtered drag force, mesoscale interphase force and solids mesoscale stress closures clearly outperformed conventional isotropic closures. An anisotropic approach is therefore strongly recommended for all future fTFM studies.

New anisotropic closures were evaluated in two ways: 1) *a priori* assessments where model predictions were compared against a large number of filtered samples from the resolved simulations, and 2) *a posteriori* assessments where coarse grid filtered simulations were verified against computationally expensive resolved simulations.

A priori assessments of the filtered drag model revealed that the conventional isotropic approach strongly underpredicts the drag correction in the directions perpendicular to gravity. This realization inspired the formulation of a new filtered drag force closure based on the drift velocity concept, which enabled accurate predictions in all directions via a single model equation. *A posteriori* assessments showed that the new anisotropic drag closures offered clear improvements in terms of grid independence and model generality.

The effect of anisotropy was even more apparent when closing the solids mesoscale stresses. In this case, *a priori* assessments showed that the conventional approach, based on the Boussinesq approximation for closing the solids mesoscale stresses, produced a very poor match to the resolved simulation data. Predicting the deviatoric components of the solids mesoscale stress tensor with the Boussinesq approximation resulted in forces of the correct average magnitude, but often the incorrect direction. As a result of this large error, *a posteriori* assessments revealed that ignoring the solids stresses resulted in better model performance than including a Boussinesq-based solids mesoscale stress closure.

Failure of the conventional approach to solids mesoscale stress modelling prompted the formulation of a new anisotropic stress closure. A novel “gradient product marker” (GPM), essentially the anisotropic equivalent of the conventionally employed filtered deviatoric shear rate magnitude, was identified to correlate well with the deviatoric stresses. This new marker allowed for the formulation of a new closure that could accurately predict all components of the solids mesoscale stress tensor using a single closure equation. *A posteriori* assessments confirmed the good performance of this new anisotropic solids mesoscale stress closure.

Aside from this primary conclusion, several secondary conclusions were also drawn:

1. Firstly, it was found that the model setup of the resolved simulations had a significant effect on the filtered statistics that are used to derive fTFM closures. Particle scale models for drag and frictional stresses had the largest effect on the resulting filtered statistics. Simpler drag models are often employed and frictional stresses are often neglected for the sake of simplicity, but it is recommended that the most sophisticated resolved simulation setup is always employed. Simplifications on this level can lead to inaccurate filtered data being used during closure development, thus reducing the accuracy of the resulting filtered closures.

2. Scaling the filtered slip velocity, drift velocity and adjusted slip velocity with the steady state sedimentation velocity removed much of the dependency of these velocities on the filtered solids volume fraction. This resulted in improved statistics for closure fitting and in simpler functional forms for the closure models.
3. It was critical to account for important physical limits in the closure models, such as zero sub-grid corrections in the dilute and dense solids volume fraction limits. This allows the closure models to be safely extrapolated to conditions for which resolved simulation data was not available during closure fitting.
4. For the direction aligned with gravity, adding additional markers to the drag closure significantly improved model performance in *a priori* tests for smaller filter sizes, but improvements became smaller as the filter size was increased. Each drag closure had a gravitational component that depended only on one marker: the filtered solids volume fraction. This component became increasingly dominant as the filter size was increased, thereby reducing the effect of adding additional markers. For the direction perpendicular to gravity, however, inclusion of additional markers clearly improved model performance for all filter sizes.
5. The filtered slip velocity, often employed as a second marker for the filtered drag force closure, was found to perform poorly in *a posteriori* assessments despite good *a priori* performance. Including the filtered slip velocity as a marker in the filtered drag force closure removes most of the slip velocity dependency of the modelled filtered drag force. As a result, even a small error in the closure requires a large change in the slip velocity to restore the balance between drag and gravity. This, in general, leads to poor closure performance. It is therefore recommended that future fTFM development efforts move away from the filtered slip velocity as a marker for the filtered drag force closure.
6. *A posteriori* assessments of the effect of adding additional markers to the filtered drag force closure were more uncertain because the filtered slip velocity was used as a second marker. As suggested in point 5 above, this caused the 2-marker closure model to perform significantly worse than the 1-marker closure model. The addition of a third marker, the novel drift GPM, restored good model performance. The resulting 3-marker closure model outperformed the much simpler 1-marker closure model in *a posteriori* tests. Future work is therefore recommended to derive a simpler 2-marker closure model using the filtered solids volume fraction and drift GPM as markers.
7. In general, *a posteriori* assessments indicated that a filter size to grid size ratio of unity appears to be the fundamentally correct ratio instead of the commonly employed ratio of 2. This ensures that only structures smaller than the grid size considered are accounted for in the sub-grid corrections.
8. However, the fTFM verification tests also revealed another important domain size effect: when the domain width approaches the size of the macro-clusters resolved in the coarse grid simulations, a larger filter size to grid size ratio than unity is required. In this situation, gas cannot slip freely around the macro-clusters and more gas is forced through the macro-clusters. This artificially increases gas-solids momentum coupling, requiring more filtering to achieve the correct solution. Further studies are recommended to account for this effect in a more general manner, possibly by including a transport equation for a heterogeneity index such as the drift velocity or the filtered solids volume fraction variance.
9. It is important to note that the effect in point 8 is not a wall effect, but rather a domain width effect. Verification tests in the present study showed that anisotropic closure models behaved well in wall-bounded flows. In the single test completed, a transition from free-slip to no-slip

wall boundary conditions had only a minor effect on the overall reactor behaviour, which could be predicted by the filtered simulations. However, further tests under different flow conditions are recommended to generalize this conclusion.

10. In cases where the wall boundary condition may be important, such as rapid flows in narrow risers, the present work showed that the conventional partial-slip boundary condition by Johnson and Jackson required the specularity coefficient to be tuned for the flow conditions considered. A more complex partial-slip boundary condition recently proposed by Schneiderbauer was shown to be more generally applicable. However, an additional closure model will be required to use partial-slip boundary conditions in filtered simulations. Future work is therefore recommended to develop such a closure for cases where the wall boundary conditions are important.
11. For reactive flows, even a relatively simple filtered reaction rate closure performed very well in *a priori* tests. *A posteriori* tests confirmed that the formulation of an accurate filtered reaction rate closure is a relatively simple task, but the accuracy of the hydrodynamic closures can have a significant effect on the overall prediction of the reactor performance. In addition, implementation of a closure from literature for the mesoscale species dispersion rate did not have a significant impact on model performance. It is therefore recommended that fTFM development efforts continue to focus on the hydrodynamics in the knowledge that even a simple filtered reaction rate closure will perform well, as long as the hydrodynamic closures are accurate.
12. Filtered closures were developed in the present study from 2D simulation data, since this allowed a more detailed verification of the developed closures with the available computational resources. Despite the closures being derived from 2D resolved simulation data, a validation study against 3D experimental results showed promising performance. The 2D closure models from the present study outperformed a literature model derived from 3D simulation data. This is possibly due to the fact that the domain in which the 3D model was derived had to be an order of magnitude smaller (due to computational costs) than the 2D domain used in the present study. This result therefore suggests that it is more important for resolved simulation data to be domain independent than to be completed in 3D. However, since simulations on large enough domains in 3D are expected to remain computationally infeasible for some years to come, a detailed quantification of the effect of deriving fTFM closures in 2D versus 3D is suggested for future work. Since this will only be a comparative analysis, such a study can be performed on a small enough domain such that 3D simulations are computationally feasible.

In conclusion, the collection of closures proposed in the present work has been proven to perform well over a range of flow conditions. These closures can form a sound basis for further fTFM development work. One important topic that was not explored in the present work is the generality with regard to particle and fluid properties. A logical next step would therefore be to investigate the scaling of the variables used in the proposed anisotropic fTFM closures with the aim of achieving good accuracy under flow situations with different particle and fluid properties.

In conjunction with several other recommendations for future work listed above, it is therefore clear that there is still a lot to learn about filtered modelling of fluidized bed reactors. Even so, informed application of the anisotropic models proposed in the present work can already start adding value to certain large-scale fluidized bed reactor applications. Such a learning-by-doing approach will surely further accelerate progress in this field.

Nomenclature

Abbreviations

CFD	Computational Fluid Dynamics
FCC	Fluid catalytic cracking
fTFM	Filtered Two Fluid Model
GPM	Gradient Product Marker
KTGF	Kinetic Theory of Granular Flow
PDE	Partial Differential Equation
PR-DNS	Particle-Resolved Direct Numerical Simulation
PU-EL	Particle-Unresolved Euler-Lagrange
RMSE	Root mean square error
SA-TFM	Spatially-Averaged Two Fluid Model
SRM	Filtered deviatoric shear rate magnitude
TFM	Two Fluid Model

Main Symbols

C	Drag correction factor
C_{NL}	Non-linearity correction factor
C_p	Heat capacity ($J/(kg.K)$)
D	Mass diffusivity (m^2/s)
d_p	Particle diameter (m)
e_w	Normal restitution coefficient
F_M	Volumetric mesoscale interphase force (N/m^3)
G	Weight function
$\vec{g}$	Gravity vector (m/s^2)
g_0	Radial distribution function
h	Specific enthalpy (J/kg)
$\bar{\bar{I}}$	Identity matrix
K_{sg}	Interphase momentum exchange coefficient ($kg/(m^3.s)$)
k_A	Reaction rate constant of species A
k_g	Gas phase thermal conductivity ($W/(m.K)$)

k_{Θ_s}	Granular temperature diffusion coefficient ($kg/(m.s)$)
N	Normal shear stress (N/m^2)
p	Pressure (Pa)
Q	Heat transfer correction factor
q_s	Granular temperature flux at the wall (W/m^2)
R	Reaction rate correction factor
$\bar{\bar{S}}$	Deviatoric shear rate tensor ($1/s$)
T	Temperature (K)
t	Time (s)
U	Fluidization velocity (m/s)
u	X-direction velocity (m/s)
v	Y-direction velocity (m/s)
$\bar{v}_{ss\_slip}$	Steady state sedimentation velocity (m/s)
v_t	Particle terminal velocity (m/s)
X_A	Mass fraction of species A
x, y	Lateral and vertical directions
$\vec{x}, \vec{y}$	Position vector
α	Volume fraction
β_0	Tangential restitution coefficient
δ_{ij}	Kronecker delta
ϕ_{gs}	Interphase energy transfer (W/m^3)
ϕ	Specularity coefficient or generic scalar value
φ	Thiele modulus
γ	Heat transfer coefficient (W/m^3)
γ_{Θ_s}	Dissipation rate (W/m^3)
κ_A	Mass fraction of A scaled with domain averaged mass fraction
λ	Filtered scalar-velocity co-variance ($kg/(m^2 s)$)
λ_s	Solids bulk viscosity ($kg/(m.s)$)
μ_s	Solids viscosity ($kg/(m.s)$)
μ_w	Friction coefficient
μ	Dynamic viscosity ($kg/(m.s)$)
ρ	Density (kg/m^3)
$\bar{\bar{\tau}}$	Stress tensor (Pa)

$\bar{\bar{\tau}}_{s,fil}$	Solids mesoscale deviatoric stress tensor (Pa)
$\vec{\tau}_s$	Shear stress at the wall (N/m^2)
υ	Velocity (m/s)
v_d	Drift velocity (m/s)
v_{adj}	Adjusted slip velocity (m/s)
$\overline{v_s}$	Normalised particle slip velocity at the wall
ξ	Gradient constant (m^{-1})
Δ_f	Filter size (m)
Θ	Granular temperature (m^2/s^2)
M	Gradient product marker
Π	Heat transfer source term constant (W/m^3)
$\bar{\bar{\Sigma}}_s$	Solids mesoscale stress tensor (Pa)

Sub- and superscript definitions

fil	Filtered value
$fric$	Frictional
g	Gas
k	Generic phase
i, j	Coordinate indexes
s	Solid
$slip$	Slip velocity
w	Wall
x, y	Lateral and vertical directions
$\|$	Slip velocity parallel to wall

Operator definitions

$\|x\|$	Absolute value
$\bar{x}$	Algebraic volume average
$\langle x \rangle_d$	Domain average
x'	Fluctuation from algebraic average
x''	Fluctuation from phase-weighted average
$\|\|x\|\|$	Magnitude
$\hat{x}$	Non-dimensionalized value
$\tilde{x}$	Phase-weighted volume average

x^*	Scaled value
$\vec{x}$	Vector quantity

References

[1] F. Municchi, S. Radl, Consistent closures for Euler-Lagrange models of bi-disperse gas-particle suspensions derived from particle-resolved direct numerical simulations, International Journal of Heat and Mass Transfer, 111 (2017) 171-190.

[2] S. Radl, S. Sundaresan, A drag model for filtered Euler–Lagrange simulations of clustered gas–particle suspensions, Chem. Eng. Sci., 117 (2014) 416-425.

[3] L. Lu, S. Benyahia, T. Li, An efficient and reliable predictive method for fluidized bed simulation, AIChE J., (2017).

[4] S. Cloete, A. Zaabout, S.T. Johansen, M. van Sint Annaland, F. Gallucci, S. Amini, The generality of the standard 2D TFM approach in predicting bubbling fluidized bed hydrodynamics, Powder Technol., 235 (2013) 735-746.

[5] S.A. Wassie, F. Gallucci, S. Cloete, A. Zaabout, M. van Sint Annaland, S. Amini, The effect of gas permeation through vertical membranes on chemical switching reforming (CSR) reactor performance, International Journal of Hydrogen Energy, 41 (2016) 8640-8655.

[6] N. Ellis, M. Xu, C.J. Lim, S. Cloete, S. Amini, Effect of Change in Fluidizing Gas on Riser Hydrodynamics and Evaluation of Scaling Laws, Ind. Eng. Chem. Res., 50 (2011) 4697-4706.

[7] F. Taghipour, N. Ellis, C. Wong, Experimental and computational study of gas-solid fluidized bed hydrodynamics, Chem. Eng. Sci., 60 (2005) 6857-6867.

[8] F. Hernández-Jiménez, S. Sánchez-Delgado, A. Gómez-García, A. Acosta-Iborra, Comparison between two-fluid model simulations and particle image analysis and velocimetry (PIV) results for a two-dimensional gas–solid fluidized bed, Chem. Eng. Sci., 66 (2011) 3753-3772.

[9] A. Bakshi, C. Altantzis, R.B. Bates, A.F. Ghoniem, Study of the effect of reactor scale on fluidization hydrodynamics using fine-grid CFD simulations based on the two-fluid model, Powder Technol., 299 (2016) 185-198.

[10] P. Ostermeier, A. Vandersickel, S. Gleis, H. Spliethoff, Three dimensional multi fluid modeling of Geldart B bubbling fluidized bed with complex inlet geometries, Powder Technol., 312 (2017) 89-102.

[11] S. Cloete, S. Amini, S.T. Johansen, On the effect of cluster resolution in riser flows on momentum and reaction kinetic interaction, Powder Technol., 210 (2011) 6-17.

[12] Y. Igci, A.T. Andrews, S. Sundaresan, S. Pannala, T. O'Brien, Filtered two-fluid models for fluidized gas-particle suspensions, AIChE J., 54 (2008) 1431-1448.

[13] A. Sarkar, F.E. Milioli, S. Ozarkar, T. Li, X. Sun, S. Sundaresan, Filtered sub-grid constitutive models for fluidized gas-particle flows constructed from 3-D simulations, Chem. Eng. Sci., 152 (2016) 443-456.

[14] C.C. Milioli, F.E. Milioli, W. Holloway, K. Agrawal, S. Sundaresan, Filtered two-fluid models of fluidized gas-particle flows: New constitutive relations, AIChE J., 59 (2013) 3265-3275.

[15] S. Schneiderbauer, S. Pirker, Filtered and heterogeneity-based subgrid modifications for gas–solid drag and solid stresses in bubbling fluidized beds, AIChE J., 60 (2014) 839-854.

[16] Y. Igci, S. Sundaresan, Constitutive Models for Filtered Two-Fluid Models of Fluidized Gas–Particle Flows, Ind. Eng. Chem. Res., 50 (2011) 13190-13201.

[17] J.-F. Parmentier, O. Simonin, O. Delsart, A functional subgrid drift velocity model for filtered drag prediction in dense fluidized bed, AIChE J., 58 (2012) 1084-1098.

[18] A. Ozel, P. Fede, O. Simonin, Development of filtered Euler–Euler two-phase model for circulating fluidised bed: High resolution simulation, formulation and a priori analyses, Int. J. Multiphase Flow, 55 (2013) 43-63.

[19] Y. Igci, S. Sundaresan, Verification of filtered two-fluid models for gas-particle flows in risers, AIChE J., 57 (2011) 2691-2707.

[20] S. Schneiderbauer, A spatially-averaged two-fluid model for dense large-scale gas-solid flows, AIChE J., 63 (2017) 3544-3562.

[21] K. Agrawal, P.N. Loezos, M. Syamlal, S. Sundaresan, The Role of Meso-Scale Structures in Rapid Gas-Solid Flows, J. Fluid Mech., 445 (2001) 151-185.

[22] P.N. Loezos, S. Sundaresan, The role of meso-scale structures on dispersion in gas–particle flows, Circulating Fluidized Beds VII, 2002, pp. 427-434.

[23] A.T. Andrews, P.N. Loezos, S. Sundaresan, Coarse-grid simulation of gas-particle flows in vertical risers, Industrial and Engineering Chemistry Research, 44 (2005) 6022-6037.

[24] Y. Igci, S. Pannala, S. Benyahia, S. Sundaresan, Validation Studies on Filtered Model Equations for Gas-Particle Flows in Risers, Ind. Eng. Chem. Res., 51 (2012) 2094-2103.

[25] S. Cloete, S.T. Johansen, S. Amini, Evaluation of a filtered model for the simulation of large scale bubbling and turbulent fluidized beds, Powder Technol., 235 (2013) 91-102.

[26] S.S. Ozarkar, X. Yan, S. Wang, C.C. Milioli, F.E. Milioli, S. Sundaresan, Validation of filtered two-fluid models for gas–particle flows against experimental data from bubbling fluidized bed, Powder Technol., 284 (2015) 159-169.

[27] K. Agrawal, W. Holloway, C.C. Milioli, F.E. Milioli, S. Sundaresan, Filtered models for scalar transport in gas–particle flows, Chem. Eng. Sci., 95 (2013) 291-300.

[28] W. Holloway, S. Sundaresan, Filtered models for reacting gas–particle flows, Chem. Eng. Sci., 82 (2012) 132-143.

[29] S. Schneiderbauer, Validation study on Spatially Averaged Two Fluid Model for dense gas-solids flows, CFB-12, Krakow, Poland (2017).

[30] W. Holloway, S. Sundaresan, Filtered models for bidisperse gas–particle flows, Chem. Eng. Sci., 108 (2014) 67-86.

[31] A. Ozel, J. Kolehmainen, S. Radl, S. Sundaresan, Fluid and particle coarsening of drag force for discrete-parcel approach, Chem. Eng. Sci., 155 (2016) 258-267.

[32] A. Ozel, Y. Gu, C.C. Milioli, J. Kolehmainen, S. Sundaresan, Towards filtered drag force model for non-cohesive and cohesive particle-gas flows, Physics of Fluids, 29 (2017) 103308.

[33] S. Schneiderbauer, S. Pirker, The impact of different fine grid simulations on the sub-grid modification for gas–solid drag, 9th International Conference on Multiphase Flow, Firenze (2016).

[34] S. Schneiderbauer, D. Schellander, A. Löderer, S. Pirker, Non-steady state boundary conditions for collisional granular flows at flat frictional moving walls, Int. J. Multiphase Flow, 43 (2012) 149-156.

[35] P.C. Johnson, R. Jackson, Frictional-Collisional Constitutive Relations for Granular Materials, with Application to Plane Shearing, J. Fluid Mech., 176 (1987) 67-93.

[36] L. Huilin, D. Gidaspow, Hydrodynamics of binary fluidization in a riser: CFD simulation using two granular temperatures, Chem. Eng. Sci., 58 (2003) 3777-3792.

[37] S. Ergun, Fluid Flow through Packed Columns, Chemical Engineering Progress, 48 (1952) 89-94.

[38] C.Y. Wen, Y.H. Yu, Mechanics of Fluidization, Chem. Eng. Prog. S. Ser., 62 (1966) 100-111.

[39] C.K.K. Lun, S.B. Savage, D.J. Jeffrey, N. Chepurniy, Kinetic Theories for Granular Flow: Inelastic Particles in Couette Flow and Slightly Inelastic Particles in a General Flow Field, J. Fluid Mech., 140 (1984) 223-256.

[40] D. Gidaspow, R. Bezburuah, J. Ding, Hydrodynamics of Circulating Fluidized Beds, Kinetic Theory Approach, 7th Engineering Foundation Conference on Fluidization (1992).

[41] S. Ogawa, A. Unemura, N. Oshima, On the Equation of Fully Fluidized Granular Materials, J. Appl. Math. Phys, 31 (1980) 483.

[42] D.G. Schaeffer, Instability in the Evolution Equations Describing Incompressible Granular Flow, J. Differ. Equations, 66 (1987) 19-50.

[43] S.B. Pope, Tubulent Flows, Cambridge University Press, Cambridge, UK, 2000.

[44] J. Capecelatro, O. Desjardins, R.O. Fox, Effect of Domain Size on Fluid–Particle Statistics in Homogeneous, Gravity-Driven, Cluster-Induced Turbulence, Journal of Fluids Engineering, 138 (2015) 041301-041301-041308.

[45] S. Patankar, Numerical Heat Transfer and Fluid Flow, Hemisphere Publishing Corporation1980.

[46] B.P. Leonard, S. Mokhtari, ULTRA-SHARP Nonoscillatory Convection Schemes for High-Speed Steady Multidimensional Flow, NASA TM 1-2568 (ICOMP-90-12)NASA Lewis Research Center, 1990.

[47] F. Municchi, C. Goniva, S. Radl, Highly efficient spatial data filtering in parallel using the opensource library CPPPO, Computer Physics Communications, 207 (2016) 400-414.

[48] S. Schneiderbauer, S. Pirker, S. Sundaresan, The Dependence of the Effective Gas-Solid Drag in Filtered Two-Fluid Models on the Sub-Filter Solid Turbulence, AIChE Annual Meeting Salt Lake City, 2015.

[49] S. Schneiderbauer, Cluster induced turbulence (CIT) - A spatially averaged two-fluid model (SA-TFM) for dense gas-solid flows, 24th ERCOFTAC ADA Pilot Center Meeting (2016).

[50] S. Cloete, J.H. Cloete, S. Amini, Comparison of the Filtered Two Fluid Model and Dense Discrete Phase Model for Large-Scale Fluidized Bed Reactor Simulations, AIChE Annual Meeting San Franciso, USA (2016).

[51] D.Z. Zhang, W.B. VanderHeyden, The effects of mesoscale structures on the macroscopic momentum equations for two-phase flows, Int. J. Multiphase Flow, 28 (2002) 805-822.

[52] J. De Wilde, Reformulating and quantifying the generalized added mass in filtered gas-solid flow models, Physics of Fluids, 17 (2005) 113304.

[53] J. De Wilde, The generalized added mass revised, Physics of Fluids, 19 (2007) 058103.

[54] S. Sundaresan, Instabilities in Fluidized Beds, Annual Review of Fluid Mechanics, 35 (2003) 63-88.

[55] W.D. Fullmer, C.M. Hrenya, The Clustering Instability in Rapid Granular and Gas-Solid Flows, Annual Review of Fluid Mechanics, 49 (2017) 485-510.

[56] A. Srivastava, S. Sundaresan, Analysis of a frictional–kinetic model for gas–particle flow, Powder Technol., 129 (2003) 72-85.

[57] S. Schneiderbauer, A. Aigner, S. Pirker, A comprehensive frictional-kinetic model for gas–particle flows: Analysis of fluidized and moving bed regimes, Chem. Eng. Sci., 80 (2012) 279-292.

[58] H.T. Bi, J.R. Grace, Flow regime diagrams for gas-solid fluidization and upward transport, Int. J. Multiphase Flow, 21 (1995) 1229-1236.

[59] J.H. Cloete, S. Cloete, S. Radl, S. Amini, Verification of filtered Two Fluid Models for reactive gas-solid flows, CFD 2017, Trondheim, Norway (2017).

[60] H. Zhu, J. Zhu, G. Li, F. Li, Detailed measurements of flow structure inside a dense gas-solids fluidized bed, Powder Technology, 180 (2008) 339-349.

[61] H. Zhu, Turbulent Fluidized Bed vs. High Density Riser - Regimes and Flow Characterizations, The University of Western Ontario, 2006.

[62] L. Shadle, M. Shahnam, R. Cocco, A. Issangya, C. Guenther, M. Syamlal, J. Spenik, J.C. Ludlow, F. Shaffer, R. Panday, B. Gopalan, R. Dastane, Challenge Problem III, Circulating Fluid Bed X, Sun River Valley, Oregon, USA (2011).

[63] D. Geldart, Types of gas fluidization, Powder Technol., 7 (1973) 285-292.

[64] S. Schneiderbauer, Validation study on spatially averaged two-fluid model for gas-solid flows: I. A-priori analysis of wall bounded flows, AIChE J., Under review (2017).

[65] S. Cloete, S.T. Johansen, S. Amini, Grid independence behaviour of fluidized bed reactor simulations using the Two Fluid Model: Effect of particle size, Powder Technol., 269 (2015) 153-165.

[66] S. Cloete, S.T. Johansen, S. Amini, Grid independence behaviour of fluidized bed reactor simulations using the Two Fluid Model: Detailed parametric study, Powder Technol., 289 (2016) 65-70.

[67] M. Syamlal, T.J. O'Brien, Computer simulation of bubbles in a fluidized bed, AIChE Symposium Series, 1989, pp. 22-31.

[68] H. Iddir, H. Arastoopour, Modeling of multitype particle flow using the kinetic theory approach, AIChE J., 51 (2005) 1620-1632.

[69] G. Ahmadi, D. Ma, A thermodynamical formulation for dispersed multiphase turbulent flows—1, Int. J. Multiphase Flow, 16 (1990) 323-340.

[70] S. Cloete, S. Amini, S.T. Johansen, A fine resolution parametric study on the numerical simulation of gas-solid flows in a periodic riser section, Powder Technol., 205 (2011) 103-111.

[71] A. Almuttahar, F. Taghipour, Computational fluid dynamics of high density circulating fluidized bed riser: Study of modeling parameters, Powder Technol., 185 (2008) 11-23.

[72] A. Soleimani, S. Schneiderbauer, S. Pirker, A comparison for different wall-boundary conditions for kinetic theory based two-fluid models, Int. J. Multiphase Flow, 71 (2015) 94-97.

[73] Y. Zhao, Y. Zhong, Y. He, H.I. Schlaberg, Boundary conditions for collisional granular flows of frictional and rotational particles at flat walls, AIChE J., 60 (2014) 4065-4075.

[74] B. Chalermsinsuwan, P. Piumsomboon, D. Gidaspow, Kinetic theory based computation of PSRI riser: Part I-Estimate of mass transfer coefficient, Chem. Eng. Sci., 64 (2009) 1195-1211.

[75] H. Lu, S. Wang, Y. He, J. Ding, G. Liu, Z. Hao, Numerical simulation of flow behavior of particles and clusters in riser using two granular temperatures, Powder Technol., 182 (2008) 282-293.

[76] S. Benyahia, M. Syamlal, T.J. O'Brien, Study of the ability of multiphase continuum models to predict core-annulus flow, AIChE J., 53 (2007) 2549-2568.

[77] J.T. Jenkins, Boundary Conditions for Rapid Granular Flow: Flat, Frictional Walls, Journal of Applied Mechanics, 59 (1992) 120-127.

[78] M.Y. Louge, Computer simulations of rapid granular flows of spheres interacting with a flat, frictional boundary, Physics of Fluids, 6 (1994) 2253-2269.

[79] T. Li, S. Benyahia, Revisiting Johnson and Jackson boundary conditions for granular flows, AIChE J., 58 (2012) 2058-2068.

[80] J.T. Jenkins, M.Y. Louge, On the flux of fluctuation energy in a collisional grain flow at a flat, frictional wall, Physics of Fluids, 9 (1997) 2835-2840.

[81] A. Yan, J. Zhu, Scale-Up Effect of Riser Reactors (1) Axial and Radial Solids Concentration Distribution and Flow Development, Ind. Eng. Chem. Res., 43 (2004) 5810-5819.

[82] A. Yan, J. Zhu, Scale-Up of Riser Reactors: Particle Velocity and Flow Development, AIChE J., 51 (2005) 2956-2964.

[83] T. Li, S. Benyahia, J.-F. Dietiker, J. Musser, X. Sun, A 2.5D computational method to simulate cylindrical fluidized beds, Chem. Eng. Sci., 123 (2015) 236-246.

[84] J.X. Zhu, G.Z. Li, S.Z. Qin, F.Y. Li, H. Zhang, Y.L. Yang, Direct measurements of particle velocities in gas–solids suspension flow using a novel five-fiber optical probe, Powder Technol., 115 (2001) 184-192.

[85] J.H. Cloete, S. Cloete, S. Radl, S. Amini, Evaluation of wall friction models for riser flow, Powder Technol., 303 (2016) 156-167.

[86] S.F. Foerster, M.Y. Louge, H. Chang, K. Allia, Measurements of the collision properties of small spheres, Physics of Fluids, 6 (1994) 1108-1115.

[87] A. Lorenz, C. Tuozzolo, M.Y. Louge, Measurements of impact properties of small, nearly spherical particles, Experimental Mechanics, 37 (1997) 292-298.

[88] M. Sommerfeld, N. Huber, Experimental analysis and modelling of particle-wall collisions, Int. J. Multiphase Flow, 25 (1999) 1457-1489.

[89] S. Cloete, S.T. Johansen, A. Zaabout, M. van Sint Annaland, F. Gallucci, S. Amini, The effect of frictional pressure, geometry and wall friction on the modelling of a pseudo-2D bubbling fluidised bed reactor, Powder Technol., 283 (2015) 85-102.

[90] A. Ozel, G. Rubinstein, S. Sundaresan, A Dynamic Drag Model Using Sub-Grid Scalar Variance of Solid Volume Fraction for Gas-Solid Suspensions, AIChE Annual Meeting San Francisco, 2016.

[91] D.J. Gunn, Transfer of Heat or Mass to Particles in Fixed and Fluidized Beds, International Journal of Heat and Mass Transfer, 21 (1978) 467-476.

Appendix

A. Publication list

A.1 Accepted journal papers

[1] J.H. Cloete, S. Cloete, S. Radl, S. Amini, Evaluation of wall friction models for riser flow, Powder Technol., 303 (2016) 156-167.

[2] J.H. Cloete, S. Cloete, F. Municchi, S. Radl, S. Amini, The sensitivity of filtered Two Fluid Model to the underlying resolved simulation setup, Powder Technol., 316 (2017) 265-277.

[3] S. Cloete, J.H. Cloete, S. Amini, Hydrodynamic validation study of filtered Two Fluid Models, Chem. Eng. Sci., 182 (2018) 93-107.

A.2 Journal papers under review

[1] J.H. Cloete, S. Cloete, S. Radl, F. Municchi, S. Amini, Development and verification of anisotropic stress closures for filtered Two Fluid Models, Chem. Eng. Sci., Under review (2018).

[2] J.H. Cloete, S. Cloete, S. Radl, S. Amini, Development and verification of anisotropic drag closures for filtered Two Fluid Models, Chem. Eng. Sci., Under review (2018).

A.3 Conference papers

[1] S. Cloete, J.H. Cloete, S. Amini, Comparison of the Filtered Two Fluid Model and Dense Discrete Phase Model for Large-Scale Fluidized Bed Reactor Simulations, AIChE Annual Meeting, San Francisco, USA, 2016.

[2] J.H. Cloete, S. Cloete, S. Radl, S. Amini, Verification of filtered Two-Fluid Models in different flow regimes, CFB-12, Krakow, 2017.

[3] J.H. Cloete, S. Cloete, S. Radl, S. Amini, Verification of filtered Two Fluid Models for reactive gas-solid flows, CFD 2017, Trondheim, Norway, 2017.

[4] J.H. Cloete, S. Cloete, S. Radl, S. Amini, Verification study of anisotropic filtered Two Fluid Model Closures, AIChE Annual Meeting, Minneapolis, USA, 2017.

A.4 Planned journal papers

[1] J.H. Cloete, S. Cloete, S. Radl, S. Amini, On the improvement of filtered Two Fluid Model drag closures by considering additional independent variables

[2] J.H. Cloete, S. Cloete, S. Radl, S. Amini, Development and verification of reactive filtered Two Fluid Models for coarse-grid fluidized bed simulations

[3] S. Cloete, J.H. Cloete, S. Radl, S. Amini, Detailed verification of filtered Two Fluid Models in different fluidization regimes

B. The sensitivity of fTFM closures to the resolved TFM configuration

In this section, the complete findings from the study summarized in Chapter 3.3.1 are reported.

B.1 Simulations

The resolved simulations from which the filtered data is obtained is similar to that described in Chapter 3, with a few exceptions. Firstly, in this study, scalar transport and heat transfer is also considered. The equations and methodology relevant to these phenomena are given in Appendix E.1 and Appendix E.2. Secondly, in this section only the following domain-averaged solids volume fractions are considered in the resolved simulations: 0.02, 0.1, 0.2, 0.3 and 0.4. Lastly, a coarser grid of 1.25 mm ($16.67d_p$) is considered to make the large number of simulations performed in this section computationally feasible. This grid size is insufficient to achieve grid independence according to general guidelines for selecting the grid size in resolved TFM simulations of fluidized beds [65, 66] given the small 75 μm particle size. However, performing "slightly unresolved" simulations is valid for this study since it only seeks to compare simulations relative to each other. The error associated with the spatial discretization is hence assumed to be similar in the different simulations.

B.2 Filtered closure quantities considered

It should be noted that, in this section, unlike the rest of this thesis, no distinction is made between fluctuations from algebraic and phase-weighted averages by making using of single and double primes.

B.2.1 Filtered drag and solids mesoscale stresses

A drag correction factor, evaluated in the vertical direction, is considered, similar to what is discussed in Chapter 3.4.1.

$$C = \frac{\overline{K_{gs}(v_{g,y}-v_{s,y})-\alpha_s{}'\frac{dp'}{dy}}}{K_{gs,coarse}(\tilde{v}_{g,y}-\tilde{v}_{s,y})} \qquad \text{Equation 95}$$

where $K_{gs,coarse}$ is evaluated at the filtered solids volume fraction and the filtered slip velocity magnitude.

When considering the solids mesoscale stresses (third term on the right in Equation 15), the mean of the normal stresses is used to calculated a filtered solids pressure as follows:

$$\hat{p}_{s,fil} = \frac{p_{s,fil}}{\rho_s v_t^2} = \frac{\frac{1}{2}(\overline{\alpha_s v_{s,x}{}' v_{s,x}{}'} + \overline{\alpha_s v_{s,y}{}' v_{s,y}{}'})}{v_t^2} \qquad \text{Equation 96}$$

The shear components still need to be considered. In the work from the Princeton group [12, 16, 27] this term is modelled as a filtered solids viscosity by calculating the ratio of the shear stress and the filtered shear gradients. However, the present study found that this produces a problem in samples in which the filtered shear gradients are small (see section B.1). Since the present study is only concerned with comparing sub-grid terms for different model formulations, and not with the actual implementation of the filtered models, it was therefore deemed unnecessary to cast the filtered shear stress into the filtered viscosity form. Only the dimensionless filtered solids mesoscale shear stress is henceforth considered, and calculated as follows:

$$\hat{\tau}_{s,fil} = \frac{\tau_{s,fil}}{\rho_s v_t^2} = \frac{\overline{\alpha_s v_{s,x}{}' v_{s,y}{}'}}{v_t^2}$$ Equation 97

B.2.2 Scalar transport

Previously, a filtered diffusivity has been considered to close the filtered scalar transport equation [27]. In the present study, the same problem with small values for the filtered scalar gradients was experienced as when calculating a filtered solids viscosity (see section B.2.1). Therefore, only the dimensionless filtered scalar-velocity co-variance (henceforth referred to as the filtered scalar co-variance) is calculated. Note, only the fluctuations of the x-velocity are considered in the present work; an extension to other directions is straight forward and will be considered in future work.

$$\hat{\lambda}_{k,fil} = \frac{\lambda_{k,fil}}{\rho_s v_t} = \frac{\overline{\alpha_k \phi_k{}' \vec{v}_s{}'}}{v_t}$$ Equation 98

B.2.3 Heat transfer

The filtered heat transfer correction is calculated in a similar way to the filtered drag correction:

$$Q = \frac{\overline{\gamma(T_s - T_g)}}{\gamma_{coarse}(\tilde{T}_s - \tilde{T}_g)}$$ Equation 99

where γ_{coarse} is, again, evaluated at the filtered phase volume fraction and filtered slip velocity.

B.2.4 Reactions

A non-locally corrected reaction rate correction is considered, as described in Chapter 3.8.2 and Appendix F.3.1.

$$R = \frac{\overline{\alpha_s \kappa_A} - m_2 \nabla \overline{\alpha_s}^T \cdot \nabla \widetilde{\kappa_A}}{\widetilde{\alpha_s \kappa_A}}$$ Equation 100

Where $m_2 = \Delta^2/12$, and Δ is the filter size.

B.3 Verification against literature results

Since the methodology followed in this paper is strongly based on the papers published by the Princeton group [12, 14, 16, 19, 27, 28], the results were compared to ensure that the methodology is applied correctly. Overall, a satisfactory comparison is achieved, indicating that the results generated in the present study can be used with confidence. However, two interesting areas of differences should be addressed.

The first topic involves the modelling of the filtered shear stress for the solids and the filtered co-variance of the scalars. In the work performed at Princeton these quantities were modelled as a filtered solids viscosity and a filtered scalar diffusivity, as follows:

$$\overline{\mu_{s,fil}} = \rho_s \overline{\alpha_s v_{s,x}{}' v_{s,y}{}'} / \left(\frac{d\widetilde{v_{s,x}}}{dy} + \frac{d\widetilde{v_{s,y}}}{dx}\right)$$ Equation 101

$$\overline{D_{k,fil}} = \rho_s \overline{\alpha_s \phi_k{}' v_{k,x}{}'} / \left(\frac{d\widetilde{\phi_k}}{dx}\right)$$ Equation 102

Samples of both of these values become problematic when the value of the denominator is small, resulting in very large sample values. These samples magnify the natural variation in the filtered shear stress and filtered scalar co-variance (numerators in Equation 101 and Equation 102) within each bin and cause problems in obtaining a smooth correlation as a function of the marker. This problem can be reduced by eliminating samples where the denominator has a value below a certain cut-off value. A good comparison with the results from the Princeton group is achieved when using cut-off values equal to the mean gradient ($100m^{-1}$ for this study) for the filtered scalar diffusivity and 1% of the non-dimensional unit for the filtered solids viscosity. However, further investigation of the cut-off values showed that the solution keeps on changing with changing values of the cut-off value.

This is shown in Figure 102 for the filtered scalar diffusivity in the gas phase, although the same is observed for the filtered solids viscosity. It is shown that, initially, increasing the cut-off value leads to a smoother curve. At very large cut-off values, the curves become less smooth again, since a large percentage of the samples are now ignored. It is also clear that the solution keeps changing with the cut-off value. Future research should therefore investigate the closure of the filtered solids shear stresses and filtered scalar co-variances in the form of Equation 101 and Equation 102. However, since this study is only concerned with investigating the effect of different resolved TFM setups relative to each other and not with the implementation of the filtered models, Equation 97 and Equation 98 are considered instead.

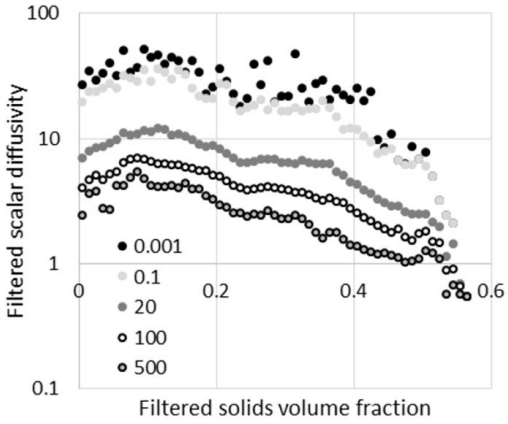

Figure 102 - Comparison of the dimensionless filtered scalar diffusivity in the gas phase considering different values for the cut-off value of the denominator.

Secondly, the main difference in the results from this study and those from Princeton is in the behaviour of the filtered variances at high volume fractions. In the work performed at Princeton, numerous simulations were performed at high domain-averaged particle volume fractions. As the domain-averaged solids volume fraction is increased above 0.3, a point is reached where the formation of gas bubbles is dramatically reduced and the flow rapidly becomes more homogenous by further increasing the domain-averaged volume fraction. In these simulations, there are therefore very small variances in each filter region. The correlations derived for the filtered solids pressure, filtered solids viscosity and filtered scalar therefore all peak at a filtered solids volume fraction of approximately 0.3 (with the exception of the scalar diffusivity in the gas phase, which peaks earlier) and then declines

towards a zero value at large volume fractions, where the solids distribution is completely homogenous.

These highly homogenous simulations concentrate the samples in a small range of bins around the domain-averaged solids volume fraction. In this narrow range of bins, the mean of the sampled values is dragged towards zero, competing with fewer samples obtained from simulations at smaller domain-averaged volume fractions. The result is a noticeable dip in the correlation around each domain-averaged solids volume fraction considered for large values of the filtered solids volume fraction (this is illustrated to some degree in Figure 103, which will be discussed shortly). To obtain a smooth curve, a large number of domain-averaged solids volume fractions would have to be considered as was done by the Princeton group. However, in the present study where several different model setups are compared, performing that many simulations is not feasible.

For this reason, five domain-averaged solids volume fractions are considered in this study, only up to domain-averaged solids volume fractions where sharp bubbles/clusters still form. This changes the nature of the filtered variances at high filtered solids volume fractions since none of the simulations includes large, dense, slow-moving zones. Instead, very dense regions only occur in small regions inside clusters of particles, where considerable velocity fluctuations still occur. This causes the fluctuations to continue rising above filtered solids volume fraction of 0.3, in contrast to the results of the Princeton group. Regardless of this difference, the values obtained up to filtered solids volume fractions around 0.3 are similar to those reported in ref. [16]. It can therefore be concluded that the nature of the variance terms in dense regions is very different depending on whether the dense region is within a small, dynamic solids cluster or within a large, homogenous solids area, as would occur in dense bubbling beds. Additional markers are clearly necessary to capture this effect and should be investigated in future studies.

At the highest domain-averaged volume fraction of 0.4 considered in this study, clear bubble formation occurs in most model setups. However, when using either the Huilin-Gidaspow or Syamlal-O'Brien drag models, the bubbles in these simulations become much less distinct. This occurs because the interphase momentum exchange coefficient is larger for these models in dense regions than for the Wen-Yu drag model, leading to larger drag forces, smaller slip velocities and more homogenous flow (as discussed in section B.5.1).

The effect of including the simulation results at a domain-averaged solids volume fraction of 0.4 is shown in Figure 103. Results from the simulations with domain-averaged volume fractions of 0.3 and 0.4 are shown when analysed individually, as well as the correlation combining data from all domain-averaged volume fractions. The results from the two different drag models are quite similar for the data obtained from the domain-averaged solids volume fraction of 0.3. On the contrary, it can be seen that, at a domain-averaged solids volume fraction of 0.4, the filtered stresses are much smaller in the simulations using the Huilin-Gidaspow drag model due to the more homogenous flow situation with fewer velocity fluctuations. This causes a sharp dip in the correlation around a filtered solids volume fraction of 0.4. Such a sudden change in behaviour makes the comparison of filtered quantities for different model setups difficult. For this reason, the information from simulations using a domain-averaged solids volume fraction of 0.4 is neglected in the following results.

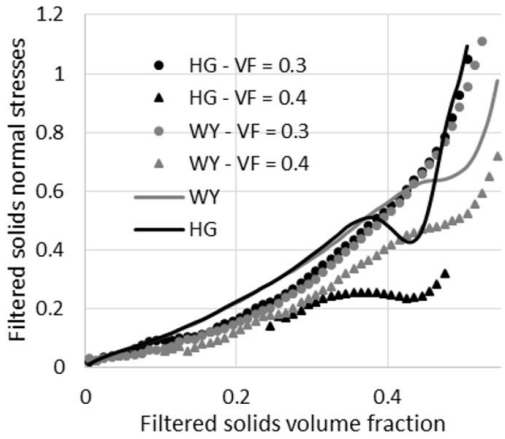

Figure 103 - Comparison of the filtered solids normal stresses for simulations performed with the Wen-Yu and Huilin-Gidaspow drag models using a filter size of 33 by 33 cells.

B.4 Overall impact assessment

This section will give an overall view of the impact of the different TFM setups on the different filtered correlations. This will be done by analysing the difference of the results of each setup from the base case (referred to as Base). The base case was chosen to be similar to the setup employed by the Princeton group in their studies and uses the Wen-Yu drag model [38], the radial distribution function by Ogawa [41], a particle-particle restitution coefficient of 0.9 and does not include a frictional pressure model. Additional TFM setups are considered with the following changes from the base case:

- Drag model
  - Huilin-Gidaspow drag model [36] (referred to as the HG case)
  - Syamlal-O'Brien drag model [67] (SO case)
- Frictional pressure
  - Including the frictional pressure model by Johnson & Jackson [35, 42] (FP case)
- Particle-particle restitution coefficient
  - 0.95 (PPR-H)
  - 0.8 (PPR-L)
- Radial distribution functions
  - Arastoopour [68] (Ara)
  - Ma & Ahmadi [69] (MA)

All filtered quantities are presented in their dimensionless forms, as presented in section B.2. It should also be noted that the filtered slip velocity, $|\tilde{v}_{g,y} - \tilde{v}_{s,y}|$, is also included as one of the filtered quantities to be assessed. The filtered slip velocity has been shown to be an important marker for the drag by ref. [14]. Although not included as a marker in this study, it is expected that it will also be an important marker for other filtered quantities as well, as the filtered slip velocity will influence the shape and definition of the solid clusters and gas bubbles, and thereby also the sub-grid effects. It therefore becomes valuable to assess the influence that different simulations setups will have on the filtered slip velocity.

The overall difference from the base case is quantified by calculating the percentage difference of a filtered quantity from the base case in each bin and then calculating the average difference in all of the bins. However, some bins at large filtered solids volume fractions contain very few samples, causing variation in the data, and should therefore be neglected. To do this, the amount of markers are calculated that would be in each bin if the samples were distributed uniformly over all the bins. All bins with fewer than 20% of this number of samples are then neglected in the comparison of TFM setups and are also not presented in the graphs following in the discussion of results. Such a comparison is given in Figure 104 for a filter size of 9x9 cells (11.25x11.25 mm^2) and in Figure 105 for a filter size of 33x33 cells (41.25x41.25 mm^2).

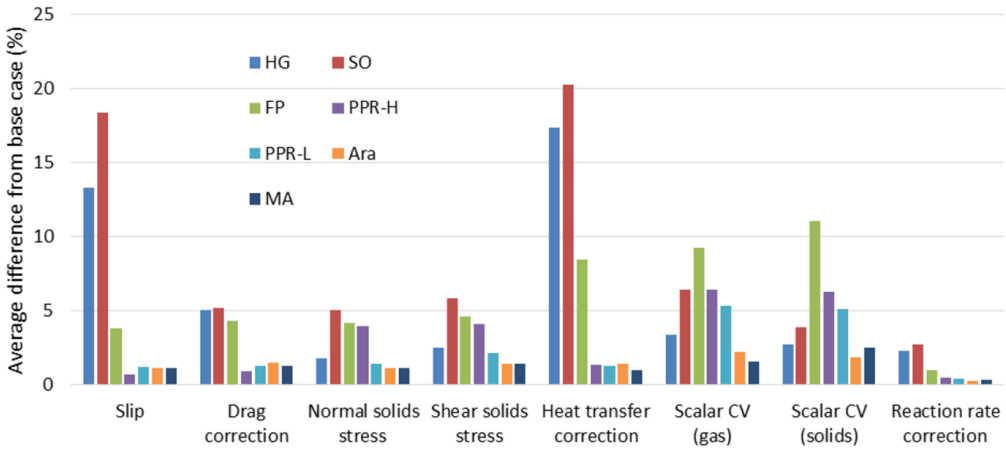

Figure 104 - Comparison of all TFM setups considered to the base case for all filtered quantities using a filter size of 9x9 cells. HG = Huilin-Gidaspow drag model, SO = Syamlal-O'Brien drag model, FP = including frictional pressure, PPR-H = particle-particle restitution coefficient of 0.95, PPR-L = particle-particle restitution coefficient of 0.8, Ara = radial distribution function of Arastoopour, MA = radial distribution function of Ma & Ahmadi.

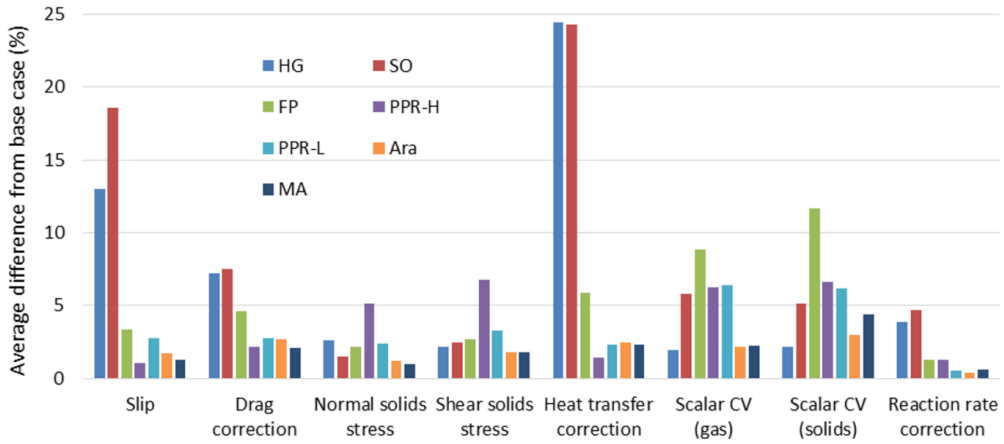

Figure 105 - Comparison of all TFM setups considered to the base case for all filtered quantities using a filter size of 33x33 cells. HG = Huilin-Gidaspow drag model, SO = Syamlal-O'Brien drag model, FP = including frictional pressure, PPR-H = particle-particle restitution coefficient of 0.95, PPR-L = particle-particle restitution coefficient of 0.8, Ara = radial distribution function of Arastoopour, MA = radial distribution function of Ma & Ahmadi.

A number of conclusions can be drawn from this overview of the results generated in this study. Firstly, it is clear that the effect of the drag law (HG and SO) is by far the most important, especially on the filtered slip velocity and filtered heat transfer correction.

Apart from the drag law, however, the average deviations from the base case are relatively small, ranging from about 1% to 10%. The effect of changing the radial distribution function is the smallest and it can in general be concluded that the choice of this closure is insignificant when deriving filtered models. The generally small impact of the TFM formulation on the filtered quantities is a positive result, since it indicates that the uncertainty associated with the choice of the resolved TFM formulation is small in most cases and therefore gives reason for increased confidence in the fTFM approach.

It can also be observed that the effect of the different model settings is mostly similar for the small and the large filter sizes, although there are some exceptions. Firstly, the effect of including frictional pressure (FP) is larger in some cases for the smaller filter size. This is because the frictional pressure is specified to only have an effect at solids volume fractions higher than 0.5. For the large filter size, there are fewer samples with very large filtered solids volume fractions, therefore reliable data is available for fewer high filtered solids volume fraction bins. The effect of including the frictional pressure is therefore smaller when using large filter sizes. The significance of changing to the Syamlal-O'Brien drag model is also reduced with the increased filter size. This effect is discussed further in section B.5.3.

It can also be noted that some filtered quantities are similarly affected by changes in the TFM setup. For example, for the filtered slip velocity, drag correction, heat transfer correction and reaction rate correction, the significant effects are all for the HG, SO and FP cases. Furthermore, the effects on the filtered solid stresses are very similar, with the SO, FP and PPR-H cases being significant. Finally, the two filtered scalar co-variances respond similarly. They also behave somewhat similarly to the filtered solids stresses, except that the frictional pressure (FP) and the lower particle-particle restitution coefficient (PPR-L) has a more significant effect for the filtered scalar co-variances.

These effects will be analysed in more detail in the following section.

B.5 Detailed analysis of significant effects

In this section, the results presented in section B.4 will be analysed in more detail, limiting the discussion to the more significant model effects on each filtered quantity. The results are visualised by plotting both the filtered quantity and the percentage deviation from the base case as a function of the filtered solids volume fraction. Furthermore, the discussion focusses on the smaller filter size (9x9 cells) since the results are similar for the two filter sizes with some effects more visible for the smaller filter.

B.5.1 Filtered slip velocity

From Figure 106 it can be seen that, at higher filtered solids volume fractions, the filtered slip velocity for the frictional pressure case rapidly decreases relative to the base case. This can be explained through Figure 107 which shows that the dense regions inside clusters tend to be larger and more homogenous when the frictional pressure is included. This is due to the much larger viscosity of the solids in the dense regions with frictional stresses included, causing the solids cluster to become more difficult to deform.

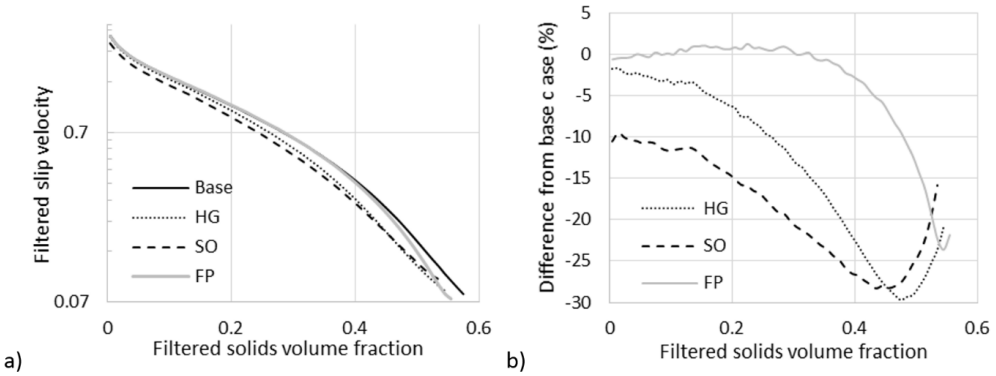

Figure 106 - Comparison of the dimensionless filtered slip velocity for the significant cases by a) the filtered quantity and b) the percentage deviation from the filtered quantity in the base case

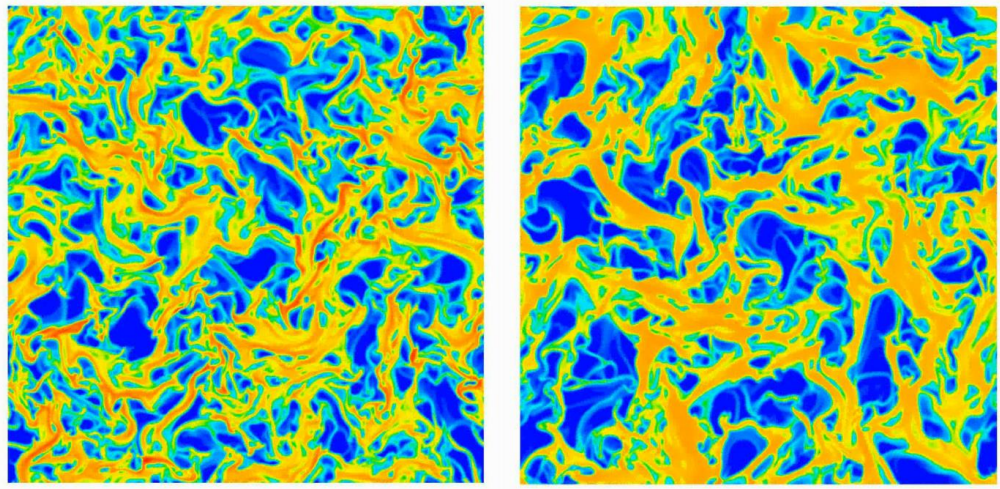

Figure 107 - Comparison of the solids volume fraction contours without frictional pressure on the left and with frictional pressure on the right. Blue corresponds to a solids volume fraction of zero and red to a solids volume fraction of 0.6.

Both the Huilin-Gidaspow and Syamlal-O'Brien drag models predict significantly lower slip velocities over the entire range of filtered volume fractions than the Wen-Yu model, as seen in Figure 106. This behaviour is explained by comparing the interphase momentum exchange coefficients for the drag models, as is done in Figure 108 at a slip velocity of 0.01 m/s (a good approximation of the slip velocities inside the dense regions). Here it can be seen that the interphase exchange coefficient of the Huilin-Gidaspow and Syamlal-O'Brien drag models are larger than that of the Wen-Yu drag model, especially in dense regions. The larger drag forces predicted lead to tighter coupling between the gas and particles, resulting in smaller slip velocities. However, the main reason for the large influence of the alternative drag models is likely to be related to less distinct cluster resolution as will be further discussed in subsequent sections.

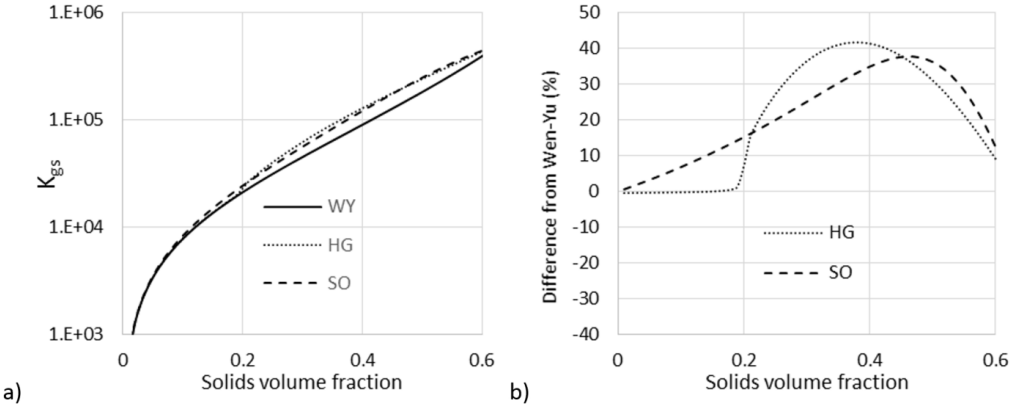

Figure 108 - Comparison of the interphase momentum exchange coefficients for the three drag models considered at a slip velocity of 0.01 m/s by a) the coefficient value and b) the percentage deviation from the Wen-Yu drag law

B.5.2 Filtered drag correction

For the drag correction, the addition of frictional pressure again has a large affect at filtered solids volume fractions above approximately 0.4. This is again due to the more homogenous nature of the clusters with frictional pressure included. In the bins at the highest filtered solids volume fraction with sufficient samples, which corresponds to the centres of the clusters, the solids distribution is essentially uniform and the filtered drag correction is close to unity.

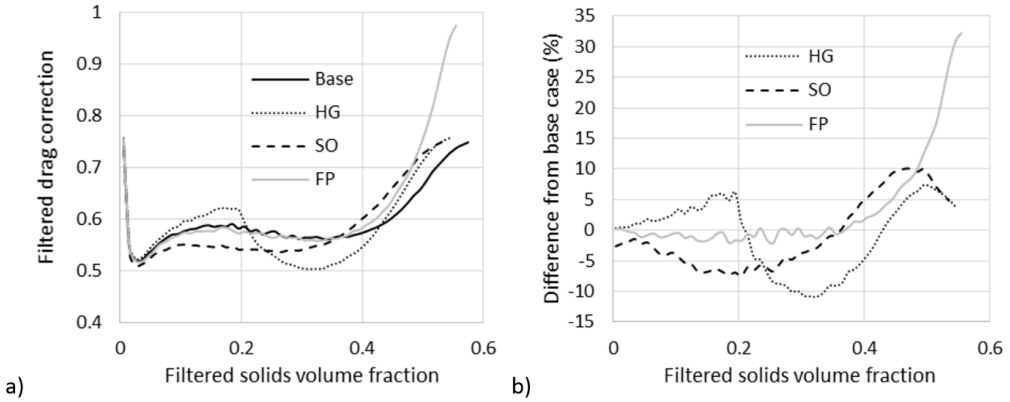

Figure 109 - Comparison of the filtered drag correction for the significant cases by a) the filtered quantity and b) the percentage deviation from the filtered quantity in the base case

The trends for the Huilin-Gidaspow and Syamlal-O'Brien drag models show that the practice of scaling the filtered drag force with the coarse grid drag force appears to work well, since the deviations of the filtered drag corrections fluctuate around zero with a maximum deviation of about 10% in both cases. The shape of the interphase exchange coefficient deviations (right-hand side of Figure 108) is clearly visible (inversed) on the right-hand side of Figure 109.

It can also be noted that for the cases where frictional pressure is not included, the drag correction factor does not return to a value of 1 near maximum packing. This is due to the nature of the dense regions in this data set where only results from periodic simulations with domain-averaged volume fractions up to 0.3 were included (as previously discussed in section B.1). Completely homogenous, dense regions that are larger than the filter size therefore do not exist in these simulations (maximum packing is approached only in small areas inside the clusters). When frictional pressure is included, however, larger clusters form, leading to dense, homogenous regions larger than the filter size and therefore also drag correction factors close to one near maximum packing. The drag correction factor is therefore also expected to return to 1 close to maximum packing for the cases without frictional pressure with the inclusion of more data from denser cases.

B.5.3 Filtered solids stresses

The normal and shear filtered solids stresses behave very similarly, therefore only the shear filtered stress is presented here in Figure 110. Both the normal and shear filtered stresses tend to increase linearly with the filtered solids volume fraction. However, at large values of the filtered solids volume fraction the slope decreases as the velocity fluctuations tend to decrease within the more homogenous regions in the centre of the clusters. This effect is clearly enhanced by including the frictional pressure in the TFM formulation.

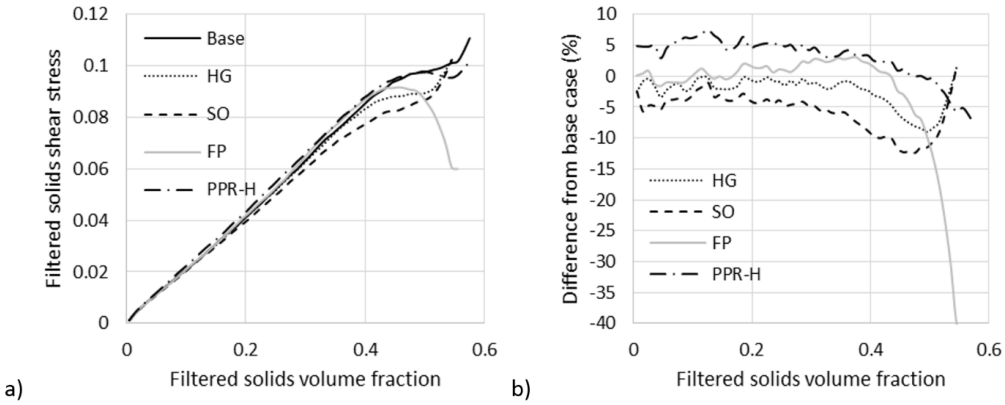

Figure 110 - Comparison of the dimensionless filtered solids shear stress for the significant cases by a) the filtered quantity and b) the percentage deviation from the filtered quantity in the base case

The alternative drag models also tend to decrease the filtered stress in the dense regions. When comparing this result with the filtered slip velocity result in Figure 106, it can be deduced that the influence of the alternative drag laws is to reduce the cluster resolution, especially at higher filtered solids volume fractions. Greater cluster resolution would naturally increase the effects of clustering such as decreased interphase exchange and increased dispersion of mass, momentum and heat. These results clearly show that the use of the Huilin-Gidaspow or Syamlal-O'Brien drag models decrease the filtered slip velocity and the filtered stresses, thus indicating reduced cluster resolution.

Finally, for the filtered stresses the effect of the particle-particle restitution coefficient becomes more significant compared to the other filtered quantities. Discussion of this effect is deferred to section B.5.5 where both the low and high particle-particle restitution coefficient cases were significant.

B.5.4 Filtered heat transfer correction

Similar to the filtered drag correction, the inclusion of frictional pressure causes the filtered heat transfer correction to proceed to unity at large filtered solids volume fractions (Figure 111). However, for the case of the filtered heat transfer correction, there is a region around filtered solids volume fractions of 0.3 where the correction is actually predicted to be larger. This may be due to the much more viscous solids phase in the dense particle regions which restricts convective heat transfer.

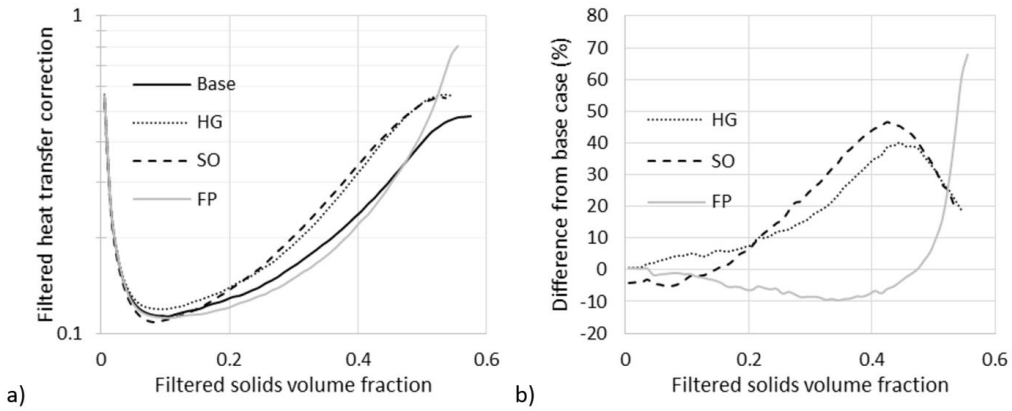

Figure 111 - Comparison of the filtered heat transfer correction for the significant cases by a) the filtered quantity and b) the percentage deviation from the filtered quantity in the base case

For the drag laws, both the Huilin-Gidaspow and Syamlal-O'Brien predict substantially smaller sub-grid drag corrections than the Wen-Yu drag model. This is again due to the degree of cluster resolution being lower with these drag models as discussed in the previous section.

B.5.5 Filtered scalar co-variances

Figure 112 and Figure 113 show the filtered scalar co-variances in the gas and solid phases, respectively. It can be noted that filtered scalar co-variance in the solids phase behave similarly to the solids shear stress, except for an increase of the slope at very large filtered solids volume fractions. The shape of the filtered correlation is very different in the gas phase. However, despite this difference, the effect of changes in the resolved TFM formulation is very similar. The effects of the frictional pressure and the two alternative drag laws can therefore be explained through similar arguments to those put forward in section B.5.3.

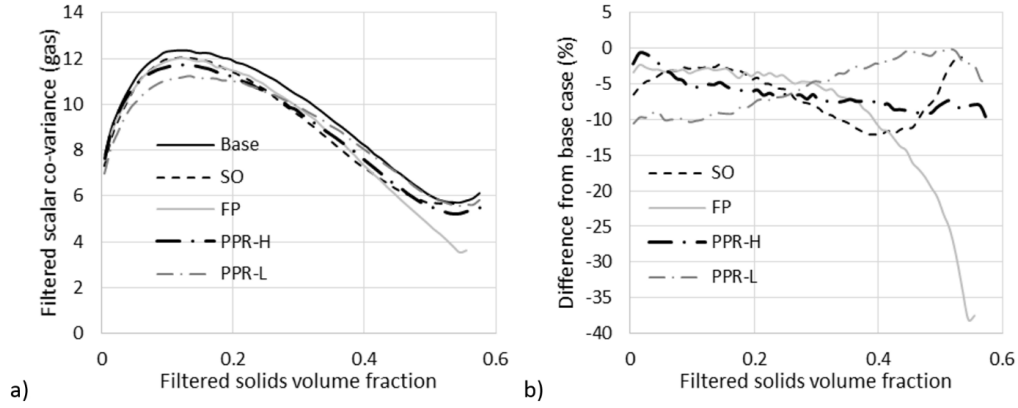

Figure 112 - Comparison of the filtered scalar co-variance in the gas phase for the significant cases by a) the filtered quantity and b) the percentage deviation from the filtered quantity in the base case

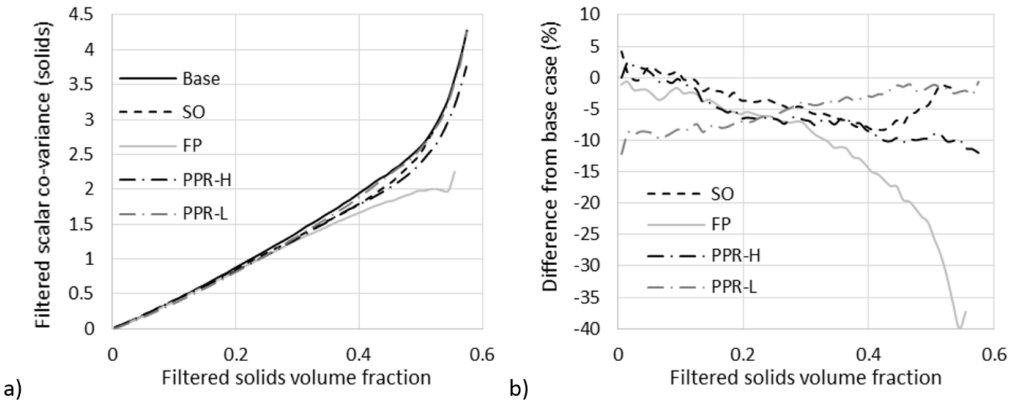

Figure 113 - Comparison of the filtered scalar co-variance in the particle phase for the significant cases by a) the filtered quantity and b) the percentage deviation from the filtered quantity in the base case

The effect of changing the particle-particle restitution coefficient, however, requires additional discussion. Unlike the filtered solids stresses, more elastic collisions now lead to smaller filtered scalar co-variances. A similar decrease is observed when the particle-particle restitution coefficient is decreased to 0.8 from 0.9. However, the particle-particle restitution coefficient of 0.95 leads to a maximum decrease in the filtered scalar co-variance at high filtered solids volume fractions, while a particle-particle restitution coefficient of 0.8 leads to a maximum decrease in the dilute regions.

To gain a better understanding of this behaviour, the solids volume fraction variance ($\overline{\alpha_s{}'\alpha_s{}'}$) was calculated for the three cases with different particle-particle restitution coefficients. For the case with the less elastic collisions, both the non-homogeneity of the solids and the scalar dispersion tends to increase relative to the base case from low solids volume fractions to high solids volume fraction, since the less elastic collisions lead to more clustering in the dense regions. Surprisingly, however, the scalar dispersion is decreased relative to the base case, whereas one would expect the increased variance in the solids volume fraction to lead to more scalar dispersion.

In the case of the more elastic collisions, the solids volume fraction variance is decreased relative to the base case in the dilute regions due to decreased clustering. The scalar variance decreases relative to the base case, but in contrast to the solids volume fraction variance, this decrease takes place in the dense regions. It can therefore be concluded that the scalar dispersion is not influenced only by the degree of volume fraction segregation and that other factors, such as the cluster shape, size and number, play an important role. Further investigations using additional markers will be required to fully understand these trends.

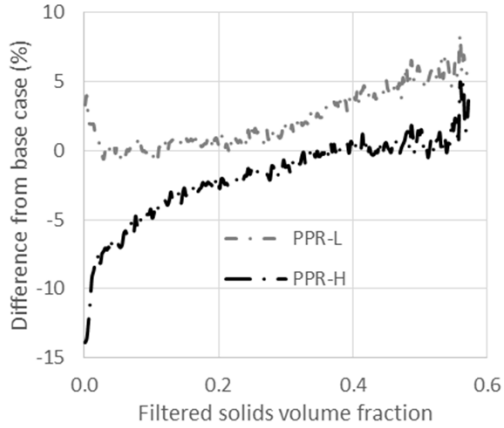

Figure 114 - Percentage deviation of the solids volume fraction variance from that in the base case

B.5.6 Filtered reaction correction

The effect of changes in the TFM formulation is nearly identical for the filtered heat transfer and filtered reaction rate correction (Figure 115). This is understandable, since interphase heat transfer and first-order, solids catalysed reaction are analogous processes. However, the changes caused by the different TFM formulations are much smaller for the filtered reaction rate correction. This is because the reaction rate chosen is relatively slow compared to the heat transfer rate.

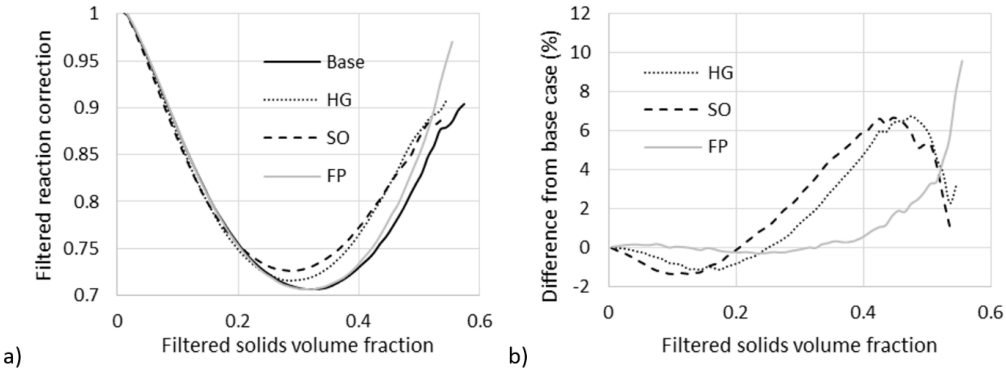

Figure 115 - Comparison of the filtered reaction rate correction in the gas phase for the significant cases by a) the filtered quantity and b) the percentage deviation from the filtered quantity in the base case

C. Evaluation of wall boundary conditions for riser flow

Particle-wall collisions play a critical role in the behaviour of risers due to the large ratio of wall area to reactor volume and the high velocity of particles typical of risers. There is general agreement in the literature that the choice of wall boundary condition for the solid phase have a significant influence on the overall hydrodynamics of the riser [70, 71]. However, it remains unclear what the correct approach is for including the wall effects, as boundary conditions in the literature include anything from free-slip to no-slip.

The most popular model for the particle-wall boundary condition, by a considerable margin, is that of Johnson and Jackson [35]. At the time of writing, the original paper describing the model had over 700 citations in the literature. This is despite the well-known limitations of the approach [72, 73]. In the Johnson and Jackson model the effect of particle-wall friction and wall roughness on the shear force is incorporated into a single heuristic constant, called the specularity coefficient. The specularity coefficient is not a physically measurable property and its desired value may change with flow conditions. This is a problem in systems such as circulating fluidised beds, which may contain dense and dilute regions, requiring very different specularity coefficients for accurate results in these different regions. The dependence on flow conditions leads to a disparity in the values of the specularity coefficient used in literature studies of risers, with one group assuming partial slip (specularity coefficients of 0.1 to 0.5) [74, 75] and another group assuming near free-slip (values smaller or equal to 0.001) [71, 76].

Furthermore, the Johnson and Jackson model assumes a linear relationship between the shear stress and the slip velocity. However, it is well known that at high slip velocities all the particles will slide at contact and that the shear stress will be limited by Coulomb friction [34, 77-79]. The Johnson and Jackson model therefore tends to overpredict the shear stress and granular temperature generation for rapid flows, which explains the use of very low specularity coefficient values in the literature.

Despite the dominance of the Johnson and Jackson model, there are alternative methods available in literature. Jenkins [77] proposed expressions for the shear stress and granular temperature flux in terms of measurable quantities, the friction coefficient (μ_w) and the tangential (β_0) and normal (e_w) particle-wall restitution coefficients. However, their theory was restricted to the limits of either non-sliding or all-sliding collisions; therefore *a priori* knowledge of the flow domain is required for using their model. Jenkins and Louge [80] improved these correlations for the flux of the granular temperature based on computer simulations of Louge [78] for the limits of non-sliding and all-sliding collisions.

Sliding and non-sliding collisions were first linked into one expression by Li and Benyahia [79], who provided an expression for the specularity coefficient based on the friction coefficient, particles-wall restitution coefficients, slip velocity and granular temperature. This approach therefore solves the problem of the specularity coefficient not being a measurable quantity, as well as its dependency on the flow conditions. However, it was recently noted that this approach does not differentiate between sliding and non-sliding collisions in the dissipation term of the boundary condition for the granular temperature, leading to an overprediction of the granular flux in rapid granular flows [72].

The model by Schneiderbauer [34] also included sliding and non-sliding collisions in one expression, dependent on the friction and particle-wall restitution coefficients. However, an improved treatment of the granular flux leads to better comparisons with the simulation data of Louge [78], compared to

the work of Li and Benyahia [79]. Additionally, the model can also account for a boundary moving in a normal direction relative to the flow, making it the only approach suitable to systems with moving parts.

Most recently, Zhao [73] achieved an even better comparison with the data of Louge [78] by also considering the rotational granular temperature of the particles. However, the approach of using a rotational granular temperature is not common practice due to the added computational expense of solving an extra conservation equation and the complexity added by the additional closures.

For this reason it can be argued that currently the model by Schneiderbauer [34] is the best alternative for replacing the Johnson and Jackson model [35] as the most commonly used wall-friction model for granular flows. It has the primary advantages of requiring only measurable quantities as input and achieving a very good match with simulation data by Louge [78] by accounting for the effect of a transition from non-sliding to sliding collisions on both the shear stress and the granular flux. Additionally, it retains most of the simplicity that makes the Johnson and Jackson model popular.

The potential benefit of the Schneiderbauer wall-friction model has been demonstrated in a spouted bed [57] for fluidised beds. However, its true advantage is expected to be best illustrated in risers, where rapid granular flow occurs at the walls. For this reason, the study presented here will aim to evaluate the Schneiderbauer model as an alternative to the Johnson and Jackson model by comparing numerical results with experimental data in risers over a range of superficial gas velocities and solids fluxes.

C.1 Simulation setup

C.1.1 Model equations

For this section, the same transport equations are solved for the hydrodynamics as those discussed in Chapter 2.1. However, of particular significance for this section of work are the equations used for modelling the particle-wall interaction. The contribution of the wall comes in a shear stress term that is included in the particle phase momentum equation (Equation 4) and a granular flux term that is included in the granular temperature equation (Equation 6).

The first formulation used is that by Johnson and Jackson [35], for which the expressions for the shear stress and the granular flux are:

$$\vec{\tau}_s = -\frac{\pi}{6}\sqrt{3}\phi\frac{\alpha_s}{\alpha_{s,\max}}\rho_s g_0\sqrt{\Theta_s}\vec{v}_{s,|} \qquad \text{Equation 103}$$

$$q_s = \vec{\tau}_s \cdot \vec{v}_{s,|} - \frac{\pi}{4}\sqrt{3}\frac{\alpha_s}{\alpha_{s,\max}}(1-{e_w}^2)\rho_s g_0 {\Theta_s}^{\frac{3}{2}} \qquad \text{Equation 104}$$

where the input parameters are the specularity coefficient (ϕ) and the particle-wall restitution coefficient (e_w).

For the Schneiderbauer model [34], the following set of equations are used:

$$\vec{\tau}_s = -n_w \mu_w \alpha_s \rho_s g_0 \Theta_s erf(\bar{v_s})\frac{\vec{v}_{s,|}}{\|\vec{v}_{s,|}\|} \qquad \text{Equation 105}$$

$$q_s = \vec{\tau}_s \cdot \vec{v}_{s,|} - \frac{\alpha_s \rho_s g_0 n_w \sqrt{\Theta_s}}{\sqrt{2}\mu_0^2\sqrt{\pi}} \exp(-\bar{v_s}^2) \times (\mu_w(2\mu_w \|\vec{v}_{s,|}\|^2(2n_w - \mu_0) + \Theta_s(14\mu_w n_w - 4\mu_0(1+\mu_w) - 6\mu_w\mu_0^2 n_w)) + \mu_0^2\sqrt{\Theta_s}\exp(\bar{v_s}^2)(\sqrt{\Theta_s}(4(n_w-1) + 6\mu_w^2 n_w) - \sqrt{2\pi}\mu_w\|\vec{v}_{s,|}\| erf(\bar{v_s})))$$ **Equation 106**

$$n_w = \frac{1}{2}(1 + e_w)$$ **Equation 107**

$$\bar{v_s} = \frac{\|\vec{v}_{s,|}\|}{\sqrt{2\Theta_s}\mu_0}$$ **Equation 108**

$$\mu_0 = \frac{7}{2}\frac{1+e_w}{1+\beta_0}\mu_w$$ **Equation 109**

where the input values are the friction coefficient (μ_w), the tangential restitution coefficient (β_0) and the normal restitution coefficient (e_w).

It can also be noted that for this section of work the radial distribution function is calculated using the equation by Arastoopour [68] to be consistent with the work by Schneiderbauer [57], where they optimised the three parameters in their wall friction model for a spouted bed.

C.1.2 Solver settings

In this study, the same solver settings were used as those described in Chapter 3.1.4 for the resolved simulations performed in fully-periodic domains.

C.1.3 Simulation geometry

The simulations are performed on a 800 mm long section of a riser with a diameter of 76mm according to the experiments by Yan and Zhu [81, 82]. A periodic section of the riser is simulated, assuming fully developed flow in the experimental setup.

Due to the large number of simulations that will be required to study the effect of changing the parameters in the Schneiderbauer model at different flow conditions, it was deemed impractical to perform 3D simulations. However, in 2D simulations the ratio of the wall area to reactor volume is significantly reduced compared to the 3D case. It is important to correctly maintain this ratio since the primary purpose of this study is to investigate the effect of the walls. For this reason a recently published 2.5D approach is utilised [83]. In this method, a single layer of 3D cells is used, with the cell volume increasing from the riser centre towards the walls to accurately reproduce the geometrical proportions in the 3D riser, as is done in an axisymmetric simulation. However, in the 2.5D model the two wedges that subsequently form are linked in the centre by a rectangle to allow particles to be transported across the centre. This solves the primary problem of using axisymmetric simulations for predicting riser flow [83].

This setup allows a much better representation of the riser geometry, while still maintaining the same number of cells as in 2D. An additional benefit of the 2.5D approach is that it does not require the boundary conditions or initial conditions to be adapted, as was done in a previous study [11], to allow for comparison between 2D simulations and experimental data. This is because the 2.5D model accurately reproduces the radial proportions of the riser geometry, except for a slight overestimation of the volume caused by the rectangle connecting the wedges.

Despite the better comparison with experimental data afforded by the 2.5D approach, it was noted by [83] that 2.5D simulations tend to overpredict the solids velocity in the centre of the reactor compared to 3D simulations. This behaviour was also observed in the present study when comparing simulation results to experimental data (Figure 123). However, keeping this behaviour in mind, 2.5D simulations results are still sufficient for the purpose of this study when limiting the comparison with experimental results to the solids velocity profile closer to the wall. In this region, the results are most sensitive to the wall boundary condition and comparison between 2.5D and 3D simulation results are reasonably good. Comparison of 2.5D simulation results and experimental data near the wall is therefore sufficient for the evaluation of different wall boundary condition settings.

A structured grid of $0.67 \times 1.34\,mm$ cells is used. This grid size was shown earlier to give mesh independent results in combination with second order time discretisation for the riser considered in an earlier study [11].

C.1.4 Boundary conditions

The top and bottom boundary conditions are specified to be translationally periodic in the length of the riser. To be able to maintain the conditions used in the experiments by Yan and Zhu [81, 82], the pressure drop is adjusted to maintain the target gas superficial velocity, as discussed in [11]. Each simulation is initialised with the domain-averaged particle volume fraction for that specific case. The superficial gas velocity and the particle volume fraction used in the simulations correspond to the five cases investigated by Yan and Zhu [81, 82]. These operating conditions are summarised in Table 2.

Table 7 - The operating conditions considered in this study

Case	Superficial velocity (m/s)	Solids flux (kg/m^2s)	Average volume fraction
1	3.5	100	0.0565
2	5.5	50	0.0106
3	5.5	100	0.0251
4	5.5	200	0.0497
5	8.0	100	0.0128

At the walls, the boundary conditions are set as no-slip for the gas phase and partial-slip, using either the Johnson and Jackson or Schneiderbauer formulation, for the particle phase.

C.1.5 Material properties

Air at room temperature is specified as the fluidising gas. The solid phase consists of FCC catalyst particles with a density of $1500\,kg/m^3$ and a mean diameter of $67\,\mu m$, as specified in the experimental work [81, 82].

C.1.6 Data collection

All simulations are performed initially for $7.5\,s$ to allow for a statistical steady state to be reached, which is determined from the average mass flux in the system. A further $20\,s$ of simulated time is

performed subsequently to allow important flow variables to be time-averaged. For Case 5 the results are time-average over $50\ s$, since it requires more time to yield symmetrical results. Time-averaged values are calculated for the solids flux and for particle velocity and volume fraction profiles. These values are compared with experimental data. The particle velocities and volume fractions are further averaged over the length of the period section. The solids velocities are calculated as a mass weighted average, since the measuring technique employed in the experiments will tend to more heavily weigh the velocities in dense regions [84]. Although no experimental data is available for it, the time-averaged granular temperature profile is also determined, since it is an important quantity in explaining the simulation behaviour during this study.

C.2 Comparison of the Johnson and Jackson and Schneiderbauer models

As a start to the investigation, the performance of the Schneiderbauer model and the Johnson and Jackson model with two different specularity coefficients is investigated over a large range of flow conditions, as summarised in Table 2. The simulations using the Schneiderbauer model is performed using the following values of the friction parameters: $\mu_w = 0.5$, $e_w = 0.9$ and $\beta_0 = 0.4$. These are the values that Schneiderbauer [57] found to be the optimum in their study considering a spouted bed. Since the spouted bed was operated using glass spheres with a diameter of $3\ mm$, compared to the $67\ \mu m$ FCC catalyst particles in this study, it is expected that the performance of the model could still be improved significantly from this starting point by optimising the values for this particular case.

Two cases will be considered for the Johnson and Jackson model, corresponding to the two different approaches often used in literature. For the low friction approach, a specularity coefficient of 0.001 is specified. For the high friction approach, the specularity coefficient is calculated in such a way that the shear stress will be similar to that of the Schneiderbauer model settings used in this section for the limit of all non-sliding collisions (when the value of the normalised slip velocity, $\overline{v_s}$, in Equation 108 is low). This criterion can be calculated by setting the shear stress in Equation 103 and Equation 105 equal and using the knowledge that at low values of $\overline{v_s}$ the gradient of the error function is constant and therefore $erf(\overline{v_s}) = \frac{2}{\sqrt{\pi}}\overline{v_s}$. This holds to within 5% for $\overline{v_s} <\approx 0.275$ and yields the condition that

$$\phi = \frac{6\sqrt{2}\varepsilon_{s,\max}}{7\pi\sqrt{3\pi}}(1+\beta_0) \qquad \text{Equation 110}$$

giving $\phi = 0.111$ for this study, using a maximum packing of 0.63. A particle-wall restitution coefficient of 0.9 was used for both of the Johnson and Jackson approaches.

The results for the conditions considered are summarised in Figure 116. Plots are shown for the time-averaged values of the solids y-velocity and the solids volume fraction for each case, where experimental data are available. An additional plot is also shown for the granular temperature, since the granular temperature helps to explain some of the behaviour observed. It is assumed that the experimental data, given as a function of the radius, is completely symmetric, since no mention of any asymmetry is made [81, 82].

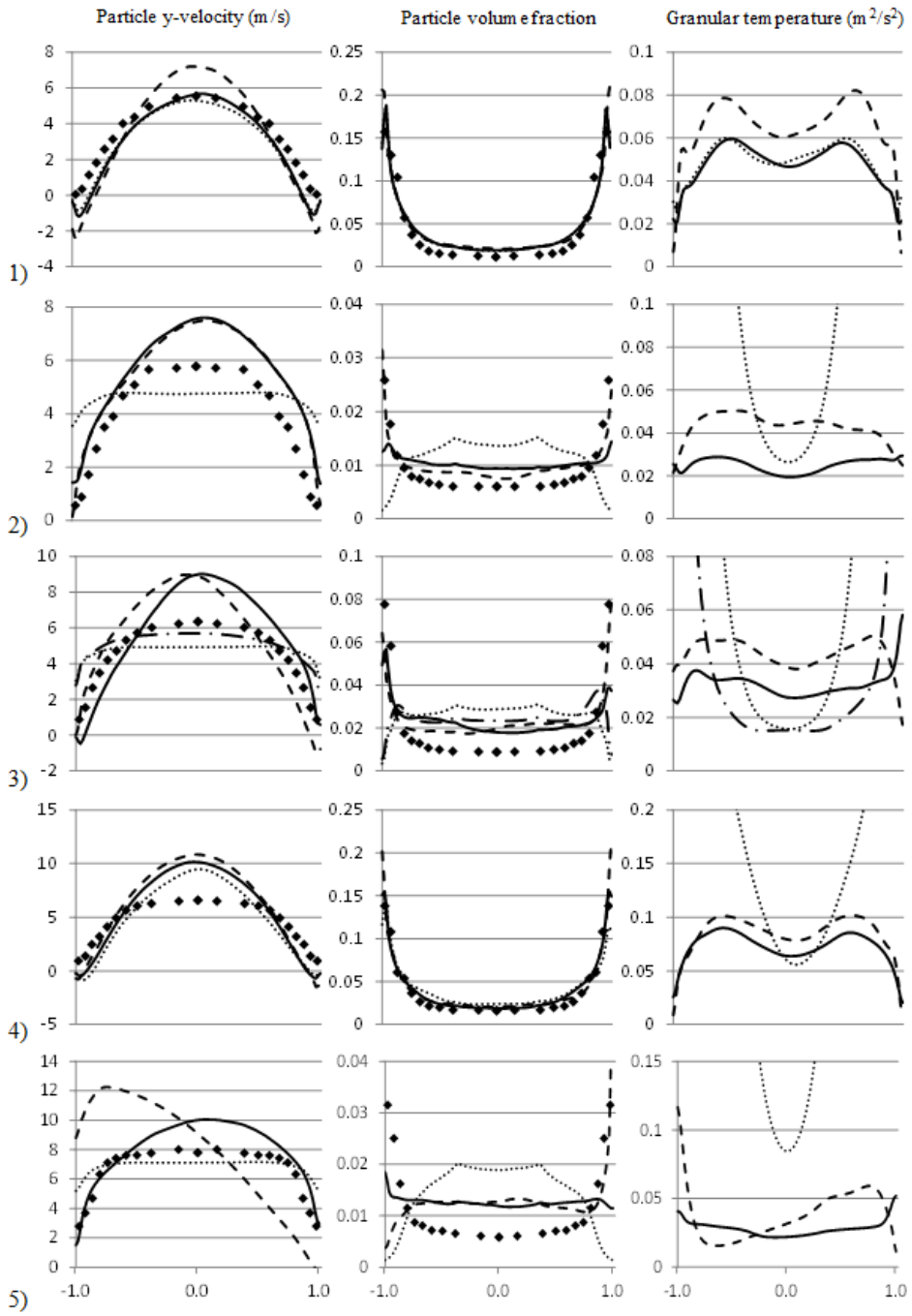

Figure 116 - Results comparing the solids y-velocity, particle phase volume fraction and granular temperature for simulations and experiments. Experiments (◆ ◆ ◆), Schneiderbauer model (——), Johnson and Jackson with $\phi = 0.111$ (·····), Johnson and Jackson with $\phi = 0.001$ (– – –), Johnson and Jackson with $\phi = 0.111$ and $e_w = 0.2$ (— · —).

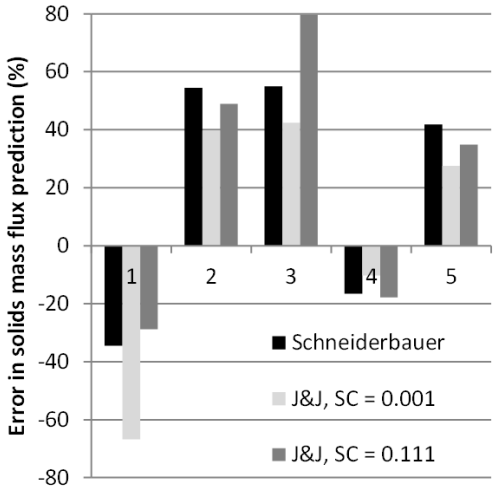

Figure 117 – Error in the solids mass flux prediction for each of the wall friction modelling methods.

These results will now be discussed in a sequential manner.

C.2.1 Case 1

Considering the solids velocity and volume fraction for Case 1 in Figure 116 it can immediately be observed that the Schneiderbauer model and the Johnson and Jackson model at the non-sliding limit ($\phi = 0.111$) give very similar results. The reason is that, in the dense case with low gas velocity, large, slow-moving clusters form at the wall, shielding the wall from the fast-moving particles. Most of the solids at the wall subsequently have a low slip velocity, leading to non-sliding collisions. The agreement of both methods with the experimental data is good, except for a small overprediction in the downwards solids flux at the walls, leading to an underprediction in the solids flux, shown in Figure 117. For the simulation with the low specularity coefficient the low friction at the walls often leads to thin streaks of solids rapidly falling at the wall. This causes a slightly larger overestimation of the downward solids flux at the wall and a substantial increase in the underprediction of the solids flux (67%, compared to 34% for the Schneiderbauer model). A video illustrating the flow behaviour described for Case 1 can be found with the publication from this study [85].

C.2.2 Cases 2 and 3

The conclusions that can be drawn for Cases 2 and 3, where faster, more dilute flows occur, are similar. Here, the Johnson and Jackson model with a high specularity coefficient fails completely, predicting much too high upward solids velocities and very low solids volume fractions at the walls. This indicates that there are essentially no solids clusters forming at the walls. By examining the granular temperature profiles, the cause can be seen to be very large granular temperatures at the walls. Since the flow is fast, a high shear stress at the wall causes large velocity gradients in the wall region. These large gradients give rise to large generation of granular temperature (first term on the RHS of Equation 6) which creates higher granular viscosities. The resulting highly viscous flow causes even more granular temperature generation in Equation 6 and also forces more slip at the wall despite the high degree of wall shear stress, thus resulting in a significant positive granular temperature flux at the wall according to Equation 104. To separate the effects of Equation 6 and Equation 104, an additional

simulation was performed using a specularity coefficient of 0.111 and a very low restitution coefficient of 0.2 in Case 3 to test whether the problem with large granular temperatures at the wall can be solved by substantially increasing the dissipation term in Equation 104. However, results in Figure 116 show that despite a small improvement, the effect is not sufficient to deliver good results. Additionally, such nearly completely inelastic collisions are not physically realistic for the FCC catalyst particles considered in this study.

This problem with the Johnson and Jackson model is overcome by using a very low specularity coefficient value, such as 0.001. In such a case, the self-strengthening mechanism for granular temperature generation described above is avoided, allowing clusters to form. It can be observed from Figure 116 that this approach yields a very good comparison with experimental data for the particle velocity and volume fraction close to the walls. However, the deviations are observed at the centre of the riser. In the experiments, the peak velocity is significantly lower and the profile flatter. The volume fraction in the centre is also overpredicted in the simulations. Similar results occur for the Schneiderbauer model and at most of the operating conditions. Therefore, it is likely that these errors are due to the 2D domain discretization employed, limitations of the KTGF closures used or the periodic assumption, and not due to the wall friction models. For this reason, this discussion will generally focus more on the comparison with experimental data close to the walls.

The solids velocities estimated by the Schneiderbauer model are similar to that of the low friction Johnson and Jackson simulations. However, lower volume fractions are obtained at the walls, indicating that the current setup underestimates the cluster formation at the walls. The granular temperature plots for Case 2 and 3 shows a slight increase in the granular temperature close to the walls. This suggests that the generation of granular temperature at walls might be too high with the current friction parameters, deterring cluster formation.

C.2.3 Case 4

In Case 4 all three approaches perform reasonably well. Therefore, this denser case somehow allows the formation of clusters in the case of the Johnson and Jackson model with a specularity coefficient of 0.111, despite the high granular temperature still observed for this approach in Figure 116. By observing videos of the flow for this case it was determined that for this approach cluster formation is much slower than for the other two. During start up solids clusters form in the centre of the riser, but are not allowed to form at the walls. Eventually, these clusters become sufficiently dense to overcome the excessive granular pressure gradient and reach the walls where they are maintained in a manner similar to Case 1. The time-averaged granular temperature remains excessively high due to contributions from dilute wall regions (dense and dilute regions are weighed equally in the averaging procedure).

For all three approaches in Case 4 the upward particle velocity at the centre and the downward solids flow at walls are overestimated, but otherwise the general comparison is good. All three methods yield exceptional comparisons with the experimental data for the particle volume fraction. Figure 117 shows that all three methods slightly underpredicts the average solids flux through the domain, with the low friction Johnson and Jackson method performing slightly better than the other two methods.

C.2.4 Case 5

For Case 5 it is clear that the large friction Johnson and Jackson approach fails in a similar way as was described for Cases 2 and 3. For the other two methods highly asymmetric flow can be observed, which is characteristic of all instances of Case 5 considered in this study. Clusters will initiate at one wall first and start falling, lowering the upward gas velocity on that side. The gas flow then tends to move towards the other wall to bypass the solids and accelerates to maintain the same gas flux through the system. Due to the high gas velocity used in this case, this leads to high granular temperatures at the wall opposite to the one containing clusters, preventing clusters from forming on the side as well. A video illustrating the flow behaviour described for Case 5 can be found with the publication from this study [85].

However, viewing Figure 116 for Case 5, a clear difference between the Schneiderbauer model and the Johnson and Jackson model with a low specularity coefficient is evident. For the Johnson and Jackson model the particle velocity and volume fractions are completely skewed, indicating that the asymmetrical flow described above persists for the entire simulation. From viewing videos of the flow behaviour, it can be seen that the reason for this is that, when using the Johnson and Jackson model with a specularity coefficient of 0.001, every time a cluster starts growing a part of it is sheared off before it can become large enough to be swept from the wall completely. This is because of the very large shear caused by the rapidly falling clusters in this near free-slip condition.

For the Schneiderbauer model there is little cluster formation occurring, most likely due to large granular temperature at the walls. However, when it forms, clusters on one wall can break up completely, allowing a chance for clusters to be formed at the opposite side. If enough time is allowed for averaging the results, periods with clusters at each wall will cancel each other out, leading to more symmetrical results in the profile. Despite the more symmetric averaged profile for the Schneiderbauer model, the comparison with the experimental solids volume fractions is still relatively poor. The simulation predicts much higher solids volume fractions at the centre, while failing to predict enough cluster formation next to the walls.

C.2.5 Summary of initial results

From the results discussed in this section it can be concluded that there are two different regimes for solids flows next to the walls, both of which should be treated correctly. The first is rapid, dilute flows occurring before the onset of cluster formation. In this regime, it is important that wall shear stresses should be sufficiently small to prevent excessive strain rates in the wall regions which leads to unphysical self-strengthening granular temperature generation. This confirms the conclusion by Benyahia [76] that a specularity coefficient close to free-slip should be used to limit the granular temperature generation at the walls.

The second regime occurs when solids clusters have already formed at the wall. Here dense clusters will fall under the influence of gravity and it becomes important that sufficient wall shear stresses are included to limit the slip velocity of these dense clusters next to the wall. If the flow is sufficiently dense, the Johnson and Jackson model with a high specularity coefficient correctly models this regime and the dense clusters shield the wall from high velocity flows, thereby preventing excessive granular temperatures in dilute regions as described above.

The promise of the Schneiderbauer model therefore lies therein that it can treat both regimes accurately. By accounting for sliding collisions at large slip velocities the granular temperature generation should be limited enough to allow cluster formation at the walls, while realistic shear stresses at the walls are retained for clusters falling relatively slowly at the walls. It therefore has the best potential to give reasonable results over the entire wide range of flow conditions considered in this study with a single set of model parameters. However, since the cluster formation at the walls with the Schneiderbauer model is insufficient in Cases 2, 3 and 5, it appears as if the granular temperature generation is still too large with the settings used in this section. The rest of the study will therefore aim to optimise the friction parameters used in the Schneiderbauer model and to evaluate the performance of the optimised model.

C.3 Attempted optimisation of the Schneiderbauer model

Although the Schneiderbauer model parameters have the advantage of being measurable properties, they will still mostly be obtained by fitting simulation results to experimental results. This is because experimental measurements for particle-wall collision properties, as in these studies from literature [86-88], are limited and most often reliable data will not be available for the specific material and particle size under investigation. This is especially the case for smaller particles sizes, as in this study, due to the practical difficulties of measuring collision properties for small particles. For this reason, a large number of simulations will be performed to determine the combination of friction parameters that will yield the best comparison with experimental results over all the flow conditions considered.

C.3.1 Theoretical considerations

To do this in a logical and structured manner, it is best to first obtain an understanding of how the Schneiderbauer model behaves with changing friction parameters. This is achieved by plotting the shear stress and the normalised granular flux ($q_s/\sqrt{3\Theta_s N^2}$) against a dimensionless slip velocity, $r = \|\vec{v}_{s,|}\|/\sqrt{3\Theta_s}$. The values of the three friction parameters are varied around those considered earlier in this study to gain a better understanding of their influence. Additionally, the following equations are derived for the shear stress at the limits of all non-sliding ($erf(\bar{v_s}) = \frac{2}{\sqrt{\pi}}\bar{v_s}$) and all sliding collisions ($erf(\bar{v_s}) = 1$):

$$\|\vec{\tau}_s\| = -\frac{\sqrt{2}}{7\sqrt{\pi}}(1+\beta_0)\alpha_s\rho_s g_0\sqrt{\Theta_s}\|\vec{v}_{s,|}\| \qquad \text{Equation 111}$$

$$\|\vec{\tau}_s\| = -\frac{1}{2}(1+e_w)\mu_w\alpha_s\rho_s g_0\Theta_s \qquad \text{Equation 112}$$

First considering the shear stress, it can immediately be seen from Equation 111 that the shear stress in the non-sliding regime is only dependent on the tangential restitution coefficient, while in the sliding regime, Equation 112, the shear stress is dependent on the friction coefficient and the normal restitution coefficient. This can be confirmed from the plots in Figure 118. For sliding collisions the shear stress is independent of the slip velocity and its value decreases with a reduction in either the friction coefficient or the normal restitution coefficient. For non-sliding collisions the shear stress is directly proportional to the tangential slip velocity. It is also clear that the friction coefficient has a larger influence on the shear stress than the restitution coefficients, due to the restitution coefficients

occurring in the form $(1 + e_w)$. The friction parameters also influence the onset of sliding collisions. The friction coefficient again has the largest influence with sliding collisions starting earlier at low friction coefficient values.

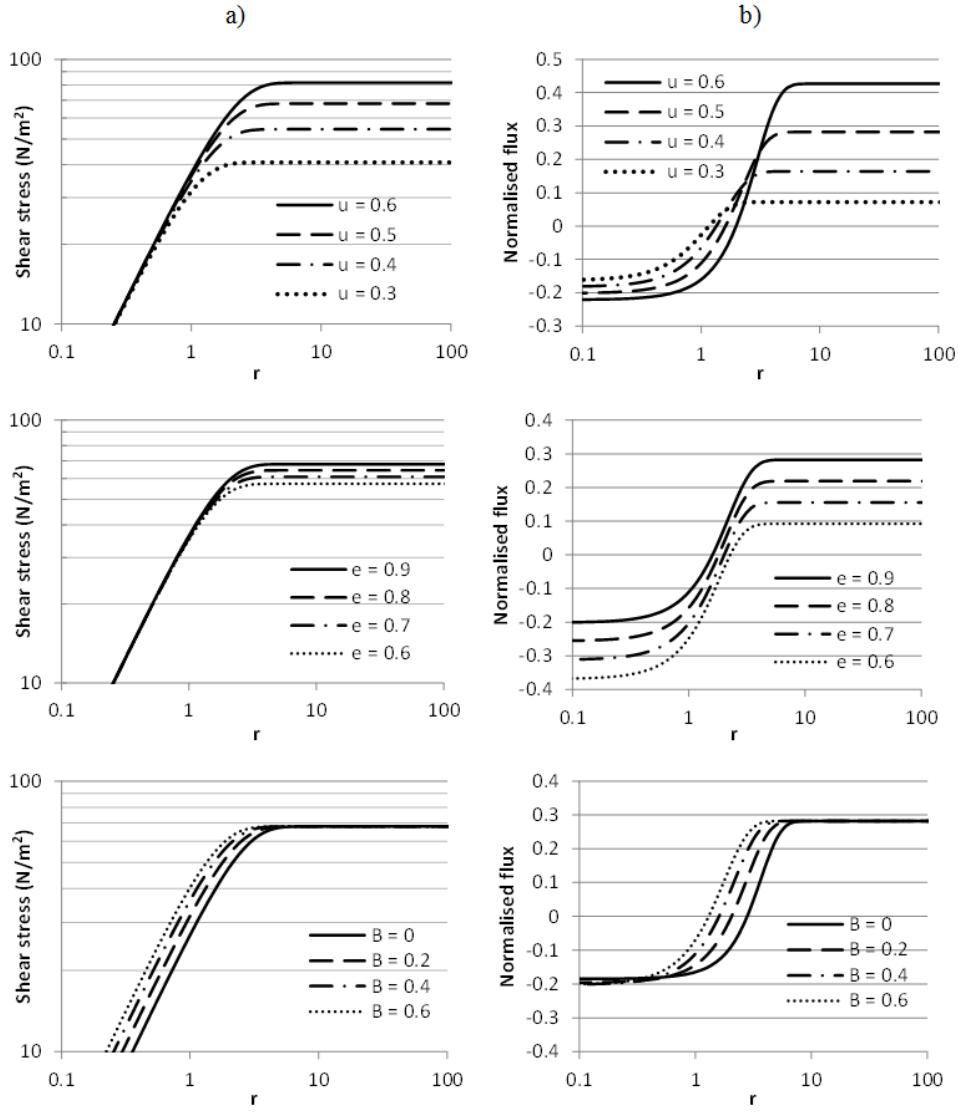

Figure 118 – Plot of a) the shear stress and b) the normalised flux, $q_s/\sqrt{3\Theta_s N^2}$, plotted against the non-dimensional slip velocity, $r = \|\vec{v}_{s,i}\|/\sqrt{3\Theta_s}$. The effects of changes in the friction coefficient, normal restitution coefficient and tangential restitution coefficient are shown separately.

Due to the complexity of the granular flux equation, the behaviour of the granular flux cannot that easily be deduced from simplified equations. However, by plotting the behaviour of the granular temperature flux with changing values of the friction parameters, several important observations can be made. Firstly, the friction coefficient is once again the most influential. Increasing its value both

increases the positive granular temperature flux in the sliding regime and the negative flux in the non-sliding regime. The normal restitution coefficient has a smaller, but more regular, effect. By specifying more elastic collisions the granular temperature flux to the solids increases. Lastly, the tangential restitution coefficient has the smallest influence on the granular temperature flux, with an increase in its value primarily allowing sliding collisions to start at lower velocities.

Since the number of simulations required to test the influence of all three parameters on all 5 cases would be impractically large, the sensitivity analysis will be carried out only for the two most influential parameters and two most interesting cases. Regarding the parameters, the tangential restitution coefficient is not considered in this optimisation study. Results in section C.2 showed the primary shortcoming of the current setting in the Schneiderbauer model is its ability to predict cluster formation in fast, dilute flows. Excluding the tangential restitution coefficient is therefore reasonable, since the tangential restitution coefficient has no influence on the granular flux in the sliding regime. The current value of 0.4 delivered good results in the denser cases, where mostly non-sliding collisions occur at the wall and the tangential restitution coefficient will therefore be most influential, and therefore appears to be an appropriate choice. Consequently, it was decided to run simulations for all combinations of $\beta_0 = 0.4$, $\mu_w = 0.5, 0.4, 0.3$ and $e_w = 0.9, 0.7, 0.5$. Lower values of the parameters were explored, since in both cases this will lead to less granular temperature generation at high slip velocities.

Regarding the cases, it was decided to focus on Cases 1 and 5 because they represent the outer bounds of the range of conditions considered in this study.

C.3.2 Simulation results

To allow for easier interpretation of results, the profiles will from now on be displayed averaged over the plane of symmetry. From Figure 116 is can be seen that the results for all cases, except Case 5, is highly symmetric and this approach is therefore justified. Figure 119 shows that, given enough averaging time, the profile for Case 5 will also become symmetric when using the Schneiderbauer model. To maintain practical computational times, simulations of Case 5 are therefore run for 50s, after which the profiles are averaged over the symmetry plane.

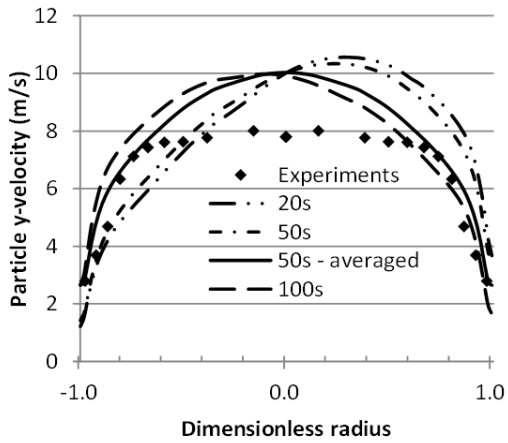

Figure 119 – Plot of the time-averaged particle y-velocity for Case 5 using the Schneiderbauer model with a friction coefficient of 0.5 and a normal restitution coefficient of 0.7.

The effect of changing the friction parameters in Case 5 can best be seen from the time-averaged solids volume fraction profiles shown in Figure 120, since the solids velocity profile proved to be insensitive to changes in the wall boundary conditions. It is evident that the solids volume fraction at the wall increases as the value of either the friction coefficient or the normal restitution coefficient is lowered. This is a result of less granular temperature generation at the walls producing the desired effect of more clusters forming at the walls. However, even at very low friction values the simulations are unable to reproduce the high solids volume fraction at the walls or the low volume fraction at the riser centre.

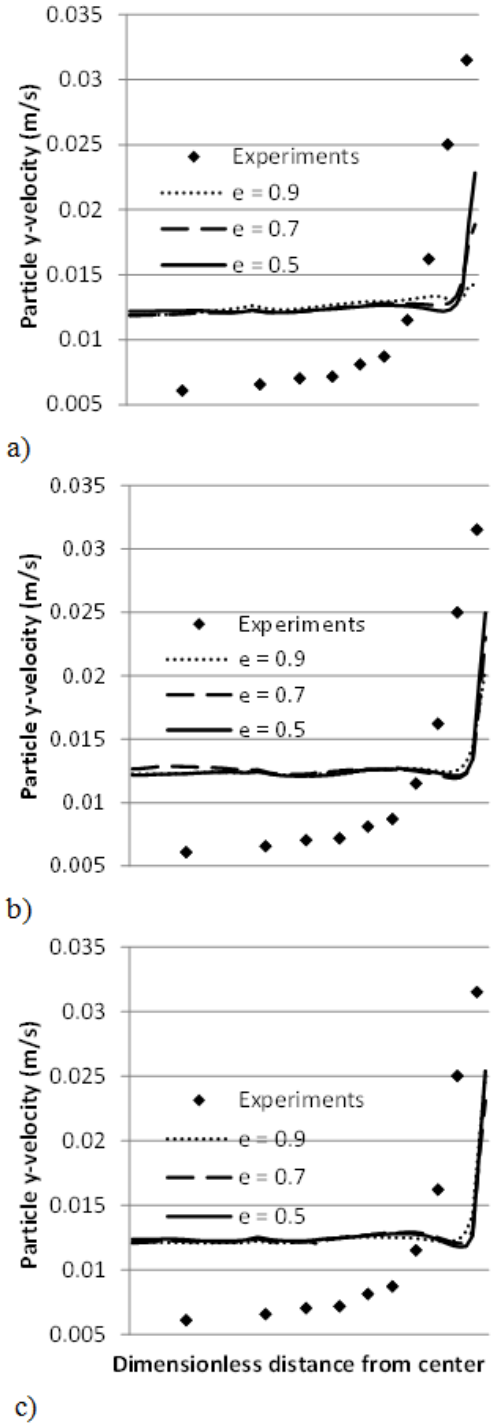

Figure 120 – Time-averaged particle volume fraction profiles for Case 5 using the Schneiderbauer model at different normal restitution coefficients for friction coefficient values of a) 0.5, b) 0.4 and c) 0.3

For Case 1 it was established that for these conditions the time-averaged volume fraction is insensitive to changes in the wall boundary conditions, therefore the solids y-velocity is shown in Figure 121. Here it is shown that, at the highest friction coefficient investigated ($\mu_w = 0.5$), a small reduction in solids velocity next to the wall is seen when lowering the normal restitution coefficient to a value of 0.5. This seemingly small effect created a considerable increase in the underestimation of the solids flux (39% to 67% by changing e_w from 0.7 to 0.5), shown in Figure 122. At lower friction coefficients, it can be seen that, by further decreasing the normal restitution coefficient, the simulations strongly overpredict down-flow at the walls. This leads to even greater underpredictions of the solids flux and even negative fluxes in the worst scenarios. To maintain the same gas flow rate through the system, the gas in the centre accelerates, leading to a considerable overprediction of the upwards solids velocity in the centre.

This significant change in behaviour is because combinations of sufficiently low values for the friction coefficient and normal restitution coefficient lead to the onset of sliding collisions at lower velocities. This causes clusters falling at the walls (normally considered to be in the non-sliding regime) to enter the sliding regime, where the shear stress is highly dependent on the friction coefficient and the normal restitution coefficient. In this way, the shear stress on solids clusters at the walls is reduced, resulting in the large downward flux of solids that is observed.

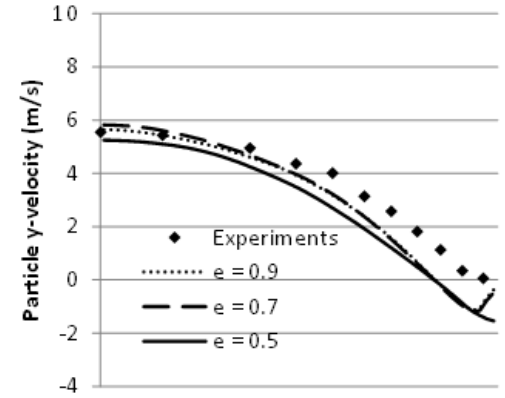

a)

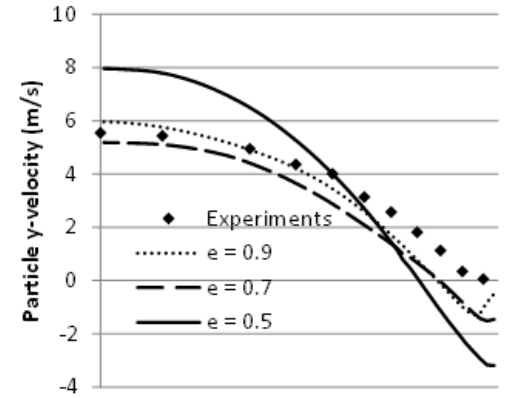

b)

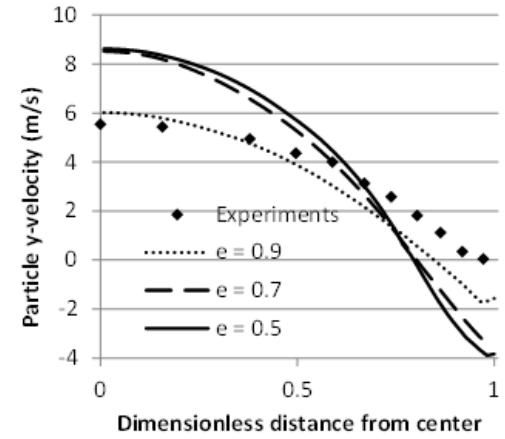

c)

Figure 121 – Time-averaged particle y-velocity profiles for Case 1 using the Schneiderbauer model at different normal restitution coefficients for friction coefficient values of a) 0.5, b) 0.4 and c) 0.3.

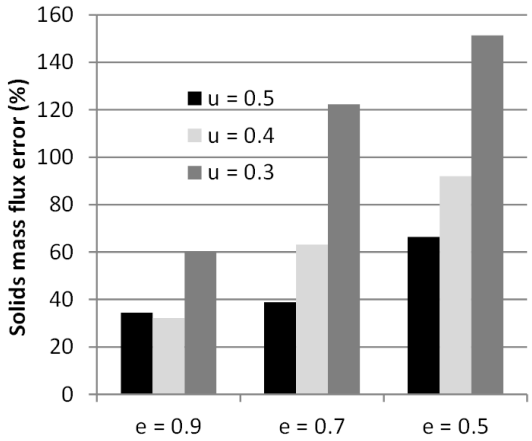

Figure 122 – Comparison of the percentage underprediction in the solids mass flux compared to experimental data for Case 1 when performing simulations using the Schneiderbauer model and different combinations of values for the friction coefficient and the normal restitution coefficient.

It can therefore be concluded that by lowering the values of the two parameters considered, the granular temperature generation is decreased and more clusters will form, lessening this shortcoming described in section C.2. However, this also decreases the shear stress at the walls, which can lead to too large downward solids flows at the walls. To obtain the optimum setting for the Schneiderbauer model in this study the settings that greatly overpredicts the downward flow of the solids at the walls in the dense case (Case 1) were first eliminated. This leaves the following settings as options: $\mu_w = 0.5, e_w = 0.9$, $\mu_w = 0.5, e_w = 0.7$ and $\mu_w = 0.4, e_w = 0.9$. From these alternatives, the setting was chosen that predicts the largest solids volume fraction at the wall, and therefore also the most clusters, in the fast and dilute case (Case 5). This gives the setting of $\mu_w = 0.4, e_w = 0.9$, with a particle volume fraction of 0.0206 at the wall. This represents only a minor change from the original setting ($\mu_w = 0.5, e_w = 0.9$). It was therefore not possible to substantially improve the general performance of the Schneiderbauer model further through parameter tuning, although this small modification did successfully increase the solids volume fraction at the walls in the more dilute cases (Cases 2, 3 and 5 in Figure 123).

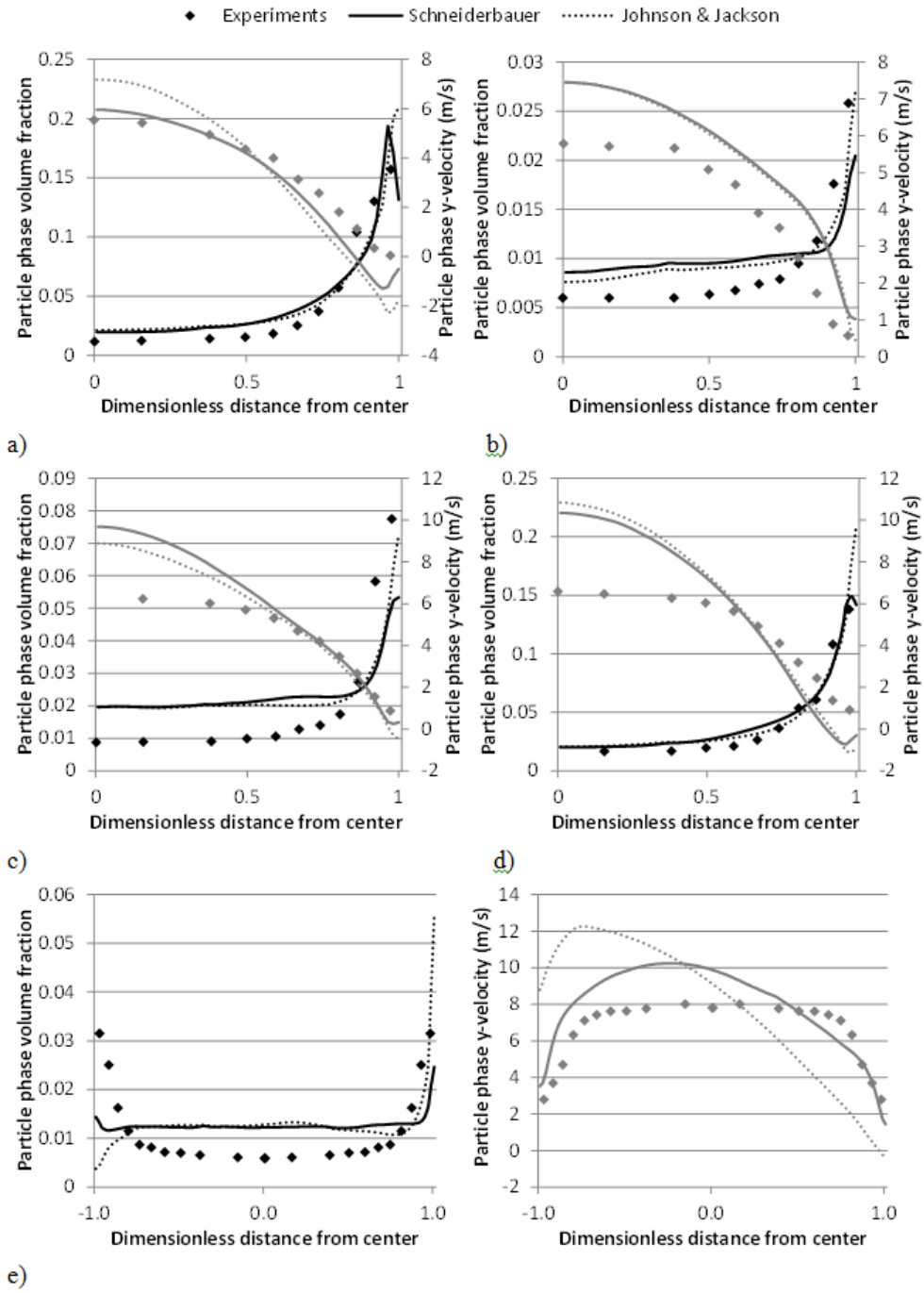

Figure 123 – Comparison of the performance of the optimised Schneiderbauer model to that of the Johnson and Jackson model using a specularity coefficient of 0.001 in a) Case 1, b) Case 2, c) Case 3, d) Case 4 and e) Case 5. Black is used for the time-averaged particle volume fraction, grey for the time-averaged particle y-velocity.

The ultimate performance of the Schneiderbauer model over the range of cases investigated is therefore comparable to that of the near free-slip implementation of the classic Johnson and Jackson model. However, it should again be emphasized that this near free-slip implementation is not generally applicable. For example, previous work conducted by the authors in a pseudo-2D setup [4, 89] showed that high wall friction on the large front and back walls must be included to reasonably predict experimentally measured solids velocity profiles. The primary advantage of the Schneiderbauer approach is that it can deliver reasonable results in fast and dilute flows with settings which can also achieve reasonable results in slow and dense flows.

Despite returning comparable mean performance, the near free-slip Johnson and Jackson implementation resulted in significantly different dynamic behaviour to that of the Schneiderbauer model. This can be seen from the video included with the publication based on this study [85]. Clusters tend to fall much faster next to the wall and the flow is more prone to asymmetric behaviour (seemingly permanent in Case 5). As an example, the root-mean-square of the near-wall particle y-velocity in the near free-slip Johnson and Jackson implementation is 127% and 164% greater than the Schneiderbauer prediction in Cases 3 and 4 respectively.

In addition, the larger strain rates in the near free-slip Johnson and Jackson implementation also leads to substantially higher granular temperatures (Figure 116). This tends to mask the error caused by underpredicted wall shear stress by increasing the granular viscosity and thereby the resistance to further strain. A lack of shear stress on the clusters at the wall is therefore compensated for by an increase in the viscous shear force exerted by the upward flow at the centre of the geometry.

It therefore becomes clear that more detailed experimental data on the dynamic behaviour of clusters at the walls will be required to properly evaluate model performance. Such work can be strongly recommended for future study.

C.4 Summary and Conclusions

Two formulations for the particle-wall boundary condition, the Johnson and Jackson and Schneiderbauer models, were investigated over a range of riser flow conditions in this study. The Johnson and Jackson model was tested both with reasonable partial slip settings (specularity coefficient of 0.111) and with near free-slip settings (specularity coefficient of 0.001), whereas the Schneiderbauer model was implemented with recommended coefficients. The recommended Schneiderbauer coefficients were shown to be close to optimal for the range of flow conditions considered in this study.

Results revealed that the Johnson and Jackson model with the larger specularity coefficient could only simulate denser and slower cases, failing completely in faster and more dilute cases. In such cases, this implementation of the Johnson and Jackson model strongly overpredicts the shear stress and the granular temperature generation at the walls, thus resulting in an unphysical self-strengthening generation of granular temperature in the near-wall regions.

This problem can be solved by specifying a very low specularity coefficient, as is commonly done in literature. However, this near free-slip condition is not physically reasonable and causes the Johnson and Jackson approach to perform poorly in dense flows, where the low shear stress at the walls allows solids to fall rapidly. In general, however, this approach performs surprisingly well when measured according to mean velocities and volume fractions. Despite this comparable mean performance, it was

shown that the dynamic cluster behaviour at the walls differs significantly between the two approaches. In particular, the near free-slip Johnson and Jackson implementation is more prone to an asymmetric flow situation where clusters fall rapidly on one side of the geometry while the rising gas is pushed to the other side. More detailed experimental data on the dynamic flow behaviour will therefore be required to draw definitive conclusions on this matter and is recommended for future study.

In general, however, the Schneiderbauer model appears to offer a clear improvement over the broadly deployed classic Johnson and Jackson model. As opposed to the Johnson and Jackson model, a single set of model parameters can give reasonable results both in dense, slow moving flows and dilute, fast moving flows. Additionally, it has the benefits of using measurable properties as parameters. It can therefore be recommended for future work in simulating fluidised bed risers.

D. Supplementary results and discussion

D.1 Process for developing a 3-marker model

This section briefly describes the process followed to derive the complex 3-marker closure in Chapter 3.4.2.6. To start, a closure model was derived for each filter size considered individually. This approach i) substantially reduces the number of bins considered for each fit and ii) removes the interactions with the filter size.

Furthermore, different contributions were analysed separately, slowly building up the closure model piece-by-piece. The gravitational contribution, k_1, could be isolated by simply considering the vertical direction for instances when both the filtered slip velocity and the drift GPM were zero. The slip contribution, $\tilde{v}^*_{slip,i}\left(1-10^{-k_2}\right)$, was closed by considering the lateral direction when the drift GPM was zero. Next, the gradient contribution, k_3, was investigated, based on the lateral direction. Firstly, the slip velocity independent part was obtained by considering instances when the filtered slip velocity was zero. Secondly, the symmetrical slip-GPM interaction contribution was identified by looking at instances when the filtered slip velocity and the drift GPM had the same sign. Lastly, the asymmetrical slip-GPM interaction contribution was identified by considering the remaining data and noting the deviation from symmetrical behaviour.

Following such a procedure, coefficient values were obtained for each filter size. Based on these values, filter size dependencies of the coefficients were identified and simple filter size dependent correlations were fitted for the coefficients. Using these correlations as initial values, a closure model could then be fitted to the entire set of data, including all filter sizes.

D.2 Marker evaluation for isotropic drag closures

Trends emerging from the use of the solids volume fraction variance as the second marker in an isotropic drag closure are displayed in Figure 124. It is clear that the use of this marker collapses the data onto a shape that will relatively easy to fit a correlation to. However, it is clear that the sample are not evenly distributed through the parameter space. This can be explained from the physical understanding that there will be a correlation between the two markers: a high variance in the solids volume fraction will most likely occur at intermediate filtered solids volume fractions. The sample count trends in the bottom two graphs in Figure 124 clearly show that samples at a high solids volume fraction variance are concentrated at intermediate filtered solids volume fractions, while samples at a high solids volume fraction variance are concentrated at low and high filtered solids volume fractions. It should be noted that for all plots of the filtered drag correction factor in this paper, bins with fewer than 500 samples, which will add scatter to the plots and obscure the trends in the data, are not shown.

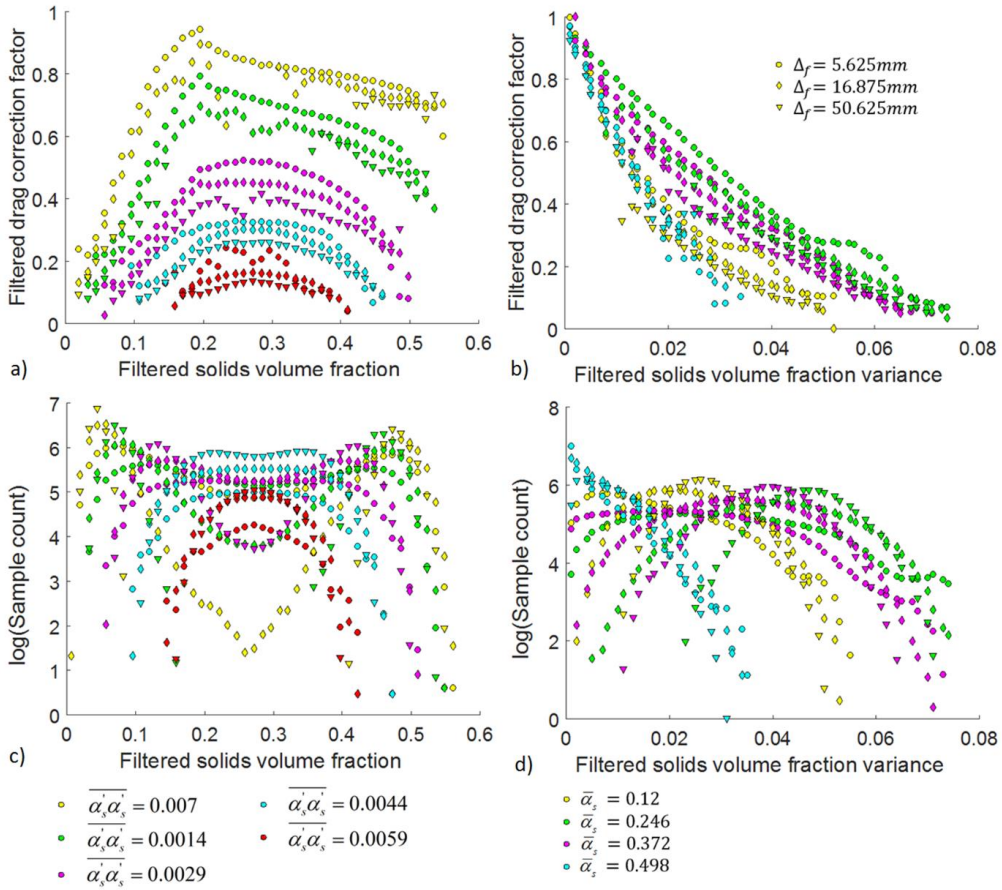

Figure 124 - The drag correction factor (top) and sample count (bottom) as a function of the filtered solids volume fraction (left) and the solids volume fraction variance in the filtered region (right).

Model fitting through a 2D parameter space with such unevenly distributed data must be done very carefully. If the closure model does not prevent the flow situation from entering regions of the parameter space where little or no sample data is available, large inaccuracies can result. Another observation from the top two graphs in Figure 124 is that there appears to be little or no filter size dependency in the trends. However, a preliminary closure model proposed for the solids volume fraction variance [90] is a strong function of the filter size. Also, the algebraic correlation for the solids volume fraction variance used in the models from Schneiderbauer [20] makes used of the filtering length scale in several places. This therefore implies that this approach does not remove the filter size as a variable.

Trends resulting from the use of the scaled filtered turbulent kinetic energy of the solid phase ($k_s^* = \frac{1}{2}\overline{\alpha_s^*}^2(\overline{1-\alpha_s^*})^2\frac{\overline{\alpha_s\vec{v}_s'\cdot\vec{v}_s'}}{\overline{\alpha_s}}$, where $\alpha_s^* = \frac{\alpha_s}{\alpha_{s,\max}}$) as the second marker are shown in Figure 125. In this case the data does not collapse into a shape that will be simple to model, neither is there a good distribution of data in the parameter space. The area where samples occur will depend on a complex interaction of the filter size, solids volume fraction and solids kinetic energy. In particular, samples appear to be

concentrated in a much narrower band of high filtered turbulent kinetic energy when the filter size becomes large.

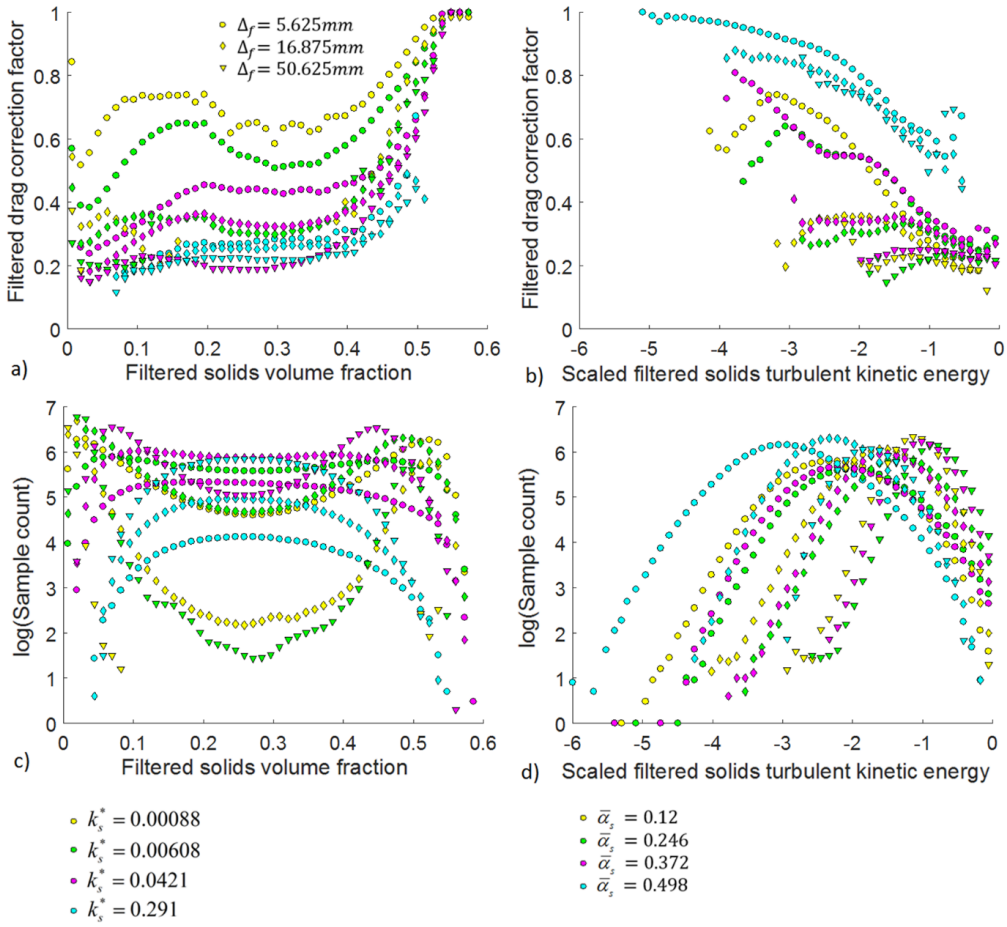

Figure 125 - The drag correction factor (top) and the sample count (bottom) as a function of the filtered solids volume fraction (left) and the base-10 log of the scaled solids turbulent kinetic energy in the filter region (right).

It should be noted that the use of these markers was only evaluated as part of the approach for fitting closure models from statistically analysed resolved simulation data, as followed in this study. In the Spatially-averaged TFM of Schneiderbauer [20], the drag closure, a function of the gas and solids turbulent kinetic energies and the solids volume fraction variance, is derived from theoretical considerations. As a result, the importance of an easily recognizable dependence of the drag on the markers and an even distribution of samples in the parameter space does not apply in the same way as it does here, since no closure fitting is involved.

E. Additional equations

E.1 Scalar transport equations

It is found that in both the filtered species and enthalpy transport equations contain a mesoscale scale dispersion rate term that requires closures. To keep the calculation of these sub-grid scalar fluctuations completely independent from the reactions and heat transfer, an additional scalar variable was solved for each phase. It was assumed that the diffusive flux for the scalars is zero, i.e., scalar quantities are not dispersed by sub-grid-scale fluid or particle motion, or molecular diffusion.

$$\frac{\partial}{\partial t}(\alpha_k \rho_k \phi_k) + \nabla \cdot (\alpha_k \rho_k \vec{v}_s \phi_k) = 0 \qquad \text{Equation 113}$$

A similar approach as in ref. [27] was used to impose a mean gradient. In this case, the following substitution was performed: $\phi_k = \phi_k^* + \xi x$, where the value of ξ was chosen as $100 m^{-1}$. Substituting this relation into Equation 113, the following conservation equation for the scalar is obtained:

$$\frac{\partial}{\partial t}(\alpha_k \rho_k \phi_k^*) + \nabla \cdot (\alpha_k \rho_k \vec{v}_s \phi_k^*) = -\alpha_k \rho_k \upsilon_{k,x} \phi_k^* \xi \qquad \text{Equation 114}$$

The transport equations are then solved for ϕ_k^*, thus introducing a source term proportional to the phase x-velocity, which is then used to calculate ϕ_k in each cell. The filtered statistics are then calculated for ϕ_k, for which there will always be a mean gradient in the x-direction.

Applying a spatial average to Equation 113, the filtered scaled transport equation is obtained:

$$\frac{\partial}{\partial t}(\rho_k \overline{\alpha_k} \widetilde{\phi_k}) + \nabla \cdot (\rho_k \overline{\alpha_k} \widetilde{\phi_k} \widetilde{\vec{v}_s}) = -\nabla \cdot (\rho_k \overline{\alpha_k \phi_k}'' \vec{v}_s'') \qquad \text{Equation 115}$$

The mesoscale scaled dispersion rate (right-hand side term) requires closure. Such a closure can then be used in the filtered species and the filtered enthalpy transport equations.

E.2 Energy transport equations

The enthalpy equation is solved to calculate the filtered heat transfer correction. Similar to Agrawal et al. [27], a source term in the solids and an equally-strong sink in the gas phase to conserve energy in the system, was used to maintain a temperature gradient between the phases. The constant Π is selected such that the particles are heated at a rate of $0.1°C/s$. The heat transfer coefficient was calculated from the correlation provided by Gunn [91]. It is assumed that heat conduction due to particle-particle collisions is negligible. Consequently, the following enthalpy transport equations are solved.

$$\frac{\partial}{\partial t}(\alpha_s \rho_s h_s) + \nabla \cdot (\alpha_s \rho_s h_s \vec{v}_s) = -\gamma(T_s - T_g) + \Pi \alpha_s \qquad \text{Equation 116}$$

$$\frac{\partial}{\partial t}(\alpha_g \rho_g h_g) + \nabla \cdot (\alpha_g \rho_g h_g \vec{v}_g) = \nabla \cdot (k_g \alpha_g \nabla T_g) + \gamma(T_s - T_g) + \Pi \frac{\langle \alpha_s \rangle_d}{\langle \alpha_g \rangle_d} \alpha_g \qquad \text{Equation 117}$$

The following thermal properties are considered for the present study: $k_g = 0.024\ W/(m.K)$, $C_{p_g} = 1.15 \times 10^3\ J/(kg.K)$ and $C_{p_s} = 1 \times 10^3\ J/(kg.K)$.

Performing a spatial average, the filtered energy equation for the solids phase becomes:

$$\frac{\partial}{\partial t}(\rho_s\overline{\alpha_s}\widetilde{h_s}) + \nabla\cdot(\rho_s\overline{\alpha_s}\widetilde{h_s}\widetilde{\vec{v}_s}) = -\overline{\gamma(T_s - T_g)} + \Pi\overline{\alpha_s} - \nabla\cdot(\rho_s\overline{\alpha_s h_s{}'\vec{v}_s{}'}) \qquad \text{Equation 118}$$

As can be seen, the source term, i.e., the second term on the right-hand side, does not require a closure, while the first term (i.e., that characterizing heat transfer between the phases) does. Similarly to the fluctuation term in the species equation (Equation 19), the third term on the right of Equation 118 can be modelled using the closure obtained from the filtered scalar transport equation (Equation 115).

E.3 Drift velocity formulation derivation

$$\overline{K_{gs}(v_{g,\iota} - v_{s,\iota})}$$

$$= \overline{\frac{K_{gs}}{\alpha_s}(\alpha_s v_{g,\iota} - \alpha_s v_{s,\iota})}$$

$$= C_1\overline{K_{gs}}\frac{\overline{(\alpha_s v_{g,\iota} - \alpha_s v_{s,\iota})}}{\bar{\alpha}_s}$$

$$= C_1 C_2 K_{\text{gs,hom}}\frac{\overline{(\alpha_s v_{g,\iota} - \alpha_s v_{s,\iota})}}{\bar{\alpha}_s}$$

$$= C_1 C_2 K_{\text{gs,hom}}\left(\overline{\frac{\alpha_s v_{g,\iota}}{\bar{\alpha}_s}} - \overline{\frac{\alpha_s v_{s,\iota}}{\bar{\alpha}_s}}\right)$$

$$= C_1 C_2 K_{\text{gs,hom}}\left(\overline{\frac{\alpha_s v_{g,\iota}}{\bar{\alpha}_s}} - \tilde{v}_{s,i}\right)$$

$$= C_1 C_2 K_{\text{gs,hom}}\left(\overline{\frac{(1-\alpha_g) v_{g,\iota}}{\bar{\alpha}_s}} - \tilde{v}_{s,i}\right)$$

$$= C_1 C_2 K_{\text{gs,hom}}\left(\frac{\bar{v}_g - \overline{\alpha_g v_{g,\iota}}}{\bar{\alpha}_s} - \tilde{v}_{s,i}\right)$$

$$= C_1 C_2 K_{\text{gs,hom}}\left(\frac{\bar{v}_g}{\bar{\alpha}_s} - \frac{\bar{\alpha}_g\tilde{v}_g}{\bar{\alpha}_s} - \tilde{v}_{s,i}\right)$$

Now consider:

$$\tilde{v}_g = \frac{\overline{\alpha_g v_{g,\iota}}}{\bar{\alpha}_g} = \frac{\overline{(\bar{\alpha}_g + \alpha_g')(v_{g,\iota} + v_{g,i}')}}{\bar{\alpha}_g} = \frac{\overline{\alpha_g v_{g,\iota}} + \overline{\alpha_g' v_{g,\iota}'}}{\bar{\alpha}_g} = \overline{v_{g,\iota}} + \frac{\overline{\alpha_g' v_{g,\iota}'}}{\bar{\alpha}_g}$$

$$\therefore \overline{v_{g,\iota}} = \tilde{v}_g - \frac{\overline{\alpha_g' v_{g,\iota}'}}{\bar{\alpha}_g}$$

Then,

$$C_1 C_2 K_{\text{gs,hom}}\left(\frac{\bar{v}_g}{\bar{\alpha}_s} - \frac{\bar{\alpha}_g\tilde{v}_g}{\bar{\alpha}_s} - \tilde{v}_{s,i}\right)$$

$$= C_1 C_2 K_{\text{gs,hom}}\left(\frac{\tilde{v}_g - \overline{\alpha_g' v_{g,\iota}'}/\bar{\alpha}_g}{\bar{\alpha}_s} - \frac{\bar{\alpha}_g\tilde{v}_g}{\bar{\alpha}_s} - \tilde{v}_{s,i}\right)$$

$$= C_1 C_2 K_{\text{gs,hom}} \left(\frac{(1-\bar{\alpha}_g)\tilde{v}_g}{\bar{\alpha}_s} - \frac{\overline{\alpha_g' v_{g,i}'}}{\bar{\alpha}_s \bar{\alpha}_g} - \tilde{v}_{s,i} \right)$$

$$= C_1 C_2 K_{\text{gs,hom}} \left(\tilde{v}_g - \tilde{v}_{s,i} - \frac{\overline{\alpha_g' v_{g,i}'}}{\bar{\alpha}_s \bar{\alpha}_g} \right)$$

F. Supplementary fTFM closures

F.1 Isotropic closure for the filtered drag force

Using the isotropic closure, the filtered drag force is closed as follows:

$$\widetilde{K_{gs}(\vec{v}_g - \vec{v}_s)} = CK_{gs,hom}(\widetilde{\vec{v}_g} - \widetilde{\vec{v}_s}) \quad \text{Equation 119}$$

The filtered drag correction factor, C, is modelled with the expression in Equation 45 and the following coefficients: $x_1 = 28.8$, $x_2 = 15.9$, $x_3 = 2.23$, $x_4 = 0.829$, $x_5 = 0.235$, $x_6 = 0.131$, $x_7 = 3.01$, $x_8 = 8.99$ and $\bar{\alpha}_{max} = 0.551$. A fit with $R^2 = 0.985$ is obtained against the binned data, as illustrated in Figure 126.

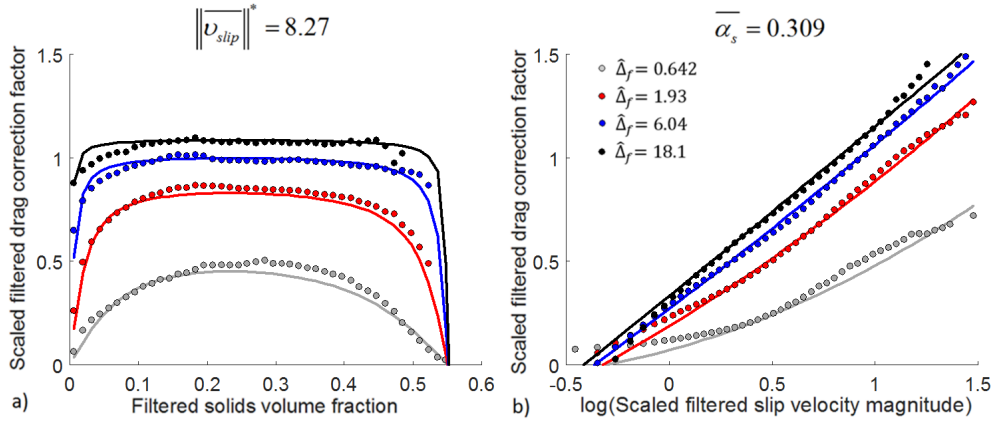

Figure 126 - The scaled filtered drag correction factor, $-\log(C)$, calculated based on the data for the direction aligned with gravity as a function of a) the filtered solids volume fraction and b) the scaled slip velocity magnitude for different dimensionless filter sizes. The symbols show the binned data obtained from resolved simulations and the lines the model predictions.

F.2 Solids mesoscale stresses closures

F.2.1 Isotropic filtered solids pressure for the mean normal solids mesoscale stresses

A model fit with $R^2 = 0.992$, shown in Figure 127, was obtained with the following coefficients: $x_1 = 0.774$, $x_2 = 1.72$, $x_3 = 0.403$, $x_4 = 0.610$, $x_5 = 1.19$, $x_6 = 0.684$, $x_7 = 1.57$, $x_8 = 1.00$, $x_9 = 0.331$, $x_{10} = -0.103$, $x_{11} = 0.123$, $x_{12} = 0.621$ $x_{13} = 2.89$, $x_{14} = 0.591$ and $x_{15} = 1.05$. In can be noted that, in the first term of Equation 77, the exponent of the filter size factor is 1.57, whereas the exponent of the shear rate factor ($x_8 + x_9 \Delta_f^{*x_{10}}$) ranges from 1.245 to 1.380 for the filter sizes considered in the model fit. These values are significantly lower than the exponents of roughly 2 that were previously reported in literature [13-15, 20]. The most likely reason for this is that the other filter sizes and shear rate dependencies in the proposed equation explains part of the variance in the filtered solids pressure usually modelled by only these two factors in the simpler Smagorinsky-type models.

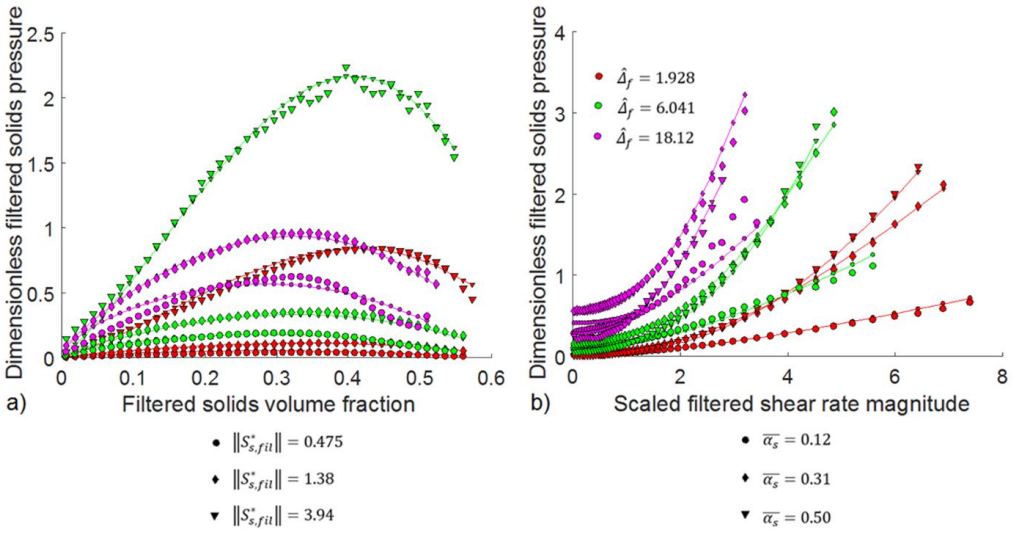

Figure 127 - Comparison of the binned data to the model fit (line with smaller symbols) for the dimensionless filtered solids pressure as a function of a) the filtered solids volume fraction and b) the scaled SRM.

F.2.2 Filtered solids viscosity for the deviatoric solids mesoscale stresses

A model fit with $R^2 = 0.990$, shown in Figure 128, was obtained with the following coefficients: $x_1 = 0.350$, $x_2 = 0.545$, $x_3 = 2.43$, $x_4 = 0.141$, $x_5 = 0.772$, $x_6 = 0.624$, $x_7 = 1.83$, $x_8 = 1.40$, $x_9 = 0.348$, $x_{10} = -0.0905$, $x_{11} = 0.130$, $x_{12} = -0.498$, $x_{13} = 3.58$, $x_{14} = 0.618$ and $x_{15} = 0.968$.

The mesoscale stress calculated from Equation 77 is related to the filtered solids viscosity as:

$$\hat{\mu}_{s,fil} = \frac{\hat{\tau}_{s,fil}}{\|\hat{S}_{s,fil}\|} \qquad \text{Equation 120}$$

, where $\hat{\mu}_{s,fil} = \frac{\mu_{s,fil}}{\rho_s v_t^3/g}$. It can be seen that due to the non-zero stresses at zero values of $\|\hat{S}_{s,fil}\|$, the filtered viscosity tends to increase rapidly as $\|\hat{S}_{s,fil}\|$ tends to zero, an effect that was not included in previous studies [13, 14]. Furthermore, it can be noted that for the filtered viscosity model fit in this study the exponent of the filter size factor is 1.83 and the exponent of the shear rate magnitude factor ranges from 0.668 to 0.794. These values are slightly lower than the values of roughly 2 and 1, respectively, previously reported in literature [13-15].

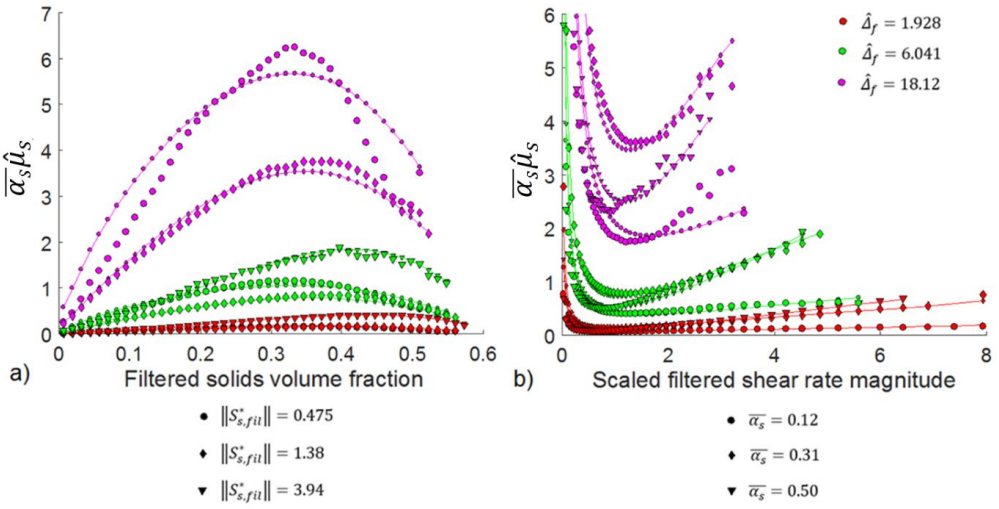

Figure 128 - Comparison of the binned data to the model fit (line with smaller symbols) for the filtered solids volume fraction times the dimensionless filtered solids viscosity as a function of a) the filtered solids volume fraction and b) the scaled SRM. The dependent variable is chosen to be consistent with the definition of the filtered solids viscosity used in literature [13, 14].

F.2.3 Isotropic closure for the lateral direction normal solids mesoscale stress

A model fit with $R^2 = 0.976$ was obtained with the following coefficients: $x_1 = 3.60$, $x_2 = 2.20$, $x_3 = 0.187$, $x_4 = 0.717$, $x_5 = 1.43$, $x_6 = 0.660$, $x_7 = 1.53$, $x_8 = 1.00$, $x_9 = 0.0594$, $x_{10} = -0.561$, $x_{11} = 11.11$, $x_{12} = 1.06$, $x_{13} = 0.0764$, $x_{14} = 0.582$ and $x_{15} = 1.03$.

F.2.4 Isotropic closure for the vertical direction normal solids mesoscale stress

A model fit with $R^2 = 0.972$ was obtained with the following coefficients: $x_1 = 0.327$, $x_2 = 1.32$, $x_3 = 1.37$, $x_4 = 0.459$, $x_5 = 1.08$, $x_6 = 0.651$, $x_7 = 1.70$, $x_8 = 1.00$, $x_9 = 0.638$, $x_{10} = -0.0652$, $x_{11} = 0.106$, $x_{12} = 0.432$, $x_{13} = 3.50$, $x_{14} = 0.605$ and $x_{15} = 1.11$.

F.2.5 Simplified anisotropic closure for the solids mesoscale stresses

The anisotropic closure model for the solids mesoscale stresses proposed in Chapter 3.6.3 can be simplified as follows when only the range of filter sizes, $\hat{\Delta}_f \geq 1.93$, is considered:

$$\begin{aligned}\hat{\Sigma}_{s,fil,ij} = {} & sign(\widehat{M}_{ij}) \left(\frac{2}{\pi}\right)^2 x_1 \operatorname{atan}\left(x_2 {\Delta_f^*}^{x_3} {\widehat{M}_{ij}}^{x_4} \overline{\alpha_s}\right) \\ & \times \operatorname{atan}\left(x_5 {\Delta_f^*}^{x_3} {\widehat{M}_{ij}}^{x_4} \max(x_6 - \overline{\alpha_s}, 0)\right) {\Delta_f^*}^{x_7} {\widehat{M}_{ij}}^{x_8} \\ & + D\left(\frac{2}{\pi}\right) x_9 \operatorname{atan}(x_{10}\overline{\alpha_s}) \max(x_6 - \overline{\alpha_s}, 0)\, {\Delta_f^*}^{x_{11}}\end{aligned} \qquad \text{Equation 121}$$

By removing some coefficients and by using others multiple times, the number of coefficients are reduced from 18 in Equation 89 to 11 in Equation 121. Still, an excellent fit to the binned data is obtained, with $R^2 = 0.985$ (compared to $R^2 = 0.989$ for the more elaborate model), using the following coefficients: $x_1 = 0.193$, $x_2 = 17.1$, $x_3 = -0.489$, $x_4 = -0.578$, $x_5 = 701$, $x_6 = 0.576$,

$x_7 = 2.15$, $x_8 = 1.19$, $x_9 = 0.268$, $x_{10} = 2.45$ and $x_{11} = 1.01$. Figure 129 and Figure 130 shows that the fit to the binned data is still good with this simplified closure model.

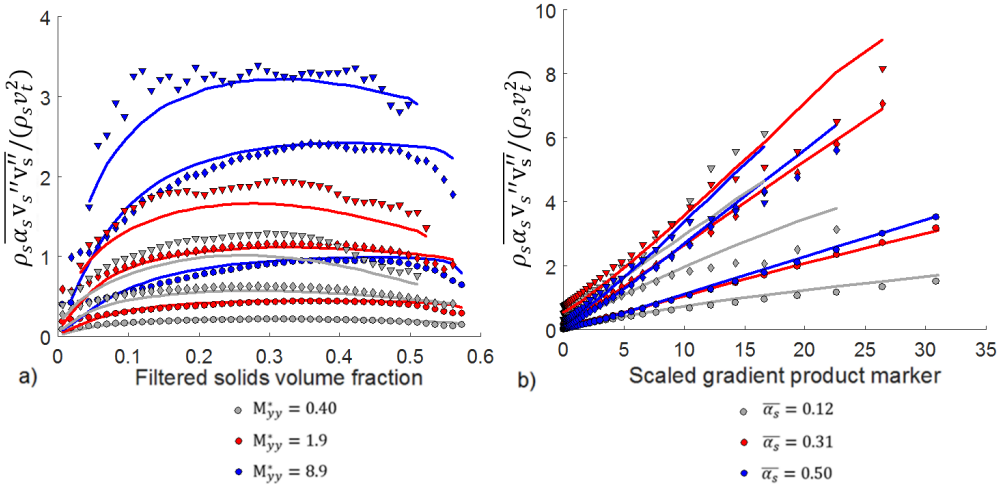

Figure 129 - Comparison of the binned data (symbols) to the model fit (lines) for the dimensionless y-direction diagonal component of the solids mesoscale stress as a function of a) the filtered solids volume fraction and b) the scaled gradient product marker.

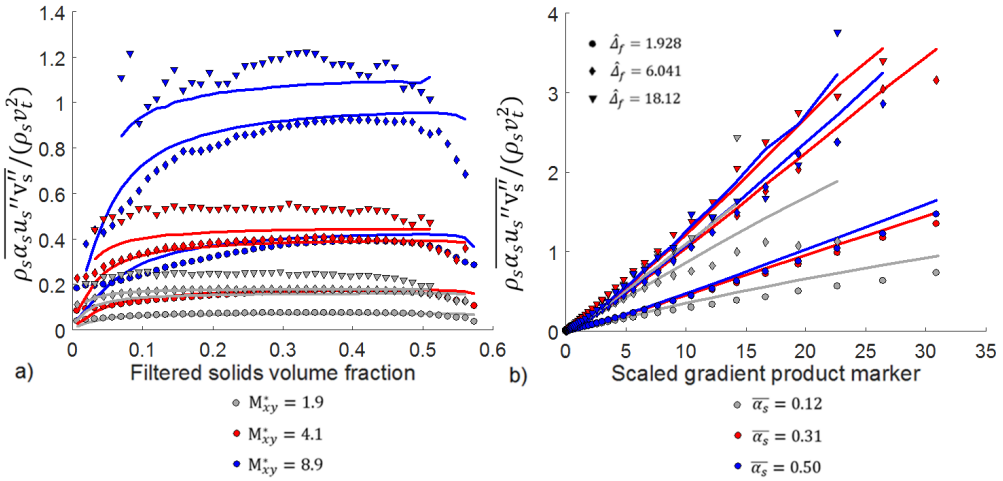

Figure 130 - Comparison of the binned data (symbols) to the model fit (lines) for the dimensionless off-diagonal component of the solids mesoscale stress as a function of a) the filtered solids volume fraction and b) the scaled gradient product marker.

F.3 Filtered reaction rate closures

F.3.1 2-marker non-locally corrected reaction rate correction factor

The non-locally corrected reaction rate correction factor is defined by Holloway and Sundaresan [28] as:

$$\mathrm{R} = \frac{\overline{\alpha_s \kappa_A} - m_2 \nabla \overline{\alpha_s}^T \cdot \nabla \widetilde{\kappa_A}}{\overline{\alpha_s} \tilde{\kappa}_A} \qquad \text{Equation 122}$$

where $m_2 = \Delta_f^2/12$, and Δ_f is the filter size. It was found that this quantity could be closed with the expression in Equation 94, using the following coefficients: $x_1 = 7.93$, $x_2 = -0.0925$, $x_3 = 17.3$, $x_4 = -0.00372$, $x_5 = 0.563$, $x_6 = 0.137$, $x_7 = 0.777$, $x_8 = 1.01$ and $x_9 = 0.351$. The fit of the model predictions to the binned data is shown in Figure 131. It can clearly be seen, compared to Figure 38, that the non-local correction substantially reduces the correction in the reaction rate. Additionally, the dependency on the scaled filtered slip velocity magnitude is of lesser of importance when the non-local correction is applied. It can therefore be speculated that the slip velocity magnitude dependency compensates for the effect of the gradients in the flow field on the filtered reaction rate.

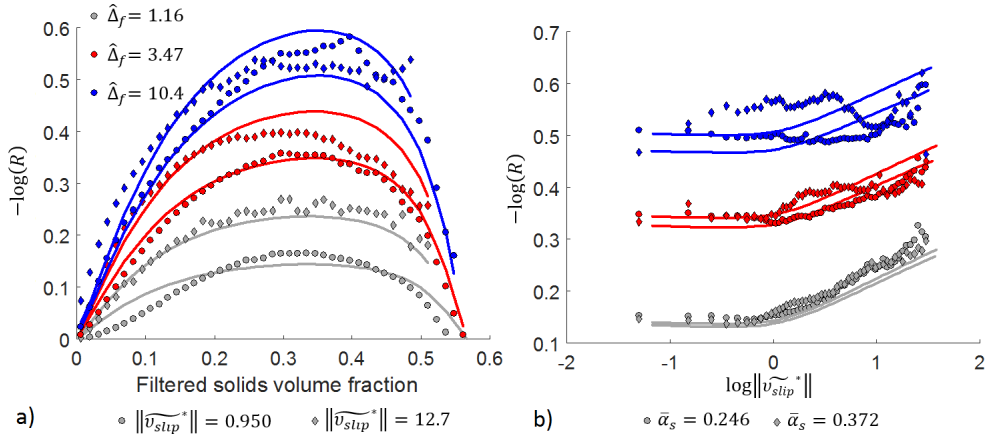

Figure 131 - The scaled non-locally correction reaction rate correction factor, $-log(R)$, as a function of a) the filtered solids volume fraction and b) the scaled filtered slip velocity magnitude. The symbols show the binned data from the resolved simulations and the lines the model predictions.

F.3.2 1-marker reaction rate correction factor

The 1-marker model for the reaction rate correction factor is fitted by simply neglecting the scaled filtered slip velocity magnitude term in Equation 94. Consequently:

$$-\log(R) = \left(\frac{2}{\pi}\right)^3 \operatorname{atan}\left(x_1 \Delta_f^{*x_2} \bar{\alpha}_s\right) \operatorname{atan}\left(x_3 \Delta_f^{*x_4} \max(\mathrm{x}_5 - \bar{\alpha}_s, 0)\right) x_6 \operatorname{atan}(x_7 \Delta_f^*) \qquad \text{Equation 123}$$

The fit shown in Figure 132 is obtained with the following coefficients: $x_1 = 3.19$, $x_2 = 0.214$, $x_3 = 8.39$, $x_4 = 0.536$, $x_5 = 0.564$, $x_6 = 1.23$ and $x_7 = 1.54$.

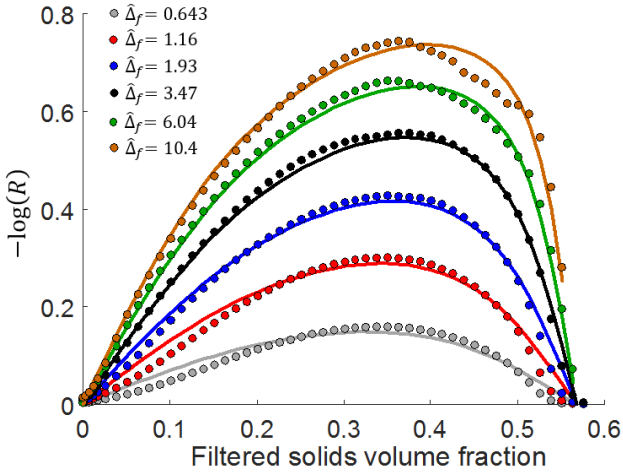

Figure 132 - The scaled reaction rate correction factor, $-log(R)$, as a function of the filtered solids volume fraction and the filter sizes considered in the model fit. The symbols show the binned data from the resolved simulations and the lines the model predictions.

G. Filtered TFM closures used in the validation study

G.1 NTNU model

G.1.1 Filtered interphase momentum exchange

The filtered drag and mesoscale interphase forces are lumped together and approximated by the filtered drag correction factor (C) applied to the Huilin-Gidaspow drag law [36].

$$\overline{K_{gs}(\vec{v}_g - \vec{v}_s)} - \overline{\alpha_s' \nabla p'} = C K_{gs}(\widetilde{\vec{v}_g} - \widetilde{\vec{v}_s}) \quad \text{Equation 124}$$

$$-\log(C) = \operatorname{atan}(x_1 \Delta_f^* \bar{\alpha}_s) \operatorname{atan}\left(x_2 \Delta_f^* (\bar{\alpha}_{\max} - \bar{\alpha}_s)\right) \operatorname{atan}(x_3 \Delta_f^*) \left(\frac{2}{\pi}\right)^3 \times \left(x_4 \log\left\|\widetilde{v_{slip}}^*\right\| + x_5 {\Delta_f^*}^{x_6} + x_7 \left(\log\left\|\widetilde{v_{slip}}^*\right\|\right)^2 \left(1 - \frac{\operatorname{atan}(x_8 \Delta_f^*)}{\pi/2}\right)\right) \quad \text{Equation 125}$$

$$-\log(C) = 0 \qquad \text{if} \quad \Delta_f^* < 0 \quad \text{or} \quad \bar{\alpha}_s > \bar{\alpha}_{\max}$$

$x_1 = 36.59, x_2 = 22.63, x_3 = 1.676, x_4 = 0.8350, x_5 = 0.1399, x_6 = 0.1881,$
$x_7 = 1.329, x_8 = 3.280, \hat{\Delta}_{fine} = 0.1286$ and $\bar{\alpha}_{max} = 0.5511.$

$$\Delta_f = 2V^{1/3} \quad \text{Equation 126}$$

$$\hat{\Delta}_f = \frac{\Delta_f}{v_t^2/g} \quad \text{Equation 127}$$

$$v_t = 0.2038 \text{ m/s}$$

$$\Delta_f^* = \hat{\Delta}_f - \hat{\Delta}_{fine} \quad \text{Equation 128}$$

$$\left\|\widetilde{v_{slip}}^*\right\| = \frac{\left\|\widetilde{v_{slip}}\right\|}{\bar{v}_{ss\_slip}} \quad \text{Equation 129}$$

Instead of the conventional scaling via the single particle settling velocity, the steady state sedimentation velocity $(\bar{v}_{ss\_slip})$ is used to scale the filtered slip velocity magnitude. This value is approximated from the Huilin-Gidaspow drag law:

$$\bar{v}_{ss_{slip},WY} = \frac{\mu_g \overline{\mathrm{Re}}_{ss_{slip},WY}}{\rho_g d_p} \quad \text{Equation 130}$$

$$\overline{\mathrm{Re}}_{ss\_slip,WY} \approx \frac{A}{\bar{\alpha}_g (1 + 0.2296 A^{0.5329})^{0.7642}} \quad \text{Equation 131}$$

$$A = \frac{\bar{\alpha}_g^{3.65} g(\rho_s - \rho_g) d_p^3 \rho_g}{18 \mu_g^2} \quad \text{Equation 132}$$

$$\bar{v}_{ss\_slip,Ergun} = \frac{-b + \sqrt{b^2 - 4ac}}{2a} \quad \text{Equation 133}$$

$$a = 1.75 \frac{\rho_g \bar{\alpha}_s}{d_p} \quad \text{Equation 134}$$

$$b = 150\frac{\bar{\alpha}_s^2 \mu_g}{\bar{\alpha}_g d_p^2} \quad \text{Equation 135}$$

$$c = -(\rho_s - \rho_g)\bar{\alpha}_s g \quad \text{Equation 136}$$

$$\psi = \frac{1}{2} + \frac{\arctan\left(262.5(\bar{\alpha}_s - 0.2)\right)}{\pi} \quad \text{Equation 137}$$

$$\bar{v}_{ss\_slip} = \psi \bar{v}_{ss\_slip,Ergun} + (1-\psi)\bar{v}_{ss\_slip,WY} \quad \text{Equation 138}$$

G.1.2 Solids mesoscale stresses

The different components of the solids mesoscale stress tensor are described as follows:

Normal stresses (nondimensionalized by $v_t^2 \rho_s$):

$$\hat{\Sigma}_{s,fil,ii} = \left(\frac{2}{\pi}\right)^2 x_1 \text{atan}\left(x_2 \Delta_f^{*\,x_3} \widehat{M}_{ii}^{\;x_4}(\bar{\alpha}_s + x_5)\right) \times \text{atan}\left(x_6 \Delta_f^{*\,x_7} \widehat{M}_{ii}^{\;x_8}(x_9 - \bar{\alpha}_s)\right) \Delta_f^{*\,x_{10}} \widehat{M}_{ii}^{\;x_{11} + x_{12}\Delta_f^{*\,x_{13}}} + \left(\frac{2}{\pi}\right)^2 x_{14} \text{atan}(x_{15}\bar{\alpha}_s)\text{atan}(x_{16}(x_{17} - \bar{\alpha}_s))\Delta_f^{*\,x_{18}} \quad \text{Equation 139}$$

$x_1 = 0.550$, $x_2 = 2.91$, $x_3 = 0.102$, $x_4 = -0.515$, $x_5 = 0.0358$, $x_6 = 3.04$, $x_7 = 0.960$, $x_8 = 0.240$, $x_9 = 0.691$, $x_{10} = 1.75$, $x_{11} = 0.80$, $x_{12} = 0.608$, $x_{13} = -0.219$, $x_{14} = 53.2$, $x_{15} = 2.49$, $x_{16} = 0.00719$, $x_{17} = 0.604$ and $x_{18} = 1.08$

Shear stresses (nondimensionalized by $v_t^2 \rho_s$):

$$\hat{\Sigma}_{s,fil,ij} = \left(\frac{2}{\pi}\right)^2 x_1 \text{atan}\left(x_2 \Delta_f^{*\,x_3} \widehat{M}_{ij}^{\;x_4}(\bar{\alpha}_s + x_5)\right) \times \text{atan}\left(x_6 \Delta_f^{*\,x_7} \widehat{M}_{ij}^{\;x_8}(x_9 - \bar{\alpha}_s)\right) \Delta_f^{*\,x_{10}} \widehat{M}_{ij}^{\;x_{11} + x_{12}\Delta_f^{*\,x_{13}}} \quad \text{Equation 140}$$

$x_1 = 0.630$, $x_2 = 1.76$, $x_3 = 0.0844$, $x_4 = -0.394$, $x_5 = 0.0767$, $x_6 = 4.89$, $x_7 = 0.514$, $x_8 = 0.157$, $x_9 = 0.685$, $x_{10} = 1.79$, $x_{11} = 0.80$, $x_{12} = 0.528$ and $x_{13} = -0.167$.

The new gradient product marker is defined as follows (non-dimensionalized):

$$\widehat{M}_{ij} = \frac{2}{3}\bar{\alpha}_s \left(\frac{d\widetilde{v_{s_i}}}{dx}\frac{d\widetilde{v_{s_j}}}{dx} + \frac{d\widetilde{v_{s_i}}}{dy}\frac{d\widetilde{v_{s_j}}}{dy} + \frac{d\widetilde{v_{s_i}}}{dz}\frac{d\widetilde{v_{s_j}}}{dz}\right)\frac{v_t^2}{g^2} \quad \text{Equation 141}$$

G.2 Sarkar model

G.2.1 Filtered interphase momentum exchange

The same drag correction factor philosophy is used as in the NTNU model, only using the Wen-Yu drag law [38] instead of the Huilin-Gidaspow drag law.

$$C = 1 - \min\left[\left(a + \frac{b}{\left\|\widetilde{v_{slip}}\right\|/v_t}\right)\overline{\alpha_s}^{\left(c+\frac{d}{\left\|\widetilde{v_{slip}}\right\|/v_t}\right)}, 0.97\right]$$ Equation 142

$$a = 0.9506,\ b = 0.1708,\ c = 0.049\left(\frac{1}{\bar{\Delta}_f} - 1\right) \text{ and } d = 0.3358$$

G.2.2 Filtered solids stresses

A dedicated model is provided for the filtered kinetic theory solids pressure and viscosity:

$$\bar{p}_s = 0.01797\rho_s\Delta_f^2\bar{S}_s^2\frac{\bar{\alpha}_s^{1.645}}{\bar{\alpha}_{s,max} - \bar{\alpha}_s}$$ Equation 143

$$\bar{\alpha}_{s,max} = 0.63$$

$$\bar{\mu}_{kin,s} = 0.00307\rho_s\left(\frac{g}{v_t^2}\right)^{-6/7}\Delta_f^{8/7}\bar{S}_s\frac{\bar{\alpha}_s^{1.544}}{\bar{\alpha}_{s,max} - \bar{\alpha}_s}$$ Equation 144

$$\bar{\bar{\tau}}_s \approx \bar{\mu}_{kin,s}\bar{s}_s$$ Equation 145

$$\bar{s}_s = [\nabla\tilde{v}_i + (\nabla\tilde{v}_i)^T] - \frac{2}{3}(\nabla\cdot\tilde{v}_i)\bar{\bar{I}}$$ Equation 146

$$\bar{S}_s = \sqrt{\bar{s}_s{:}\,\bar{s}_s/2}$$ Equation 147

The solids mesoscale stresses are approximated as follows:

$$\rho_s\overline{\alpha_s\vec{v}_s''\vec{v}_s''} \approx \bar{p}_{meso,s}\bar{\bar{I}} + \bar{\mu}_{meso,s}\bar{s}_s$$ Equation 148

$$\bar{p}_{meso,s} = 0.0236\rho_s\left(\frac{g}{v_t^2}\right)^{3/7}\Delta_f^{17/7}\bar{S}_s^2\frac{\bar{\alpha}_s^{1.115}}{\bar{\alpha}_{s,max} - \bar{\alpha}_s}$$ Equation 149

$$\bar{\mu}_{meso,s} = 0.02518\rho_s\left(\frac{g}{v_t^2}\right)^{-2/7}\Delta_f^{12/7}\bar{S}_s\frac{\bar{\alpha}_s^{1.123}}{\bar{\alpha}_{s,max} - \bar{\alpha}_s}$$ Equation 150

G.3 Igci model

G.3.1 Interphase momentum exchange

Similar to the Sarkar model, the Igci model applies the drag correction factor to the Wen-Yu [38] drag law.

$$C = 1 - \frac{\left(\frac{g\Delta_f}{v_t^2}\right)^{1.6}}{\left(\frac{g\Delta_f}{v_t^2}\right)^{1.6} + 0.4}h$$ Equation 151

$$h = \begin{cases} 2.7\bar{\alpha}_s^{0.234}, & \bar{\alpha}_s < 0.0012 \\ -0.019\bar{\alpha}_s^{-0.455} + 0.963, & 0.0012 \le \bar{\alpha}_s < 0.014 \\ 0.868\exp(-0.38\bar{\alpha}_s) - 0.176\exp(-119.2\bar{\alpha}_s), & 0.014 \le \bar{\alpha}_s < 0.25 \\ -4.59 \times 10^{-5}\exp(19.75\bar{\alpha}_s) + 0.852\exp(-0.268\bar{\alpha}_s), & 0.25 \le \bar{\alpha}_s < 0.455 \\ (\bar{\alpha}_s - 0.59)(-1501\bar{\alpha}_s^3 + 2203\bar{\alpha}_s^2 - 1054\bar{\alpha}_s + 162), & 0.455 \le \bar{\alpha}_s \le 0.59 \\ 0, & \bar{\alpha}_s > 0.59 \end{cases} \quad \text{Equation 152}$$

G.3.2 Solids stresses

Models for mesoscale solids pressure and viscosity are added to the kinetic theory pressure ($p_{s,p}$) and viscosity ($\mu_{s,p}$) at a solids volume fraction below 0.59:

$$\frac{p_{meso,s}}{\rho_s v_t^2} = \begin{cases} \frac{p_{s,p}}{\rho_s v_t^2} + X_p(\alpha_s - 0.59)(-1.69\alpha_s - 4.61\alpha_s^2 + 11\alpha_s^3), & \alpha_s \le 0.59 \\ \frac{p_{s,p}}{\rho_s v_t^2}, & \alpha_s > 0.59 \end{cases} \quad \text{Equation 153}$$

$$X_p = 0.48\left(\frac{g\Delta_f}{v_t^2}\right)^{0.86}\left(1 - \exp\left(-\frac{g\Delta_f}{1.4v_t^2}\right)\right) \quad \text{Equation 154}$$

$$\frac{\mu_{meso,s}g}{\rho_s v_t^3} = \begin{cases} \frac{\mu_{s,p}g}{\rho_s v_t^3} + X_\mu(\alpha_s - 0.59)(-1.22\alpha_s - 0.7\alpha_s^2 - 2\alpha_s^3), & \alpha_s \le 0.59 \\ \frac{\mu_{s,p}g}{\rho_s v_t^3}, & \alpha_s > 0.59 \end{cases} \quad \text{Equation 155}$$

$$X_\mu = \frac{0.37\left(\frac{g\Delta_f}{v_t^2}\right)^{1.22}}{0.28\left(\frac{g\Delta_f}{v_t^2}\right)^{0.43} + 1} \quad \text{Equation 156}$$

G.3.3 Wall corrections

The Igci model employs dedicated wall corrections for the interphase momentum exchange coefficient and the solids mesoscale stresses based on the distance from the wall (x):

$$K_{sg,eff} = \frac{K_{sg}}{1 + 6.0\exp(-0.4x_d)} \quad \text{Equation 157}$$

$$p_{meso,s,eff} = \frac{p_{meso,s}}{1 + 9.1\exp(-0.45x_d)} \quad \text{Equation 158}$$

$$\mu_{meso,s,eff} = \frac{\mu_{meso,s}}{1 + 5.6\exp(-0.15x_d)} \quad \text{Equation 159}$$

$$x_d = \frac{xg}{v_t^2} \quad \text{Equation 160}$$